Numerical Simulation and Experimental Investigations for Mechanical Scribing of $\mathbf{Cu(In,Ga)Se_2}$ Thin-Film Solar Cells

Dissertation

zur Erlangung des Doktorgrades der Ingenieurwissenschaften
(Dr.-Ing.)

der

Naturwissenschaftlichen Fakultät II
Chemie, Physik und Mathematik

der Martin-Luther-Universität
Halle-Wittenberg

vorgelegt von

Herr Shashi Bahl
geb. am 20.10.1977 in Gurdaspur, India

Gutachter: Prof. Dr. Roland Scheer
Prof. Dr. Jörg Bagdahn
Prof. Dr. Hans Joachim Möller

Tag der öffentlichen Verteidigung: 02.03.2016

Contents

1 Introduction

This chapter provides a brief outline of the mechanical structuring of $\mathrm{Cu(In,Ga)Se_2}$ (CIGS) thin-film solar modules in which the problem setting is done. After this, the objective of present work is defined and an outline of the thesis structure is summarized.

1.1 Motivation

Solar cells available today are produced by a number of techniques and are based on different materials. Important examples are cells based on crystalline Si or III-V semiconductor materials, those produced by thin-film techniques, or those belonging to the group of dye-sensitized or organic solar cells. All of these different types of photovoltaic cells have different advantages and disadvantages. Ever since the introduction of photovoltaic (PV) cells for electrical power generation by Bell Laboratories in 1954 [1], one of the main hurdles to overcome is to produce electricity at a cost that can compete with other sources. This is where thin-film technology can make a great difference. The PV cell material is deposited on the surface of a structural component which is in most cases a plate of glass. The amount of semiconductor material can be dramatically reduced since it is no longer required to present mechanical strength. Thin-film solar cell is a promising technology in order to achieve a significant cost reduction in materials, large area deposition capability and the use of cheap and flexible substrates. CIGS material has become an exciting material for the production of thin film photovoltaic panels. The main advantages of commercial CIGS PV modules are that they have more efficiency, are relatively non-toxic and environmentally benign, and have a very stable performance over time and environmental exposure. CIGS-based solar cells have yielded highest efficiencies of all the thin-film solar cells to date which indicates the bright future for CIGS. The CIGS thin-film solar cells on soda lime glass as substrate hold the laboratory world record of 21.7% as claimed by the German Center for Solar Energy and Hydrogen Research Baden-Württemberg [2].

Since CIGS is a relatively new material, there are some challenges associated with this material. Monolithic cell isolation and series interconnection are the most important manufacturing processes in the fabrication of thin-film solar cells. The interconnected modules are manufactured with thin-film technology in a very elegant way by sandwiching the semiconductor material between two conducting layers and isolating these layers from each other and then this is repeated at regular intervals of time to make up consecutive cells [3]. Interconnects must have low series resistance and high shunt resistance, and the dead area between cells should be minimum. The

CIGS thin-film solar cell basically consists of three components. These three components are: 1) a metal back contact which is made from molybdenum, 2) the CIGS absorber layer which is the photovoltaic active layer and 3) the front contact consisting of a ZnO layer. Substrate which is made of soda lime glass material supports the solar cell mechanically. The ZnO front contact consists of two separately sputtered ZnO layers where the first layer is a thin, undoped ZnO buffer layer and the second is an aluminium doped ZnO layer. There is a very thin-film of CdS buffer layer between the CIGS and the ZnO layers.

The automation steps such as lay-up and soldering which are necessary for traditional wafer-based cell assembly are excluded by the use of monolithic cell isolation and series interconnection which helps in simplifying the production process. The adjacent cells are connected together during the course of material deposition. This is achieved with the help of intermediate patterning steps that allow back contact isolation, back-to-front contact interconnection and finally front contact isolation. For PV modules based on CIGS, laser is used for scribing of the metal back contact isolating pattern (P1), however a mechanical tip is used most commonly in order to scribe back-to-front contact interconnecting pattern (P2) and front contact isolation pattern (P3). The interconnect zone occupied by the scribe lines is inactive as a solar cell and therefore should be minimized. This can be achieved by placing these scribe lines as close to each other as possible without risking short circuiting of adjacent cells or shunting between front and back contacts. Another advantage of monolithically integrated solar modules is that the cell width which is the distance between interconnect zones can be varied in order to tune the current/voltage output of a certain size.

Laser scribing has some advantages from the processing point of view. Since there is no tool wear, the process is stable over time, and does not require dressing steps at regular intervals. It is a non-contact process which limits the mechanical stress on the materials that are machined. It is suitable for high speed mass production with a scribing speed of around 1 m/s. The scribe widths are narrower and the surrounding material is less damaged [4–6]. Compaan et al [5, 7, 8] have presented thorough evaluations of the use of several different laser systems for the purpose of scribing thin-film PV modules. It was found that CIGS can be selectively removed without damaging the underlying Mo layer, however the presence of melted CIGS at the edges of the grooves was pointed out as a problem which could cause short-circuiting and shunting of cells. So, laser scribing has two drawbacks related to manufacturing. Firstly the laser scribing leaves a heat-affected-zone (HAZ) around the scribe which can cause poor isolation between cells and low shunt resistance and secondly it leaves high protruded ridges along the edge of the scribe line, which contributes to electrical shorts [5]. Due to these drawbacks, the mass production of CIGS thin-film solar cells has until now defied the traditional P2 and P3 laser scribing processes [9] that have proven so valuable in creating the monolithic series interconnect structures required to achieve useful working voltage and current in large scale thin-film amorphous silicon and CdTe PV modules. While there is a state-of-the-art laser process for the CIGS P1 scribe that utilizes 1064 nm wavelength and nanosecond pulses, until now the lasers used have proven completely ineffective

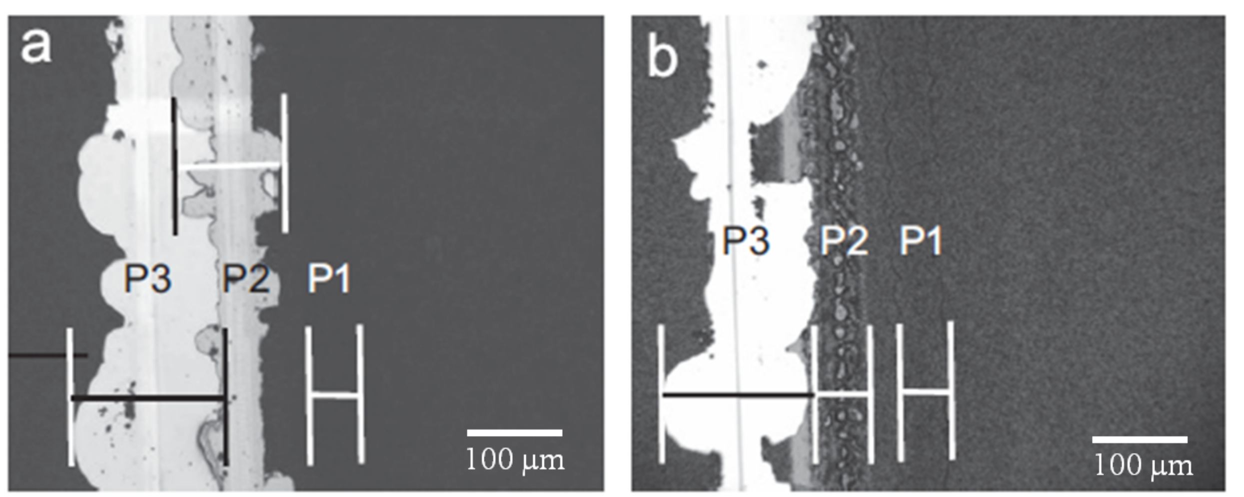

Figure 1.1: *Optical microscope images showing the dead zone (interconnect zone) to compare (a) standard mechanical patterning with (b) laser. The laser P2 scribe is approximately 60 μm wide while the mechanical P2 scribe reaches about 150 μm which is almost three times that [10].*

for the P2 and P3 scribes. With the failure of laser based processes, mechanical scribing with a force-controlled stylus has become the method of choice to obtain P2 and P3 structures which are required to achieve the monolithic serial interconnection and isolation respectively between the neighboring cells.

Mechanical tip is used for the material removal in mechanical scribing of thin-films. This is a direct contact method which induces mechanical stress and damage to the material. The state-of-the-art mechanical patterning of P2 and P3 causes chipping and broadens the dead zone. Figure 1.1 presents the comparison between the width of P2 scribes performed with mechanical and laser scribing respectively [10]. The laser-formed scribe lines are well defined and the width of scribe is about 60 μm. However, the width of P2 mechanical scribe is about 150 μm and the scribe lines have an uneven appearance due to the chipping at the CIGS/Mo interface. Also, the width of P3 mechanical scribe is about 200 μm. The non-deterministic nature of the material removal mechanism in mechanical scribing yields wide, irregular scribe lines that necessitate large spacing between adjacent scribes.

It has been reported that mechanical scribing of CIGS thin-film solar cells results in bigger dead area, partly because it requires higher safety margins between the scribes due to the chipping of the layers [11]. The increased dead zone thereby increases non-productive area (dead area) which results in the loss of active solar cell area. As a result, the CIGS modules suffer decreased efficiency [12]. So, the combined surface of the scribes P1, P2 and P3 make up the entire loss of active area of the solar module. The narrower the scribes and the closer they are spaced together, the more efficient the solar module, as solar module efficiency is based on the entire module area. Extensive investigations have been done regarding the laser scribing, however not much research work has been carried out till now with regard to mechanical scribing of CIGS thin-film solar cells. Therefore, the mechanism of material removal in the process of mechanical scribing needs to be analyzed and understood. The key challenge is how to enhance the performance of mechanical scribing processes for P2 and P3 structures in order to reduce the scribe width which will thereby decrease the non-productive area (dead area) and hence increase the effective solar cell area available for power generation resulting in increase of solar cell efficiency.

1.2 Objective of the work

The narrower the P2 and P3 mechanical scribes and the closer they are spaced together, the more efficient will be the solar module as solar module efficiency is based on the entire module area. The ultimate goal is to obtain the reproducible, clean scribe lines with least or in the best case no chipping, which may result in decreased dead area leading to increased efficiency of the CIGS solar module. The objective of present work is to increase the understanding of the processes surrounding the mechanical scribing of CIGS thin-film solar cells with the help of experimental investigations and numerical simulation. This is to be achieved by working in accordance to the below listed points:

- Identification of suitable experimental methods for the mechanical characterization of CIGS thin-film to determine its Young's modulus,
- Performing the mechanical scribing experiments for P2 and P3 structures with the help of scribing needles of different tip geometries on the CIGS thin-film solar cell specimens with different adhesion strengths of CIGS/Mo interface,
- Studying the influence of scribing parameters such as force normal to the specimen and scribing speed on the scribe form
- Studying the influence of adhesion strength of CIGS/Mo interface and the geometry of needle tip on the scribe form
- Determining the dependence of scribing force on the needle displacement
- Developing the numerical finite element model to simulate the mechanical scribing process
- Validating the simulation results with the experimental findings with the target of optimizing the mechanical scribing process and the design of scribing setups
- Setting up the scheme of mechanism for mechanical scribing process after analyzing the experimental and simulation results

If the above mentioned points are processed successfully, it is ultimately possible to describe the process of mechanical scribing of CIGS thin-film solar cells with the knowledge gained from the numerical simulation and experimental investigations. The knowledge gained regarding the mechanical scribing process is a prerequisite for the optimization of scribing process and the design of scribing setups.

1.3 Outline of the thesis

After the introduction chapter, the present work is divided into five subsequent chapters. The outline of thesis is as follows:

Chapter 2 describes the theoretical background that have been used throughout this thesis. It covers basic concepts regarding the basic structure, monolithically integrated series connection and state-of-the-art mechanical scribing in CIGS thin-film solar cells. Then, the buckling driven delamination of thin-films is described with the focus on the post buckling solution for the straight-sided blister. Thereafter, the basics of nanoindentation experiments to determine the Young's modulus of thin-films are presented followed by the brief description on the basics of fracture mechanics and the cohesive zone material model for the interface delamination.

Chapter 3 presents the experimental and finite element simulation methods used in the present work. In beginning, the nanoindentation experiments performed to characterize the CIGS thin-film are described. Then, the mechanical scribing experiments used to perform P2 and P3 structures on CIGS thin-film solar cell specimens are described which is followed by the description of 2D and 3D finite element models used to carry out the numerical simulation of the mechanical scribing process.

Chapter 4 presents the results of all the experiments and finite element simulations that have been performed in the present work. The focus is on the results obtained from the nanoindentation experiments performed to determine Young's modulus of CIGS thin-film, mechanical scribing experiments used to perform P2 and P3 structures and the finite element simulations of CIGS thin-film solar cells.

Chapter 5 presents the scheme of the mechanism for the mechanical scribing process in CIGS solar cells which is being proposed after analyzing and understanding the results obtained from the experimental and numerical investigations carried out in the present work.

Chapter 6 presents and compares the experimental and simulation results. Here, the simulation results obtained from the different finite element models are compared and validated with the experimental findings regarding the mechanical scribing of CIGS thin-film solar cells.

Finally, chapter 7 presents the summary of all the experimental and simulation investigations done in the present work followed by the brief outlook for the future work.

2 Basics

This chapter describes the theoretical background that have been used throughout the thesis. The basic structure and function of $\mathrm{Cu(In,Ga)Se_2}$ (CIGS) solar cell is presented in section 2.1. Section 2.2 describes the state-of-the-art laser and mechanical scribing processes of CIGS solar cells. The buckling driven delamination of thin-films is dicussed in section 2.3 wherein the post buckling solution for the straight-sided blister is also presented and thereafter, the basics of nanoindentation experiments for the mechanical characterization of thin-films in order to determine the Young's modulus of thin-film are discussed in section 2.4. Section 2.5 presents the basic concepts of fracture mechanics and finally, the cohesive zone material model for the interface delamination is discussed in section 2.6.

2.1 Structure and function of CIGS solar cells

CIGS solar cells are the thin-film solar cells used to convert sunlight into electric power. They are produced by depositing a thin layer of copper, indium, gallium and selenide on glass or other substrate material, along with electrodes on the front and back side to collect the current. A much thinner film of CIGS material is required as compared to the other semiconductor materials, the reason being that the CIGS has a high absorption coefficient and it strongly absorbs sunlight. CIGS is one of three mainstream thin-film Photovoltaic technologies. The other two important thin-film PV technologies are cadmium telluride and amorphous silicon. CIGS layers are thin enough to be flexible allowing them to be deposited on flexible substrates. All these thin-film PV technologies normally use high-temperature deposition techniques where the best performance is obtained by using glass as the substrate material. Even then the performance is marginal compared to modern polysilicon-based panels. Advancements in deposition of CIGS cells at low-temperature has reduced much of this difference in performance. Thin-film market share stagnated at around 15%, leaving the rest of the PV market to conventional solar cells made of crystalline silicon. 14.3% of CIGS panel are now made by Stion Corp which is one of the prominent manufacturers since year 2006. The market share of CIGS thin-film solar cells was about 4% in the year 2013 and the combined market share of all thin-film technologies fell below 10% [13]. CIGS thin-film solar cells continue to develop and look promising to reach silicon-like efficiencies, while maintaining the low costs which is typical for thin-film technology [14]. The record cell efficiency in laboratory achieved so far for CIGS thin-film solar cells with soda lime glass as substrate is 21.7% as claimed by the German Center for Solar Energy and Hydrogen Research Baden-Württemberg [2].

2.1.1 Properties of CIGS material

CIGS is a $I-III-VI_2$ compound semiconductor material. It is composed of copper, indium, gallium, and selenium. The CIGS material is a solid solution of copper indium selenide and copper gallium selenide. It has a chemical formula of $CuIn_xGa_{(1-x)}Se_2$. The value of x can vary from 1 for pure copper indium selenide to 0 for pure copper gallium selenide. CIGS is a tetrahedrally bonded semiconductor with the chalcopyrite crystal structure. Its bandgap varies with x from about 1.0 eV for copper indium selenide to about 1.7 eV for copper gallium selenide [15]. CIGS material has high absorption coefficient of more than $10^5 cm^{-1}$ for the photons with energy equal to or greater than 1.5 eV [16].

2.1.2 Basic structure of a CIGS device

Figure 2.1 shows the cross-section profile for the most common cell configuration of CIGS thin-film solar cell. CIGS thin-film solar cells are mostly manufactured on rigid substrates like soda lime glass (SLG), but in general any substrate can be used. There are some important reasons behind using soda lime glass quite often as the substrate. It contains sodium which can yield a substantial open-circuit voltage increase [17] mainly through surface and grain boundary defects passivation [18], it provides good electrical insulation, relatively cheap, thermally stable and has a smooth surface. The thickness of substrate is around 1-3 mm. Titanium and polymide foils are among the other materials which are used as substrate. The back contact is deposited on the substrate by using the process of physical vapor deposition (PVD), most often sputtering. Molybdenum (Mo) is the material of choice for the back contact in the CIGS thin-film solar cells because of its inertness in subsequent deposition steps and its ability to create an ohmic contact to the CIGS material in the presence of $MoSe_2$ [19, 20]. The Mo back contact layer reflects most unabsorbed light back into the CIGS absorber. The thickness of Mo layer is usually between 300-500 nm.

A p-type CIGS absorber layer of thickness between 1.5-2.5 μm is deposited on the top of Mo back contact. CIGS can be prepared in different ways, however physical vapor deposition process is the most important process today. Most of the companies that produce CIGS thin-film solar cell modules commercially use physical vapor deposition technology. There are several companies and research institutions working with low-cost solutions, like printing of nanoparticle compounds or electrodeposition [21, 22]. The PVD methods for depositing CIGS absorber layer can be divided into several groups, the two most important methods being the sequential elemental sputtering followed by selenization and co-evaporation. In the method of sequential elemental sputtering, layers of copper, indium and gallium are sputtered onto the substrate. Thereafter, the metal precursors are annealed in the selenium atmosphere, so that they are selenized and form a layer of $Cu(In,Ga)Se_2$ [23]. In the co-evaporation method of depositing CIGS absorber layer, the three metals are evaporated from elemental sources, in an atmosphere of selenium abundance. The composition of materials can be controlled through parameters like the rates of the sources, their position, the geometry of the deposition chamber and the movement of substrates. An in-

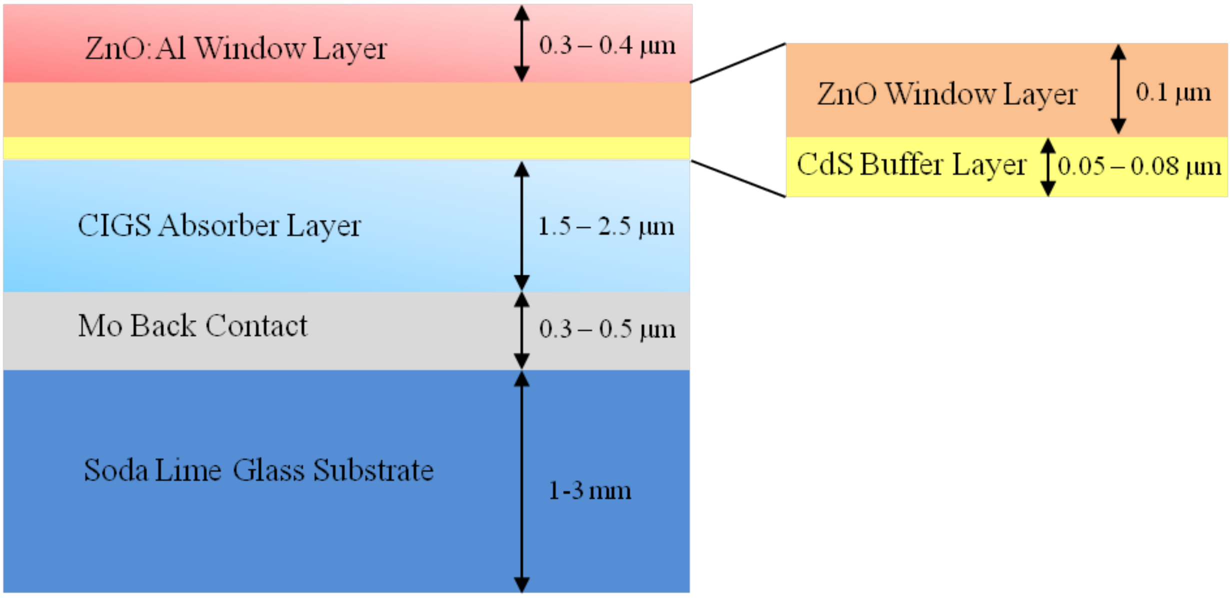

Figure 2.1: *Schematic diagram of the cross-section profile for the most common cell configuration of CIGS thin-film solar cell.*

line process is typically used in a production type deposition system, with stationary sources and the substrates moving past them [24]. A thin n-type buffer layer of thickness between 50-80 nm is deposited on the top of CIGS absorber layer by using a wet chemical method called chemical bath deposition (CBD). The main roles of buffer layer are to passivate the absorber surface and to provide a suitable partnering material to make up the heterojunction, combined with the following iZnO/ZnO:Al double layer. CdS is the most common material today which is used for buffer layer. However, research is in progress for the alternative materials like (Zn,Mg)O and Zn(O,S) deposited using both wet chemical and vacuum methods since they may provide spectral response benefits and are also non-toxic as opposed to cadmium used in CdS [25, 26]. The CdS buffer layer is followed by a thin layer (approximately 100 nm) of intrinsic zinc oxide (i-ZnO). The i-ZnO layer is used for the protection of CdS buffer layer and the CIGS absorber layer from sputtering damage while depositing the ZnO:Al window layer, since the latter is usually deposited by DC sputtering which is known as a damaging process [27]. The most important use of i-ZnO is that it evens out the potential, so that small shunt conductances are isolated and rendered practically harmless. The solar cell devices are finished off with the window (front contact) layer consisting of a hevily Al-doped ZnO of thickness between 300-400 nm. The Al doped ZnO acts as a transparent conducting oxide (TCO) to collect and move electrons out of the cell while absorbing as little light as possible.

2.2 Electrical connection of thin-film solar cells

In thin-film solar cell modules, the individual cells are interconnected monolithically to establish the electrical connection between them. The series connection is performed in the manufacturing process itself without the need to solder individual cells into strings. Three patterning steps P1,

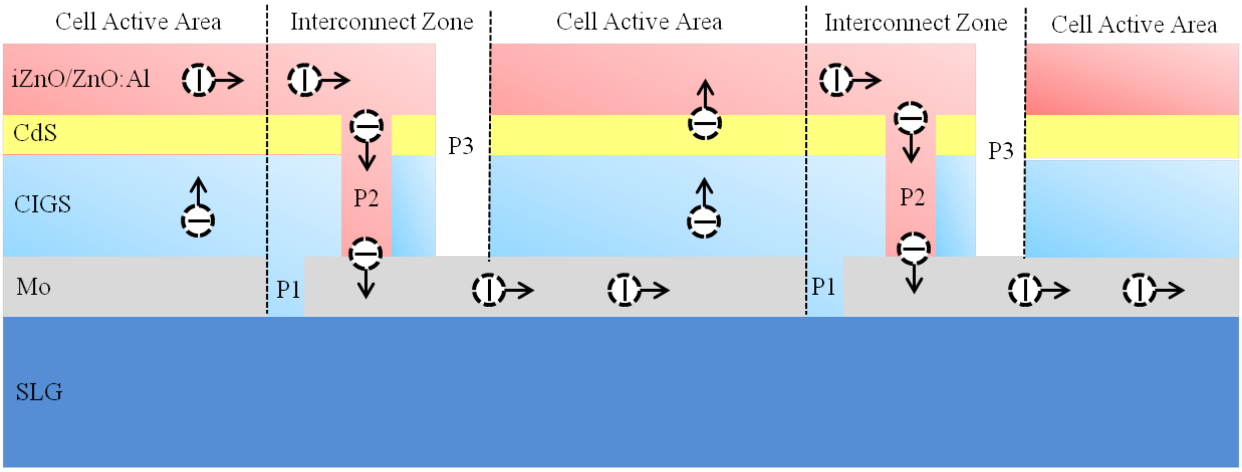

Figure 2.2: *Schematic representation of monolithically integrated series connection of CIGS thin-film solar modules indicating flow of electrons and showing the isolating P1-laser scribe, the interconnect P2-mechanical scribe and the isolating P3-mechanical scribe.*

P2 and P3 are required to make a series connection of cells. The metal back contact (Mo) isolating pattern (P1) is accomplished through laser scribing, however, a mechanical tip is used most commonly in order to scribe back-to-front contact interconnecting pattern (P2) and front contact isolation pattern (P3).

2.2.1 Monolithically integrated series connection

The availability of monolithically integrated series connection as shown in Figure 2.2 is one of the advantages of the CIGS thin-film solar module. The current is constant through the cells in series, while the voltage increases for each cell. The series connections enable the generation of a higher voltage power from the solar modules which can reduce heat loss during electric power transmission. In monolithic series connection, during the production process, individual layers are already separated in such a way that at the end, cell strips are created which are interconnected to each other in series instead of fabricating, tabbing, and stringing the cells together to make a series of interconnections, as is required in silicon wafer solar cells [28]. The monolithically integrated series connection provides an advantage in thin-film technology over crystalline solar modules, as it is then no longer necessary to connect with contact strips the individual silicon wafers which have been processed into cells. All processes are therefore conducted directly on the final substrate size, and can be fully automated from the beginning itself.

The individual layers are separated either mechanically [29,30] or with the help of laser [5,31]. This series interconnection is achieved by patterning the layers during the in-line processing. In order to make a series connection of cells, three patterning steps called as P1, P2 and P3 scribes are typically required [32, 33]. The first patterning step P1 as shown in Figure 2.2 separates the molybdenum back contact material for the different cells by making trenches in the metal layer. This patterning is most often performed with laser scribing. The role of P1 scribes is to isolate the areas on which individual solar cells will be fabricated. Thereafter, the CIGS absorber and CdS buffer layers are deposited as well as the highly resistive ZnO layer. These layers are then patterned using a mechanical scriber such as needle by making a trench (see P2 in Figure 2.2) that does not penetrate the molybdenum layer. The role of P2 scribes is to achieve current flow between adjacent solar cells and connect the back contact Mo layer with a front contact which is typically made of a transparent conductive oxide (TCO). When the conducting window material (iZnO/ZnO:Al) is deposited it forms an essentially ohmic contact to the molybdenum back contact of the next cell in the P2 trench. This P2 trench can also be made before the ZnO layer, or by modifying the CIGS to a conducting material through laser exposure [10]. The final patterning step P3 in series connection comprises of a mechanical scribe as shown in Figure 2.2 which is made through all layers except the molybdenum back contact, so that the front contacts of adjacent cells are separated from each other. The spacing between P1 and P2 scribes and between P2 and P3 determines the size of the so called dead-zone (interconnect zone) of the cell. For CIGS, a typical width of the scribed area is around 300 μm, which means that about $3-5\%$ of the total area of a module is dead area [34]. The dead area should be as small as possible for an effective usage of a photoactive area.

2.2.2 Laser scribing of CIGS solar cells

Laser scribing process utilizing 1064 nm wavelength and nanosecond pulses has been accepted as a standard process for accomplishing P1 scribe in state-of-the-art CIGS manufacturing. Laser scribing has some advantages from the processing point of view. Due to no tool wear, the process is stable over time, and does not require dressing steps at regular intervals which are common to counteract the gradual degradation of a mechanical tool. It is a non-contact process which limits the mechanical stress on the materials that are machined. It provides better scribe quality and faster processing. It is a standard process for high speed mass production with a scribing speed of around 1 m/s. The scribe widths are narrower and the surrounding material is less damaged [4–6]. Thorough evaluations of the use of several different laser systems for the purpose of scribing thin-film PV modules have been presented [5, 7, 8], wherein the influence of laser parameters such as wavelength, pulse duration, beam delivery and focus, when considering laser scribing is highlighted. It was found that CIGS can be selectively removed without damaging the underlying Mo layer, however the presence of melted CIGS at the edges of the grooves was pointed out as a problem which could cause short-circuiting and shunting of cells. So, laser scribing has two manufacturing related drawbacks. First, laser scribing leaves a heat-affected-zone (HAZ) around the scribe which can cause poor isolation between cells and low shunt resistance. Second, laser scribing leaves high protruded ridges along the edge of the scribe line, which contributes to electrical shorts [5]. While scribing reduces resistive losses by decreasing photocurrent, it also forms dead zones between P1 and P3 slots, which contribute to reductions in module efficiency [35]. Due to these drawbacks, the mass production of CIGS thin-film solar cells has until now defied the traditional P2 and P3 laser scribing processes [9] that have proven so valuable in creating the monolithic series interconnect structures required to achieve useful working voltage and current in large scale thin-film amorphous silicon and CdTe PV modules.

2.2.3 Mechanical scribing of CIGS solar cells

Laser scribing has been accepted as a standard process for accomplishing P1 scribe in CIGS thin-film solar cells. This laser scribing process utilizes 1064 nm wavelength and nanosecond pulses. However, until now the lasers used have proven completely ineffective for the P2 and P3 scribes. No laser scribing process has been developed yet for the P2 and P3 stage scribing in the CIGS thin-film solar cell structure. With the failure of laser based processes, mechanical scribing with a force-controlled stylus has become the method of choice to obtain P2 and P3 structures which are required to achieve the monolithic serial interconnection and isolation respectively between the neighboring cells. Needles are used for the material removal in mechanical patterning of thin-film layers. This is a direct contact method which induces mechanical stress and damage to the material. In mechanical scribing, the roughness of the substrate plays an important role as this method is sensitive to the height variations of the scribed surface. Therefore this method could only be applied if thin-films are deposited on a hard and smooth substrate [10] and is not suitable for thin-films on soft flexible substrates. The state-of-the-art mechanical patterning of P2 and P3 causes chipping and broadens the dead zone. The increase in dead zone thereby reduces the effective solar cell area which in turn reduces the efficiency of the solar cell. Since the P1/P2/P3 interconnect zone does not contribute to the efficiency of the solar module, a reduction of the dead zone is one of the important measure to enhance solar module efficiency.

Mechanical scribing experiments for P2 and P3 structures have been performed in the past on CIS $\mathrm{Cu(In,Ga)(S,Se)_2}$ thin-film solar cells [36]. In the pattern 2 (P2) mechanical scribing process, the CIS layer was removed completely to enable a good contact of the molybdenum layer to the ZnO layer being deposited in a later process step, whereas the pattern 3 (P3) mechanical scribing was performed to remove the complete combined ZnO/CIS layer from the top of the Mo layer. Also, P2 and P3 laser scribes were performed using the ultrafast laser at a wavelength 1064 nm with a pulse duration of about 10 ps and a maximum power of 30 W. The results of mechanical and laser scribing were compared. Figure 2.3 shows the direct comparison of interconnect region scribed mechanically and scribed with picosecond lasers. It can be seen that the mechanical scribes were broadened because of chipping. It was observed that especially P2 chipping limits reduction of the dead area as P2 chippings crossing P1 causes shunts between front and back electrode. Furthermore mechanical P3 does not work equally effective on areas being affected by mechanical P2 chipping where there is a direct deposition of ZnO on Mo. The dead zone was measured to be nearly twice in case of mechanical scribing.

Mechanical scribing of CIGS thin-film solar cells results in bigger dead area, partly because it requires higher safety margins between the scribes due to the chipping of the layers [11], as shown in Figure 2.4. Here, isolating P3 patterning was done using standard mechanical scribing after performing the P2 laser patterning which welds the front contact and CIGS layers along the scribe line. The increase in dead area due to the use of mechanical scribing for P3 pattern resulted in decreased efficiency of the solar module. Extensive investigations have been done regarding the laser scribing, however not much research work has been carried out till now with

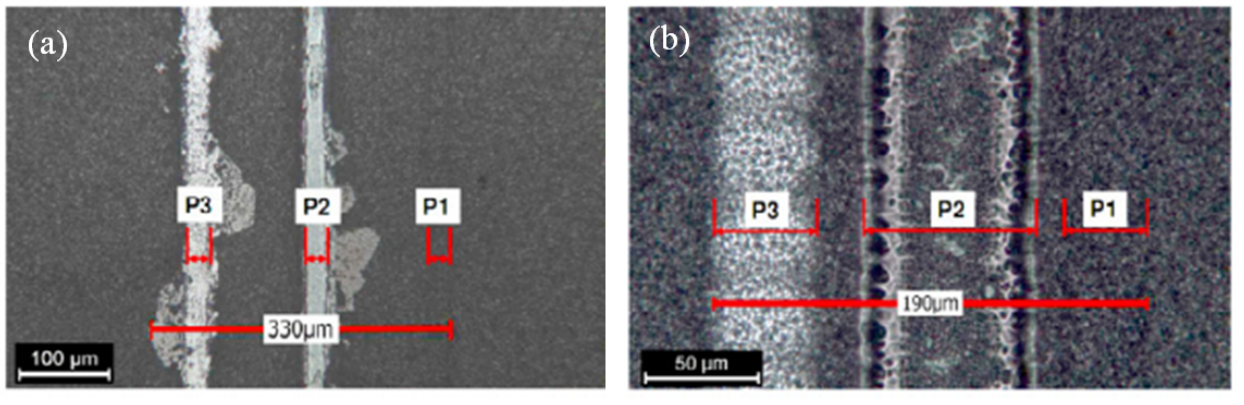

Figure 2.3: *Optical micrographs showing the dead zone for the P2 and P3 (a) mechanical, and (b) laser scribes performed on CIS thin-film solar cells. The dead zone is nearly two times in case of mechanical scribing [36].*

regard to mechanical scribing of CIGS thin-film solar cells. The challenge lies in understanding the mechanics of material removal in the process of mechanical scribing of CIGS solar cells. The knowledge thus gained can then be applied to optimize the process which in turn may result in incresed eficiency of the CIGS solar module.

2.3 Buckling driven delamination of thin-films

Thin-film materials on substrates and multilayers are used for their functional properties in a wide range of applications in an increasing number of engineering fields such as microelectronics, coatings, aeronautics, medical devices and thin-film solar cells. The reliability of such coatings strongly depends on their mechanical behavior and their stability [37]. Buckling of thin-films which results in interfacial delamination and fracture is the common failure mechanism in these materials [38, 39]. A thin-film which is bonded to a substrate and is subjected to compressive stresses may delaminate by a mechanism involving buckling [40–45]. The buckling phenomenon of coatings and thin-films on substrates at the mesoscale has been analyzed in the framework of classical Föppl – von Kármán (FvK) theory of thin plates [46–49]. A number of configurations such as circular blisters, straight-sided wrinkles or telephone-cord structures [50–53] have been characterized under the action of different sources of stress such as the residual stress coming from the deposition methods [54], the mismatch of thermal coefficient or external applied stresses [55–57]. Finite element simulations have been used to investigate the influence of elasticity of the substrate [58–61]. The substrate deformation can strongly modify the shape of buckling patterns and the critical stress for buckling [62]. The analysis and understanding of buckling patterns has led to applications in the fields of optical gratings [63], stretchable interconnects [64, 65] and metrology [66–68].

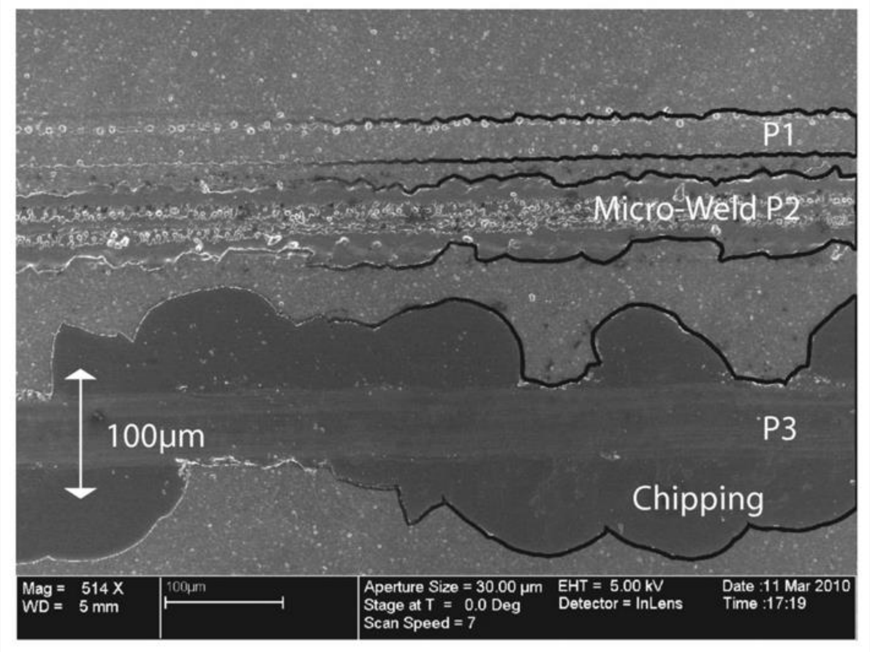

Figure 2.4: *SEM image of scribed CIGS thin-film solar cell. P3 mechanical scribe shows chipping and requires a large safety margin between itself and the P2 scribe, in this case an experimental micro-weld [11].*

2.3.1 Buckling modes in thin-films

The mechanical instability which causes the thin-film to develop large out-of-plane displacement above a critical load is called buckling. The study of buckling as a stress-driven mechanical instability can be traced back to the classical Euler theory of the buckling of an elastic column. The fundamental mode of buckling depends on the type of constraints and minimizes the elastic strain energy. Previous studies regarding the buckling of thin-films have mainly focused on the two buckling modes namely wrinkling and buckling driven delamination. Figure 2.5 presents the schematics of two buckling modes in thin-films. Wrinkling considers the buckling of the thin-film with no delamination from the substrate since the substrate deforms coherently with the film [69–71], whereas, the buckling driven delamination considers buckling of the thin-film when it is delaminated partly from the substrate [38, 50]. The characteristics of both buckling modes are often observable, with homogeneous patterns for wrinkling and localized patterns for buckling driven delamination such as telephone cord blisters.

In case of a thin elastic film bonded to a thick elastic substrate, the buckling is constrained by the substrate. Buckling of thin-film without delamination which is called wrinkling requires the coherent deformation of substrate. The coherent deformation of substrate is possible only when the substrate is relatively compliant. The critical stress for wrinkling on the basis of energetic analysis [69–71] is given by the following expression:

$$\sigma_w = \frac{\bar{E}_f}{4}\left(\frac{3\bar{E}_s}{\bar{E}_f}\right)^{2/3} \tag{2.1}$$

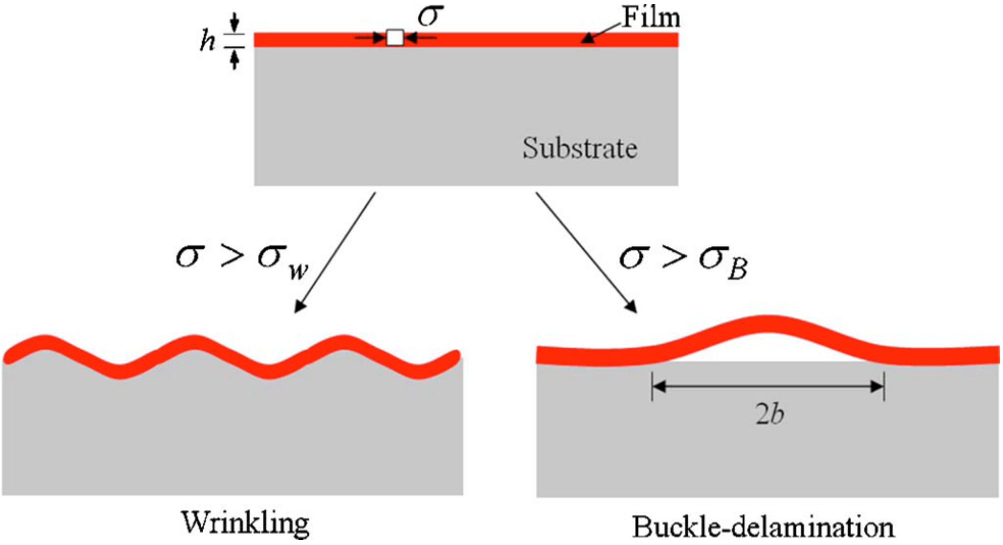

Figure 2.5: *Schematic illustration of two buckling modes in thin-films; h and $2b$ stand for thickness of film and delamination width of the buckle respectively; σ, σ_w and σ_B stand for compressive stress in the thin-film, critical stress for wrinkling and critical stress for buckling respectively [72].*

where:
$\bar{E}_f = (1-\nu^2)/E_f$ is the plane-strain elastic modulus of the thin-film, and
$\bar{E}_s = (1-\nu^2)/E_s$ is the plane-strain elastic modulus of the substrate.

When the compressive stress in thin-film (σ) exceeds the critical stress for wrinkling (σ_w), the film buckles and the wrinkles are formed throughout the film surface. A particular wrinkle wavelength is established to minimize the total elastic energy in the film and the substrate [69–71]. The critical stress for wrinkling is influenced by the thicknesses of the thin-film and the substrate and this has been investigated in the previous studies [71,73].

The deformation of thin-film due to buckling is highly constrained in case of stiff substrates leading to high critical stresses for wrinkling. However, the substrate constraint may be locally mitigated by the interfacial defects which lead to partial delamination of the film. The portion of thin-film which is delaminated undergoes buckling which in turn drives growth of delamination through interfacial fracture [38, 50]. The buckling and delamination develop together leading to a number of blister patterns such as straight-sided, circular and telephone cord blisters as shown in Figure 2.6. The buckling driven delamination patterns are typically localized and sensitive to interfacial defects as compared to wrinkling [74, 75]. A fixed-end condition at the edge of delamination which essentially neglected the effect of elastic deformation in the substrate was often assumed in the early studies of buckling driven delamination. The critical stress for the onset of buckling (σ_{BO}) is identical to that for a freestanding sheet [38] under this condition and is given by the following expression:

$$\sigma_{BO} = \frac{\pi^2}{12}\left(\frac{h}{b}\right)^2 \bar{E}_f \tag{2.2}$$

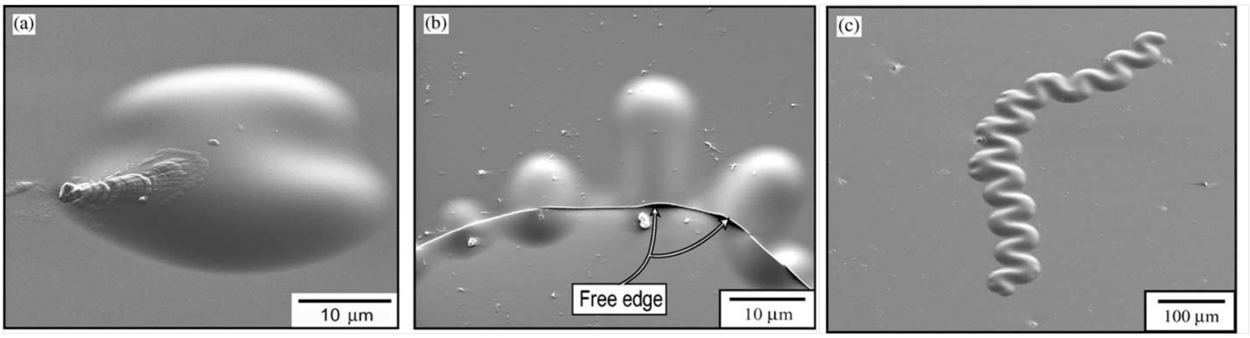

Figure 2.6: *Illustrations of (a) straight-sided, (b) circular and (c) telephone cord blisters [75].*

where:
σ_{BO} = critical stress for the onset of buckling,
h = thickness of thin-film, and
b = half-width of delamination.

The critical stress for the onset of buckling, σ_{BO} is independent of the properties of substrate but it depends on the relative size of the interfacial delamination, b/h. It has been shown in the recent studies [60, 76, 77] that when the elastic deformation of the substrate is considered, especially for complaint substrates, the critical stress for the onset of buckling σ_B can be significantly lower than that predicted by the Equation 2.2. An implicit expression has been derived by Yu and Hutchinson [77] as given below:

$$\sqrt{\frac{\sigma_{BO}}{\sigma_B}}\, tan\left(\pi\sqrt{\frac{\sigma_B}{d}\sigma_{BO}}\right) = \frac{\pi h}{12b}\left(\frac{a_{12}^2}{b/h+a_{11}} - a_{22}\right) \tag{2.3}$$

where, σ_B is the critical stress for the onset of buckling when the elastic deformation of the substrate is considered. The coefficients a_{11}, a_{22}, a_{12} are determined numerically, either by direct finite element calculations or by solving an integral equation, as dimensionless spring constants at the edge of the buckled film. These coefficients are functions of both b/h and the Dundurs elastic mismatch parameters α_1 and α_2. The Dundurs parameters α_1 and α_2 for the plane strain problems are given by the following equations:

$$\alpha_1 = \frac{\bar{E}_f - \bar{E}_s}{\bar{E}_f + \bar{E}_s} \tag{2.4}$$

$$\alpha_2 = \frac{1}{2}\,\frac{\bar{E}_f(1-\nu_f)(1-2\nu_s) - \bar{E}_s(1-\nu_s)(1-2\nu_f)}{\bar{E}_f(1-\nu_f)(1-2\nu_s) + \bar{E}_s(1-\nu_s)(1-2\nu_f)} \tag{2.5}$$

where:
$\bar{E}_f = (1-\nu^2)/E_f$ is the plane-strain elastic modulus of the thin-film, and
$\bar{E}_s = (1-\nu^2)/E_s$ is the plane-strain elastic modulus of the substrate.

The first Dundurs parameter α_1 is a measure of the mismatch in the plane tensile modulus across the interface. It approaches +1 when the film is extremely stiff as compared to the substrate, and approaches -1 when the film is extremely compliant as compared to the substrate. The second Dundurs parameter α_2 is a measure of the mismatch in the in-plane bulk modulus and it plays relatively less important role than α_1 [77] in determining the coefficients a_{11}, a_{22} and a_{12}.

2.3.2 Post buckling solution for the straight-sided blister

Due to the mismatch in the thermal expansion coefficients and high deposition temperature, residual compressive stresses are often induced in thin-films of the film/substrate structures. Different stress relief mechanisms have been observed in thin-films. In case of thin-film bonded on relatively stiff substrate, one of the mechanisms involves buckling-driven delamination of thin-film from the substrate, as in the case of a ceramic thermal barrier coatimng or a diamond-like carbon wear resistant coating on a metallic substrate [78]. The buckles propagate beneath the film if the induced energy release rate exceeds the interface fracture toughness. The morphology which is adopted by the thin-film after buckling is called a buckle or blister. Buckling driven delamination of thin-films can lead to very simple shapes of blisters such as the straight and circular blisters [38] as shown in Figure 2.6. The buckled thin-films often form the periodic patterns such as telephone-cord blisters [38] under the large in-plane equi-biaxial loading as shown in Figure 2.6 (c). Although it is possible to model properly the behavior of a straight blister and couple the non-linear response of a plate with the interfacial rupture, a general approach for understanding the more complex shapes of blisters is still lacking. Consider a z-independent portion of the straight-sided blister as shown in Figure 2.6 (b). The thin-film is assumed to be elastic and isotropic with thickness h, Young's modulus E_f and Poisson's ratio ν_f. The substrate is assumed to be uniform, isotropic and very thick as compared to the thin-film, with Young's modulus E_s and Poisson's ratio ν_s. The thin-film is subjected to an equi-biaxial compressive mismatch stress of magnitude σ. There exists an unattached region $-b \leq x \leq b$ in the interface of the thin-film and the substrate. The problem is analyzed as a plain strain problem. Dundurs elastic mismatch parameters α_1 and α_2 are already defined above in Equation 2.4 and Equation 2.5 to denote the elastic mismatch between the film and the substrate. Typically, α_1 is the more important of the two parameters for most bilayer crack problems. When the substrate is stiff as compared with the film, with the assumption of $h \ll b$, the film is modeled as a wide, clamped Euler column of width $2b$. M and ΔN are the moment and change in resultant force per unit length at the right hand end of the column as shown in Figure 2.6.

By Föppl – von Kármán nonlinear plate theory with fully clamped conditions at the boundary, the solutions are given below [79]:

$$M = \frac{\pi^2}{2} \frac{Dh}{b^2} \delta \tag{2.6}$$

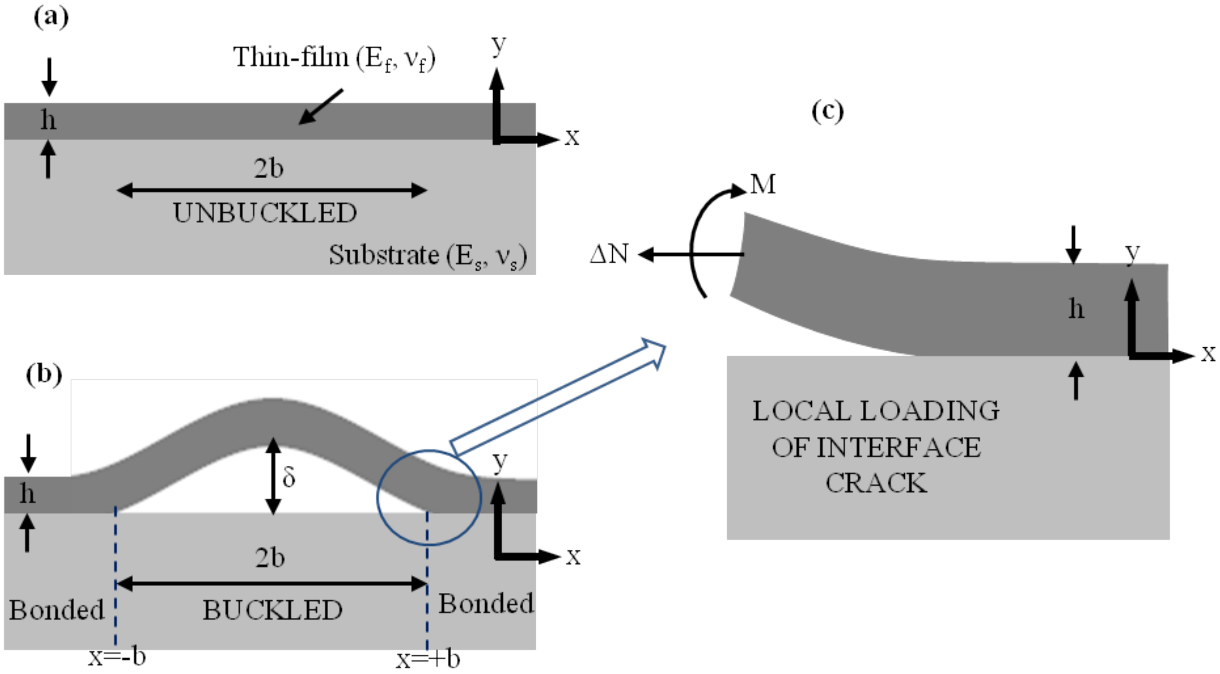

Figure 2.7: *Geometry of the one-dimensional straifght-sided blister and conventions for the elasticity solution characterizing conditions near the tip of an interface crack between a thin-film and an infinitely thick substrate (a) unbuckled, (b) buckled, and (c) local loading of interface crack [79].*

$$\Delta N = \frac{3\pi^2}{4}\frac{D}{b^2}\delta^2 \tag{2.7}$$

where D=$\bar{E}_f h^3/12$ is the bending stiffness of the thin-film and δ is the amplitude of the buckling deflection.

The energy release rate G is given by the equation below:

$$G = \frac{6}{\bar{E}_f h^3}\left(M^2 + \frac{h^2 \Delta N}{12}\right) = \frac{h}{2\bar{E}_f}(\sigma - \sigma_0)(\sigma + 3\sigma_0) \tag{2.8}$$

where, σ_0 is the classical buckling stress of a wide plate with clamped edges and is defined as below:

$$\sigma_0 = \frac{\pi \bar{E}_f}{12}\left(\frac{h}{b}\right)^2 \tag{2.9}$$

Let b_0 be the critical half-width of the blister for case of thin-film with clamped edges. The critical half-width is defined as the miniumum half-width of the blister so that the film may buckle up and is given by the follwing equation:

$$b_0 = \frac{\pi h}{2\sqrt{3}}\sqrt{\frac{\bar{E}_f}{\sigma}} \tag{2.10}$$

2.4 Mechanical characterization of thin-films

The development of nanostructured materials, thin-film technology and the increasing demand for miniaturization of engineering and electronic components has motivated the quantitative study of mechanical properties at nanoscale. The properties of thin-film materials mainly depend on the structure of materials, vapor deposition conditions, film thickness, type of substrate etc. The mechanical properties of thin-films are generally different from their isotropic bulk values. The analytical derivation of the properties of thin-films is hard to achieve. Nanoindentation is one of the most important out of few technologies available today for conducting such measurements at nanoscale structures. In the last two decades, the ultra-low load indentation systems have been developed to make possible in situ testing of mechanical properties of materials [80–82]. The nanoindentation method has been successfully utilized in the recent times to measure the mechanical properties of materials at the micrometer to nanometer length scales [83–86]. Many researchers have employed this method to investigate the elastic and plastic properties of various thin-films [87–92].

2.4.1 Introduction

The instrumented indentation technique for measuring hardness and elastic modulus has widely been used for the characterization of mechanical behavior of materials at small scales [82, 93]. With the help of this technique, the mechanical properties can be determined directly from indentation load and displacement measurements. The material properties at the micrometer and nanometer scales can be measured with the use of high-resolution testing equipment [80, 94, 95]. So, the method has become a primary technique for determining the mechanical properties of thin-films and small structural features. Several important changes are being made to the method during the past decade that both improve its accuracy and extend its application area [96]. These changes have been brought because of testing a large number of materials and by improvements to testing equipment and techniques. For example, the measurement of contact stiffness by dynamic techniques provides for the continuous measurement of properties as a function of depth and it also facilitates more accurate identification of the point of first surface contact [97].

2.4.2 Basic principles of nanoindentation

The indentation test provides the load-displacement data for loading and unloading cycles. The nanoindentation method was developed to measure the hardness and elastic modulus of a material from this load-displacement data. The displacement of indenter as a function of applied force is recorded continuously for the complete cycle of loading and unloading during a nanoindentation test. Figure 2.8 (a) presents the schematic representation of a typical data set obtained with a Berkovich indenter where the parameter P represents the load and h the displacement relative to the initial undeformed surface. Different approaches have been developed over several decades to

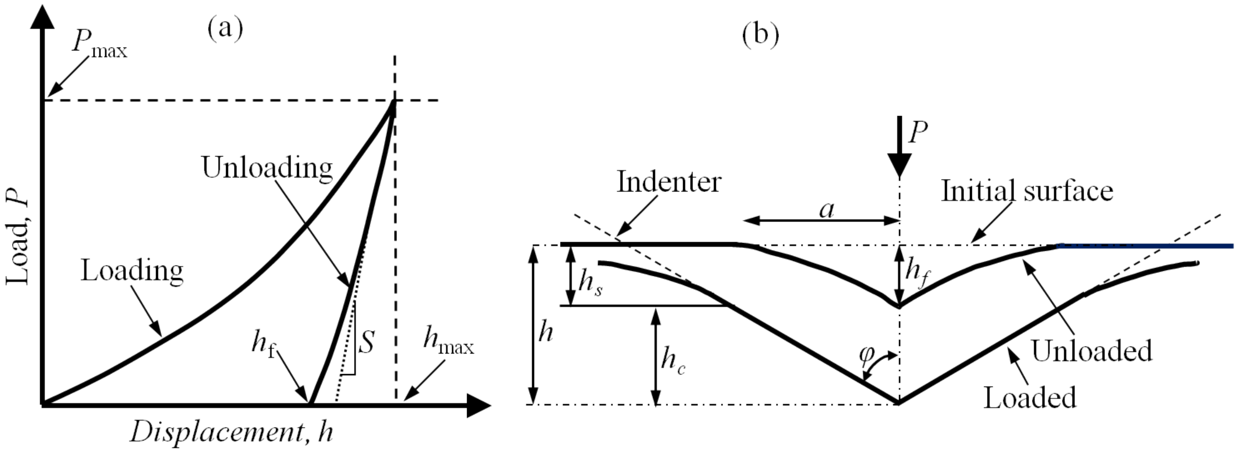

Figure 2.8: *Schematic illustration of (a) indentation load-displacement data, and (b) the unloading process [82]*

analyze the nanoindentation data [81, 93, 98, 99]. The Oliver and Pharr method [82] is the most often used method till now. It is based on the research by Doerner and Nix [81] and Sneddon [99]. The three important quantities that must be measured from the $P-h$ curves are the maximum load, P_{max}, the maximum displacement, h_{max}, and the elastic unloading stiffness, $S = dP/dh$. The elastic unloading stiffness is defined as the slope of the upper portion of the unloading curve during the initial stages of unloading. How well these parameters can be measured experimentally decides the accuracy of hardness and modulus measurement. Another important quantity is the final depth, h_f, the permanent depth of penetration after the indenter is fully unloaded. The analysis used to determine the elastic modulus, E, and hardness, H, is an extension of the method proposed by Doerner and Nix [81] that accounts for the fact that unloading curves are distinctly curved in a manner that cannot be accounted for by the flat punch approximation. The contact area remains constant as the indenter is withdrawn, and the resulting unloading curve is linear in the flat punch approximation used by Doerner and Nix. The unloading curves have been shown to be distinctly curved and usually well approximated by the power law relation as given below (where α and m are constants):

$$P = \alpha(h - h_f)^m \tag{2.11}$$

E and H are measured by using the procedure based on the unloading processes shown in Figure 2.8 (b). It is assumed that the behavior of the Berkovich indenter can be modeled by a conical indenter with a half-included angle, $\phi = 70.3°$, that gives the same depth-to-area relationship. The basic assumption is that the contact periphery sinks in a manner that can be represented by the models for indentation of a flat elastic half-space by rigid punches of simple geometry [99–103]. This assumption regarding the contact periphery limits the applicability of the nanoindentation method since it does not account for the pile-up of material at the contact periphery which occurs in some elastic-plastic materials. Assuming the negligible pile-up, the elastic models show that the amount of sink-in, h_s, is given by the following equation:

$$h_s = \varepsilon \frac{P_{max}}{S} \tag{2.12}$$

where ε is a constant which depends on the indenter geometry. Some of the important values are: ε=0.72 for a conical punch, ε=0.75 for a paraboloid of revolution and ε=1.00 for a flat punch. The depth along which contact is made between the indenter and the specimen, h_c is given by the following equation:

$$h_c = h_{max} - \varepsilon \frac{P_{max}}{S} \tag{2.13}$$

Assuming $F(d)$ to be the area function which represents the cross sectional area of the indenter at a distance d back from its tip, the contact area A may then be given by the following equation:

$$A = F(h_c) \tag{2.14}$$

where h_c is the contact dept defined as the vertical distance from the edge of the contact area to the indenter tip as shown in Figure 2.8 (b).

The Berkovich indenter is a three-sided pyramid which is geometrically self-similar. It has a very flat profile, with a large included angle of 142.3^0 which minimizes the influence of friction. The centerline-to-face-angle is 65.3^0. It has the same projected area-to-depth ratio as a Vickers indenter. The Berkovich indenter is used routinely for nanoindentation testing to measure mechanical properties on the nanoscale because it is more readily fashioned to a sharper point than the four-sided Vickers geometry, thus ensuring a more precise control over the indentation process. It is not easily damaged and can be readily manufactured. There are many applications for the Berkovich indenter tips, some of them include bulk materials, thin-films, scratch testing, wear testing, micro-electromechanical systems etc. For a perfect Berkovich indenter, the projected contact area, $A_{Berkovich}$, is given by the following equation [81, 82]:

$$A_{Berkovich} = 3\sqrt{3}h_c^2 \tan^2 65.3^0 = 24.56h_c^2 \tag{2.15}$$

In order to take in to account the deviations from non-ideal indenter geometry, the area function must be carefully calibrated by independent measurements. The hardness of the material is determined by the maximum loading point of the curve. The hardness is defined as the mean pressure under the indenter [81, 82]. Let P_{max} represents the maximum applied force and A the projected contact area of indenter tip with the material. After determining the contact area, the hardness is calculated by the following equation:

$$H = \frac{P_{max}}{A} \tag{2.16}$$

The maximum applied force is obtained directly from the force-displacement curve. This definition of hardness measurement is based on the area of under applied force and it may vary from the traditional hardness value which is measured from the area of the residual hardness impression, if there is significant elastic recovery under unloading. However, this is generally important only in the case of materials that have very low values of E/H [87]. The initial slope of the unloading curve can be used as a measure of the elastic properties of the material. The contact stiffness S can be determined by the following equation:

$$S = \frac{dP}{dh} = \beta \frac{2}{\sqrt{\pi}} E_{eff} \sqrt{A} \tag{2.17}$$

where, dP/dh is the initial slope of the unloading curve, P is the applied force, h is the indenter displacement, β is geometrical correction factor used to account for deviations in stiffness caused by the lack of axial symmetry for pyramidal indenters and E_{eff} is the effective elastic modulus. The effective elastic modulus is defined by the equation given below:

$$\frac{1}{E_{eff}} = \frac{1-\nu^2}{E} + \frac{1-\nu_i^2}{E_i} \tag{2.18}$$

The expression for the effective elastic modulus considers the fact that elastic displacements occur in both the specimen and the indenter. E and ν denote the Young's modulus and the Poisson's ratio of specimen, whereas E_i and ν_i represent the Young's modulus and Poisson's ratio of the indenter. Equation 2.17 is a relation that generally applies to any axisymmetric indenter [93, 104]. It is often associated with flat punch indentation. Even though it was originally derived for elastic constant only [93], however, it has subsequently been shown to apply equally well to elastic-plastic contact [104]. The correction factor β in Equation 2.17 is significantly important when accurate property measurements are required. It not only affects the elastic modulus but the hardness as well. If the wrong value of β is used then we may obtain the incorrect value of indenter area function which in turn will lead to the incorrect determination of the value for elastic modulus. So, without a good working knowledge of correction factor, it is not possible to determine the accurate values of E and H. It has been shown that even for indentation of an elastic half-space by axisymmetric rigid cone, β can deviate significantly from unity. β=1 in the case of small deformation of an elastic material by a rigid axi-symmetric punch of smooth profile. However, non-axisymmetric indenters are used in real indentation experiments and these involve large strains, therefore other values for β may be more appropriate. It has been found that β should be slightly greater than unity for the Berkovich indenter. β=1.05 is probably as good choices as any, with a potential for error of approximately ± 0.05. Woirgard has demonstrated analytically that the exact value of β for the perfectly sharp Berkovich indenter should be 1.062 [105].

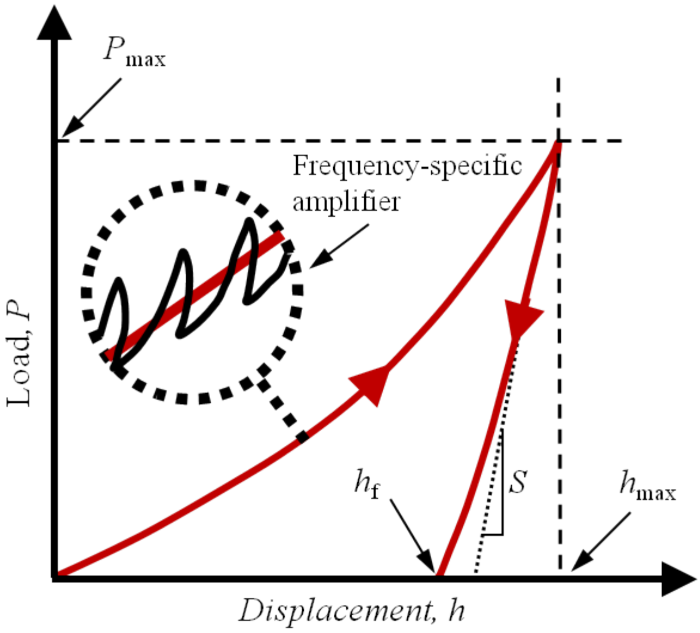

Figure 2.9: *Schematic illustration of the dynamic indentation loading cycle: measurement of stiffness by the contact stiffness measurement technique [108].*

2.4.3 Continuous stiffness measurement

The contact stiffness is determined from the force versus displacement curve during unloading in the case of conventional quasi-static indentation testing. This provides a single measurement for the given indentation depth. Advancements have been made in measurement and calibration procedures have been made by improvements in testing techniques and apparatus. The continuous stiffness measurement technique (CSM) is one of the most important of them. In CSM technique, the stiffness is measured continuously during the loading of the indenter by imposing a small dynamic oscillation (usually 2 nm of amplitude) with a given frequency, ω, (usually 45 Hz) on the force or displacement signal and measuring the amplitude and phase of the corresponding displacement or force signal by means of a frequency-specific amplifier as shown in Figure 2.9. This technique allows to calculate the elastic stiffness and so the elastic properties continuously during the loading of the indenter [82, 97, 106, 107]. The CSM technique has matured over the last 10 years and has dramatically reduced the dependence on unloading curves.

The CSM technique offers several distinct advantages. First, it has the advantage of providing continuous results as a function of depth. Secondly, since there is no need for multiple indentations, the time required for calibration and testing procedures is dramatically reduced. Third, this technique allows to avoid some of the complicating effects of time-dependent plasticity and thermal drift at high frequencies, which caused so much consternation in the original calibration method. Fourth, with the help of CSM technique, the effects of stiffness changes as well as damping changes can be measured at the point of initial contact. The point of initial contact of the indenter with the sample can be determined precisely. How well the location of surface can be determined is clearly affected by the resolution in the load and displacement signals as well as the data acquisition rates. It is also significant to resolve and detect near-surface forces since these can significantly affect the interpretation of surface location. The techniques that use preloads or back-extrapolation of the data in order to determine the point of initial contact can be misleading. So, observing the entire mechanical response of the system before, during and after the point of initial contact and identifying the point of contact by examining the overall observed behavior is the preferred approach.

2.5 Basic concepts of fracture mechanics

The growth and localization of material damage like micro-cracks and voids result in a macroscopic crack which may then grow very fast resulting in global failure. Fracture mechanics is the field of mechanics which is concerned with the study of the propagation of cracks in materials. Fracture mechanics makes use of the methods of analytical solid mechanics to determine the driving force on a crack and those of experimental solid mechanics in order to characterize the materials resistance to fracture. Although previous studies have focused on predicting fracture by analyzing the behavior of atomic bonds, Griffith [109] who used the energy approach to model fracture has shown in 1921 that attention should be given to the behavior of an existing crack. In fracture mechanics attention is basically focused on a single crack. The field of fracture mechanics can be subdivided in to several specializations, each with its own concepts, theory and terminology. Experimental techniques ranging from simple and cheap to sophisticated and expensive are used for the detection of cracks. Experimental fracture mechanics (EFM) is the field of fracture mechanics which uses and developes the hardware and procedures, not only for the crack detection, but, also for the accurate determination of its geometry and loading conditions [110]. Linear elastic fracture mechanics (LEFM) [110] uses concepts and theories in which linear elastic material behavior is an essential assumption. The crack growth can be predicted on the basis of energy balance. According to the Griffith criterion, crack growth will occur, when there is enough energy available to generate new crack surface [109]. The energy release rate is an essential quantity in energy balance criteria. The crack growth criterion based on energy balance is referred to as being global, because a rather large volume of material is considered. The crack growth criterion can also be based on the stress state at the crack tip. This stress field can be determined analytically. It is characterized by the stress intensity factor. The crack growth criterion based on the stress state at the crack tip is referred to as local, because attention is being focused at a small material volume at the crack tip. The assumption of linear elastic behavior for the material leads to infinite stresses at the crack tip. This is obviously not possible in reality because plastic deformation will occur in the crack tip region. However, the crack tip plastic zone can be determined by using the yield criteria (Von Mises, Tresca). When the crack tip plastic zone is small enough (the situation being referred to as Small Scale Yielding, SSY), the concepts of LEFM can be used. Dynamic fracture mechanics (DFM) [110] is the field of fracture mechanics which makes use of theories and methods not only to predict that whether a crack will grow or not but also to predict the speed and direction of its growth. The stress and strain fields from LEFM are not valid any more when the crack tip plastic zone becomes too large and also when the material behavior is nonlinear elastic as in case of polymers and composites. The concept of stress intensity factor can no longer be used to formulate the crack growth criterion. The field of fracture mechanics dealing with such cases is called Elastic-plastic fracture mechanics (EPFM) [110]. In EPFM, the crack growth criteria are derived on the basis of crack tip opening displacement (CTOD). Its calculation is done using the models of Irwin [111] or Dugdale-Barenblatt [112, 113] for the crack tip zone. The crack growth parameter known as J-integral which characterizes the stress/deformation state in the crack tip zone is used extensively in NLFM.

2.5.1 Stress concentrations

The work of Inglis in 1913 [114] contributed in the progress toward a quantitative definition of toughness. It was shown by Inglis that the local stresses around a corner or hole in a plate under stress could be many times higher than the average applied stress. The presence of notches, sharp corners and cracks result in the concentration of applied stress at these points. It was shown that the degree of stress magnification at the edge of the hole in a stressed plate depends on the radius of curvature of the hole. The smaller the radius of curvature, the greater the stress concentration. Inglis found that the stress concentration factor (κ) for an elliptical hole is given by the equation below:

$$\kappa = 1 + 2\sqrt{\frac{c}{\rho}} \tag{2.19}$$

where:
κ = stress concentration factor,
c = hole radius, and
ρ = radius of curvature of the tip of hole.

The stress concentration factor may be much greater than one for a very narrow elliptical hole. Equation 2.19 gives $\kappa = 3$ for a circular hole as shown in Figure 2.10. The stress concentration factor does not depend on the absolute size or length of the hole but only on the ratio c/ρ.

2.5.2 The Griffith energy balance criterion

A.A. Griffith studied the effect of scratches and surface finish on the strength of machine parts subjected to alternating loads in the year 1920 [116]. Inglis's theory proved that the stress increase at the crack tip depended only on the geometry of the crack and not its absolute size. This was in contradiction to the well known fact that larger cracks are propagated more easily than smaller ones. This anomaly led Griffith to a theoretical analysis of fracture based on the concept of minimum potential energy. According to Griffith, the decrease in strain energy due to the formation of a crack must be equal to or greater than the increase in surface energy required by the new crack

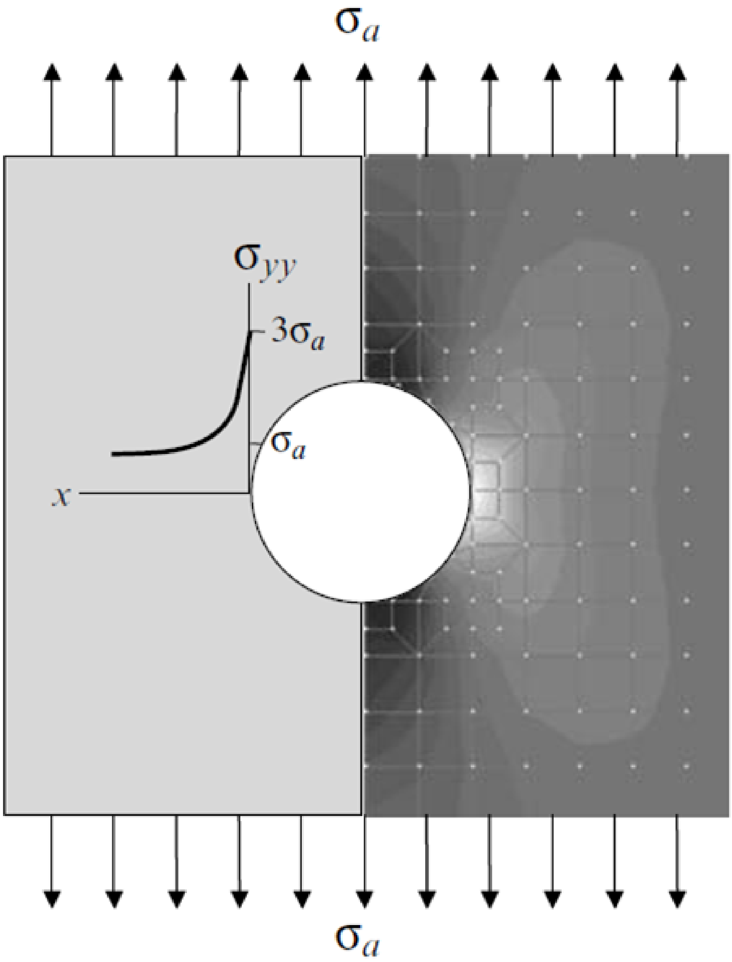

Figure 2.10: *Stress concentration around a hole in a uniformly stressed plate. The contours for* σ_{yy} *were generated using the finite element method [115].*

faces. He stated that the crack may grow if the two conditions are satisfied. First, that the bond at the crack tip must be stressed to the point of failure. The stress at the crack tip is a function of the stress concentration factor (κ) which in turn depends on the ratio of its radius of curvature to its length. Secondly, for an increment of crack extension, the amount of strain energy released must be equal to or greater than the surface energy of the two new crack faces. The mathematical expression for the second condition is given below:

$$\frac{dU_s}{dc} \geq \frac{dU_\gamma}{dc} \tag{2.20}$$

where:
U_s = strain energy,
U_γ = surface energy, and
dc = increment in crack length.

Griffith used Inglis's calculations regarding the stress field for a very narrow elliptical crack to show that the strain energy released by introducing a double-ended crack in an infinite plate of unit width under a uniformly applied stress as shown in Figure 2.11 is given by the following equation [116]:

$$U_s = \frac{\pi \sigma_a^2 c^2}{E} \, Joules \; (per \; meter \; width) \tag{2.21}$$

where:
c = half of the length of double-ended crack,
σ_a = uniformly applied stress, and
E = Young's modulus.

Consider the strain energy released over an area of a circle of diameter $2c$ as shown in Figure 2.11. E should be replaced by $E/(1-\nu^2)$ in Equation 2.21 for the cases of plane strain, where the thickness of specimen is significant. The total surface energy for two surfaces of unit width and length $2c$ is given by the equation below:

$$U_\gamma = 4\gamma c \, Joules \; (per \; meter \; width) \tag{2.22}$$

where, γ is the fracture surface energy of the solid and the factor 4 in Equation 2.22 is used because there are two crack surfaces of length $2c$.

The fracture surface energy is usually larger than the surface free energy because the process of fracture involves atoms located a small distance into the solid away from the surface. The fracture surface energy may also involve the energy dissipative mechanisms such as microcracking, plastic deformation and phase transformations. The strain energy release rate (Joules per meter per unit width) is obtained by taking the derivative with respect to c in Equation 2.21. Similarly, the surface energy creation rate (Joules per meter per unit width) is obtained by taking the derivative with respect to c in Equation 2.22. The critical condition for the growth of the crack is as given below:

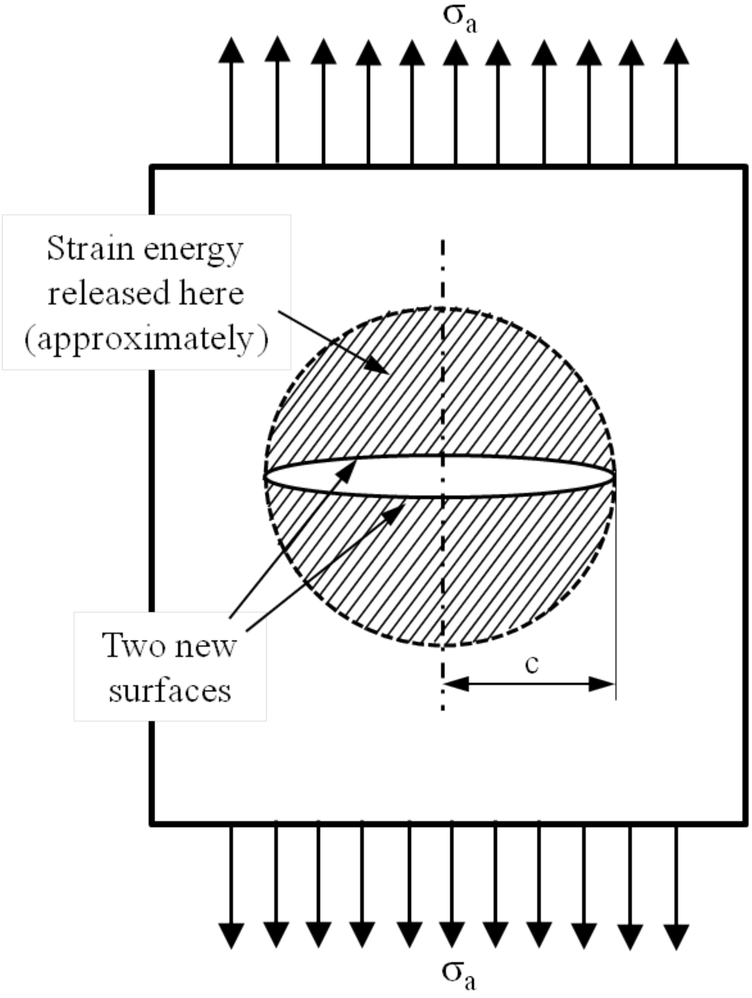

Figure 2.11: *The geometry of a straight, double-ended crack of unit width and total length 2c under a uniformly applied stress* σ_a. *Stress concentration exists at the crack tip and strain energy is released over an approximately circular area of radius c. New surfaces are created because of crack growth [115].*

$$\frac{\pi\sigma_a^2 c}{E} \geq 2\gamma \tag{2.23}$$

The left-hand side of Equation 2.23 represents the rate of strain energy release per crack tip and it applies to a double-ended crack in an infinite solid loaded with a uniformly applied tensile stress. Equation 2.23 shows that the required rate of surface energy per increment of crack length is constant and the rate of strain energy release per increment of crack length is linearly proportional to the crack length. Equation 2.23 presents the energy balance criterion for the growth of crack as given by Griffith. When the strain energy release rate becomes equal to or greater than the surface energy requirement, the crack starts growing since more energy becomes available by the released strain energy than is required by the newly created crack surfaces. This leads to unstable crack growth and the specimen fractures. Whether the crack growth is possible or not is indicated by the energy balance criterion, but whether it will actually occur depends on the state of stress at the tip of crack. Even if there is sufficient strain energy stored to allow the crack to grow, the crack will not extend until the bonds at the crack tip are loaded to their tensile strength. For example in case of the blunted or rounded crack tip, the crack may not grow because of an insufficient stress concentration. The energy balance criterion is a necessary but not the sufficient condition for the fracture to take place. Fracture occurs only when the stress at the crack tip is sufficient to break the bonds there. It is customary to assume the presence of an infinitely sharp crack tip to approximate the worst case condition. However, this does not mean, that all solids fail upon the immediate application of a load. In practice, stress singularities that arise due to an infinitely sharp crack tip are avoided by plastic deformation of the material. However, if such an infinitely sharp crack tip could be obtained, then the crack would not extend unless there was sufficient energy for it to do so. There is a minimum value for the length of the crack at a given stress below which the crack will not propagate by itself and is hence safe. This minimum value of crack length is called critical crack length, c_c, and is given by:

$$c_c = \frac{2\gamma E}{\pi\sigma_a^2} \tag{2.24}$$

2.5.3 Linear elastic fracture mechanics

Assuming isotropic linear elastic material behavior, the closed-form expressions for the stresses in the body can be derived for certain cracked configurations subjected to external forces. Westergaard [117], Irwin [111], Sneddon [118], and Williams [119] were among the first to publish such solutions. Defining a polar coordinate axis with the origin at the crack tip as shown in Figure (Figure 2.13), it can be shown that the stress field in any linear elastic cracked body is given as below:

$$\sigma_{ij} = \left(\frac{k}{\sqrt{r}}\right) f_{ij}(\theta) + \sum_{m=0}^{\infty} A_m\, r^{\frac{m}{2}}\, g_{ij}^{(m)}\,(\theta) \tag{2.25}$$

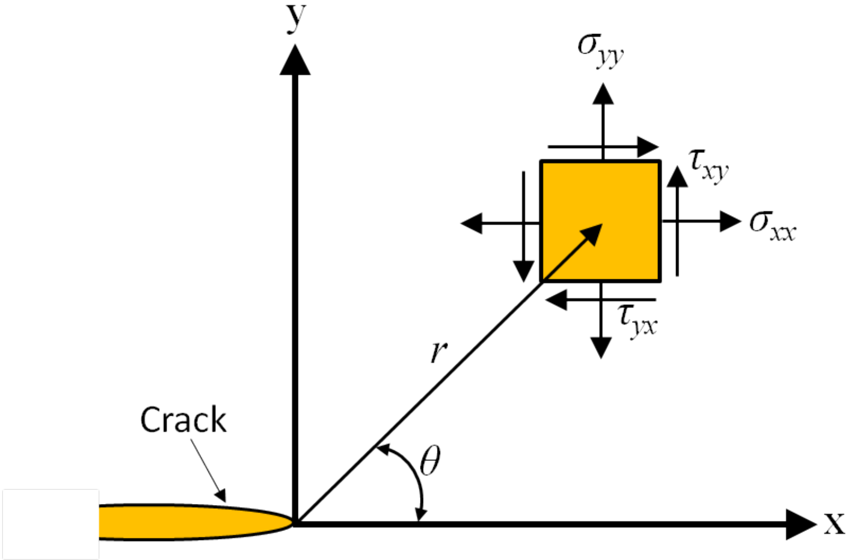

Figure 2.12: *Definition of the coordinate axis ahead of a crack tip. The z-direction is normal to the page [120].*

where:
σ_{ij} = stress tensor,
k = constant,
r, and θ = as defined in Figure 2.12 ,
f_{ij} = dimensionless function of θ in the leading term,
A_m = amplitude for the higher-order terms, and
$g_{ij}^{(m)}$ = dimensionless function of θ for the mth term.

The higher-order terms depend on geometry, but the solution for any given configuration contains a leading term that is proportional to $1/\sqrt{r}$. As r approaches zero, the leading term approaches infinty, but the other terms remain finite or approach zero. Therfore, regardless of the configuration of tzhe cracked body, the stress near the crack tip varies with $\sqrt{r}$. Let us consider a plate displaying a pre-existent crack. There are three types of loading that a crack can experience as shown in Figure 2.13. Mode-I loading, where the principal load is applied normal to the crack plane, tends to open the crack. Mode-II corresponds to in-plane shear loading and tends to slide one crack face with respect to the other. Mode-III refers to out-of-plane shear. A cracked body can be loaded in any one of these modes, or a combination of two or three modes.

Stress intensity factor (SIF)

Each mode of loading produces the $1/\sqrt{r}$ singularity at the crack tip, but the constants k and f_{ij} depend on the mode of loading. The constant k can be replaced by the stress intensity factor K, where $K = k\sqrt{2\pi}$. The stres intensity factor is generally written with a subscript to describe the mode of loading, i.e., K_I, K_{II}, or K_{III}. Hence, the stress fields ahead of a crack tip in an isotropic linear elastic material can be written as below for modes I, II and III respectively:

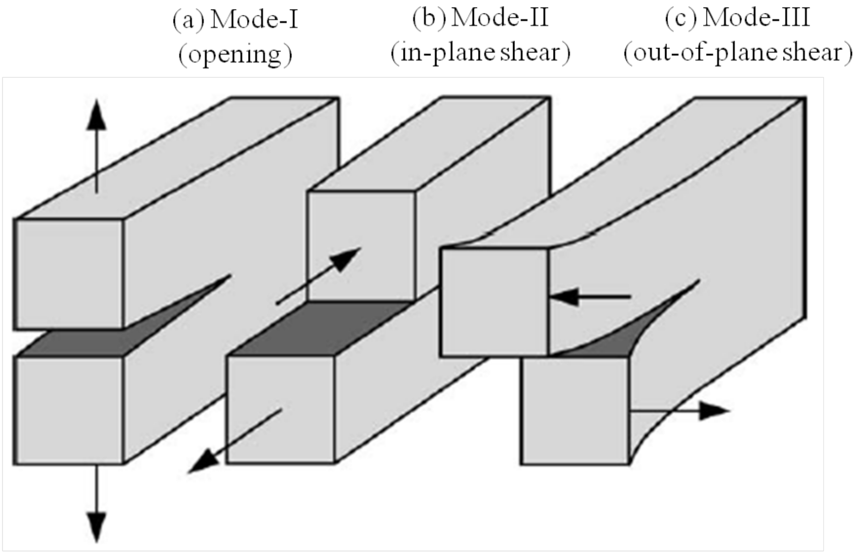

Figure 2.13: *Three modes of fracture (a) Mode-I (opening), (b) Mode-II (in-plane shear), and (c) Mode-III (out-of-plane shear) [120].*

$$\lim_{r\to 0}\sigma_{ij}^{(I)} = \frac{K_I}{\sqrt{2\pi r}} f_{ij}^{(I)}(\theta) \tag{2.26}$$

$$\lim_{r\to 0}\sigma_{ij}^{(II)} = \frac{K_{II}}{\sqrt{2\pi r}} f_{ij}^{(II)}(\theta) \tag{2.27}$$

$$\lim_{r\to 0}\sigma_{ij}^{(III)} = \frac{K_{III}}{\sqrt{2\pi r}} f_{ij}^{(III)}(\theta) \tag{2.28}$$

According the principle of linear superposition, the individual contributions to a given stress component can be added in a mixed mode loading where more than one mode of loading is present as below:

$$\sigma_{ij}^{(total)} = \sigma_{ij}^{(I)} + \sigma_{ij}^{(II)} + \sigma_{ij}^{(III)} \tag{2.29}$$

The experimental work of George R. Irwin led to the theoretical formulation of fracture in 1957 that continues to find wide application [111, 121]. Figure 2.14 shows the semi-infinite plate under a uniformly applied stress with single-ended surface crack of half-length c. Mode-I singular field is considered on the crack plane. It was shown by Irwin that the stresses in the y-direction in the vicinity of an infinitely sharp crack tip could be described by the equation given below:

$$\sigma_{yy} = \frac{K_I}{\sqrt{2\pi r}}\, cos\frac{\theta}{2}\left(1 - sin\frac{\theta}{2} sin\frac{3\theta}{2}\right) \tag{2.30}$$

The above equation arises from Westergaard's solution for the Airy stress function and it applies only to the material in the vicinity of the crack tip. The first term on the right hand side of the above equation describes the magnitude of the stress whereas the terms involving θ describe its distribution. K_I is associated with tensile loading that is mode-I fracture and is therefore called

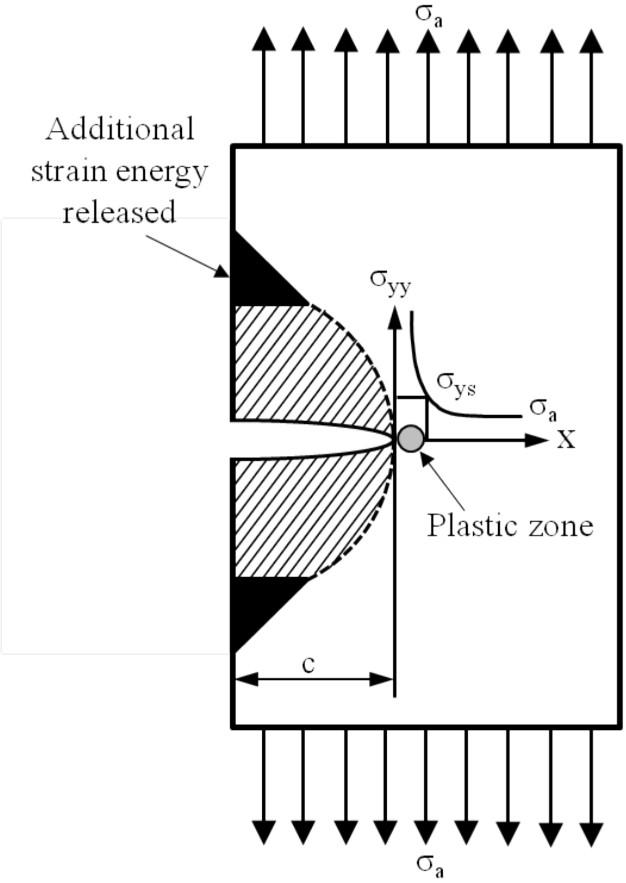

Figure 2.14: *Semi-infinite plate under the externally applied stress with single-ended surface crack of half-length* c*. The additional release in strain energy due to the presence of the surface compared to a fully embedded crack in an infinite solid is indicated by the dark shaded area [115].*

as mode-I stress intensity factor. The stress intensity factors exist for other types of loading also as shown in Figure 2.13, however mode-I type of loading is the most common type of loading that leads to brittle fracture. K_I is defined as below:

$$K_I = \sigma_a Y \sqrt{\pi c} \tag{2.31}$$

where:
σ_a = externally applied stress,
Y = geometry factor whose value depends on the geometry of the specimen, and
c = crack half-length.

Since π and Y are constants for a particular crack system, the stress intensity factor as given by Equation 2.31 indicates that the magnitude of stress at position (r, θ) as given by Equation 2.30 depends only on the externally applied stress and the square root of the crack half-length. So, the stress intensity factor, K_I characterizes the magnitude of the stress at the coordinates (r, θ) near the crack tip, however the shape of stress distribution around the crack tip is exactly the same for all the crack lengths. The stresses at the rack tip are infinite for all sizes of crack as suggested by Equation 2.30. Despite of this, the Griffith energy balance criterion must be satisfied for a crack to grow under the externally applied stress σ_a. Thus, the numerical value of stress provided by the stress intensity factor quantifies the magnitude of the effect of the stress singularity at the crack tip. The value of geometry factor, $Y = 1$ for a straight double-ended crack in an infinite solid, however for a small single-ended surface crack in a semi-infinite solid, $Y = 1.12$ [118, 122]. The additional release in the strain potential energy as compared with a completely embedded crack caused by the presence of free surface as shown by the shaded portion in Figure 2.14 gives rise to 12% correction in the value of geometry factor, Y. As the crack grows deeper into the material, the effect of this correction diminishes. The value of stress intensity factor, K_I at the point of crack growth is called the critical stress intensity factor, K_{IC}. So, K_{IC} represents the onset of crack extension. It does not indicate the fracture of the specimen as this depends on the stability of the crack. K_{IC} is a material property and can be used to characterize toughness. The accurate knowledge of the events taking place within the plastic zone is not required to determine K_{IC}. When the specimens are tested in plane strain, the consistent and reproducible values of K_{IC} can be obtained, however, in plane stress conditions, it depends on the thickness of the plate. Hence, K_{IC} is often known as plane strain fracture toughness and it has the units MPa $\mathrm{m}^{1/2}$. The low value of critical stress intensity factor indicates that for a given stress, a material can only withstand a small length of crack before a crack extends. The critical value of stress intensity factor indicates the onset of crack propagation. Whether this is a stable or unstable condition depends on the crack system. When the equilibrium condition is unstable, the catastrophic fracture occurs. The condition that the stress intensity factor reaches its critical value for the stable configuration implies that the crack is on the point of extension but will not grow unless the applied stress is increased. If this happens, it will result in a new stable equilibrium crack length. For the unstable configuration, the crack will propagate rapidly throughout the specimen and it will lead to failure.

Crack tip plasticity

The magnitude of stress, σ_{yy} approaches infinity at $r = 0$ as given by Equation 2.30. However, in practice, the stress at the crack tip can not be less than the yield strength of the material and therefore the linear elasticity cannot be assumed within a certain distance of the crack tip as can be seen in Figure 2.14. This non-linear region is called the crack tip plastic zone [123]. The Hooke's law is valid and the equations of linear elasticity are applicable outside the plastic zone. The magnitude of stress is proportional to $1/r^2$ as given by Equation 2.30. If the crack tip plastic zone is relatively small, then the strain energy release rate is not influenced much by the events occurring within the plastic zone. The approximate size of the plastic zone is given by the following equation:

$$r_p = \frac{K_I^2}{2\pi\sigma_{ys}^2} \tag{2.32}$$

where, σ_{ys} is the yield strength of the material.

Many engineers and material scientists favor the concept of crack tip plastic zone as it has useful implications for fracture in metals. On physical grounds, the existence of crack tip plastic zone in brittle solids seems to be objectionable. Th stress singularity may be avoided in brittle solids by non-linear but elastic deformations. The strain energy is absorbed by the non-linear stretching of atomic bonds in brittle solids. Therefore, under the application of even the smallest of loads, even though an infinitely large stress occurs at the tip of any surface flaws or cracks within it, the brittle materials do not fall to pieces. Such flaws can grow only if the energy balance criterion is met.

Relationship between K and G

The stress intensity factor, K, and energy release rate, G, are the two parameters that describe the behavior of cracks. The former quantity characterizes the stresses, strains and displacements near the crack tip and the latter parameter quantifies the net change in potential energy that accompanies an increment of crack extension. K is a local parameter and G describes the global behavior. For linear elastic materials, K and G are uniquely related. For a thorough crack in an infinite plate subjected to uniformly applied stress as shown in Figure 2.11, K and G are given by the equations given below:

$$K_I = \sigma\sqrt{\pi c} \tag{2.33}$$

$$G = \frac{\pi\sigma^2 c}{E'} \tag{2.34}$$

Combining Equation 2.33 and Equation 2.34 leads to the following relationship between K and G:

$$G = \frac{K_I^2}{E'} \tag{2.35}$$

where, $E' = E$ for plane stress and $E' = E/(1-\nu^2)$ for plane strain.

When $K_I = K_{IC}$, then G_c becomes the critical value of energy release rate for the material which leads to crack growth and possibly fracture of the specimen. The relationship between K and G is significant because it means that the K_{IC} condition is a necessary and sufficient criterion for crack growth since it embodies both the stress and energy balance criteria. The value of K_{IC} describes the stresses at the crack tip as well as the energy release rate at the onset of crack extension.

Hertzian theory of elastic contact

For a solid elastic cylinder held in contact with a plane by forces F uniformly distributed along the cylinder length L, the resulting pressure causes the line of contact to become a rectangular contact zone. According to the Hertz theory of elastic contact [124], the half-width b of rectangular contact zone is given as below:

$$b = \left[\frac{4R(\lambda_1+\lambda_2)P}{L}\right]^{1/2} \tag{2.36}$$

Using the Equation 2.36, Norden [125] derived the force-displacement relation for the compression between cylinder and the plane, which is given as under:

$$\delta = \frac{F}{L}(\lambda_1+\lambda_2)\left[ln\left(\frac{L^3}{4(\lambda_1+\lambda_2)FR}\right)+2.38629\right] \tag{2.37}$$

where:
F = applied force
L = length of contact between cylinder and plane
$\lambda_1 = \frac{1-\nu_1{}^2}{\pi E_1}$
$\lambda_2 = \frac{1-\nu_2{}^2}{\pi E_2}$
ν_1, ν_2 = Poisson's ratio of cylinder and plane respectively
E_1, E_2 = Young's modulus of cylinder and plane material respectively
R = radius of cylinder, and
δ= displacement of cylinder into plane.

2.6 Cohesive zone model for interface delamination

Firstly, an introuction to the concept of cohesive zone is presented in section 2.6.1 and thereafter, the bilinear cohesive zone material (CZM) model is discussed in section 2.6.2 wherein the mode-I, mode-II and the mixed mode debonding are discussed briefly.

2.6.1 Introduction to the concept of cohesive zone

The non-linear incremental analysis of interface debonding has been performed extensively by using the cohesive zone material models in the last years [126–137]. The cohesive zone material

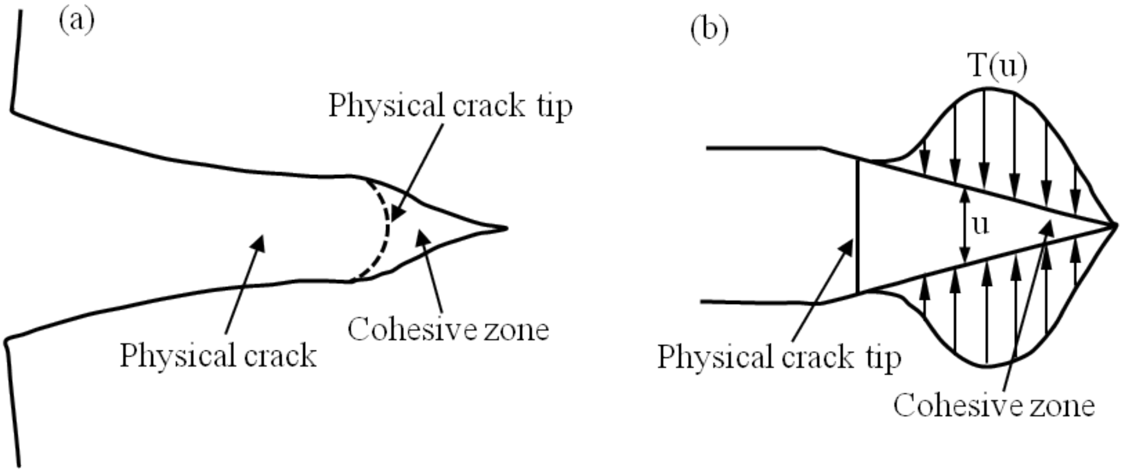

Figure 2.15: *(a) Two different parts in the crack: physical crack and the cohesive zone, and (b) A sketch of cohesive zone with traction, T, as a function of separation distance, u [139].*

models do not require the presence of an initial crack, can be more easily coupled with other material and geometric nonlinearities. They also allow for efficient implementations in a finite element setting with interface and contact elements. The cohesive zone is another way to consider cracks in the system. Barenblatt [138] proposed the concept of cohesive zone. The idea behind this concept was to describe the process of fracture in a more realistic way, such that the stress singularities, found in linear elastic fracture mechanics, do not arise. A crack is divided into two parts in the cohesive zone model. Figure 2.15 (a) shows these two parts of the crack which are denoted as the physical crack and the cohesive zone. The cohesive zone is described as two cohesive surfaces which are held together by tractions. Barenblatt [138] proposed a model which describes that the traction stems from atomic bonding forces. The cohesive zone material (CZM) model consists of a constitutive relation between the tractions in the cohesive zone and the relative displacements of the cohesive surfaces. When the relative displacements in the cohesive zone reach a critical value, a physical crack extension occurs. Figure 2.15 (b) shows the sketch of cohesive zone with traction, T, as a function of separation distance, u. According to the original model proposed by Barenblatt [138], the tractions acting on the cohesive surfaces should have a size and distribution such that the infinite stresses found in linear elastic fracture mechanics are cancelled out.

2.6.2 Bilinear cohesive zone material model

The toughness and ductility of the multi-phase materials such as thin-film solar cells, matrix-matrix composites and laminated composite structure is limited by the fracture or delamination along the interface between phases. This has motivated the research on interface failure. Cohesive zone material (CZM) model is a technique that directly introduces fracture mechanism by adopting softening relationships between tractions and the separations can be used. This in turn introduces a critical fracture energy which is defined as the energy required to break apart the interface surfaces. There are two different possibilities for the cohesive zone material modeling. One approach is the use of interface elements. By employing the interface elements, both exponential and bilinear cohesive zone materials can be used for simulating interface delamination and other fracture phenomenon. A second approach is the use of contact elements together with a cohesive law. The contact elements support a cohesive zone material model with bilinear behavior to model interface delamination. The material data can be specified by two ways using this model. One way is bilinear material behavior with tractions and separation distances and the other way is bilinear material behavior with tractions and critical fracture energies. The constitutive behavior of the interface can be characterized by using the CZM model. The CZM model consists of a constitutive relation between the traction, T, acting on the interface and the corresponding interfacial separation, u.

Interface delamination with contact elements is known as debonding. Debonding is modeled by using the contact elements which are bonded and have a cohesive zone material model defined. Modeling the interface delamination with debonding has several advantages. It is quite easy to modify the existing models with contact definitions to include debonding. The standard contact and debonding can be simulated with the same contact definitions. Modeling debonding with contact elements involves the same steps as any other contact analysis. Therefore, if one is familiar with setting up a contact analysis, then it is quite easy to include debonding in the model. Only the bonded contact option has to be added and a cohesive zone material model for the contact elements has to be defined. Debonding can be defined in any model that includes the surface-to-surface, node-to-surface, line-to-line and line-to-surface type of contact. The bonded contact must be used for the contact elements with the augmented lagrangian method or pure penalty method. The cohesive zone material model is associated with the contact elements in order to activate debonding. Debonding separates the surfaces forming an interface. The debonding mode is determined by the direction of separation. The program identifies the mode of debonding on the basis of material data that is used for normal and tangential directions. Mode-I debonding represents the separation normal to the interface whereas mode-II debonding involves slip tangent to the interface and mixed mode debonding involves both normal separation and tangential slip.

Mode-I debonding

The model proposed by Alfano and Crisfield [140] forms the basis of bilinear cohesive zone material model. Mode-I debonding defines a mode of separation of the interface surfaces where the separation normal to the interface dominates the slip tangent to the interface. The normal contact stress, T_n versus contact gap u_n is plotted in Figure 2.16. The linear elastic loading OA is followed by linear softening AC. The maximum normal contact stress is achieved at point A. Debonding starts at point A and is completed at point C where the normal contact stress falls down to zero value, any further separation occurs without any normal contact stress. The area under the curve OAC is called the critical fracture energy and is the energy released due to debonding. The slope of line OA determines the contact gap at the maximum normal contact stress and therefore characterizes how the normal contact stress decreases with the contact gap thatb is whether the fracture is brittle or ductile. After debonding has been started it is assumed to be cumulative and any unload-

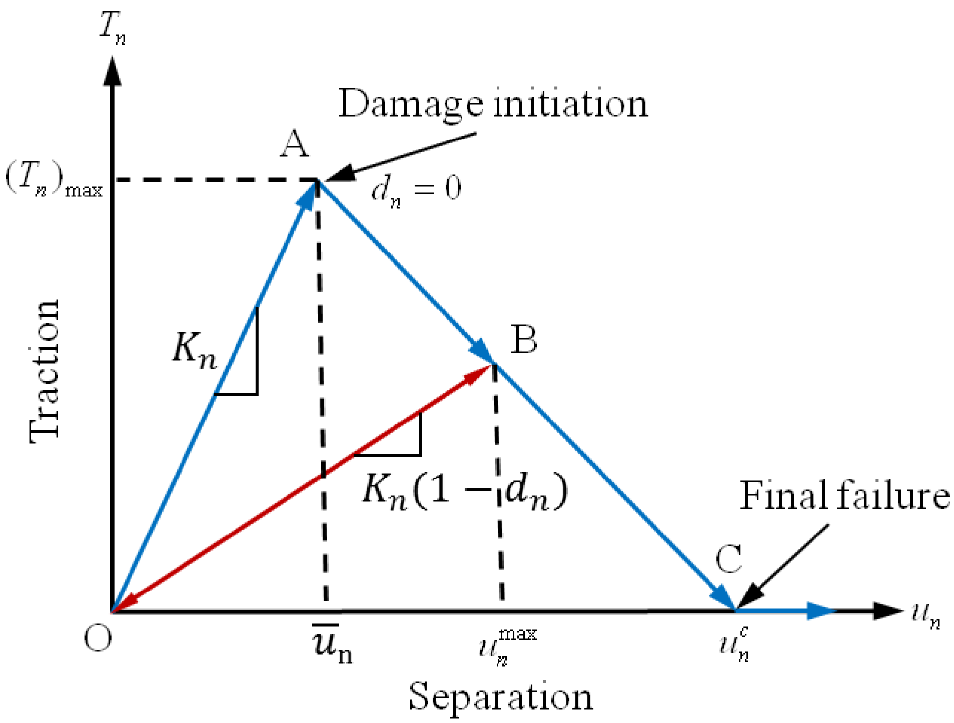

Figure 2.16: *Normal contact stress and contact gap curve for bilinear cohesive zone material.*

ing and subsequent reloading occurs in a linear elastic manner along the line *OB* at a more gradual slope. The normal contact stress is expressed as a function of contact gap by the equation below:

$$T_n = K_n \, u_n \, (1 - d_n) \tag{2.38}$$

where:

T_n = normal contact stress (tension)
K_n = normal contact stiffness
u_n = contact gap
d_n = debonding parameter

The debonding parameter for mode-I debonding, d_n, is defined by the following equation:

$$d_n = \left(\frac{u_n - \bar{u}_n}{u_n} \right) \left(\frac{u_n^c}{u_n^c - \bar{u}_n} \right) \tag{2.39}$$

with $d_n = 0$ for $\Delta_n \leq 1$ *and* $0 < d_n \leq 1$ *for* $\Delta_n > 1$.

where:

$\bar{u}_n$ = contact gap at the maximum normal contact stress
u_n^c = contact gap at the completion of debonding

and

$$\Delta_n = \frac{u_n}{\bar{u}_n} \tag{2.40}$$

The normal critical fracture energy is determined according to the equation below:

$$G_{cn} = \frac{1}{2}(T_n)_{max}\, u_n^c \tag{2.41}$$

where:
$(T_n)_{max}$ = maximum normal contact stress

For mode-I debonding, the tangential contact stress and tangential slip behavior follows the normal contact stress and contact gap behavior and is expressed as below:

$$T_t = K_t\, u_t\, (1 - d_n) \tag{2.42}$$

where:
T_t = tangential contact stress,
K_t = tangential contact stiffness, and
u_t = tangential slip distance.

Mode-II debonding

Mode-II debonding defines a mode of separation of the interface surfaces where tangential slip dominates the separation normal to the interface. The equation for the tangential contact stress and the tangential slip distance behavior is expressed as below:

$$T_t = K_t\, u_t\, (1 - d_t) \tag{2.43}$$

where, d_t is the debonding parameter for mode-II debonding and is defined as below:

$$d_t = \left(\frac{u_t - \bar{u}_t}{u_t}\right)\left(\frac{u_t^c}{u_t^c - \bar{u}_t}\right) \tag{2.44}$$

with d_t = 0 for $\Delta_t \leq 1$ and $0 < d_t \leq 1$ for $\Delta_t > 1$.

where:
$\bar{u}_t$ = tangential slip distance at the maximum tangential contact stress, and
u_t^c = tangential slip distance at the completion of debonding.

and

$$\Delta_t = \frac{u_t}{\bar{u}_t} \tag{2.45}$$

An isotropic behavior is assumed For the 3-D stress state and the debonding parameter is computed by using an equivalent tangential slip distance u_t as below:

$$u_t = \sqrt{(u_t)_1{}^2 + (u_t)_2{}^2} \tag{2.46}$$

where:
$(u_t)_1$ and $(u_t)_2$ are slip distances in the two principal directions in the tangent plane.

The components of the tangential contact stress are defined as below:

$$(T_t)_1 = K_t\ (u_t)_1\ (1 - d_t) \tag{2.47}$$

and

$$(T_t)_2 = K_t\ (u_t)_2\ (1 - d_t) \tag{2.48}$$

The tangential critical fracture energy is computed according to the equation given below:

$$G_{ct} = \frac{1}{2}(T_t)_{max}\ u_t^c \tag{2.49}$$

where:
$(T_t)_{max}$ = maximum tangential contact stress.

The normal contact stress and contact gap behavior follows the tangential contact stress and tangential slip behavior and is expressed as below:

$$T_n = K_n\ u_n\ (1 - d_t) \tag{2.50}$$

Mixed mode debonding

The interface separation depends on both normal and tangential components in mixed mode debonding. The equations for the normal and the tangential contact stress are written as below:

$$T_n = K_n\ u_n\ (1 - d_m) \tag{2.51}$$

and

$$T_t = K_t\ u_t\ (1 - d_m) \tag{2.52}$$

where, d_m is the debonding parameter for mixed mode debonding and is defined as below:

$$d_m = \left(\frac{\Delta_m - 1}{\Delta_m}\right)\chi \tag{2.53}$$

with d_m = 0 for $\Delta_m \leq 1$ *and* $0 < d_m \leq 1$ *for* $\Delta_m > 1$,

where:

$$\Delta_m = \sqrt{\Delta_n^2 + \Delta_t^2} \tag{2.54}$$

and

$$\chi = \left(\frac{u_n^c}{u_n^c - \bar{u}_n} \right) = \left(\frac{u_t^c}{u_t^c - \bar{u}_t} \right) \tag{2.55}$$

There is the constraint on χ that the ratio of the contact gap distances be the same as the ratio of the tangential slip distances. This constraint on χ is enforced automatically by appropriately scaling the contact stiffness value, K_t, as follows:

$$K_t = \left(\frac{(T_t)_{max}\, u_n^c}{(T_n)_{max}\, u_t^c} \right) K_n \tag{2.56}$$

Both normal and tangential contact stresses contribute to the total fracture energy for mixed mode debonding and debonding is completed before the critical fracture energy values are reached for the components. Therefore, in order to define the completion of debonding, a power law based energy criterion is used:

$$\left(\frac{G_n}{G_{cn}} \right)^2 + \left(\frac{G_t}{G_{ct}} \right)^2 = 1 \tag{2.57}$$

where:
$G_n = \int T_n du_n$, and
$G_t = \int T_t du_t$ are, the normal and tangential fracture energies respectively.

The integral sign above in the expressions for the fracture energies indicates that the fracture energy is given by the area under the traction-interfacial separation curve. Input data is the basis of debonding modes: Mode-I for normal data, mode-II for tangential data and Mixed mode for normal and tangential. Converging difficulties in the Newton-Raphson solution occur in debonding. Artificial damping is used in the numerical solution to overcome these problems. The normal contact stress expression for mode-I debonding is as given below:

$$T_n = T_n^{final} + (T_n^{initial} - T_n^{final})\, e^{\frac{-t}{\eta}} \tag{2.58}$$

where:
$t = t^{final}$ - $t^{initial}$ = time interval, and
η = damping coefficient.

The damping coefficient has the same units as of time. Its value should be smaller than the minimum time step size so that in debonding calculations, the maximum traction and maximum separation or critical fracture energy values are not exceeded. The output quantities for contact elements available for debonding are: normal contact stress P, tangential contact stress T_t, the components of tangential contact stress $(T_t)_1$ and $(T_t)_2$, contact gap u_n, tangential slip u_t, the components of tangential slip $(u_t)_1$ and $(u_t)_2$, etc. The debonding specific quantities are also available such as debonding time history, debonding parameter d_n, d_t or d_m, fracture energies G_n and G_t.

3 Experimental and simulation methods

In this chapter, the nanoindentation experiments used to determine the Young's modulus of CIGS thin-film alongwith the experimental and simulation methods used to investigate the mechanical scribing process of CIGS thin-film solar cells are presented. Section 3.1 presents the nanoindentation experiments performed for the mechanical characterization of CIGS thin-film. Section 3.2 describes the experimental setup and procedure adopted to perform the P3 structure by using the mechanical scribing experiments. The experimental method for performing the P2 mechanical scribing is presented in section 3.3. Thereafter, the half-symmetric 2D finite element model (top view) for crack initiation constructed to analyze the fracture mechanical behavior of CIGS layer is described in section 3.4. Finally, section 3.5 presents the 3D finite element model which is used to simulate the buckling and delamination of CIGS thin-film.

3.1 Nanoindentation experiments for CIGS thin-film

The nanoindentation experiments were performed to determine the Young's modulus of CIGS thin-film. In this section, the specimen preparation, experimental setup and procedure adopted for performing the nanoindentation experiments are described. Subsection 3.1.1 presents the different types of specimens used for experiments and the method of their preparation. However, experimental setup and procedure for carrying out the nanoindentation experiments is presented in subsection 3.1.2.

3.1.1 Specimen preparation

The three different specimens were obtained from PVComB Berlin in order to carry out the nanoindentation experiments, two specimens with glass/molybdenum/CIGS structure and the third with silicon/CIGS structure. In all the three specimens, the CIGS absorber layer was deposited by the industrial three-stage co-evaporation process. The CIGS absorber layer for one the specimens was chemically etched from the top using an aqueous solution of HBr/Br_2 to reduce their surface roughness as well as to reduce the thickness of the layer. Previous studies on the thinning of the CIGS layer using a etching process have shown that the etching leads to a flat and specular absorber [141] which in turn helps in overcoming the difficulties arising from the rough CIGS surface. Using the etching time of 15 minutes for the CIGS layer with an original thickness of 2.5 μm, the nominal thicknesses of 1.2 μm was obtained. However the CIGS layer on silicon was

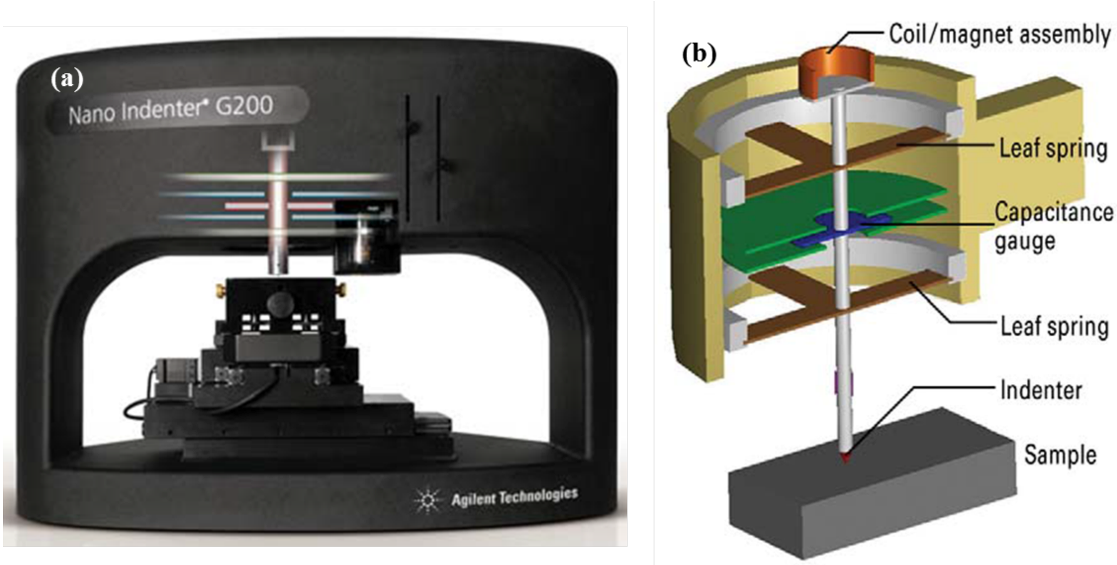

Figure 3.1: *(a) Agilent Nanoindenter G200 for the precise mechanical testing in the micro to sub-nano range of loads and displacements, and (b) Schematic diagram of the actuating and sensing mechanisms of the Nanoindenter G200 [142].*

not etched. The thicknesses were estimated by atomic absorption spectroscopy during the etching process. No apparent damages were observed on the etched surfaces. The three specimens finally used for carrying out the nanoindentation experiments had the following structure with the thickness of each layer specified in bracket:

- Specimen-1: CIGS (3 μm) / Mo (300 nm) / Glass (3 mm)
- Specimen-2: CIGS (1.2 μm) / Mo (300 nm) / Glass (3 mm)
- Specimen-3: CIGS (2.5 μm) / Silicon (500 μm)

3.1.2 Experimental setup and procedure

All experiments were performed using the Agilent Nanoindenter G200 [142]. Figure 3.1 shows the experimental setup used to perform the nanoindentation experiments. The system has load and displacement resolutions of 1 nN and 0.0002 nm respectively. The load capabilities of the Nanoindenter G200 can be expanded from 500 mN with the standard option to 10 N with the high load option. All nanoindentation experiments rely on the accuracy of the fundamental load and the displacement data, requiring the highest precision control of load applied to the sample. The Nanoindenter G200 is powered by electromagnetic actuation-based force transducers to ensure precise measurements. Electromagnetic actuation allows unparalleled dynamic range in force and displacement. It is the world's most accurate, flexible, and user friendly instrument for nanoscale mechanical testing. It enables users to measure Young's modulus and hardness in compliance with ISO 14577 standard. The G200 also enables measurement of deformation over six degrees of magnitude (from nanometers to millimeters).

A Berkovich indenter tip, a three sided pyramid was used in all experiments. The total included angle on this tip is 142.3° with a half angle of 65.35°. A tiny tip of very precise geometry was made to press into the specimens using a small load in order to make minute indentations on the specimens. On each of the three specimens, 20 single indentations were performed at different locations. The maximum depth of penetration of the tip into the surface was kept at 1000 nm in all the cases. The load applied and the depth of penetration of the tip into the surface are measured in real-time during the indentation process. The Continuous stiffness measurement (CSM) is used for continuous measurement of contact stiffness as a function of depth, thus allowing for mechanical properties to be calculated as a function of depth. From this analysis, the Young's modulus of the CIGS thin-film can be determined. The CSM technique offers a means of separating the in-phase and out-of-phase components of the load-displacement history [82, 97, 106, 107]. This separation provides an accurate measurement of the location of initial surface contact and continuous measurement of contact stiffness as a function of depth or frequency, thus eliminating the need for unloading cycles. Since the contact stiffness is determined directly, no assumptions (such as mechanical equilibrium) are required to correct for elasticity. This makes CSM a powerful tool not only for stiff materials such as metals, alloys, and ceramics but also for time-dependent materials like polymers, structural composites, and biomedical materials. The state of the art CSM option provides the means to fully characterize dynamic properties in the nanometer range. Indentation tests using CSM can be controlled with a constant strain rate, a critical test parameter for material systems such as pure metals or low-melting-point alloys, and polymer films and film/substrate systems. This level of control is not possible with the conventional method.

3.2 Mechanical scribing experiments for P3 structure

The mechanical scribing experiments were performed to produce the P3 structure on the CIGS thin-film solar cell specimens in order to understand and analyze the scribing process. P3 scribe is performed by scribing off the CIGS material and the zinc oxide front contact from the top of molybdenum back contact with the help of a flat tip tungsten needle. In this section, the specimen overview, experimental setup and procedure adopted for performing the mechanical scribing experiments to produce P3 structure are described. Subsection 3.2.1 presents the specimen overview. However, experimental setup and procedure for carrying out the mechanical scribing experiments are presented in subsection 3.2.2 and subsection 3.2.3 respectively.

3.2.1 Specimen overview

The industrial CIGS thin-film solar cell specimen is used for the experimental investigations. Figure 3.2 (a) shows the cross-sectional schematic of the material stack in CIGS solar cell specimen used for performing the P3 mechanical scribes. The physical dimensions of the CIGS thin-film solar cell specimen used for experimental investigations are: length: 100 mm and width: 100 mm. The thickness of soda lime glass substarte is 3 mm. Molybdenum (Mo) back contact (0.3 μm in

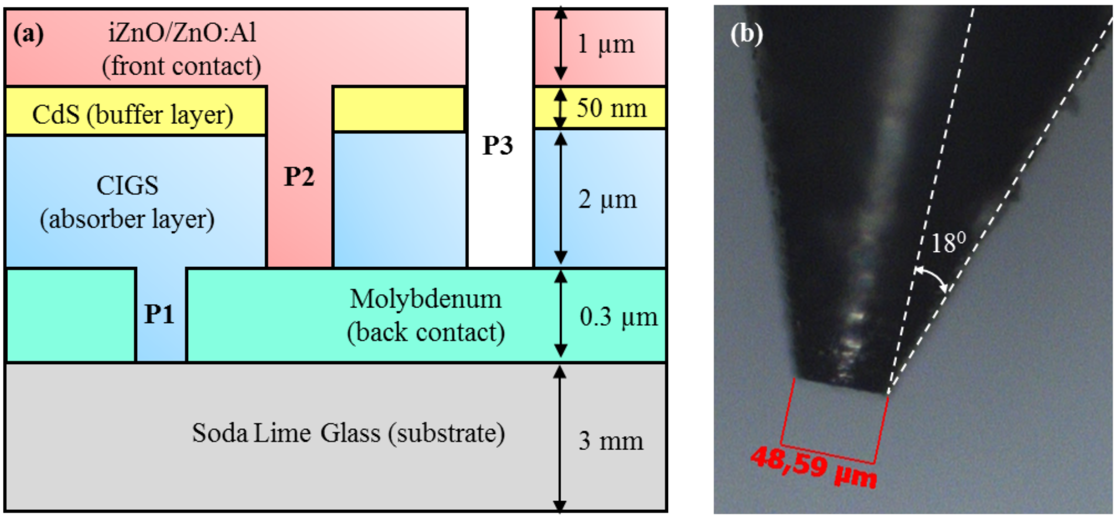

Figure 3.2: *(a) Cross-sectional schematic of the material stack in CIGS solar cell specimen (the sketch is not to scale), and (b) Optical microscope image of the flat tip tungsten needle used for scribing P3 structure.*

thickness) and the zinc oxide front contact (1 μm in thickness) are both deposited by the sputtering process. The 2 μm thick CIGS absorber layer is deposited by the three-stage co-evaporation process. However, very thin cadmium sulphide (CdS) buffer layer (0.05 μm in thickness) is deposited by the chemical bath deposition process.

3.2.2 Experimental setup

To perform the P3 mechanical scribing on the CIGS thin-film solar cell, a laser station 3D-Micromac microSTRUCT C was used. This laser station is then adapted with a mechanical scribe head by JENOPTIK. The mechanical scribe head shown in Figure 3.3 (a) basically consists of the mechanical needle unit [143] and the clamping arrangement. The detailed structure of mechanical needle unit is shown in Figure 3.3 (b). The mechanical needle unit [143] itself comprises of nine different components. The names of these components are: scribing needle, retraction spring, position sensor, needle clamp with clamping screw, linear guide, basic body with force generator, fastening hole, compressed air connection and the fastening surface. Flat tip tungsten needle, 48.59 μm in diameter as shown in Figure 3.2 (b) is used to perform all the scribes. In industrial applications, a flat tip scribing needle is used at the speed of about 1.5 m/s and with a force normal to the specimen (F_n) of the order of 3 N to perform the mechanical scribes on the CIGS thin-film solar cells. The scribing needle used is generally of flat tip gepmetry which is capable to produce the mechanical scribes of the total length of the order of 1000 Km before becoming unusable because of wear and tear.

3.2.3 Experimental procedure

P3 scribe is performed by scribing off the two layers namely CIGS material and the zinc oxide front contact from the top of molybdenum back contact with the help of a flat tip tunsgten needle.

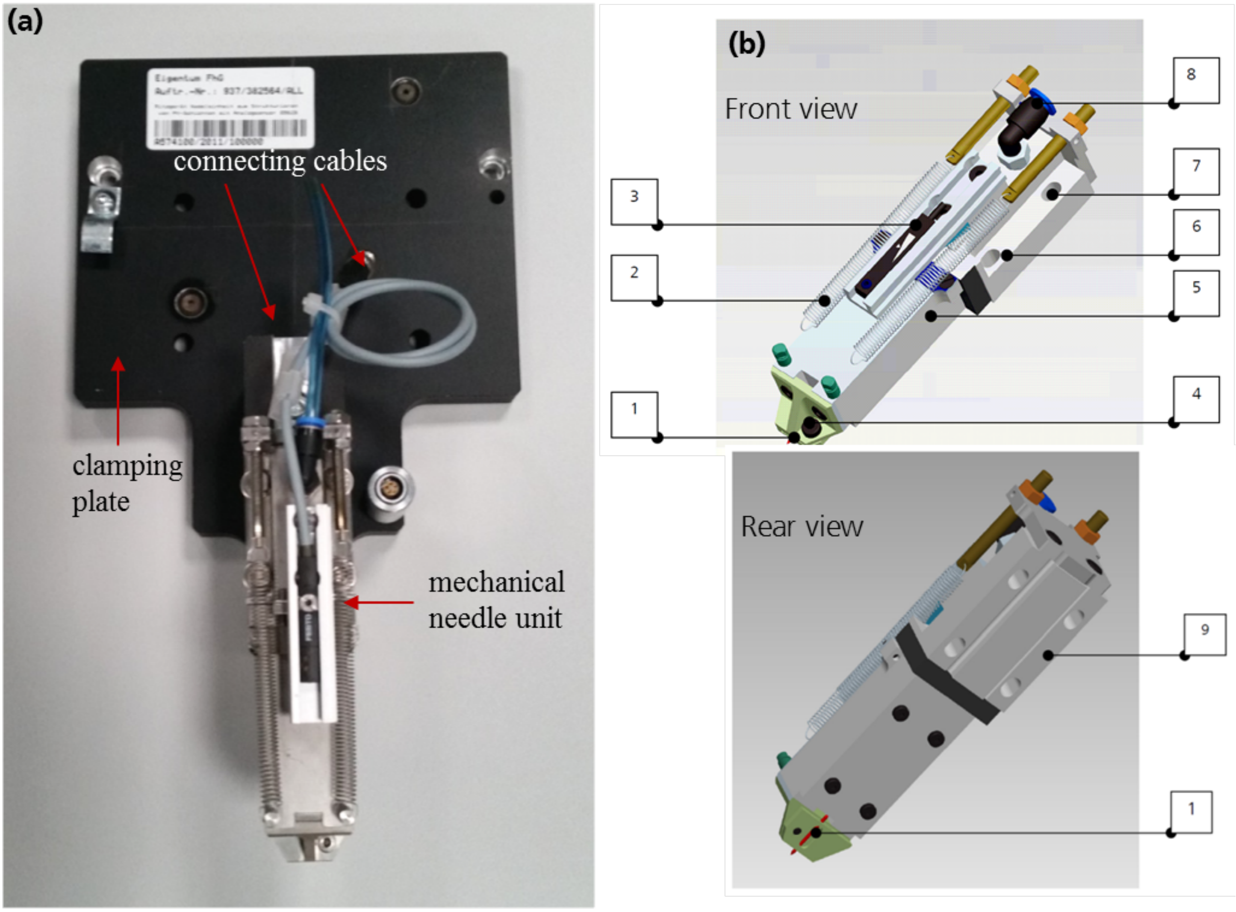

Figure 3.3: *(a) Mechanical scribe head by JENOPTIK, and (b) Structure of the mechanical needle unit by JENOPTIK; different parts of the needle unit are: 1-scribing needle, 2-retraction spring, 3-position sensor (analog magnetic position sensor), 4-needle clamp with clamping screw, 5-linear guide, 6-basic body with force generator, 7-fastening hole, 8-compressed air connection, 9-fastening surface [143].*

Mechanical scribing parameters such as force normal to the specimen (F_n) and the scribing speed (v) were systematically varied in order to achieve different P3 scribes on the CIGS specimen. All the scribes performed were 9 cm long. The force normal to the specimen was varied from 0 to 4 N whereas the scribing speed was varied from 10 mm/s to 200 mm/s to perform the different scribes. Due to the limitations of the present experimental setup, it was not possible to perform the scribing with a speed of more than 200 mm/s. After the experiments were performed, the optical microscope image analysis of the different scribes was done in order to obtain the correlation between the scribe parameters and the scribing characteristics. The purpose of the work is to understand how the parameters of the scribing process such as force normal to the specimen and scribing speed influence the scribing characteristics such as scribe width and line width.

3.3 Mechanical scribing experiments for P2 structure

In P3 scribing experiments as explained in the last section, the scribe is performed by removing the two layers namely the CIGS material and the zinc oxide front contact from the top of molybdenum back contact, whereas P2 scribe is relatively simple which involves the removal of only CIGS material from the top of Mo layer. So, for the sake of simplicity, which can be helpful while modeling the scribing process later on as a two layer system (CIGS/Mo), the P2 scribing experiments were performed on the CIGS thin-film solar cell specimens in order to understand and analyze the scribing process. In this section, the specimen overview, experimental setup and procedure adopted for performing the mechanical scribing experiments to produce P2 structure are described. Subsection 3.3.1 presents the specimen overview. However, experimental setup and procedure for carrying out the mechanical scribing experiments are presented in subsection 3.3.2 and subsection 3.3.3 respectively.

3.3.1 Specimen overview

Two types of CIGS thin-film solar cell specimens with different adhesion strengths of CIGS/Mo interface were used for the experimental investigations in order to study the influence of the adhesion strength on the mechanical scribing process. One specimen has the low adhesion strength at CIGs/Mo interface while the other has relatively higher adhesion strength. The CIGS thin-film solar cell specimens used for the experimental investigations were procured from the Martin Luther University of Halle-Wittenberg. Figure 3.4 (a) shows the cross-sectional schematic of the material stack in CIGS solar cell specimen used for performing the P2 mechanical scribes. The thickness of soda lime glass substrate is 3 mm. Molybdenum back contact (0.3 μm in thickness) is deposited by the sputtering process over the top of soda lime glass substrate. The CIGS absorber layer which is 2 μm in thickness is deposited by the three-stage co-evaporation process.

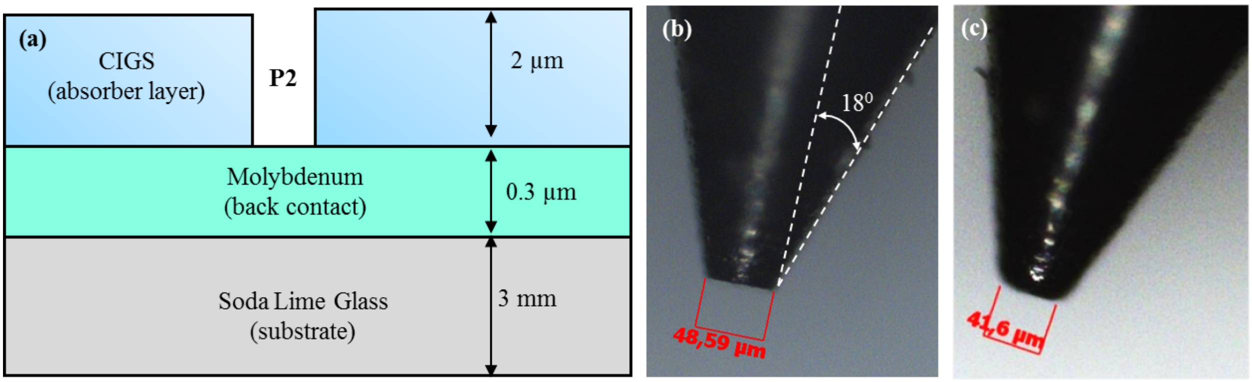

Figure 3.4: *(a) Cross-sectional schematic of the material stack in CIGS solar cell specimen (the sketch is not to scale) and, Optical microscope image of (b) flat tip tungsten needle, (c) slightly rounded tip tungsten needle used for scribing the P2 structure.*

3.3.2 Experimental setup

The experimental setup used for the P2 mechanical scribing of CIGS thin film solar cell specimen is shown in Figure 3.5. This experimental setup was built by Fraunhofer CSP at Halle (Saale) and was ready to use for performing the mechanical scribing experiments. Various components of the experimental setup are: three-axis force sensor K3D60, Z-axis piezo positioner PZ 200 OEM, working table, scribing needle, CIGS specimen, metal clamping plate and the connecting cables.

Two types of scribing needles are used as shown in Figure 3.4 in order to study the influence of needle geometry on the scribing process. Both the needles are made up of tungsten material. However, one of them has flat tip and the other has slightly rounded tip geometry. The diameter of the spherical tip of flat tip needle is measured to be 48.59 μm and that of the slightly rounded tip needle is measured to be 41.6 μm by the optical microscope. In industrial applications, a flat tip scribing needle is used at the speed of about 1.5 m/s and with a force normal to the specimen (F_n) of the order of 3 N to perform the mechanical scribes on the CIGS thin-film solar cells. The scribing needle is generally capable to produce the mechanical scribes of the total length of the order of 1000 Km before becoming unusable because of wear and tear.

The z-axis piezo positioner PZ 200 OEM [144] is shown in Figure 3.6 (a). Movable central part is driven along z-axis with piezo positioner to ensure high stiffness and stability of application. Due to the FEA optimized design as a flexure guidance system, it offers very accurate parallel motion up to 400 μm without any mechanical play, can be easily combined with other piezo electrical systems and provides high dynamic because of mechanical pre-loaded design. Its weight is 140 g, material is stainless steel and has a stiffness of 0.6 N/μm.

The K3D60 three-axis force sensor [145] as shown in Figure 3.6 (b) is used for measuring force on three mutually perpendicular axes. The K3D60 force sensor is designed as a bending beam. It is fixed on one side. At the free end of the beam the initiation of force takes place. The force is measured by the double beam principle. Thus, this force sensor is largely sensitive to the displacement of the force application. It is available for ± 10 N, ± 20 N, ± 50 N or ± 100 N in all three axes. The measurement range of the z-axis can be chosen separately from those of the

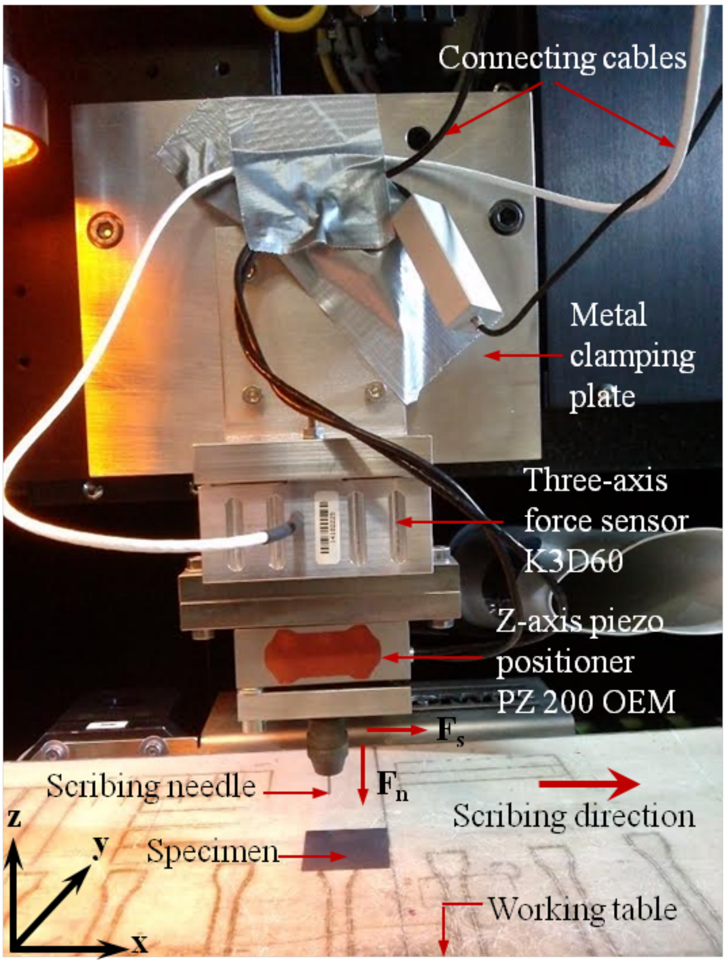

Figure 3.5: *Experimental setup used for performing the P2 mechanical scribes on CIGS thin-film solar cell specimens; F_s and F_n represent the scribing force and the force normal to the specimen respectively. This experimental setup was built by Fraunhofer CSP at Halle (Saale) and was ready to perform the mechanical scribing experiments.*

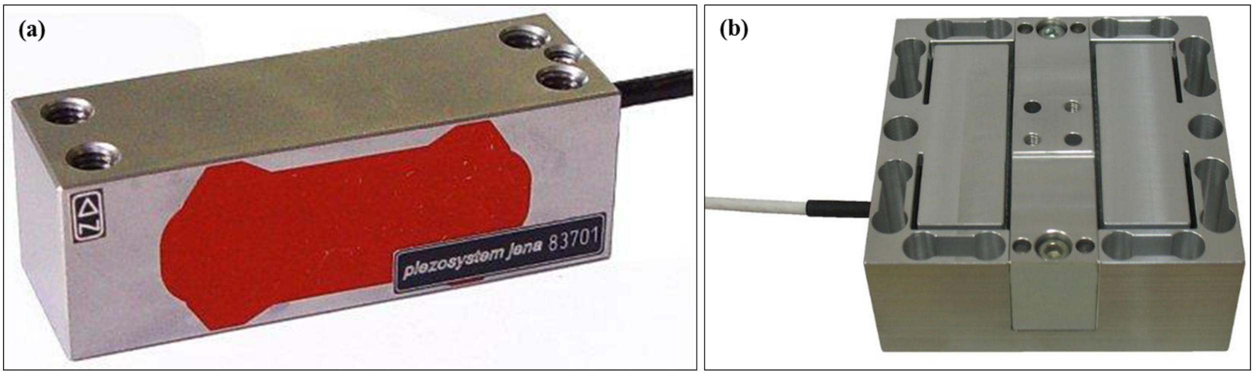

Figure 3.6: *Image of (a) z-axis piezo positioner PZ 200 OEM [144], and (b) Three-axis force sensor K3D60 [145] used in mechanical scribing experiments of P2 structure.*

x and y-axes. The force is applied via the 14 mm × 14 mm section. A component can be fixed on this surface with 2 × M3 bolts and optionally with two pins 3 mm in diameter. The bottom of the sensor is fixed with 2 × M3 bolts. To center the sensor, two 3 mm holes provide for pins. This force sensor stands out for its particularly compact size with a footprint of only 60 mm × 60 mm and a low overall height of only 27 mm. Regarding the main technical data of this three-axis force sensor, precision class is 1%, linearity error is $\leq$ 0.2% FS, and backlash width $\leq$ 0.02% FS. Here, FS stands for Full scale.

3.3.3 Experimental procedure

P2 mechanical scribe is performed by scribing off only CIGS material from the top of molybdenum back contact with the help of a scribing needle. Mechanical scribing parameters such as force normal to the specimen (F_n) and the scribing speed (v) were systematically varied in order to achieve the different scribes on the two different types of specimens. F_n was varied from 0 to 748 mN, whereas v was varied from 0.01 mm/s to 0.5 mm/s. Scribes were performed at lower scribing speeds as compared to that in case of P3 scribing so as to achieve the better understanding of the scribe form. Since the delamination of CIGS film from the Mo substrate was observed even at the normal force of as low as 58 mN, so the smaller values of normal force were used. All the scribes were 5 mm long. The values of scribing force were recorded and saved continuously with respect to time with the help of three-axis force sensor K3D60. The z-axis piezo positioner PZ 200 OEM was used to achieve the accurate parallel motion along z-axis with high stiffness and stability of application. After performing the experiments, the optical microscope image analysis of the different scribes was done in order to obtain the correlation between the scribing parameters such as force normal to the specimen and scribing speed and the scribe characteristics such as scribe width. Scribing force versus time curve was determined by utilizing the data provided by the three-axis force sensor as a result of mechanical scribing experiments.

3.4 Half-symmetric 2D FE model for crack initiation

While performing the both P3 and P2 mechanical scribing experiments of CIGS thin-film solar cells with the use of a tungsten needle, it was found that the material was always removed along the CIGS/Mo interface even with the variation in values of force normal to the specimen and the scribing speed. This is due to the low adhesion strength of CIGS/Mo interface. Therefore, it is useful to analyze the fracture mechanical behavior of CIGS thin-film during the scribing process. In order to understand what happens in the CIGS layer during the scribing process, a half-symmetric 2D finite element model (top view) comprising the CIGS layer and the spherical tip was constructed considering the static aspects of the problem. Engineering simulation software ANSYS was used for the finite element analysis (FEA). Figure 3.7 shows the schematic illustration of the geometry, mesh and applied boundary conditions for the half-symmetric 2D finite element model (top view) without initial crack which consists of CIGS layer and the spherical tip. Due to the symmetry of the scribing test configuration, a half-symmetric FE model was constructed to spare calculation time assuming plane stress conditions. The length and width of the CIGS layer are 150 μm and 200 μm respectively. The radius of spherical tip is taken to be 24.3 μm as in the experimental investigations. The spherical tip is modeled as a rigid body. An elastic material model was used for the CIGS layer. Young's modulus of CIGS material is taken as 78.22 GPa (determined from nanoindentation experiments in present work) and the Poisson's ratio is assumed to be 0.4 (dimensionless) in order to carry out the finite element simulations. The spherical tip is pressed in the downward y-direction along the surface of CIGS layer with a scribing force of 45 mN (determined as mean value of maximum scribing force in P2 mechanical scribing experiments in the present work performed by the flat tip needle on the CIGS specimen with low interface shear strength of 4.68 MPa) in order to simulate the experimental results.

To model the CIGS layer, a 2-D 8-Node structural solid element was used whereas the spherical tip was modeled as 2-D target segment and the contact surface between the CIGS layer and the tip was modeled with 2-D 3-Node surface-to-surface contact elements. In order to consider the Hertzian contact stress behavior, the specimen is meshed very fine in the region where it is expected to be in contact with the spherical tip after the specimen being loaded during simulation as compared to the rest of the part where it is meshed in a biased manner. The mesh is refined in the contact area which includes 50 μm along the positive x-direction and 50 μm along the negative y-direction from the origin of the coordinate system depicted in the Figure 3.7. The applied boundary conditions for the specimen (CIGS layer) are described below:

$$U_x^S(y=-W) = U_y^S(y=-W) = 0 \tag{3.1}$$

$$U_x^S(x=L) = 0 \tag{3.2}$$

$$U_x^S(x=0) = 0 \tag{3.3}$$

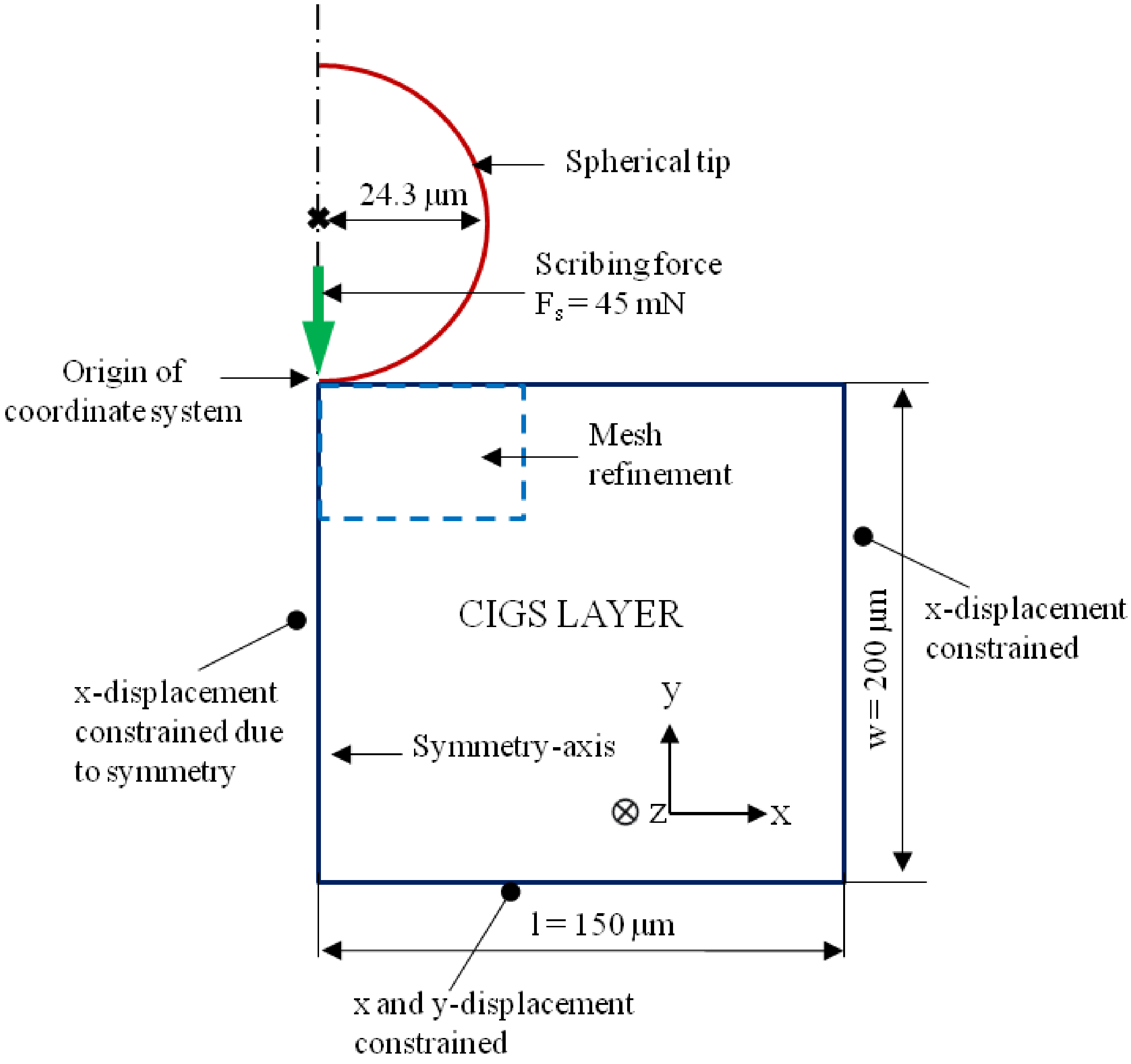

Figure 3.7: *A Schematic illustration of the geometry, mesh and applied boundary conditions for the half-symmetric 2D finite element model (top view) including CIGS layer and spherical tip without assuming the initial crack.*

Where, U_x^S and U_y^S represent the displacement of specimen (CIGS layer) along x- and y-axis respectively. As stated in Equation (3.1), the x and y-displacements of specimen are constrained along the bottom edge. The x-displacement of specimen is constrained along the right edge as stated in Equation (3.2). Equation (3.3) represents the symmetry boundary condition of the specimen along y-axis which means that the x-displacement of specimen is constrained along the left edge. Similarly, the applied boundary conditions for the spherical tip are described as under:

$$U_x^{tip} = R_z^{tip} = 0 \tag{3.4}$$

$$F_y^{tip} = -45\ mN \tag{3.5}$$

Where, U_x^{tip}, R_z^{tip}, and F_y^{tip} represent the displacement of spherical tip along x-axis, rotation of spherical tip along z-axis and the scribing force applied on the spherical tip along y-axis. As stated in the above equations, the displacement along x-axis and the rotation along z-axis are fixed for the spherical tip. The stresses induced in the CIGS layer as a result of the finite element simulations were well within the dimensions of the model and no deformation and stresses were observed near the ends of the model. So, the dimensions of the finite element model are large enough and the constraints are so considered that they don't affect the simulation results. The scribing force of 45 mN is applied on the spherical tip in the downward y-direction into the CIGS layer in order to carry out the finite element simulations.

Figure 3.8 shows the schematic of half symmetric 2D finite element model (top view) including CIGS layer and the spherical tip with the assumption of vertical initial crack. The geometrical dimensions, meshing technique, mesh refinement and the applied boundary conditions are the same as that of the half-symmetric 2D FE model without initial crack shown in Figure 3.7. However, an initial vertical crack of length L μm is assumed to be present in the CIGS layer at a distance of P μm from the origin of the coordinate system along the top edge of the layer. Five nodes are specified along the two faces of the initial crack to define the crack path for the full crack finite element model. The spherical tip is pressed in the downward y-direction along the surface of CIGS layer with a scribing force of 45 mN in order to simulate the experimental results. In order to study the qualitative trend of mode-I stress intensity factor with the changing position of initial crack along the top edge of CIGS layer, an initial vertical crack of 3 μm length is assumed to be present along the top edge of CIGS layer and the position of vertical initial crack, P, from the origin of the coordinate system is varied along the top edge of CIGS layer starting from 1 μm upto 24 μm. The mode-I stress intensity factor K_I values for the crack tip are recorded for each of these positions of the initial crack as the result of numerical simulations. For all these simulations, the boundary conditions are kept constant. Then, these stress intensity factor values are plotted against the position of initial crack. In the next investigation, an initial crack is being assumed to be present very near the contact region between the scribing needle and the CIGS layer that is at a distance of 0.5 μm from origin of the coordinate system along the top edge of CIGS layer. Now the length of initial crack is varied from 0.3 μm to 10 μm. The scribing needle is pressed in to

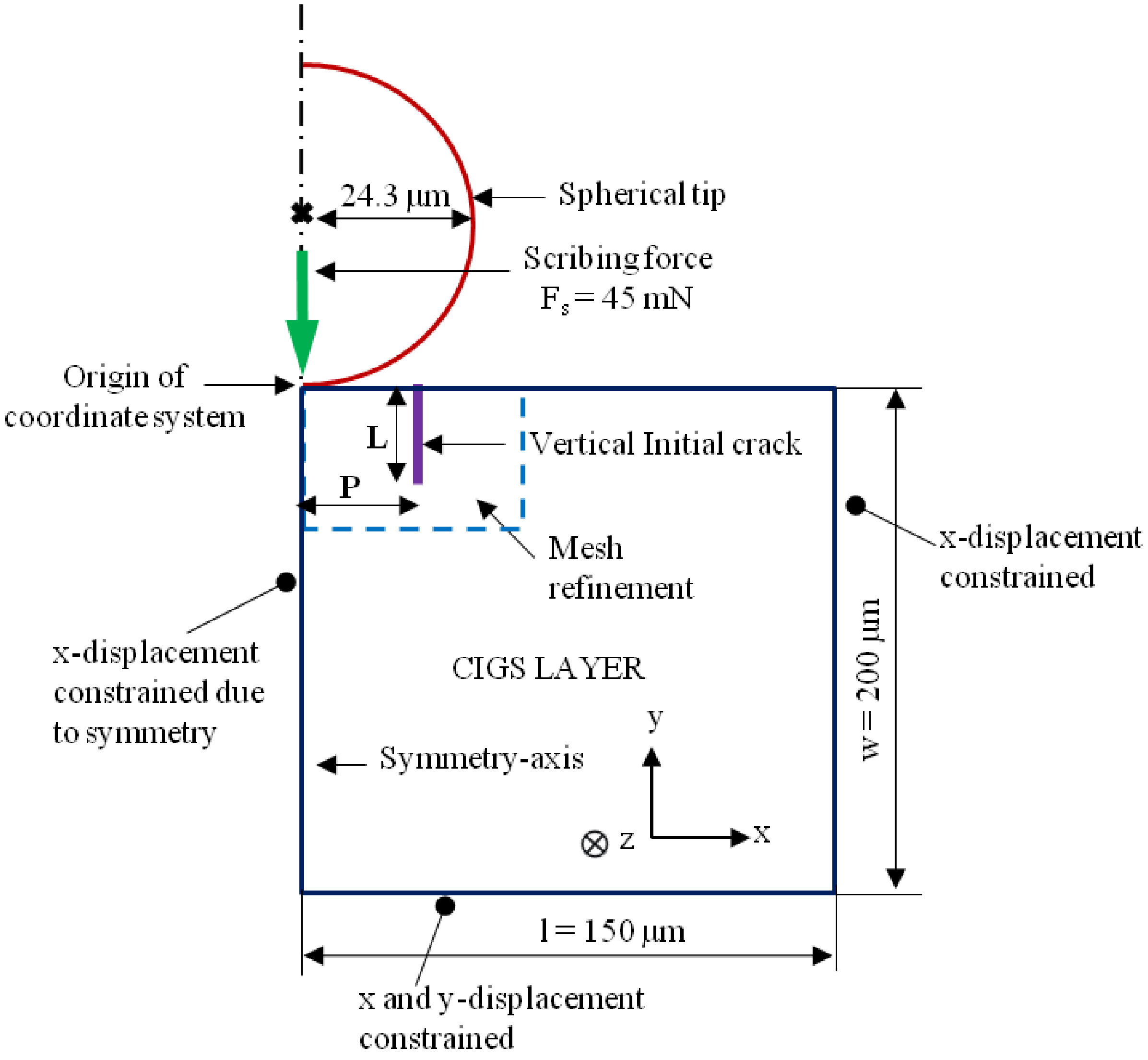

Figure 3.8: *A schematic illustration of the geometry, mesh and applied boundary conditions for the half-symmetric 2D finite element model (top view) including CIGS layer and spherical tip with the assumption of vertical initial crack.*

the layer with a force of 45 mN. In the further investigations, the length of vertical initial crack is taken to be 3 μm and 5 μm to carry out the fracture mechanical simulations in order to analyze the influence of variation in the length of initial crack. The mesh size, boundary conditions and the loading conditions are kept same for all the finite element simulations. Finally, the mode-I stress intensity factor values obtained for the lengths of initial crack that is 3 μm and 5 μm are plotted against the varying position of initial crack along the top edge of the CIGS layer.

3.5 3D finite element model for buckling and delamination

Both the P3 and P2 mechanical scribing experiments revealed almost the same piece of information regarding the key features of delamination/chipping of CIGS material and the shape of the chippings. So, for the sake of simplicity and to save the simulation time, the two layer system

(CIGS/Mo) is considered for the finite element simulation and the simulation results are correlated later on with the findings of P2 mechanical scribing experiments where the CIGS layer was being scribed off from the top of Mo layer with the help of scribing needle. To simulate the initiation and evolution of buckling driven delamination of CIGS thin-film, a 3D two layer (CIGS/Mo) finite element model was constructed using the ANSYS simulation software. Due to the symmetry of the scribing test configuration, a half-symmetric finite element model was constructed to spare calculation time. Thin-film of CIGS material is considered to be bonded to a relatively stiff molybdenum substrate, where the thin-film can buckle under compression. A layer of cohesive elements was assigned along the interface to model the interaction between the film and the substrate. The bilinear traction-separation relation was used to describe the constitutive behavior of the cohesive elements.

3.5.1 Model geometry and materials properties

Figure 3.9 presents the schematic illustration of the geometry, mesh and applied boundary conditions for the 3D FE model of thin-film buckling and delamination of CIGS/Mo system. The thin-film/substrate system is considered to be three-dimensional. Let x and y be in-plane coordinates, while z is the direction perpendicular to the mean plane of the thin-film/substrate system. The conical scribing needle has a lower radius (r) of 24.3 μm as in experiments and the length (h) equal to 10 μm. The included angle for the scribing needle used for the experiments is 18° (see Figure 3.2). Using this angle of 18°, the upper radius of the needle (R) at the length of 10 μm was calculated to be 28 μm. So the conical needle has a upper radius of 28 μm. The 3D 2-layer model is made of CIGS thin-film with the length (L) of 150 μm, the width (W) of 200 μm and the thickness (h_f) of 2 μm. The molybdenum substrate has a length (L) of 150 μm and the width (W) of 200 μm. There was no influence of the substrate on the simulation results in respect of the buckling and delamination, the most probable reason being the stiffness of Mo material, as the Mo is quite stiff as compared to CIGS (see Table3.1). So, the glass layer under the molybdenum layer was not considered to carry out the finite element simulations in order to save the simulation time. As a result of which the system was modeled as a two layer (CIGS/Mo) system. In addition to this, it was observed that there was no influence of the thickness of Mo substrate on the simulation results. So, to carry out the present finite element simulations, the thickness of Mo substrate (h_s) is taken to be 4 μm. The delamination at the CIGS/Mo interface in the finite element simulations was well within the dimensions of the model. So, the dimensions of the model are large enough to simulate the buckling and delamination of CIGS thin-film during the mechanical scribing process. A standard contact is used at the CIGS/Mo interface in order to simulate the buckling and delamination of CIGS thin-film. The standard contact represents the interface adhesion (shear) strength of 0 MPa.

However, in order to study the influence of adhesion (shear) strength of CIGS/Mo interface on the delamination and buckling behavior of CIGS thin-film, a relatively smaller finite element model is constructed to spare the simulation time. For these numerical investigations, the length

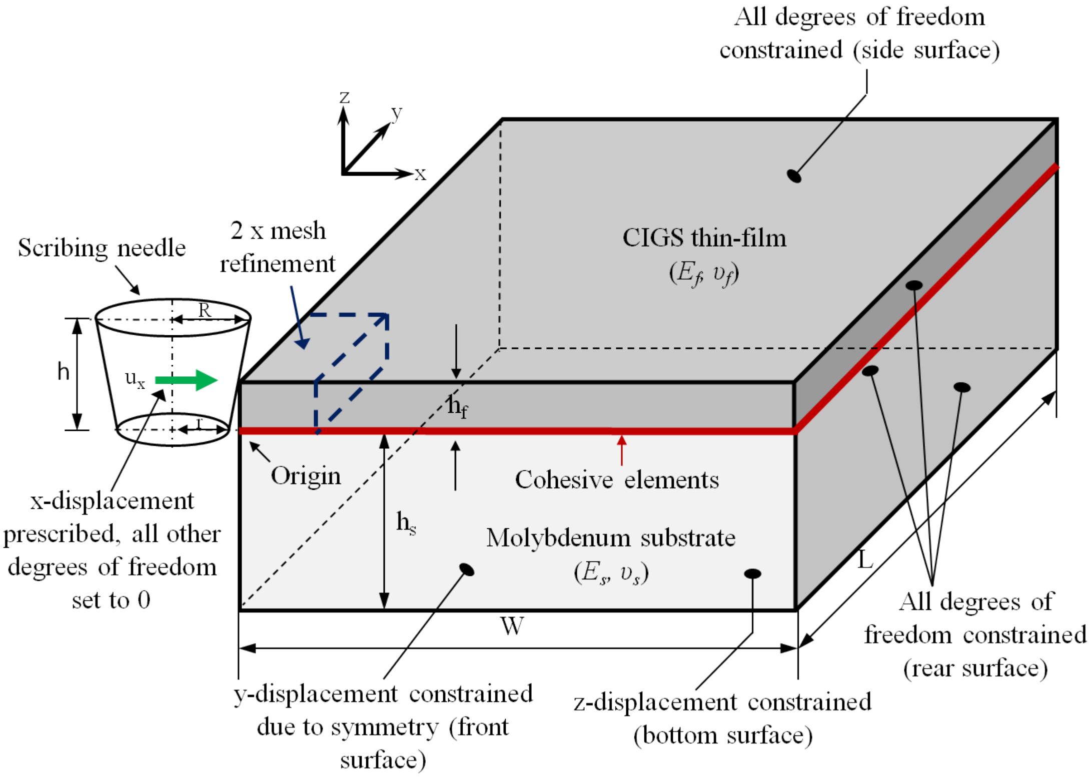

Figure 3.9: *A schematic illustration of the geometry, mesh and applied boundary conditions for the 3D finite element model of thin-film buckling and delamination of CIGS thin-film/molybdenum substrate system.*

Table 3.1: *Material properties*

Material	**Young's modulus**	**Poisson's ratio**
CIGS thin-film	78.22 GPa	0.4
Molybdenum substrate	329 GPa [146]	0.31

(L) and width (W) for both CIGS thin-film and Mo substrate are taken to be 60 μm and 120 μm respectively. However, the thicknesses of CIGS film and Mo substrate are kept to be same as 2 μm and 4 μm respectively. The parameters of scribing needle geometry are also kept same as described above. These dimensions of the model are large enough and the constraints are so considered that they do not affect the simulation results with respect to the buckling and delamination of the CIGS thin-film. The interface between the CIGS thin-film and the Mo substrate is modeled with the cohesive zone material (CZM) model and using the contact elements. The thickness of interface is zero in the beginning as recommended in ANSYS simulation software.

The conical scribing needle is modeled as a rigid body. Linear elastic model is used to describe the CIGS thin-film and the molybdenum substrate materials. The material properties of the CIGS thin-film and molybdenum substrate are listed in Table 3.1. The Young's modulus of CIGS material is taken as 78.22 GPa (determined in the nanoindentation experiments in the present work) and the Poisson's ratio is assumed to be 0.4 (dimensionless) in order to carry out the finite element simulations. The Young's modulus and Poisson's ratio for the molybdenum substrate are taken to be 329 GPa and 0.31 (dimensionless) respectively [146].

3.5.2 Elements and meshing

Three kinds of elements are employed to build the 3D finite element model for buckling and delamination. 3-D 20-node higher order solid element SOLID186 that exhibits quadratic displacement behavior is used to model both CIGS thin-film and molybdenum substrate materials. This element is defined by 20 nodes having three degrees of freedom per node: translations in the nodal x, y, and z directions. It is capable of being used in cases of large deflection and large strain. Besides, it can be coupled with CONTA174 and TARGE170 elements to define a contact pair. 3-D target element TARGE170 is used to model the conical scribing needle as rigid and the upper surface of substrate material in the contact pair between the CIGS film and the molybdenum substrate. 3-D 8-node surface to surface contact element CONTA174 is used to model the lower surface of thin-film to represent contact and sliding between thin-film and substrate. The contact element CONTA174 is also used at CIGS contact surface facing the scribing needle to model the contact pair between the needle and the CIGS layer. The contact element CONTA174 is applicable to 3-D structural and coupled field contact analysis. The element size of 2 μm is chosen to mesh the CIGS film. Thereafter, the mesh is refined in the region where the film is expected to be in contact with the scribing needle after the specimen being loaded. The mesh is refined by two times in this region that is 15 μm along the positive x- and y-axis from the origin of the coordinate system and throughout the thickness of CIGS film as depicted in Figure 3.9. There are total number of 55859 elements for the CIGS thin-film. The element size of 2 μm is chosen to mesh the full substrate material which is equal to the thickness of the CIGS thin-film. There are total number of 89492 elements used to mesh the molybdenum substrate material.

The same three kinds of elements as described above namely SOLID186, CONTA174 and TARGE170 are used in order to build the relatively smaller 3D FE model for studying the influence of interface adhesion (shear) strength on the scribe form. The element size of 2 μm is chosen to mesh the CIGS film. The mesh is refined in the contact region. The mesh is refined by two times in this region that is 15 μm along the positive x- and y-axis from the origin of the coordinate system and throughout the thickness of CIGS film as depicted in Figure 3.9. Since the model is relatively smaller, therefore the number of elements generated as a result of meshing are also less as compared to the full size model. There are total number of 12261 elements for the CIGS thin-film. The element size of 2 μm is chosen to mesh the full substrate material which is equal to the thickness of the CIGS thin-film. There are total number of 11676 elements used to mesh the molybdenum substrate material.

3.5.3 Applied load and boundary conditions

The applied boundary conditions for the 3D FE model are shown in Figure 3.9. The specimen that is film/interface/substrate system is symmetric along the $x-z$ plane on the front surface, so all the nodes in $x-z$ plane can have the displacement in y-direction. The specimen is constrained at the bottom surface in z-direction. However, all the degrees of freedom are constrained on the rear surface and the side surface as depicted in Figure 3.9. The load applied to the needle is the displacement load. This kind of load can help avoid the convergence problems caused by the initial contact gap. The scribing needle is given displacement of 1.5 μm in the positive x-direction into the CIGS thin-film and all other degrees of freedom are set to zero. However, the needle displacement of 2 μm is used for simulating the relatively smaller FE model constructed with the cohesive zone material model at the CIGS/Mo interface in order to analyze the influence of interface adhesion (shear) strength on the scribe form.

3.5.4 Cohesive zone implementation at CIGS/Mo interface

In order to study the influence of adhesion (shear) strength of CIGS/Mo interface on the process of delamination and buckling of CIGS thin-film during the mechanical scribing process, a layer of cohesive elements is assigned along the CIGS/Mo interface to model the interaction between the thin-film and the substrate. In linear elastic fracture mechanics, a real crack tip with the processing zone exists, however, in the cohesive zone concept, the interface separation takes place in the certain area. The transfer of loading is performed through the cohesive traction in this area. The cohesive elements describe the traction when the connected elements are teared apart from each other. In a finite element model, tractions can be in tensile as well as in shear directions. The bilinear traction-separation law was used to describe the constitutive behavior of the cohesive elements. The general behavior of the traction components has been described in Figure 2.16. It describes the evolution of the tractions applied to the given cohesive elements. The behavior of traction during the damage initiation and damage evolution is kept linear with respect to the separation for both mode-I and mode-II in the bilinear traction-separation law. The integral of T from 0 to u^c represents the total work of rupture where, u^c is the displacement at full rupture. It is worth to mention here that $\bar{u}$ should be kept as small as possible, especially as compared to u^c. The total work of rupture is given by $G_c = T_{max}\, u^c/2$. This bilinear behavior is defined for both mode-I and mode-II interfacial toughness through the normal traction, T_n and the shear traction, T_t. After the application of traction to the cohesive element, the displacement remains proportional to the applied traction until a criterion a certain criterion is reached. As shown in the Figure 2.16, $K = T_{max}/\bar{u}$ represents the initial loading stiffness. It is defined for both mode-I and mode-II. We choose a damage initiation criterion which is based on the maximum normal, T_n and shear, T_t tractions.

$$\left(\frac{T_n}{(T_n)_{max}}\right)^2 + \left(\frac{T_t}{(T_t)_{max}}\right)^2 = 1 \tag{3.6}$$

The cohesive traction, T_{max} is allowed to decrease irreversibly along the traction-separation curve as the maximum interfacial displacemnt, u^{max} increases from $\bar{u}$ to u^c so as to implement the irreversible decohesion. This represents the interface damage once the damage initiation criterion is met. After opening upto the maximum interfacial displacement u^{max}, if the cohesive element closes subsequently, it unloads from maximum interfacial displacement to zero with decreasing interface traction given by $T = K(1-d)u$. The damage parameter, d is so chosen that it increases

Table 3.2: *Four sets of cohesive zone parameters for the 3D FE model constructed to study the influence of interface adhesion (shear) strength on the delamination and buckling of CIGS thin-film.*

Parameter set	T_n **(MPa)**	G_{cn} **(N/mm)**	T_t **(MPa)**	G_{ct} **(N/mm)**	η	β
Model-1	0.936	1×10^{-5}	0.936	1×10^{-5}	1e-8	1
Model-2	4.68	5×10^{-5}	4.68	5×10^{-5}	1e-8	1
Model-3	10.7	2×10^{-4}	10.7	2×10^{-4}	1e-8	1
Model-4	23.4	1×10^{-3}	23.4	1×10^{-3}	1e-8	1

from 0 to 1 with $u^{max} > \bar{u}$ and satisfies the condition $T_{max}\ u^{max} = K(1-d)u^{max}$. This softening of the loading-unloading curve results in irreversibility through incomplete restitution of interface energy upon the unloading of the cohesive element. The rupture is complete when the maximum interfacial displacement reaches the displacement value at full rupture, damage parameter becomes equal to 1 and T_{max} becomes zero. Due to the elastic mismatch between the thin-film and the substrate [38], the delamination crack along the CIGS/Mo interface is typically under a mixed mode condition. Therefore, the interfacial properties are required for both the mode-I and mode-II conditions. The interface parameters which are required to be specified for the bilinear traction-separation model [147] include the following:

- T_n : Maximum normal strength,
- G_{cn} : Critical fracture energy per unit area for normal separation,
- T_t : Maximum shear strength,
- G_{ct} : Critical fracture energy per unit area for tangential slip,
- η : Artificial damping coefficient
- β : Flag for tangential slip under compressive normal cohesive traction.

Table 3.2 presents the four set of cohesive zone parameters used in the present finite element analysis. Model-1 represents the FE model with lowest interface adhesion (shear) strength of 0.936 MPa, whereas model-4 presents the FE model with the highest interface adhesion (shear) strength of 23.4 MPa. The lowest and highest values of the interface adhesion strength are assumed suitably to study the influence of varying interface adhesion strength on the scribing process. However, model-2 and model-3 represent the FE models with intermediate values of interface adhesion (shear) strengths of 4.68 MPa and 10.7 MPa respectively (determined from the experiments in the present work). The critical fracture energy densities for normal separation and tangential slip are assumed suitably as presented in Table 3.2. The value for artificial damping coefficient is specified to be 1×10^{-8} and β is taken as 1. The stiffness of cohesive elements (K) is by default established with ANSYS simulation software, however the actual value of the contact stiffness is affected by the defined material properties, the element size and the total degrees of freedom in the FE model.

4 Results

This chapter presents the results of nanoindenation experiments and therefater the results obtained from experimental and numerical investigations carried out for the mechanical scribing of CIGS thin-film solar cells are described. The results of nanoindentation experiments carried out for the mechanical characterization of CIGS thin-film are described in section 4.1. Section 4.2 presents the results of mechanical scribing experiments performed to produce the P3 structure, while section 4.3 focuses on the results for P2 structure. The numerical results of simulation for the half-symmetric 2D FE model (top view) of crack initiation are presented in section 4.4. Finally, section 4.5 describes the simulation results obtained for 3D finite element model of buckling and delamination.

4.1 Results of nanoindentation experiments

In this section, the nanoindentation experiments performed for the mechanical characterization of CIGS thin-film are presented. To investigate the Young's modulus of CIGS thin-films, 20 indentations were performed on each of the three specimens at different locations. The maximum depth of penetration of the tip into the surface was kept at 1000 nm in all the cases. Two of the specimens have glass/molybdenum/CIGS structure whereas the third specimen has silicon/CIGS structure in order to study the influence of underlying material on the modulus of the CIGS thin-film. However, for all the three specimens, the CIGS absorber layer was deposited by the industrial three-stage co-evaporation process. Subsection 4.1.1 describes the determination of Young's modulus of CIGS thin-film. The effect of underlying material on the Young's modulus of thin-film with the increse in penetration depth is presented in the subsection 4.1.2.

4.1.1 Determining the Young's modulus of CIGS thin-film

The Continuous Stiffness Measurements (CSM) data recorded by the Agilent Nanoindenter G200 regarding the Young's modulus was used to plot the Young's modulus versus displacement into surface. Figure 4.1 (a) shows the the variation of Young's modulus versus displacement into surface for all the 20 indentations made in the specimen-1 which has a structure of CIGS (3 μm) / Mo (300 nm) / Glass (3 mm). The mean value of Young's modulus at each individual contact depth is plotted in Figure 4.1 (b). The error bars shown are the standard deviations obtained from the 20 indentations at each individual contact depth. The mean value of Young's modulus was determined to be 75 ± 8.31 GPa from the CSM data for specimen-1.

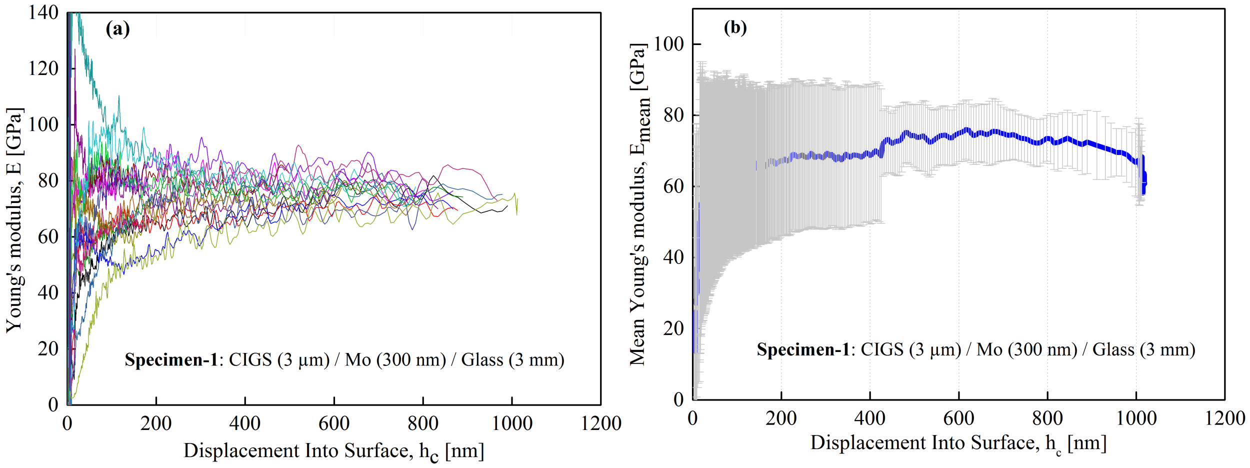

Figure 4.1: *(a) Young's modulus (E), and (b) Mean value of Young's modulus* (E_{mean}) *versus displacement into surface* (h_c) *for specimen-1 for all the 20 indentations; error bars are also included for all the indentations.*

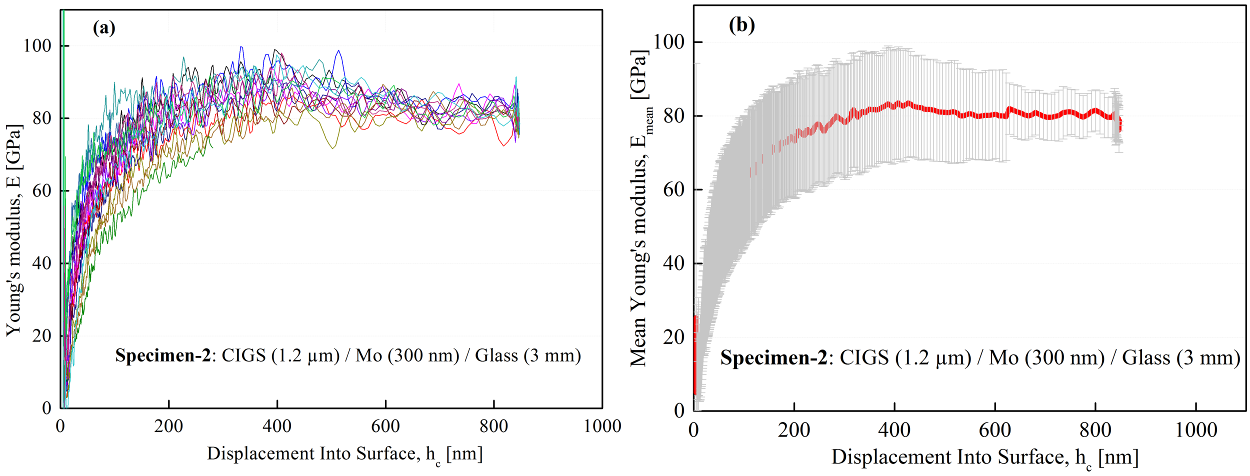

Figure 4.2: *(a) Young's modulus (E), and (b) Mean value of Young's modulus* (E_{mean}) *versus displacement into surface* (h_c) *for specimen-2 for all the 20 indentations; error bars are also included for all the indentations.*

Now, the CSM data recorded continuously by the Agilent Nanoindenter G200 during the experiments for the specimen-2 which has a structure of CIGS (1.2 μm) / Mo (300 nm) / Glass (3 mm) was analyzed. The Young's modulus was plotted against the displacement into surface. Figure 4.2 (a) shows the the variation of Young's modulus versus displacement into surface for all the 20 indentations made in the specimen-2. The mean value of the Young's modulus at each individual contact depth is plotted in Figure 4.2 (b). The error bars shown are the standard deviations obtained from the 20 indentations at each individual contact depth. The mean value of Young's modulus was calculated to be 83.19 $\pm$ 14.2 GPa from the CSM data for specimen-2.

At the end, the CSM data recorded continuously during the experiments for the specimen-3 which has a structure of CIGS (2.5 μm) / Silicon (500 μm) was analyzed. The Young's modulus was plotted against the displacement into surface. Figure 4.3 (a) shows the the variation of Young's modulus versus displacement into surface for all the 20 indentations made in the specimen-3. Figure 4.3 (b) shows the mean value of the Young's modulus at each individual contact depth. The

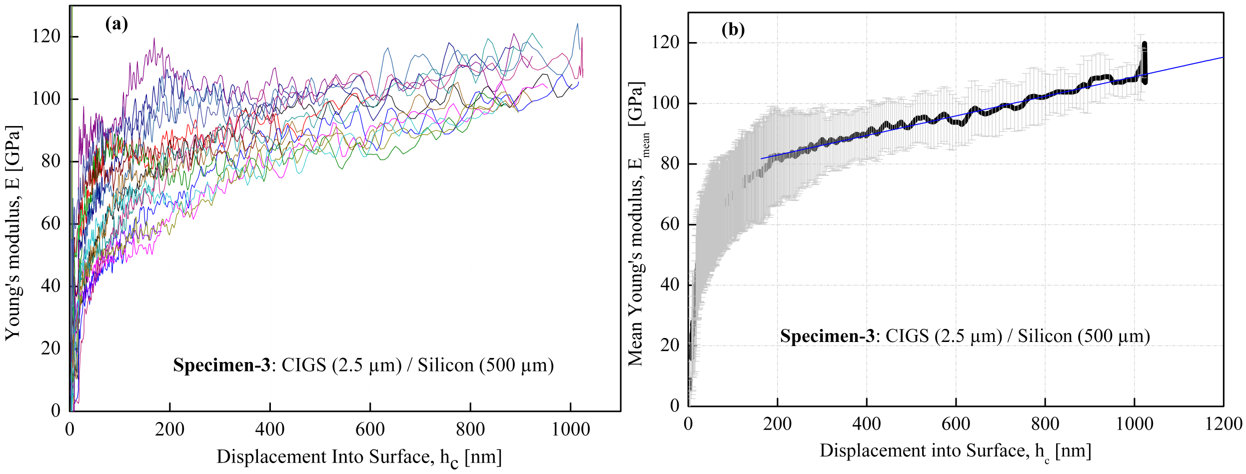

Figure 4.3: *(a) Young's modulus (E), and (b) Mean value of Young's modulus* (E_{mean}) *versus displacement into surface* (h_c) *for specimen-3 for all the 20 indentations; error bars are also included for all the indentations.*

error bars shown are the standard deviations obtained from the 20 indentations at each individual contact depth. The mean value of Young's modulus was calculated to be 76.48 ± 0.23 GPa from the CSM data for specimen-3. This value of Young's modulus is obtained by the the linear fit of the curve as shown in Figure 4.3 (b).

Nanoindentation experiments revealed the mean values of Young's modulus to be 75 ± 8.31 GPa, 83.19 ± 14.2 GPa and 76.48 ± 0.23 GPa for the three different CIGS specimens used for the investigations. The mean value of Young's modulus for the CIGS thin-film is determined to be 78.22 GPa. In all the three specimens which are investigated in the present work, the CIGS absorber layer was deposited by industrial three-stage co-evaporation process. The values of Young's modulus determined for the CIGS thin-film in the present work are in agreement with the previous reported value of 73.4 GPa by Lin et al. [148] and of 70.4 ± 6.5 GPa by Luo et al. [149]. These previous reported values of Young's modulus for the CIGS thin-films are also for the specimens where the CIGS thin-films are deposited by the industrial three-stage co-evaporation process. The values of Young's modulus determined in the present work are also in close agreement with the experimental calculations for the mechanical properties of CIS material in the past [4, 5, 150].

4.1.2 Effect of underlying material on the Young's modulus

In case of specimen-3 which has silicon/CIGS structure, it was observed that mean value of the Young's modulus continues to increase with increase in displacement into the surface (see Figure 4.4). So, the curve was extrapolated till the displacement value of 2.5 μm. The thickness of CIGS film is 2.5 μm in this case. As a result of extrapolation, the mean value of Young's modulus was determined to be 157 GPa at the displacement of 2.5 μm. This value of Young's modulus was found to be very close to that of the silicon which is 130-188 GPa [151]). So, it was revealed that with the increase in penetration depth, the effect of underlying material becomes more and more

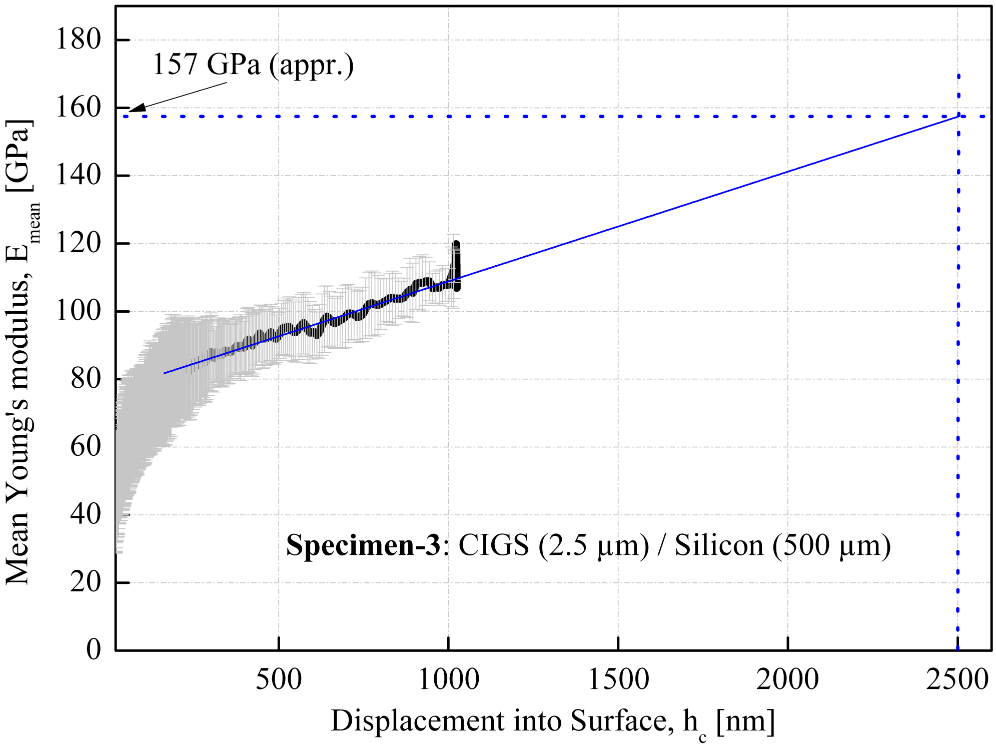

Figure 4.4: *Effect of underlying material on the Young's modulus of CIGS thin-film with the increase in displacement into the surface in case of specimen-3 comprising of CIGS (2.5 μm) / Silicon (500 μm).*

visible on the Young's modulus of thin-film and at the depth equal to the thickness of CIGS film, the value of Young's modulus for the silicon was almost reached.

4.2 Experimental results for P3 mechanical scribe

In this section, the results of mechanical scribing experiments performed to obtain P3 structure are presented. P3 scribe was performed by scribing off the the two layers namely CIGS material and the zinc oxide front contact from the top of molybdenum back contact with the help of a flat tip tungsten needle. First of all, the phenomenology of P3 scribe is presented in subsection 4.2.1 and thereafter, the effect of scribing parameters such as normal force and scribing speed on the scribe form is described in subsection 4.2.2.

4.2.1 Phenomenology of P3 scribe

Figure 4.5 shows the topography of one of the most common P3 structure performed by mechanical scribing. The line width (W_l) which is defined as the minimum possible width of the scribe in the absence of chippings is measured to be 71 μm. However, practically the width increases due to the presence of chippings and is called as effective scribe width (W_s) which is measured to be 150 μm. So, the scribe is broadened due to chipping.

The P3 mechanical scribes were investigated at the point where the scribing needle finally stopped after completely the full scribe. These investigations revealed the nearly circular shaped

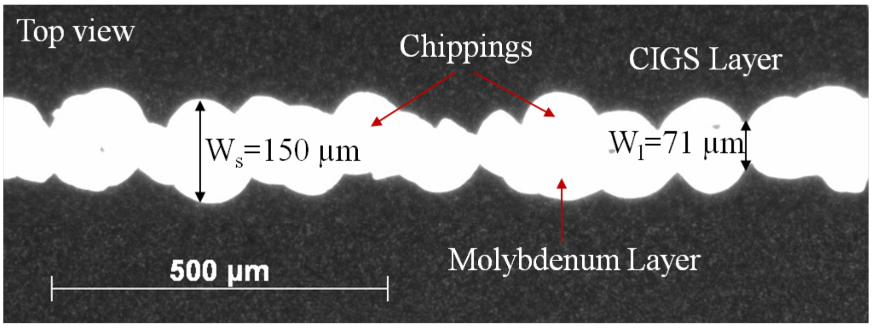

Figure 4.5: *Topography of a P3 structure performed by mechanical scribing with the help of a flat tip tungsten needle;* W_s *and* W_l *stand for scribe width and line width respectively.*

crack in the CIGS layer at the end of the scribe as can be seen in Figure 4.6. The diameter of this nearly circular shaped crack was measured to be approximately 140 μm. Though the crack initiation was not clearly visible, however it was noticed that the crack is more prominent near the contact region between the scribing needle and the CIGS layer and then fades away as it moves away from the contact region which indicates that the crack most probably starts propagating from very near of the contact region and then moves outwards which finally takes up the nearly circular shape as depicted in Figure 4.6. It was observed that the CIGS film ahead of the scribing needle was little bit lifted up (delaminated) from the molybdenum layer, however small portion of the CIGS material seemed to be intact and was not lifted up from the molybdenum layer. This experimental observation of the nearly circular shape crack at the end of P3 scribe is also explained schematically in the chapter 5 as can be seen in the Figure 5.3 (b) on the basis of scheme of mechanism for the mechanical scribing process which is being proposed after analyzing and understanding the experimental and simulation results.

Interestingly some of the P3 mechanical scribes were different from the most common scribe form. Figure 4.7 shows the optical microscope image of one of these scribes obtained. It can be seen that the upper side of scribe looks non-homogeneous in nature whereas the scribe on the lower side is quite homogeneous. Pixel frequency is plotted against scribe width for the upper and lower sides of this scribe. Figure 4.8 (a) shows that most of the scribe width values lie in a particular range i.e. from 30 μm to 70 μm and are not uniformly distributed over the entire range of values for the upper side of the scribe which confirms its non-homogeneous nature. On the other hand, for the lower side of the scribe, most of the scribe width values are quite low which confirms that the scribe is rather homogeneous at the lower side (see Figure 4.8 (b). This shape of the scribe form can be attributed to the geometry of the scribing needle and the tip surface may not be completely parallel to the specimen surface. It is possible that during the process of scribing, sometimes the scribing needle does not make the proper contact with the CIGS layer at some locations (due to surface roughness or slight lifting up of the needle). So, the improper contact between scribing needle and the CIGS layer at some locations during the scribing process might have resulted in the homogeneous shape of the scribe at its lower side.

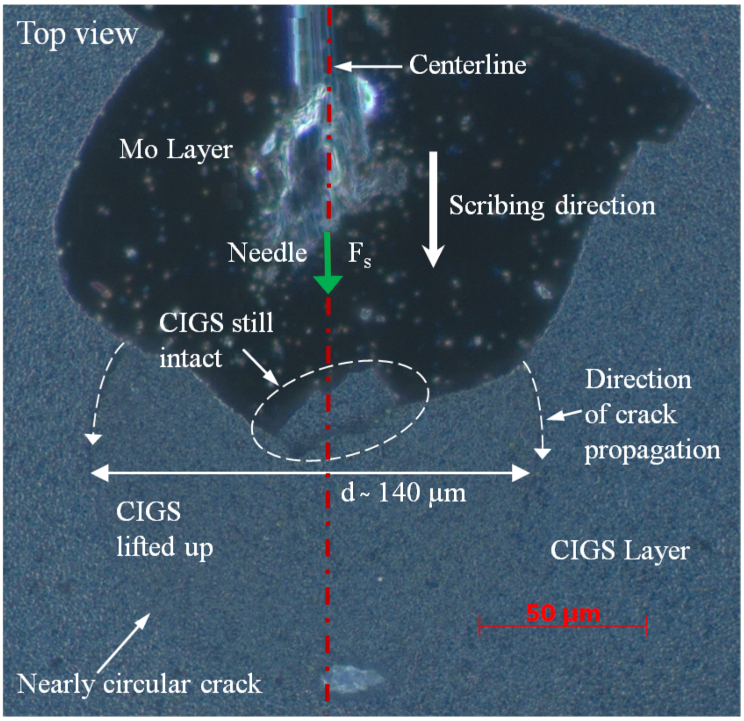

Figure 4.6: *Optical microscope image (top view) of the P3 mechanical scribe revealing the nearly circular shaped crack at the end of scribe; 'd' stands for the diameter of crack.*

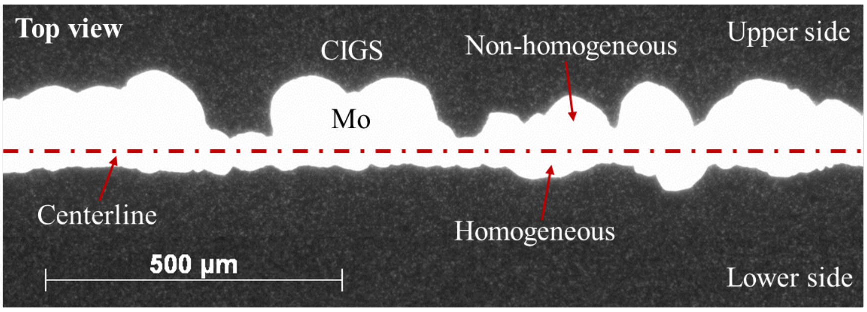

Figure 4.7: *Optical microscope image of one of the P3 scribes which are quite homogeneous on the lower side but are however non-homogeneous on the upper side of the scribe.*

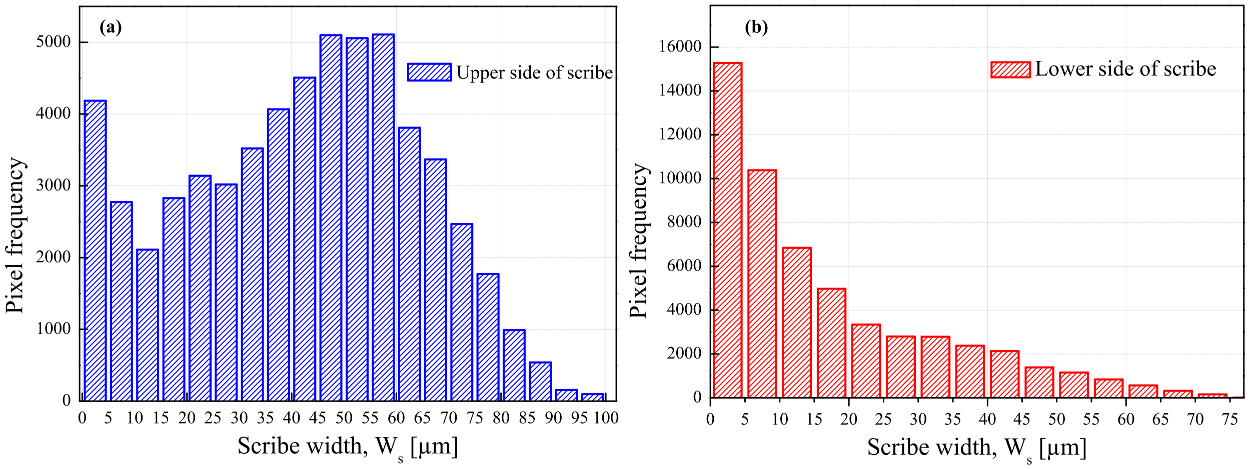

Figure 4.8: *Distribution of scribe width values for the (a) upper, and (b) lower side of the P3 mechanical scribe shown in figure 4.7.*

4.2.2 Influence of scribing parameters on the scribe form

The scribing parameters such as force normal to the specimen (F_n) and the scribing speed (v) were systematically varied in order to achieve the different P3 scribes on the CIGS specimen. The force normal to the specimen was varied from 0 to 5 N and the scribing speed was varied from 10 mm/s to 200 mm/s.

Influence of force normal to the specimen

In order to investigate the influence of force normal to the specimen (F_n) on the scribe form, different P3 mechanical scribes were performed on the CIGS thin-film solar cell specimen with the help of flat tip needle at the normal force values of 0.81 N, 1.59 N and 3.55 N. However, the scribing speed was kept constant in all these cases. The pixel frequency was plotted against the scribe width values for the upper side of the scribes performed. Figure 4.9 shows histograms for the variation of pixel frequency with scribe width for the upper side of the scribes performed with different values of normal force. Pixel frequency describes the number of pixels which have the scribe width that lies in the particular range such as from 0 to 5 μm, 6 μm to 10 μm etc. It can be seen from the histograms that the variation in force normal to the specimen does not influence the scribe width. The scribe width distribution is almost same for the different force values. Almost the same trend is observed for the lower side of these scribes.

Line width (W_l) is one of the important characteristics of the scribe form. It is the minimum possible width of the scribe in the absence of chippings (see Figure 4.5). In order to study the influence of force normal to the specimen on the line width, the scribes performed with normal force values of 0.81 N, 1.59 N and 3.55 N while keeping the scribing speed constant (10 mm/s) were investigated. Figure 4.10) reveals that there is rather no correlation between the force normal to the specimen and the line width of the scribes. This investigation was repeated at the scribing speeds of 100 mm/s and 200 mm/s. However, the same information was obtained. So, it was revealed that the normal force has no influence on the line width of the scribe.

Influence of scribing speed

In this section, investigations are made in order to see the influence of scribing speed (v) on the scribe form. Since line width (W_l) is an important characteristic of the scribe form, so influence of scribing speed on the line width is studied. In order to do that, the scribes performed with scribing speed values of 10 mm/s, 100 mm/s and 200 mm/s while keeping force normal to the specimen as constant (0.81 N) were investigated. Figure 4.11) reveals that there is rather no correlation between the scribing speed and the line width of the scribes. This investigation was repeated at the normal force values of 1.59 N and 3.55 N. However, the same information was obtained. So, it was revealed that the scribing speed has no influence on the line width of the scribe. Due to the limitation of the present experimental setup, it was not possible to perform the scribes with a speed

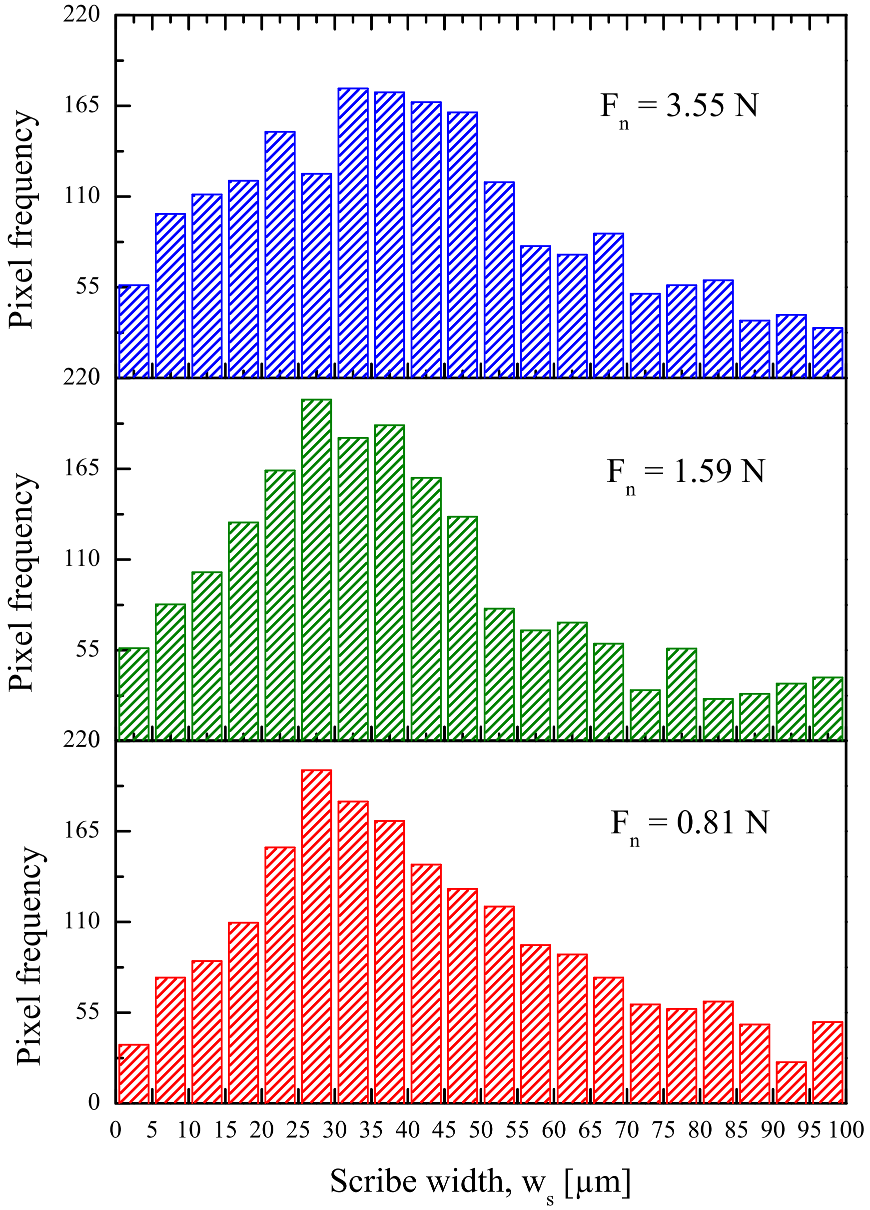

Figure 4.9: *Frequency as a function of scribe width for upper side of the P3 mechanical scribes performed at different values of normal force;* F_n *stands for the force normal to the specimen.*

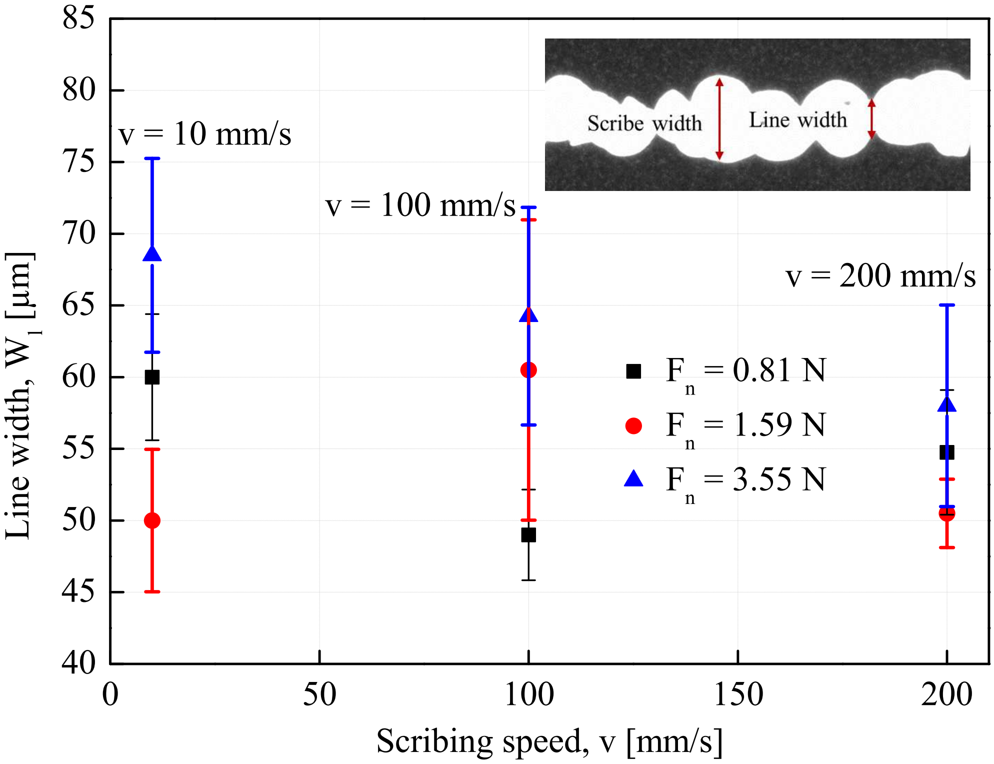

Figure 4.10: *Line width (W_l) of the P3 mechanical scribes as a function of force normal to the specimen (F_n).*

of more than 200 mm/s. So, it is quite possible that performing the scribes with speed higher than 200 mm/s may reveal some influence of scribing speed on the scribe form.

4.3 Experimental results for P2 mechanical scribe

In this section, the results of P2 mechanical scribing experiments performed with the help of flat tip and slightly rounded tip tungsten needles on two different types of CIGS specimens with low and relatively higher adhesion strength of the CIGS/Mo interface are presented. P2 scribes were performed by removing the CIGS layer from the top of Mo layer. First of all, the experimental scribing force versus time curve is presented in the subsection 4.3.1. Then, the phenomenology of P2 mechanical scribe is presented in subsection 4.3.2. The effect of scribing parameters such as force normal to the specimen and scribing speed on the scribe form is described in subsection 4.3.3. Thereafter, the influence of adhesion strength of CIGS/Mo interface and the geometry of scribing needle on the scribe characteristics such as scribe width is presented in subsection 4.3.4. Finally, the influence of maximum scribing force on the chip area is presented in the subsection 4.3.5.

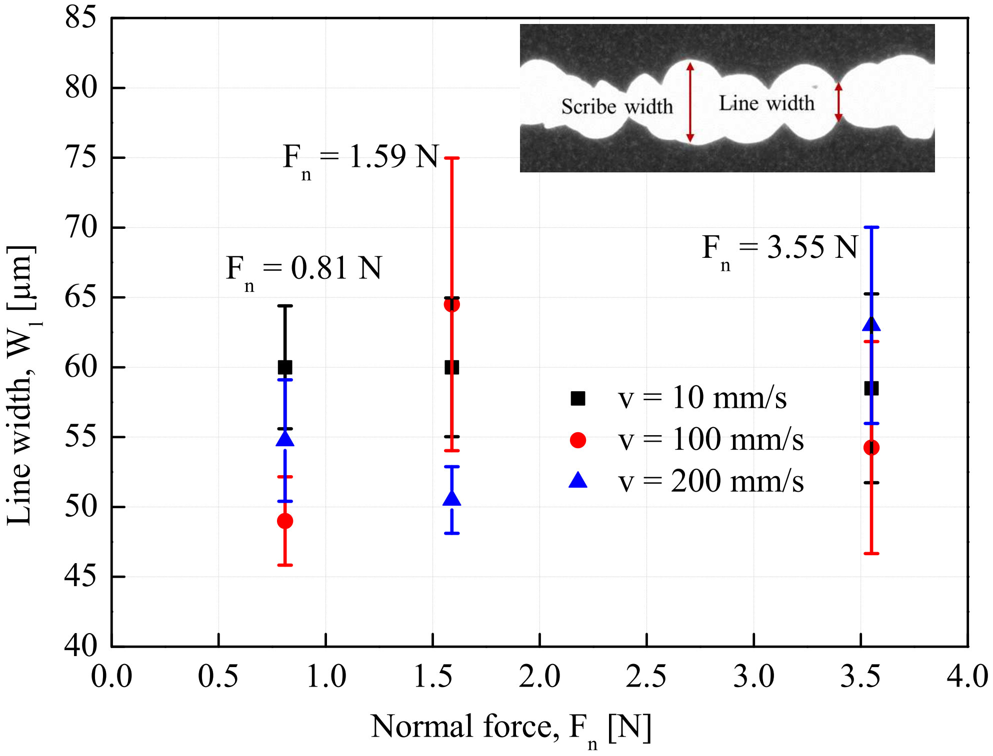

Figure 4.11: *Line width (W_l) of the P3 mechanical scribes as a function of scribing speed (v).*

4.3.1 Experimental scribing force versus time curve

Mechanical scribing experiments were performed with the help of flat tip needle on two different types of CIGS specimens with low and relatively higher adhesion strength of the CIGS/Mo interface. In this section, the frictional force between the needle and the Mo layer (F_t), the scribing force versus time curve, the maximum scribing force (F_{max}) and the interface shear strength (T_t) are determined for both types of CIGS specimens. Firstly, the detailed analysis is done for the CIGS specimen with relatively lower adhesion strength of CIGs/Mo interface. Eleven P2 mechanical scribes were performed by the flat tip needle on the CIGS specimen with relatively lower adhesion strength of CIGS/Mo interface. These scribes were performed at the different values of the force normal to the specimen (F_n) varying from 0 to 748 mN but at the same scribing speed of 0.5 mm/s. The total force acting in x-direction (F_x) was recorded continuously versus time during the complete scribing process by the three-axis force sensor K3D60. Due to the limitation of the present experimental setup, it was not possible to record the displacement of needle during the scribing process.

Determining the frictional force between needle and the Mo layer

Figure 4.12 shows the total scribing force acting in the x-direction (F_x) plotted against the force normal to the specimen (F_n) for all the eleven mechanical scribes. This total force acting in x-direction includes the frictional force between the scribing needle and the molybdenum layer (F_t). So, first of all, the frictional force between the scribing needle and the molybdenum layer is determined. By drawing a line of best fit through a scatter plot in Figure 4.12, the intercept on y-axis is determined to be 32.5 mN. This intercept on y-axis represents the force acting in x-direction in the absence of friction between the scribing needle and the Mo layer (to be called as scribing force hereafter, F_s), since F_s is constant for all the scribes performed on the same CIGS specimen. However, the frictional force between the needle and the Mo layer varies for the different scribes on the same specimen due to the fact that these scribes are being performed at the different values of force normal to the specimen. Figure 4.13 shows one of the eleven P2 mechanical scribes. This scribe is performed at the normal force (F_n) of 148 mN and the scribing speed of 0.5 mm/s and is marked as **S** in Figure 4.12. The length of this full scribe is 5 mm. This scribe exhibits the chipping mode of scribing process wherein, the full scribe comprises of approximately 47 nearly circular shaped chips of considerable scribe widths. The chipping takes place in a stepwise manner and each chip is clearly visible in the scribe image. The total force acting in x-direction for this scribe is 50.5 mN (see Figure 4.12), so the frictional force between the scribing needle and the Mo layer for this scribe performed on the CIGS specimen with relatively lower adhesion strength of CIGS/Mo interface $(F_t)_1$ is determined to be 18 mN by subtracting F_s from F_x as presented in Equation 4.1 below. From this value of frictional force, the coefficient of friction μ_1 is determined to be 0.12 as presented in Equation 4.2 below:

$$(F_t)_1 = F_x - F_s = 50.5\ mN - 32.5\ mN = 18\ mN \tag{4.1}$$

$$\mu_1 = \frac{(F_t)_1}{F_n} = \frac{18\ mN}{148\ mN} = 0.12 \tag{4.2}$$

Determining the maximum scribing force

Now, the scribing force values in the absence of frictional force between the needle and the Mo Layer (F_s) are obtained for this scribe under investigation (see Figure 4.13) versus time by subtracting F_t determined in the previous section from F_x. The scribing force versus time graph for the full length scribe of 5 mm is found to be comprised of approximately 47 curves where each of the curves corresponds to one of the chips in the full length scribe. The scribing force versus time response for four of the chippings of this P2 scribe under investigation (see Figure 4.13) is plotted as shown in Figure 4.14. The microscopic image of the corresponding chippings is also shown in the figure. As can be seen in the figure, the scribing force first increases almost linearly with time till the certain point A is reached. After this point A, the force still continues to increase with time, however, non-linearly till the point B when the maximum value of force is reached. The peak value of each of these four curves represents the maximum scribing force, F_{max}, for the corresponding chip. Most probably, the chip is removed completely and finally flipped away as soon as the maximum scribing force value is reached. The immediate falling down of scribing force after reaching the maximum value indicates that most probably, the scribing needle jumps as soon as

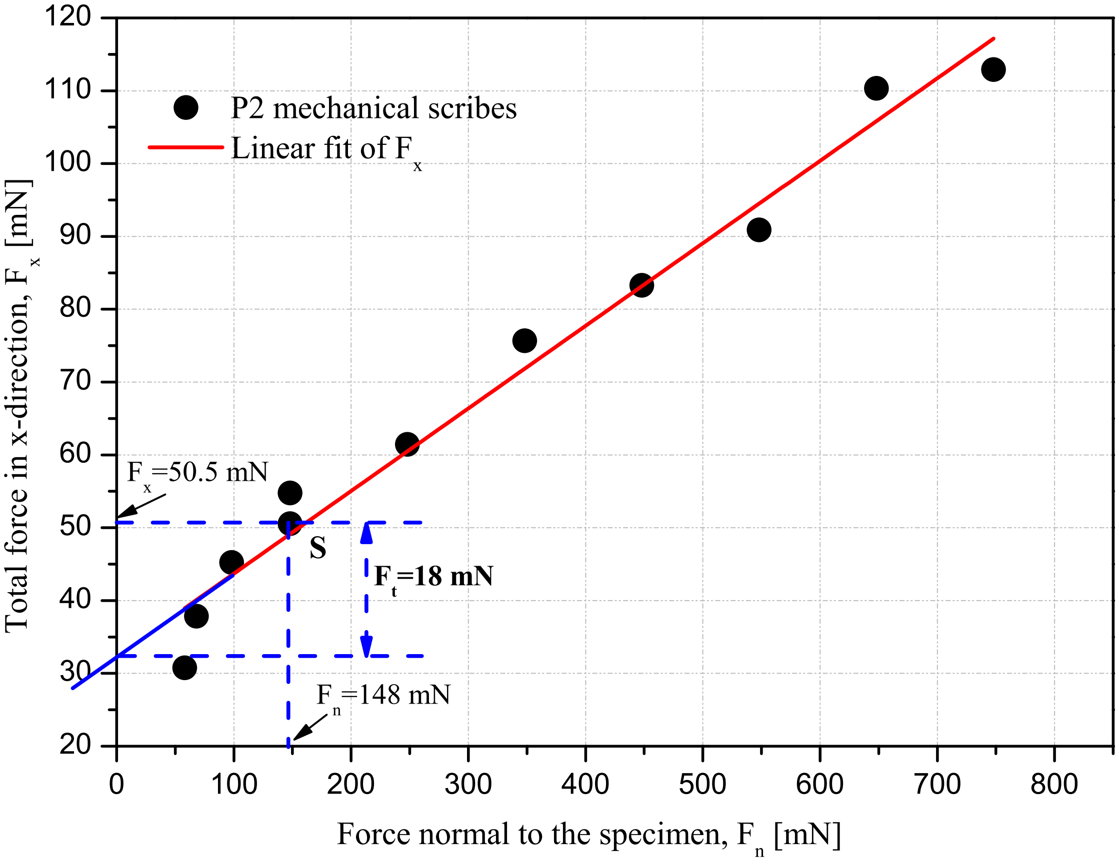

Figure 4.12: *Determining the frictional force between the scribing needle and the Mo layer (F_t) for the P2 mechnical scribe marked as **S** and shown in Figure 4.13 performed by the flat tip needle on the CIGS specimen with the relatively lower adhesion strength of CIGS/Mo interface.*

Figure 4.13: *Topography of one of the P2 mechanical scribes performed by the flat tip scribing needle on the CIGS specimen with relatively lower adhesion strength of CIGS/Mo interface at the normal force (F_n) of 148 mN and scribing speed (v) of 0.5 mm/s; this scribe is marked as **S** in Figure 4.12.*

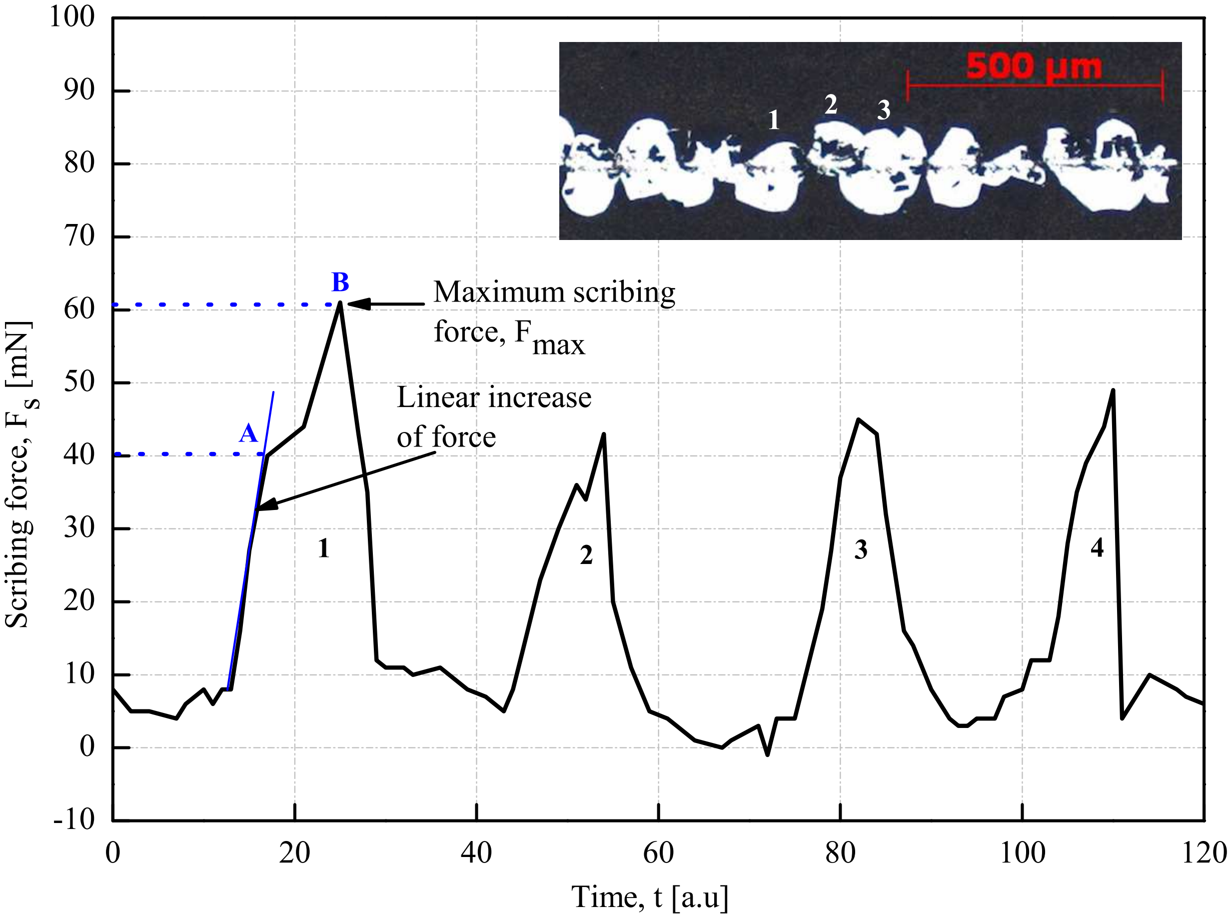

Figure 4.14: *Scribing force versus time curve for the P2 mechanical scribe shown in Figure 4.13 produced by the flat tip scribing needle on the CIGS specimen with relatively lower adhesion strength of CIGS/Mo interface; the curve is linear till point A and the maximum value of scribing force is reached at point B; microscopic image of the corresponding chippings is also shown.*

the maximum value of force is reached. The mean value of maximum scribing force is determined to be 45.46 ± 10.07 mN.

Determining the interface shear strength

The mean area of one chip (A_{mean}) is calculated to be 0.0097 mm^2 from the Figure 4.13 by using *ImageJ* which is a Java-based image processing program [152, 153]. Now, the interface shear strength $(\mathrm{T}_t)_1$ for CIGS specimen with relatively lower adhesion strength of CIGS/Mo interface on the basis of scribe under investigation (see Figure 4.13) is determined to be 4.68 MPa by dividing the mean value of maximum scribing force with the mean area of one chip as below:

$$(T_t)_1 = \frac{F_{max}}{A_{mean}} = \frac{45.46\ mN}{0.0097\ mm^2} = 4.68\ MPa \tag{4.3}$$

Similarly, four P2 mechanical scribes were performed by the flat tip needle on the CIGS specimen with relatively higher interface adhesion strength. These scribes were performed at the different values of the force normal to the specimen (F_n) varying from 0 to 548 mN but at the same scribing speed of 0.5 mm/s. By following the same procedure as described above, the scribing force in the absence of frictional force between the needle and the Mo layer (F_s) is determined to be 32.9 mN. This value of F_S is same for all the scribes performed on the same CIGS specimen, however, the frictional force between the needle and the Mo layer varies for the diffrent scribes on the same specimen. Figure 4.15 shows the optical microscope image of one of the these four scribes. This scribe is performed at the normal force (F_n) of 148 mN and the scribing speed of 0.5 mm/s. The length of this full scribe is 5 mm. This scribe exhibits the chipping mode of scribing process wherein, the full scribe comprises of approximately 63 nearly circular shaped chips of considerable scribe widths. The chipping takes place in a stepwise manner and each chip is clearly visible in the scribe image. The total force acting in x-direction (F_x) for this scribe is 43.57 mN. So, the frictional force between the scribing needle and the molybdenum layer $(F_t)_2$ for this scribe under investigation (see Figure 4.15) performed on the specimen with relatively higher adhesion strength of CIGS/Mo interface is calculated to be 10.67 mN by subtracting F_s from F_x as presented in Equation 4.4 below. From this value of frictional force, the coefficient of friction μ_2 is determined to be 0.07 as presented in Equation 4.5 below:

$$(F_t)_2 = F_x - F_s = 43.57\ mN - 32.9\ mN = 10.67\ mN \tag{4.4}$$

$$\mu_2 = \frac{(F_t)_2}{F_n} = \frac{10.67\ mN}{148\ mN} = 0.07 \tag{4.5}$$

Now, the frictional force of 10.67 mN is subtracted from the total force acting in x-direction (F_x) in order to obtain the scribing force in the absence of any frictional force between the needle and the molybdenum layer (F_s) for this scribe. The scribing force versus time response for this P2 mechanical scribe (see Figure 4.15) produced on the CIGS specimen with relatively higher interface adhesion strength is shown in Figure 4.16. The complete scribing force versus time graph comprised of approximately 63 curves where each curve belongs to and represents one of the approximately 63 chips in the full length scribe. The peak of each of these 63 curves gives the maximum value of the scribing force, F_{max}, for the corresponding chip. The mean value of maximum scribing force is determined to be 53.54 ± 5.85 mN. The mean area of one chip is calculated to be 0.005 mm^2 from the Figure 4.15 by using *ImageJ* which is a Java-based image processing program [152, 153]. Now, the interface shear strength $(\mathrm{T}_t)_2$ for CIGS specimen with relatively higher adhesion strength of CIGS/Mo interface on the basis of scribe under investigation (see Figure 4.15) is determined to be 10.7 MPa by dividing the mean value of maximum scribing force with the mean area of one chip as presented in Equation 4.6 below:

$$(T_t)_2 = \frac{F_{max}}{A_{mean}} = \frac{53.54\ mN}{0.005\ mm^2} = 10.7\ MPa \tag{4.6}$$

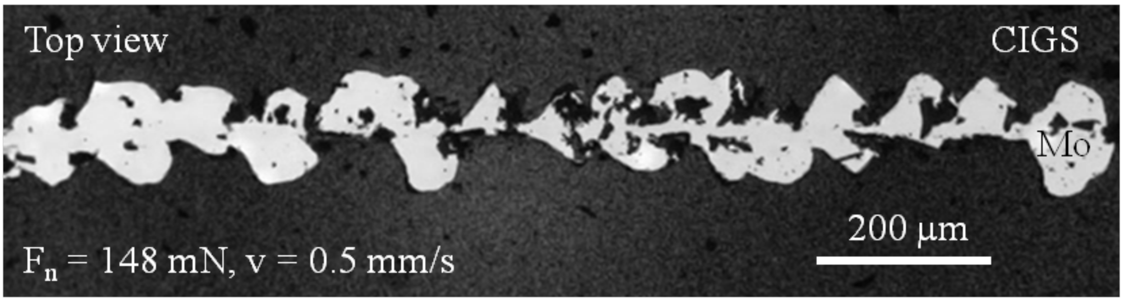

Figure 4.15: *Topography of one of the P2 mechanical scribes performed by the flat tip scribing needle on the CIGS specimen with relatively higher adhesion strength of CIGS/Mo interface at the normal force (F_n) of 148 mN and the scribing speed (v) of 0.5 mm/s.*

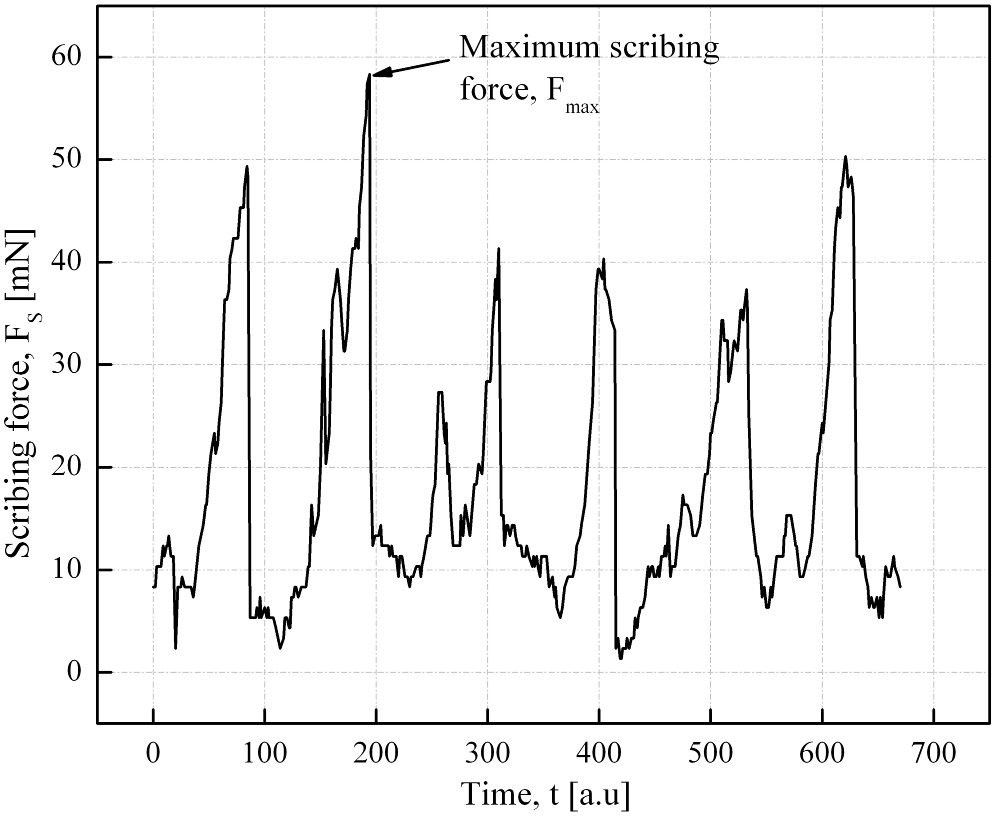

Figure 4.16: *Scribing force versus time curve for the P2 mechanical scribe shown in Figure 4.15 produced by the flat tip scribing needle on the CIGS specimen with relatively higher adhesion strength of CIGS/Mo interface.*

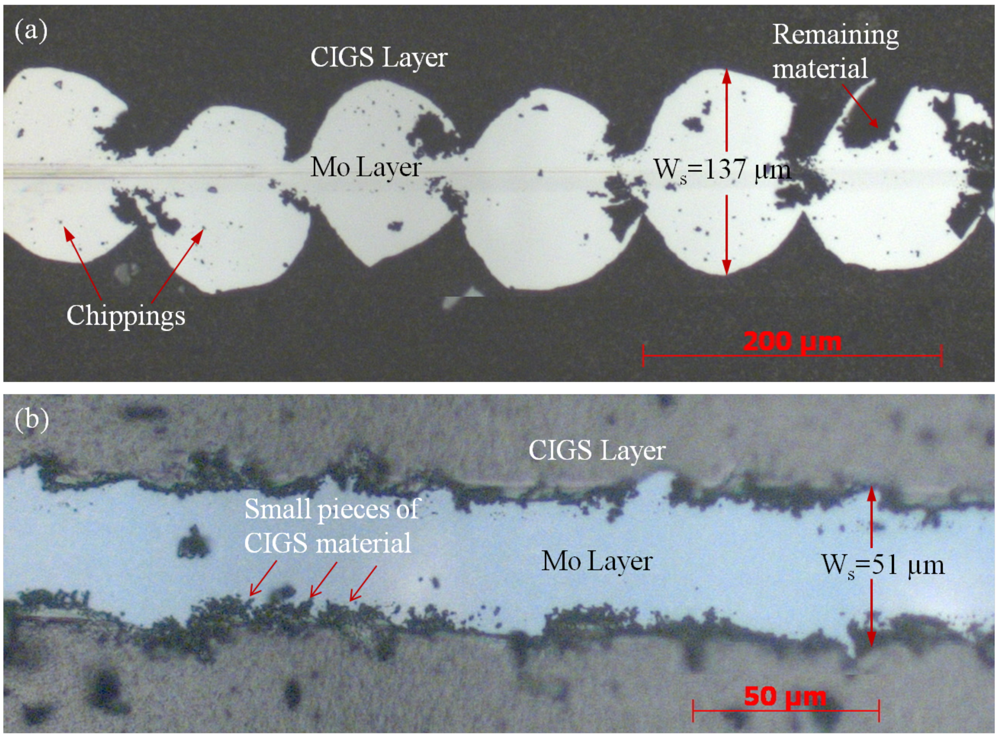

Figure 4.17: *Topography of P2 structures performed by mechanical scribing with (a) flat tip scribing needle and (b) a slightly rounded tip scribing needle;* W_s *stands for the scribe width.*

4.3.2 Phenomenology of P2 scribe

Figure 4.17 shows the topography of the most common P2 structures performed by mechanical scribing with flat tip and the slightly rounded tip scribing needles respectively. It can be seen in Figure 4.17 (a) that the chipping happened in a stepwise manner and each chip was clearly visible in the image while scribing with a flat tip needle. The scribe width increases due to the presence of chippings which is measured to be 137 μm. So, the scribe is broadened due to chipping. However, while scribing with a slightly rounded tip needle, the grinding mode of scribing is observed as can be seen in Figure 4.17 (b), where the CIGS material is being removed in the form of very small pieces and also the scribe width is relatively very less which is measured to be 51 μm.

4.3.3 Effect of scribing parameters on the scribe form

The scribing parameters such as force normal to the specimen (F_n) and the scribing speed (v) were systematically varied in order to achieve the different P2 scribes on the two different specimens. The normal force is varied from 0 to 748 mN and the scribing speed is varied from 0.01 mm/s to 0.5 mm/s.

Effect of force normal to the specimen

In order to analyze the influence of normal force as a scribing parameter on the scribe form for a P2 structure, the scribing speed was kept constant at 0.5 mm/s and the normal force is varied from 0 to 748 mN. Seven scribes were performed on each of the specimen with both types of scribing

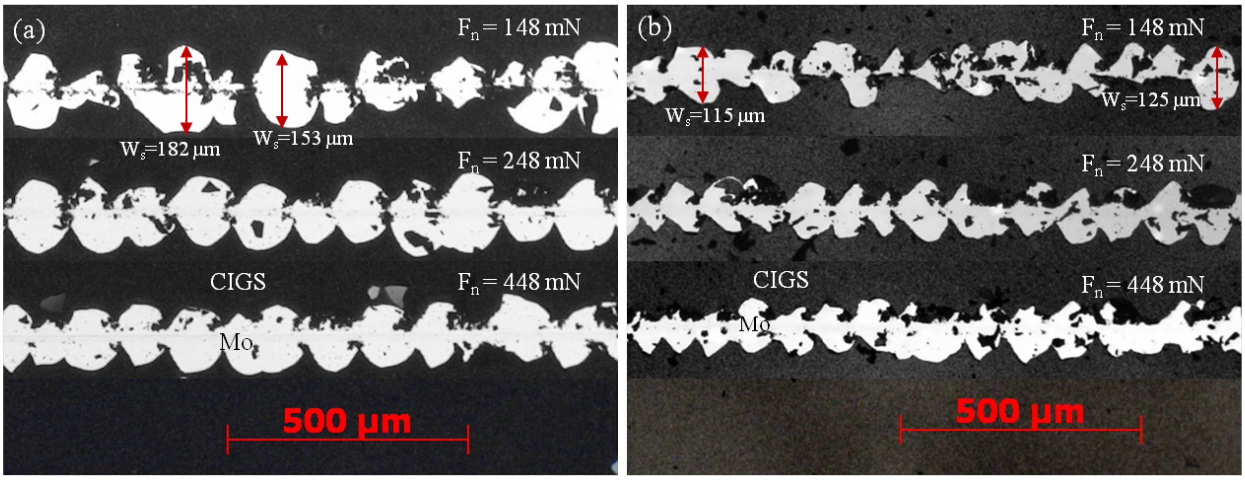

Figure 4.18: *Optical microscope images of P2 mechanical scribes (top view) performed by the flat tip scribing needle on the (a) low (T_t = 4.68 MPa), and (b) high adhesion (shear) strength (T_t = 10.7 MPa) specimens at different normal force values; scribing speed is 0.5 mm/s in all cases; W_s and F_n stand for scribe width and force normal to the specimen respectively.*

needles and the length of each of the scribe was 5 mm. Figure 4.18 and Figure 4.19 show the optical microscope images (top view) of the P2 mechanical scribes performed on the low (T_t = 4.68 MPa) and high (T_t = 10.7 MPa) interface shear strength specimens respectively by the flat tip and the slightly round tip needles respectively. It was observed that varying the normal force does not have any influence on the width of the scribe while scribing with any one of the two types of needle on any one of the two types of specimens used in experiments. However, as a result of scribing with a flat tip needle, it was observed that delamination of CIGS film from the top of molybdenum layer occurred even at the force value of as low as F_n=58 mN, while scribing with a slightly rounded tip needle, no delamination was observed below the force value of F_N=98 mN, where F_n is the force normal to the specimen.

Effect of scribing speed

In order to analyze the influence of scribing speed on the scribe form of a P2 structure, the normal force was kept constant at 148 mN and the scribing speed was varied from 0.01 mm/s to 0.5 mm/s. Seven scribes were performed on each of the specimen with both types of scribing needles and the length of each of the scribe is 5 mm. Figure 4.20 shows the optical microscope images (top view) of P2 mechanical scribes performed on the low adhesion (shear) strength (T_t = 10.7 MPa) specimen with the scribing speeds of 0.01 mm/s, 0.1 mm/s and 0.5 mm/s respectively. It was seen that the higher speed causes the chips of CIGS material to move out of the scribe area in both the specimens. However, it does not influence the scribe width of the chips which is considered to be the most important characteristic of the mechanical scribing process. Similarly, in the case of scribing with a slightly rounded tip needle, it was observed that again the scribes performed with higher speed values looked cleaner, however the line width (dominant scribing mode is grinding) of the scribes was almost the same. So, the scribing speed showed no influence on the scribe form as it was observed while scribing for the P3 structure. Due to the limitation of the present

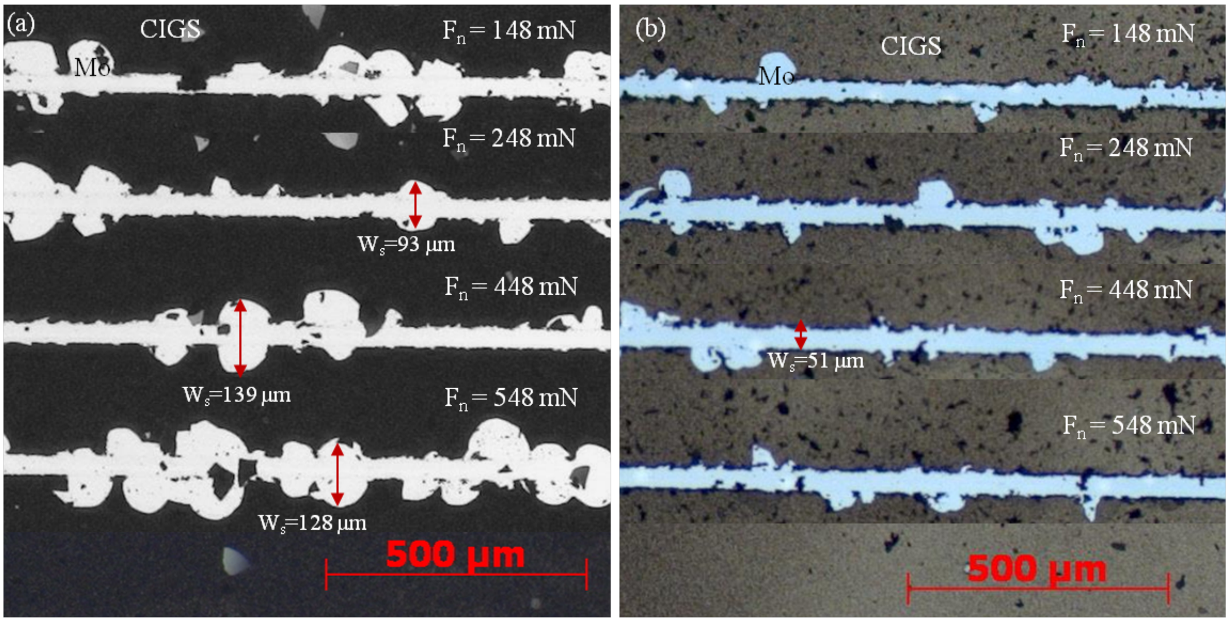

Figure 4.19: *Optical microscope images (top view) of P2 mechanical scribes performed by the slightly rounded tip scribing needle on the (a) low (T_t = 4.68 MPa), and (b) high adhesion (shear) strength (T_t = 10.7 MPa) specimens at different normal force values; scribing speed is 0.5 mm/s in all cases; W_s and F_n stand for scribe width and force normal to the specimen respectively.*

experimental setup, it was only possible to perform the scribes with the speed not more than 200 mm/s. So, it is quite possible that performing the scribes with speed higher than 200 mm/s may reveal some influence of scribing speed on the scribe form.

4.3.4 Influence of adhesion (shear) strength and needle tip geometry

Mechanical scribing experiments for P2 structure were performed with the help of flat tip and slightly rounded tip tungsten needles on the CIGS thin-film solar cell specimens having low and relatively higher adhesion (shear) strength at the CIGS/Mo interface.

Influence of adhesion (shear) strength of CIGS/Mo interface

In this section, the P2 mechanical scribes performed on CIGS solar cell specimens with different adhesion (shear) strengths (T_t) of CIGS/Mo interface are investigated. Figure 4.18 shows the scribes performed with a flat tip needle on the low (T_t = 4.68 MPa) and high (T_t = 10.7 MPa) adhesion strength specimens respectively. It can be seen that the increase in adhesion strength results in the decrease of the scribe width of the chips. The scribe width of 182 μm was obtained in the low adhesion (shear) strength specimen, however in case of high adhesion (shear) strength specimen, it was determined to be 125 μm. This indicates that the specimen with higher adhesion at the interface produces better scribes with lower scribe width values. Similarly, Figure 4.19 shows the scribes performed with a slightly rounded tip needle on the low and high adhesion (shear) strength specimens respectively. As can be seen, the dominant scribing mode is grinding, however the high adhesion strength specimen produces the chips (which are very few in number)

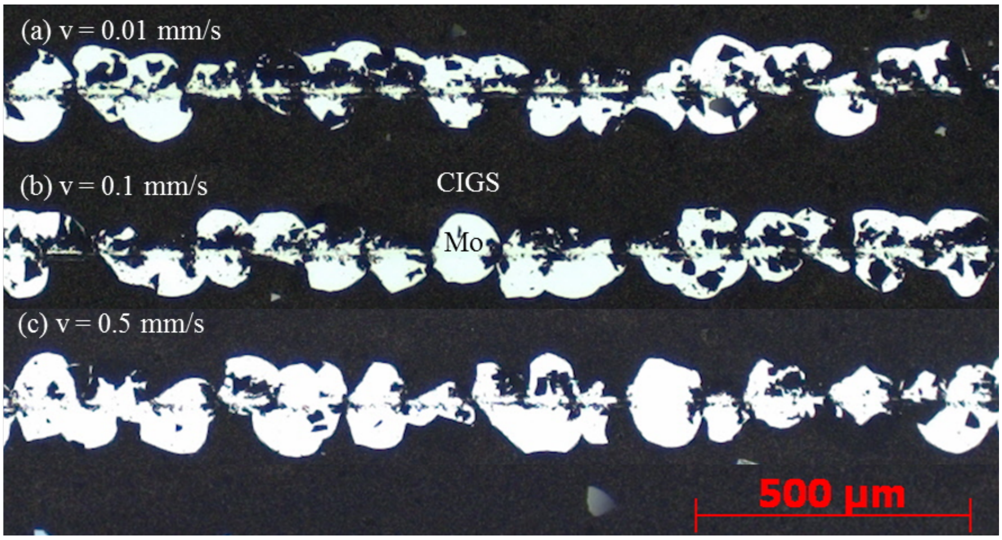

Figure 4.20: *Topography of P2 mechanical scribes performed by the flat tip scribing needle on the low adhesion (shear) strength (T_t = 4.68 MPa) specimen at different scribing speeds, force normal to the specimen (F_n) is 148 mN in all cases.*

with much low scribe width values and also the line width of the overall scribe (in the absence of chippings) is also reduced significantly.

Influence of needle tip geometry

The mechanical scribing experiments were performed with the help of conical needles of two different geometries, one of the needles has flat tip and the other has slightly rounded tip geometry. The diameter of the spherical tip of the flat tip scribing needle is 48.59 μm whereas it is 41.6 μm in case of slightly rounded tip needle (see Figure 3.4). Figure 4.18 shows the mechanical scribes performed by the flat tip needle on the low and high adhesion (shear) strength specimens respectively. It is observed that almost all the scribes comprise of near to circular shaped chips of considerable size. Chipping seems to happen in a stepwise manner and almost every chip of the removed CIGS material is visible in the images. This indicates that the dominant scribing mode here is chipping which reveals that the scribe is performed as a result of the removal of the CIGS thin film material in the form of number of significant sized chips. Figure 4.19 shows the mechanical scribes performed by the slightly rounded tip needle on the low and high adhesion (shear) strength specimens respectively. It can be seen clearly that the chipping reduces significantly for both the specimens. The dominant scribing mode is no longer chipping mode. However, grinding is the dominant scribing mode here. The mechanical scribes obtained are near to the ideal scribes with the reduced or no chippings. It was seen that scribing the high adhesion (shear) strength specimen with the slightly rounded tip needle produced the near to ideal scribes in the present work.

4.3.5 Influence of maximum scribing force on the chip area

The mechanical scribe produced on the specimen with relatively lower interface adhesion (shear) strength of 4.68 MPa as shown in Figure 4.13 is investigated further to study the influence of

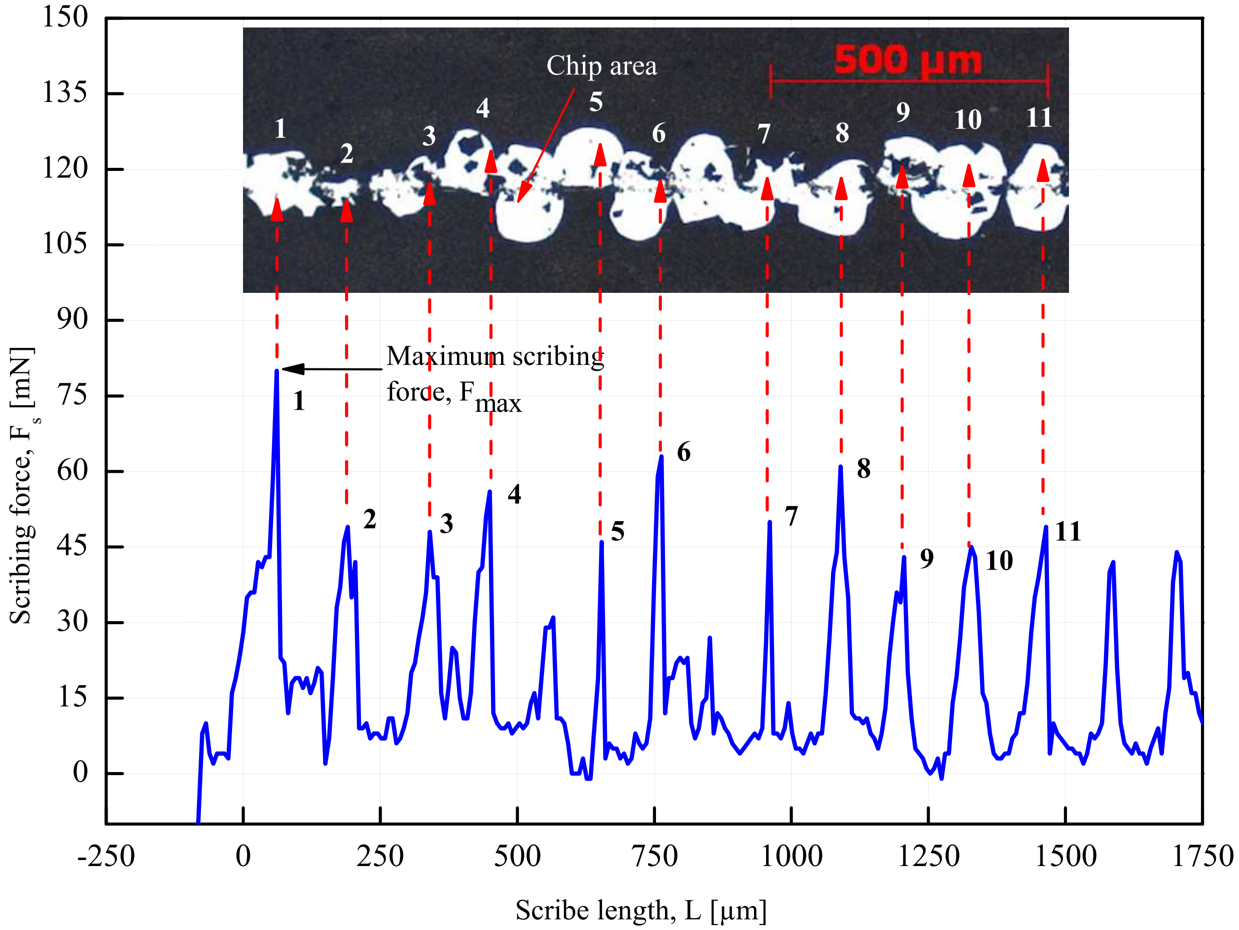

Figure 4.21: *Scribing force versus scribe length for the P2 mechanical scribe shown in Figure 4.13; each curve corresponds to a particular chip.*

maximum scribing force (F_{max}) on the chip area. In order to correlate the peaks of the scribing force versus time curve to the corresponding chips in the scribe, the time values along x-axis were replaced by that of the scribe length using the fact that the length of each of the scribes performed was 5 mm. The peaks are correlated to the corresponding chips for 1.5 mm of the scribe length. Now, in order to analyze the influence of maximum scribing force (representing the maximum value of the scribing force for each chip) on the chip area, the scribing force is plotted versus scribe length for some of the the chips of the P2 mechanical scribe as shown in Figure 4.21. Each peak is also correlated to the corresponding chip in the scribe image. The peak of each curve gives the maximum value of scribing force, F_{max} for the corresponding chip.

Now, the maximum scribing force values for all the identified eleven chips are obtained and the areas of the chips are measured. Then, the maximum scribe force values are plotted against the chip areas of these chippings as shown in Figure 4.22. It was noted that in the very beginning of the scribing process, the value of maximum scribing force for the first chip is highest and is equal to 80 mN. This highest value of maximum scribing force in the beginning of the scribing process can be attributed to the contact friction between the scribing needle and the CIGS thin-film. Thereafter, the maximum scribing force values for the remaining of the 10 chips lie almost in the range of 43 mN to 63 mN which is quite below its highest value as observed in the beginning of the process.

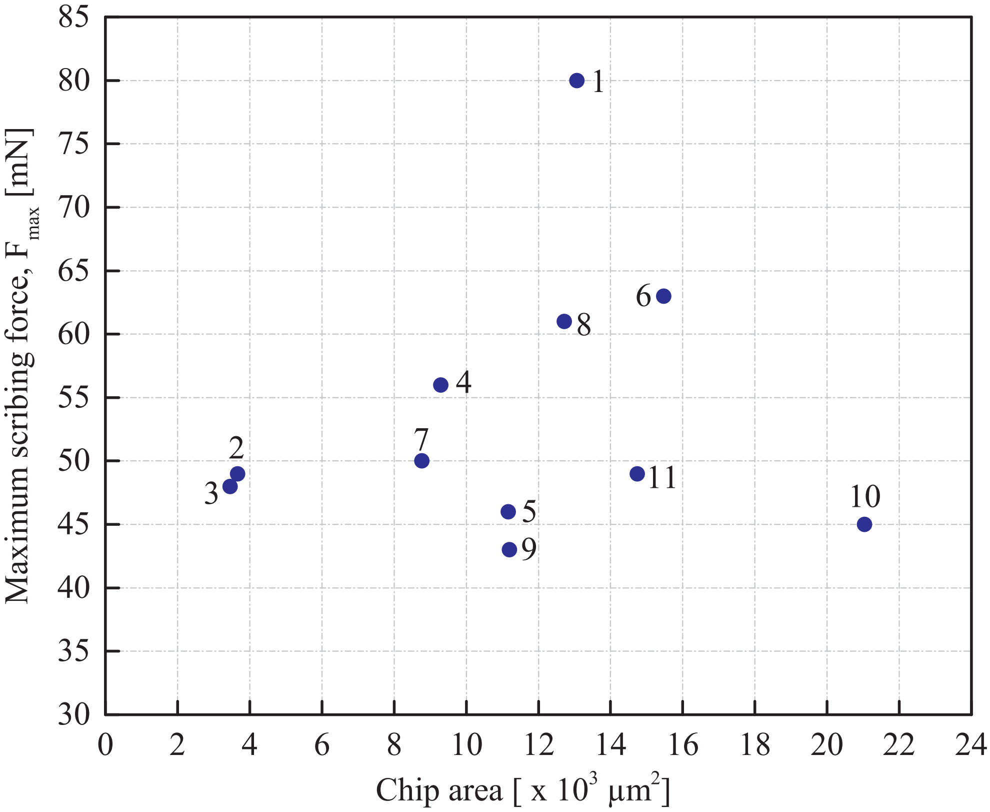

Figure 4.22: *Dependence of maximum scribing force on chip area for the P2 mechanical scribe shown in Figure 4.13; the chip number is also indicated for all the chippings as was marked in Figure 4.21.*

However, no correlation as such is observed between the maximum scribing force and the chip area.

4.4 Half-symmetric 2D FE model for crack initiation

The half-symmetric 2D finite element model (top view) without initial crack as shown in Figure 3.7 is investigated for the scribing force of 45 mN. The mean value of the maximum scribing force was determined to be 45 mN for the P2 mechanical scribe performed in the present work by the flat tip needle on the CIGS specimen with interface shear strength of 4.68 MPa. The CIGS layer is pressed by the spherical tip 24.3 μm in radius as in experiments.

4.4.1 Dependence of scribing force on the needle displacement

Figure 4.23 shows the force-displacement curve obtained as a result of the finite element simulation. It is observed that the scribing force continues to increase almost linearly with the increasing needle displacement, since no failure criterion is defined in the present model. The needle displacement of 0.892 μm is achieved with the maximum scribing force of 45 mN.

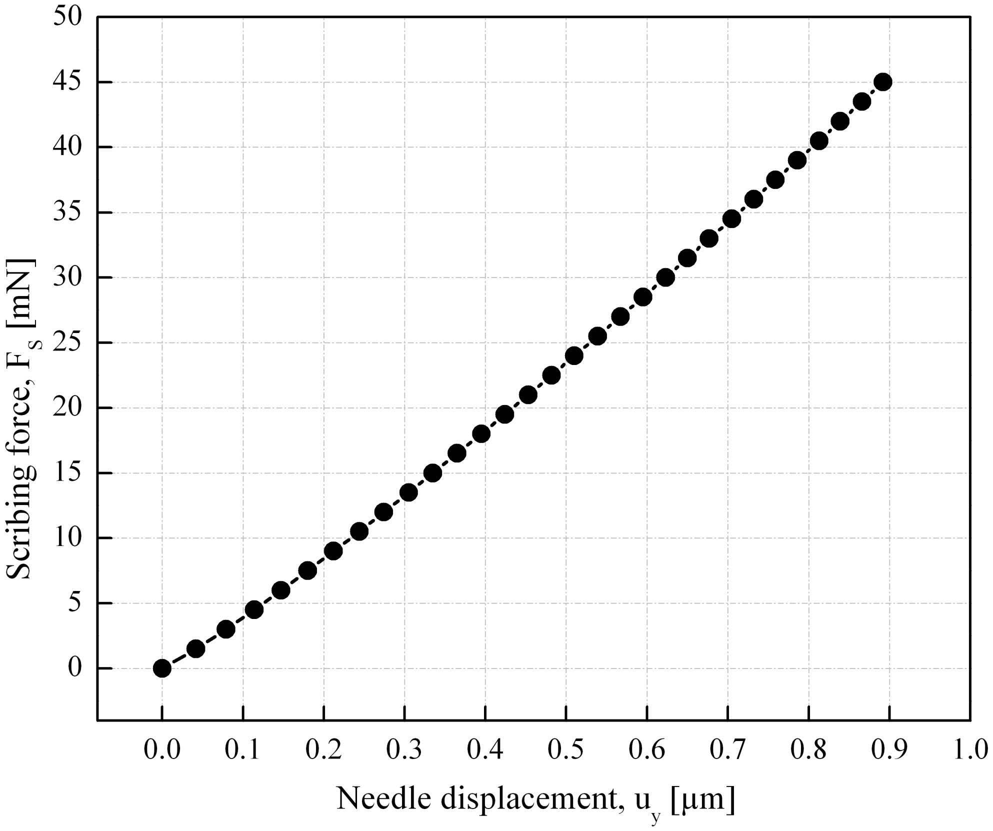

Figure 4.23: *Scribing force versus needle displacement curve for half-symmetric 2D finite element model (top view) of crack initiation comprising of CIGS layer and spherical tip shown in Figure 4.23.*

4.4.2 Comparison of FEA results with Hertz theory

Equation 2.37 of Hertzian contact-mechanics, presents the force-displacement relation for the compression between cylinder and the plane. Using this equation of Hertzian contact-mechanics, the force-displacement curve is plotted and compared with the finite element simulation results as shown in Figure 4.24. As can be seen, finite element analysis (FEA) results showed excellent agreement with Hertzian contact-mechanics results regarding the dependence of scribing force on needle displacement.

4.4.3 Influence of coefficient of friction on the force-displacement curve

In the next investigation, the half-symmetric 2D FE model (top view) without initial crack (see Figure 3.7 is investigated by taking different values of coefficient of friction (COF) for the tangential behavior of friction between the spherical tip and the CIGS layer. Different values of COF used for investigation are: zero (frictionless), 0.1, 0.2 and 0.3. Figure 4.25 shows that the force-displacement curves obtained with different values of COF are almost similar. This indicates that the variation in coefficient of friction does not affect the response regarding the force-displacement curve. So, the frictionless behavior is considered to carry out all the further simulations.

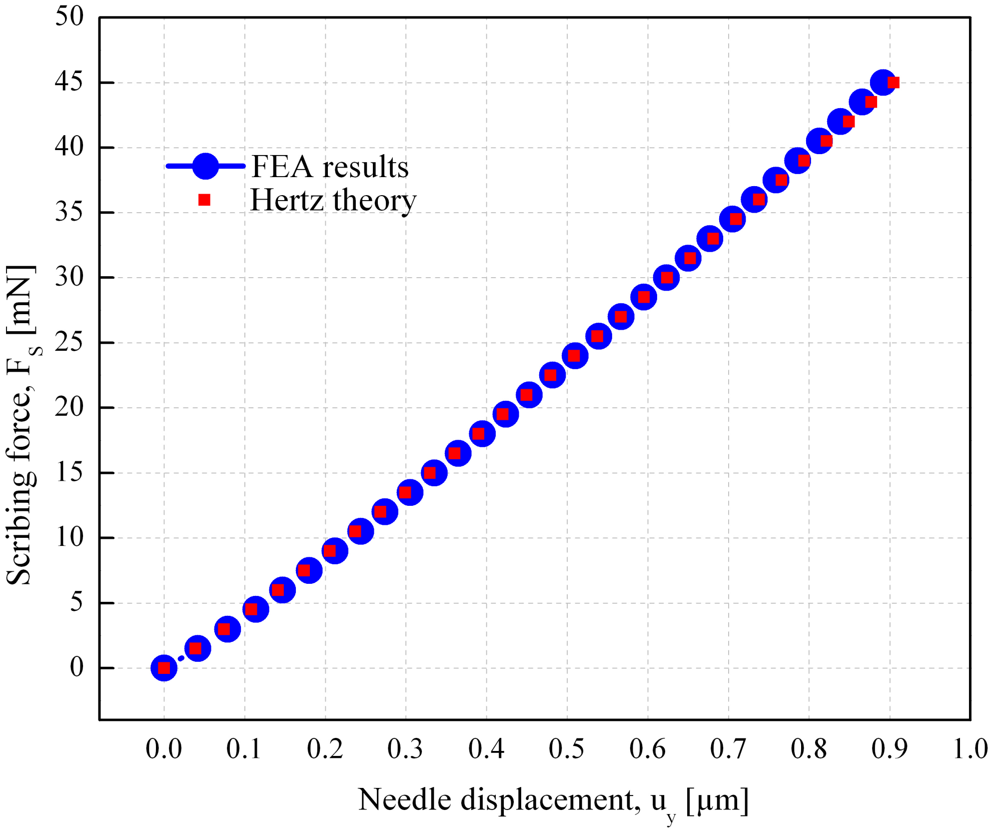

Figure 4.24: *Comparison between FEA (finite element analysis) results and Hertz theory in terms of scribing force versus needle displacement for half-symmetric 2D finite element model (top view) of crack initiation shown in Figure 4.23.*

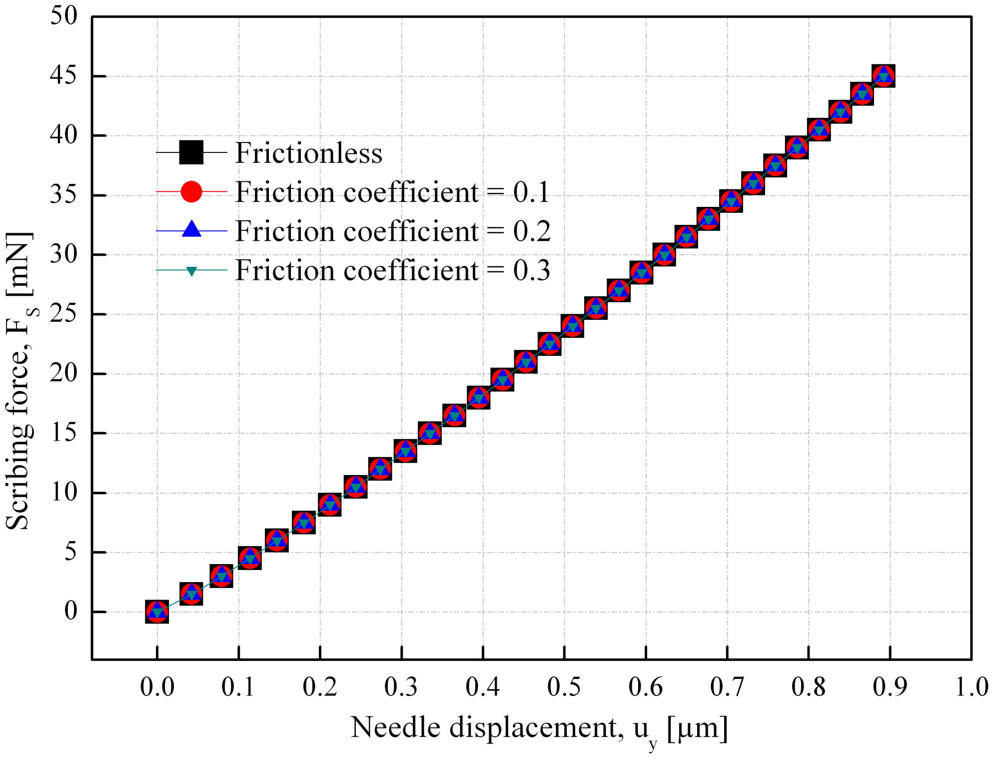

Figure 4.25: *Comparison of scribing force versus needle displacement curves for half-symmetric 2D finite element model (top view) without initial crack shown in Figure 4.23 with different values of coefficient of friction for the tangential behavior of friction between the spherical tip and the CIGS layer.*

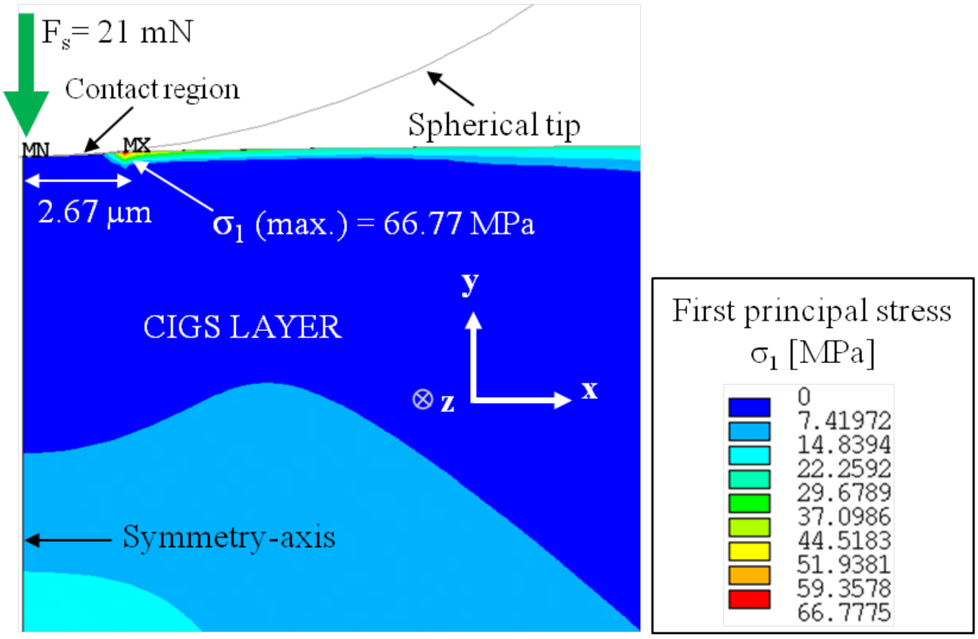

Figure 4.26: *Stress field of the first principal stresses with tensile stresses near the contact region between the spherical tip and the CIGS layer for the half-symmetric 2D FE model (top view) without initial crack shown in Figure 4.23.*

4.4.4 Distribution of first principal stresses in the CIGS layer

Figure 4.26 shows the distribution of first principal stresses in the CIGS layer at the scribing force of 21 mN for the half-symmetric 2D finite element model (top view) without initial crack (see Figure 3.7). The maximum tensile stress of 66.77 MPa is obtained at a distance of 2.67 μm from the origin along the positive x-direction in the CIGS layer. In Figure 4.27, the position of maximum tensile stresses from the origin along the positive x-direction in the CIGS layer is plotted for different values of the scribing force. It can be seen that the maximum tensile stress is always located almost very near to the contact region between the spherical tip and the CIGS layer for all values of the scribing force. The farthest position of maximum tensile stress is 3.67 μm for the scribing force of 45 mN which is also very close to the contact region. The presence of maximum tensile stresses near the contact region between the spherical tip and the CIGS layer indicates that the crack most probably starts propagating from very close to the contact region. The maximum tensile stress values at different values of scribing force are also indicated in the Figure 4.27.

4.4.5 Influence of the position of vertical initial crack

The half-symmetric 2D finite element model (top view) with vertical initial crack (see Figure 3.8) is investigated to find out the mode-I stress intensity factor (K_I) values by varying the position of vertical initial crack, P, along the top edge of CIGS layer from the origin of the coordinate system. The CIGS layer with a vertical initial crack of 3 μm is pressed by the spherical tip with the scribing force of 45 mN. The position of initial crack is varied along the top edge of CIGS layer from 1 μm to 24 μm and the K_I value is recorded for each of the positions. The K_I values obtained from

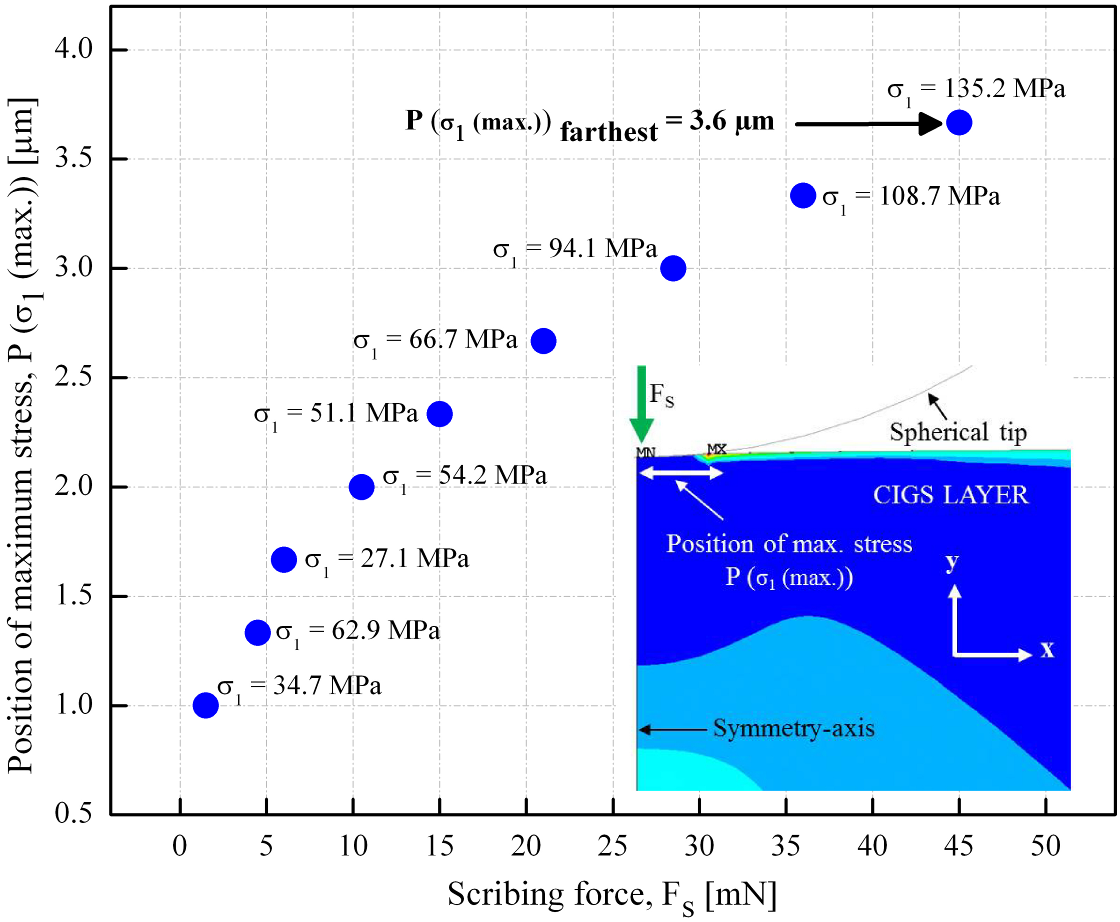

Figure 4.27: Position of maximum tensile stresses (σ_1) along the positive x-direction in CIGS layer plotted against the scribing force for the half-symmetric 2D FE model (top view) without initial crack shown in Figure 4.23.

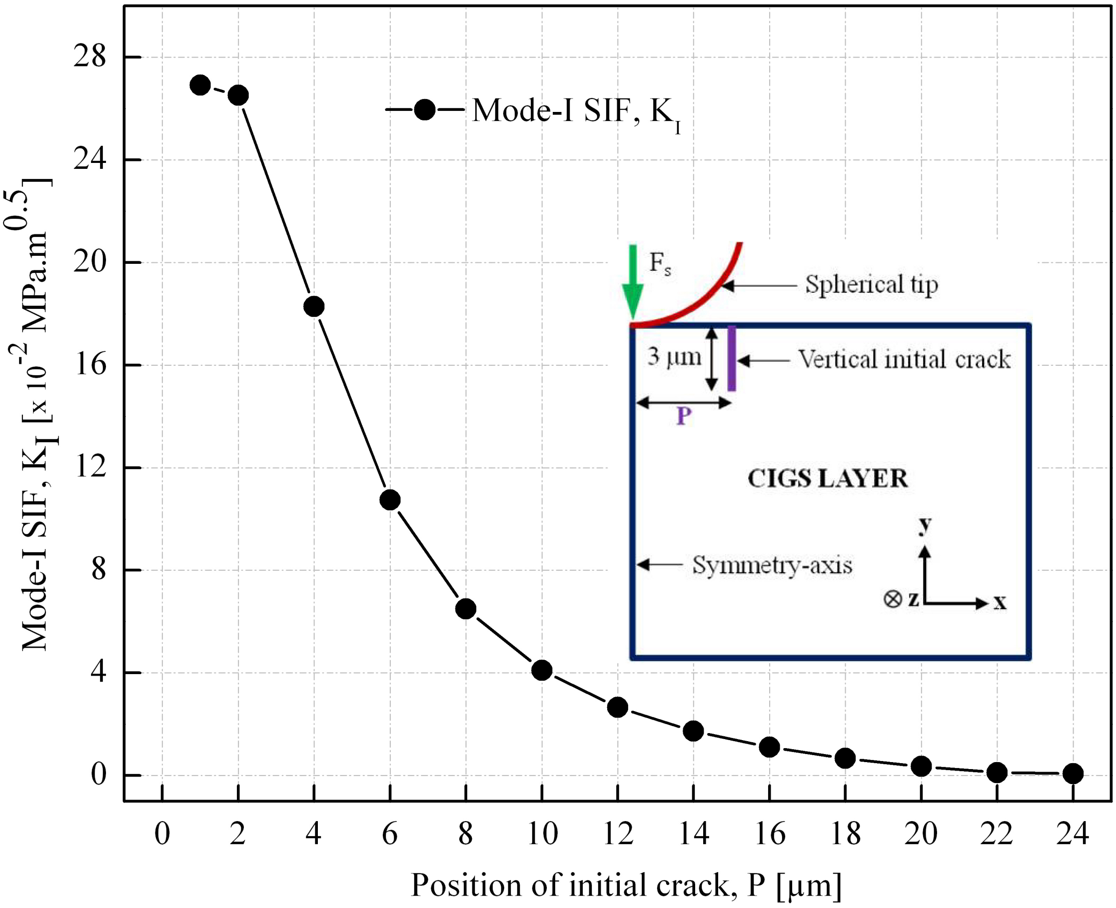

Figure 4.28: *Mode-I stress intensity factor (K_I) plotted against the position of vertical initial crack (P) along top edge of the CIGS layer; the length of initial crack is 3 μm.*

numerical simulation of full crack finite element model are plotted as shown in Figure 4.28. The maximum value of stress intensity factor obtained is 26.9×10^{-2} $MPa\sqrt{m}$ and it is obtained at a distance of 1 μm from the origin. It can be seen from the figure that the stress intensity factor increases as we move more towards the contact region between the CIGS layer and the spherical tip. It indicates that the crack most likely starts propagating from very near of the contact region between the spherical tip and the CIGS layer.

In the next investigation, an initial crack is being assumed to be present very near to the contact region between the scribing needle and the CIGS layer that is at a distance of 0.5 μm from origin along the top edge of CIGS layer. Now the length of initial crack, L, is varied from 0.3 μm to 10 μm. The CIGS layer is pressed by the scribing needle with a force of 45 mN. Figure 4.29 shows the variation of mode-I stress intensity factor with the crack length. It was found that the value of K_I goes on increasing continuously with the decrease in length of initial crack. In this investigation, the maximum value of K_I was obtained to be 52.11×10^{-2} $MPa\sqrt{m}$ for the crack length of 0.3 μm. So the maximum value of stress intensity factor is obtained for the vertical initial crack of length 0.3 μm present very close to the contact region that is at a distance of 0.5 μm from the origin. This again suggests that the crack most likely starts propagating from very near to the contact region between the scribing needle and the CIGS layer.

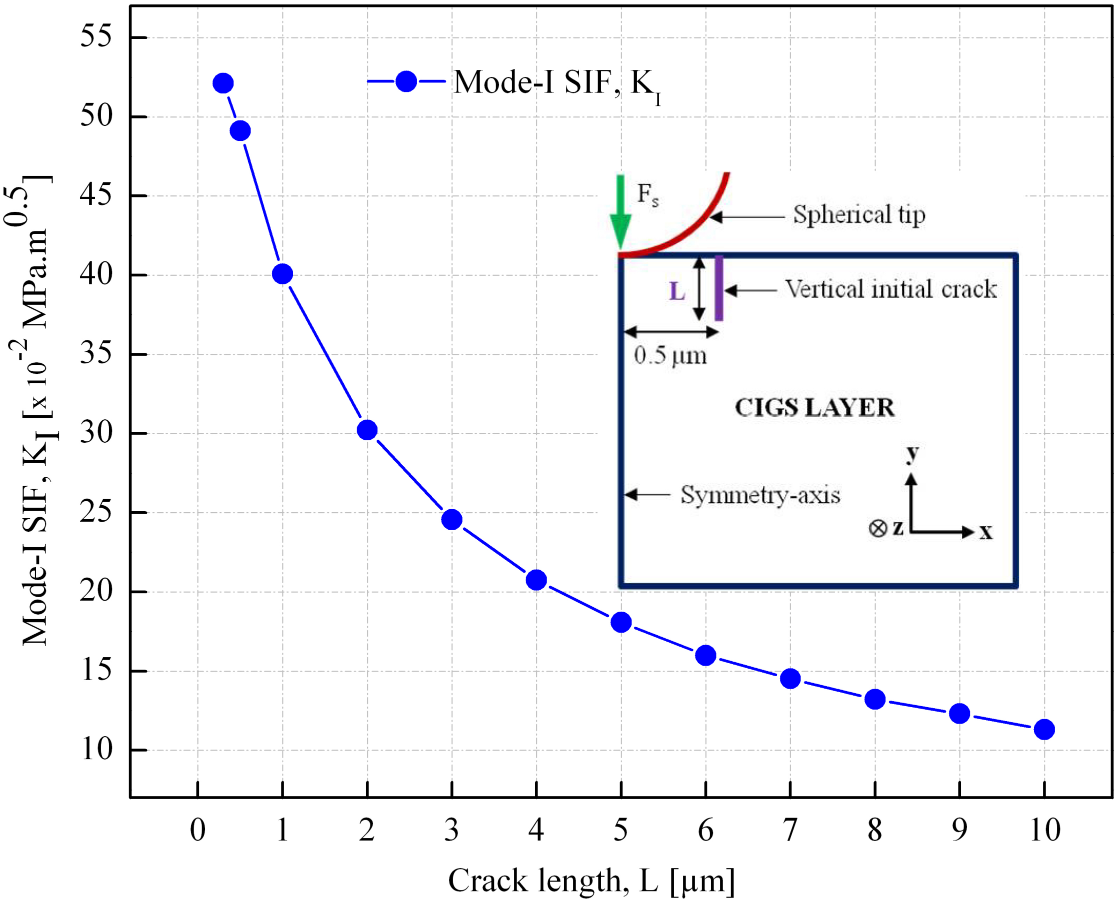

Figure 4.29: *Mode-I stress intensity factor (K_I) versus length of initial crack (L) considered at a distance of 0.5 μm from the origin along the top edge of the CIGS layer.*

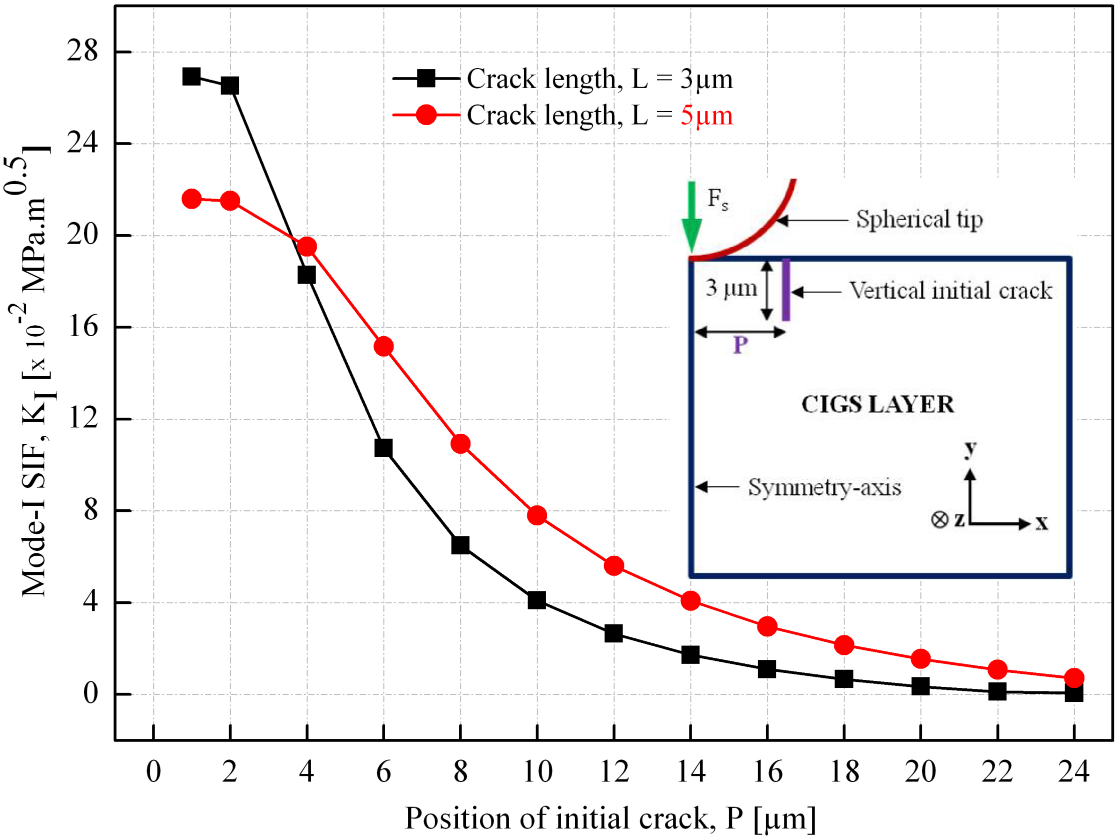

Figure 4.30: *Qualitative trend of mode-I stress intensity factor (K_I) for the varying position of vertical initial crack of length 3 μm and 5 μm from the origin of coordinate system along the top edge of the CIGS layer.*

The half-symmetric 2D FE model (top view) with vertical initial crack (see Figure 3.8) is further investigated to study the influence of variation in the length of initial crack on the qualitative trend of mode-I stress intensity factor. The fracture mechanical simulations are performed with the vertical initial crack of two different lengths of 3 μm and 5 μm. As earlier, the scribing force of 45 mN is used to perform the simulations and the position of initial crack from the origin is varied along the top edge of CIGS layer from 1 μm to 24 μm. K_I value is recorded for each of the positions of the initial crack. The K_I values obtained from numerical simulation of full crack FE model are plotted as shown in Figure 4.30. For the vertical initial crack of length 5 μm, the maximum value of stress intensity factor obtained is 21.58×10^{-2} $MPa\sqrt{m}$ and it is obtained at very near to the contact region that is at a distance of 1 μm from the origin. It can be seen that the stress intensity continues to increase as we move more towards the contact region between the CIGS layer and the spherical tip for both the lengths of the initial crack. This shows that the variation in length of initial crack does not effect the qualitative trend regarding the stress intensity factor and the crack most likely starts propagating from very close to the contact region between the scribing needle and the CIGS layer.

4.5 3D finite element model for buckling and delamination

The 3D finite element model for buckling and delamination of CIGS thin-film shown in Figure 3.9 is investigated for the needle displacement of 1.5 μm. The load applied to the needle is the displacement load. This kind of load can help avoid the convergence problems caused by the initial contact gap. So, the scribing needle is given the displacement of 1.5 μm in the positive x-direction into the CIGS thin-film and all other degrees of freedom are set to zero.

4.5.1 Numerical results of simulation for crack initiation

Figure 4.31 (a) shows the distribution of first principal stresses in the contact surface (surface of the CIGS layer which is in contact with the conical needle) of CIGS thin-film at the needle displacement of 0.6 μm for the 3D finite element model shown in Figure 3.9. The maximum tensile stresses of 963.2 MPa are obtained in the contact surface of CIGS thin-film at a distance of 2.03 μm from the origin along the positive y-direction of the coordinate system. The contour plot of contact penetration for the contact surface of CIGS film is shown in the Figure 4.31 (b). It can be seen that the contact penetration is maximum in the region where the conical needle presses the film. This suggests that the compressive stresses are induced in the contact region between the scribing needle and the CIGS layer and the maximum tensile stresses are generated very near to the contact region. The direction of first principal stresses suggests that the crack must propagate along the contact surface in the positive y-direction parallel to the CIGS layer. It appears that this crack may split the CIGS layer along the thickness, however, since the layer is very thin with 2 μm thickness, it is very unlikely that this crack may result in the splitting of thin film along its thickness. Anyhow, this is not the crack which may propagate through the CIGS layer and finally taking up the nearly circular shape in front of the scribing needle. So, in the next step, the tensile stresses generated in the bottom surface of CIGS thin-film are analyzed.

Figure 4.32 shows the distribution and direction of first principal stresses in the bottom surface of the CIGS thin-film after being loaded at the needle displacement of 1.09 μm. The maximum tensile stresses of the magnitude of 1919.44 MPa represented by the red color occur very near to the contact region between the needle and the CIGS layer in the bottom surface. In Figure 4.33, the position of maximum tensile stresses in the bottom surface of CIGS thin-film from the origin along the positive x-direction is plotted for different values of needle displacement. It can be seen that the maximum tensile stresses are always located almost very near to the contact region between the needle and the layer for all the values of the needle displacement. The nearest position of maximum tensile stress is at 0.98 μm from the origin. However, the farthest location of maximum tensile stress is at 4.4 μm from the origin which is also very close to the contact region. This indicates that the crack most likely starts propagating from very near to the contact region between the needle and the layer in the botom surface of CIGS layer.

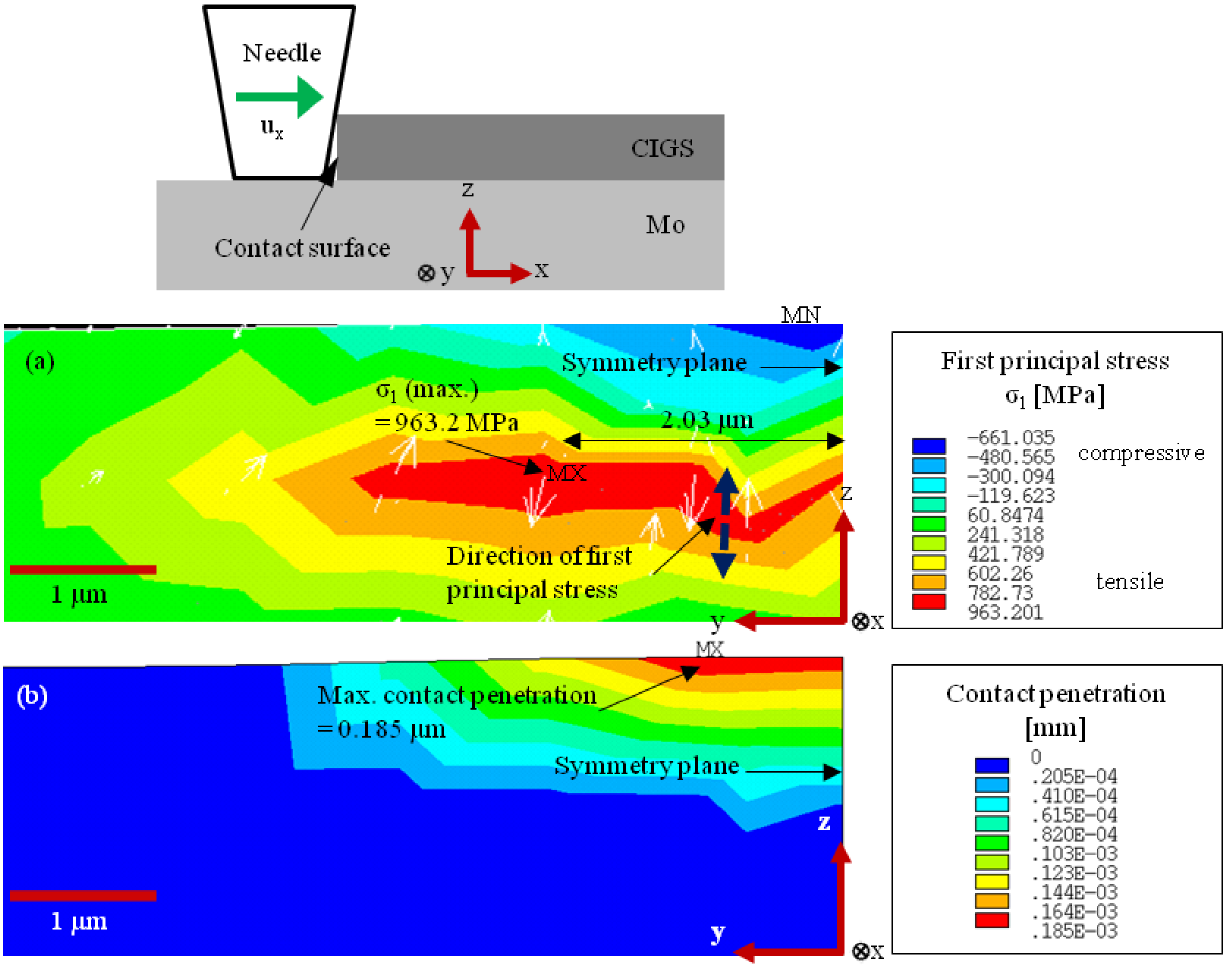

Figure 4.31: *(a) Stress field of the first principal stresses, and (b) contour plot for the contact penetration in the contact surface of CIGS thin-film at the needle displacement of 0.6 µm for the 3D FE model of buckling and delamination; adhesion (shear) strength of CIGS/Mo interface is zero.*

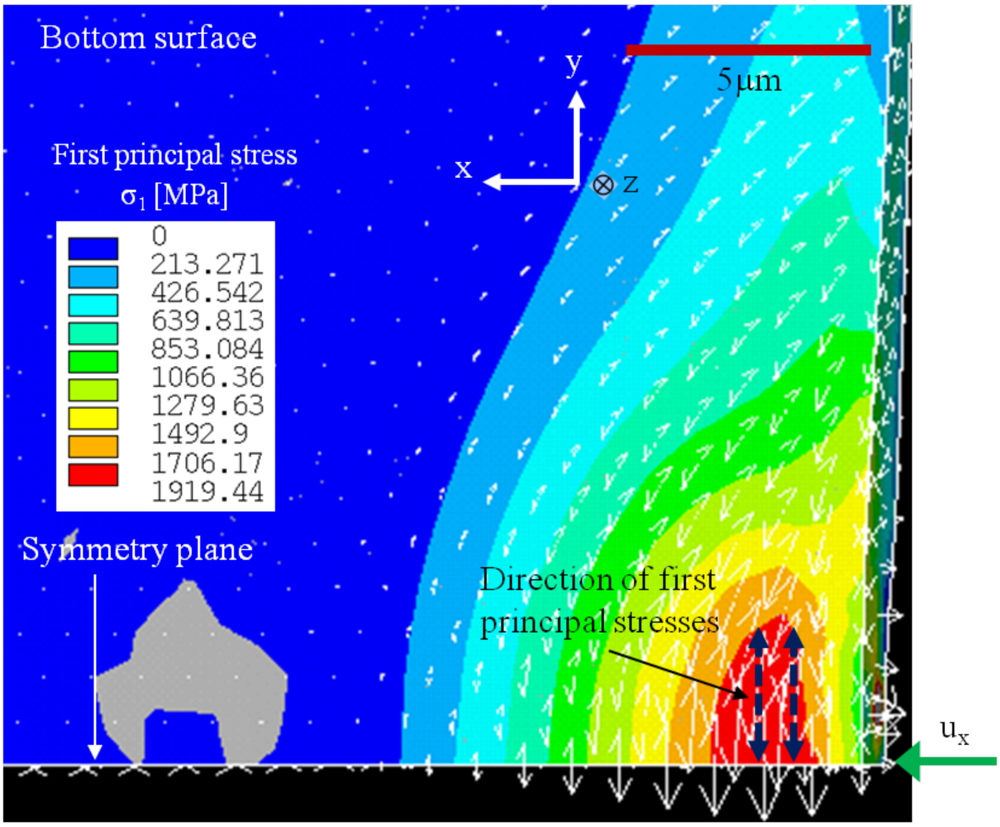

Figure 4.32: *Stress field of the first principal stresses in the bottom surface of CIGS layer at the needle displacement of 1.09 μm for the 3D FE model of buckling and delamination; adhesion (shear) strength of CIGS/Mo interface is zero.*

4.5.2 Delamination and buckling of CIGS thin-film

After carry out the finite element simulation with the 3D finite element model for buckling and delamination, the nodal out-of-plane displacement (u_z) of the CIGS layer of 2 μm thickness was observed at different values of the needle displacement. Figure 4.34 shows the nodal out-of-plane displacement of the CIGS layer at the different stages of needle movement. It was observed that u_z was maximum at the needle displacement of 1.09 μm. Therefore, the node at which the out-of-plane displacement of the CIGS layer was maximum when the needle displacement was 1.09 μm was noted down and the values of out-of-plane displacement at this particular node was recorded for the different values of needle displacement. The value of needle displacement is indicated on the top of the image of each of the six stages in the figure. The six stages of the behavior of the CIGS thin-film in terms of its out-of-plane displacement are described as below:

Stage 1 presents the behavior of the CIGS film in terms of out-of-plane displacement at the needle displacement of 0.4 μm after the specimen is being loaded. Here, it can be seen that no delamination has taken place at the CIGS/Mo interface till the displacement value of 0.4 μm.

Stage 2 shows the behavior of CIGS thin-film at the needle displacement of 0.75 μm. The nodal out-of-plane displacement for the CIGS layer reaches the value of 0.0245 μm. This indicates that the delamination at CIGS/Mo interface is being initiated. The value of scribing force at which the interface delamination is initiated (F_{DI}) is determined to be 24.31 mN.

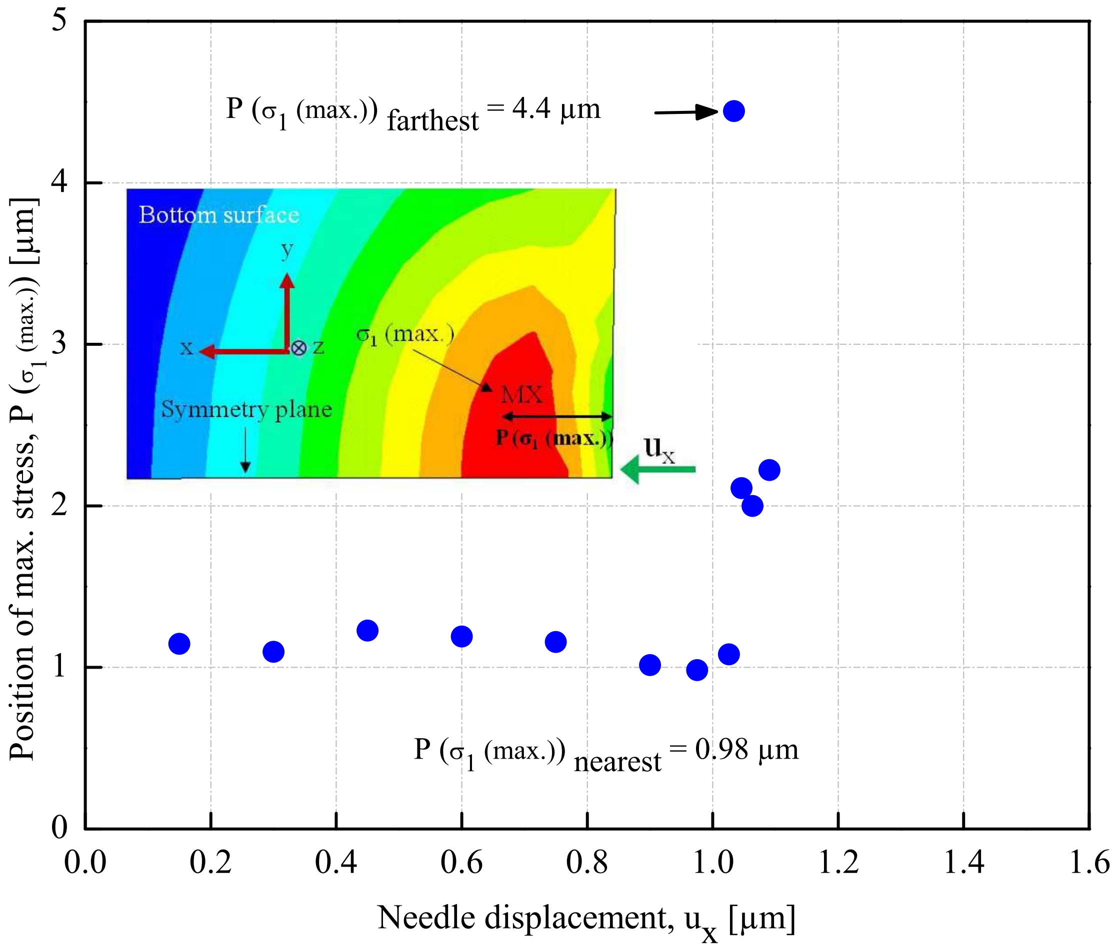

Figure 4.33: *Position of maximum tensile stresses (σ_1) in the bottom surface of CIGS thin-film along the positive x-direction plotted against the needle displacement; adhesion (shear) strength of CIGS/Mo interface is zero.*

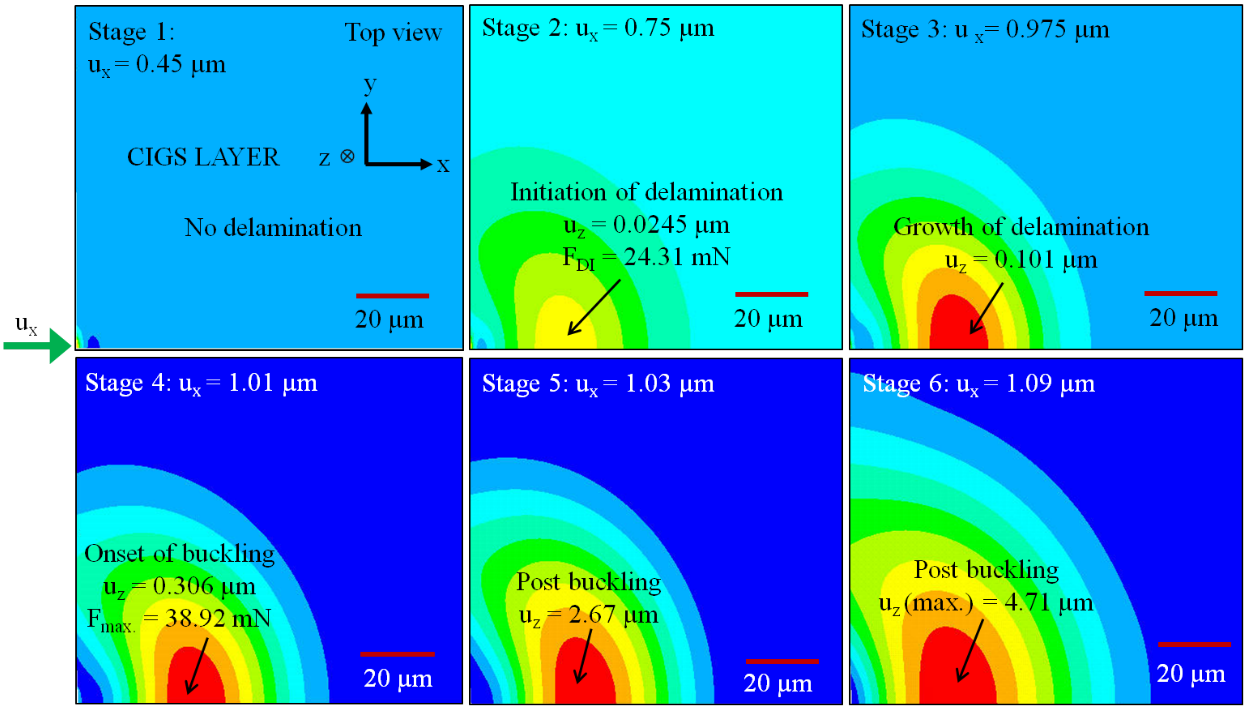

Figure 4.34: *Contour plot for nodal out-of-plane displacement (u_z) of CIGS thin-film (top view) at different values of needle displacement showing the initiation and growth of delamination at CIGS/Mo interface leading to the buckling of CIGS layer; adhesion (shear) strength of CIGS/Mo interface is zero; green arrow represents the direction of needle displacement (u_x) which is same for all the six stages shown here.*

Stage 3 depicts the contour plot for u_z of CIGS layer at the needle displacement of 0.975 μm. The red colour of the contour plot shows that the maximum out-of-plane displacement takes place in this region. The maximum value of u_z determined in this stage is 0.101 μm. This stage depicts the growth of delamination at the CIGS/Mo interface.

Stage 4 shows the behavior of CIGS layer in terms of its out-of-plane displacement when the needle displacement reaches the value of 1.01 μm. The maximum value of u_z determined in this stage is 0.306 μm. The scribing force reaches the maximum value in this stage. This represents the onset of buckling of the CIGS thin-film. The value of scribing force at which the buckling starts (onset of buckling) is called the maximum scribing force (F_{max}) and it is determined to be 38.92 mN. After this point, the scribing force starts falling down for the further increase in the needle displacement.

Stage 5 presents the post buckling behavior of CIGS layer at the needle displacement of 1.03 μm. The out-of-plane displacement of the film increases very fast and reaches the value of 2.67 μm in this stage which represents the post buckling behavior. However, the scribing force continues to fall down in this stage after reaching the maximum value of 38.92 mN in the stage 4.

Stage 6 also depicts the post buckling behavior of CIGS thin-film at the needle displacement of 1.09 μm. As observed in the stage 5, here also in this stage, scribing force after decreasing continuously reaches the minimum value of zero. However, the out-of-plane displacement reaches the maximum value of 4.71 μm.

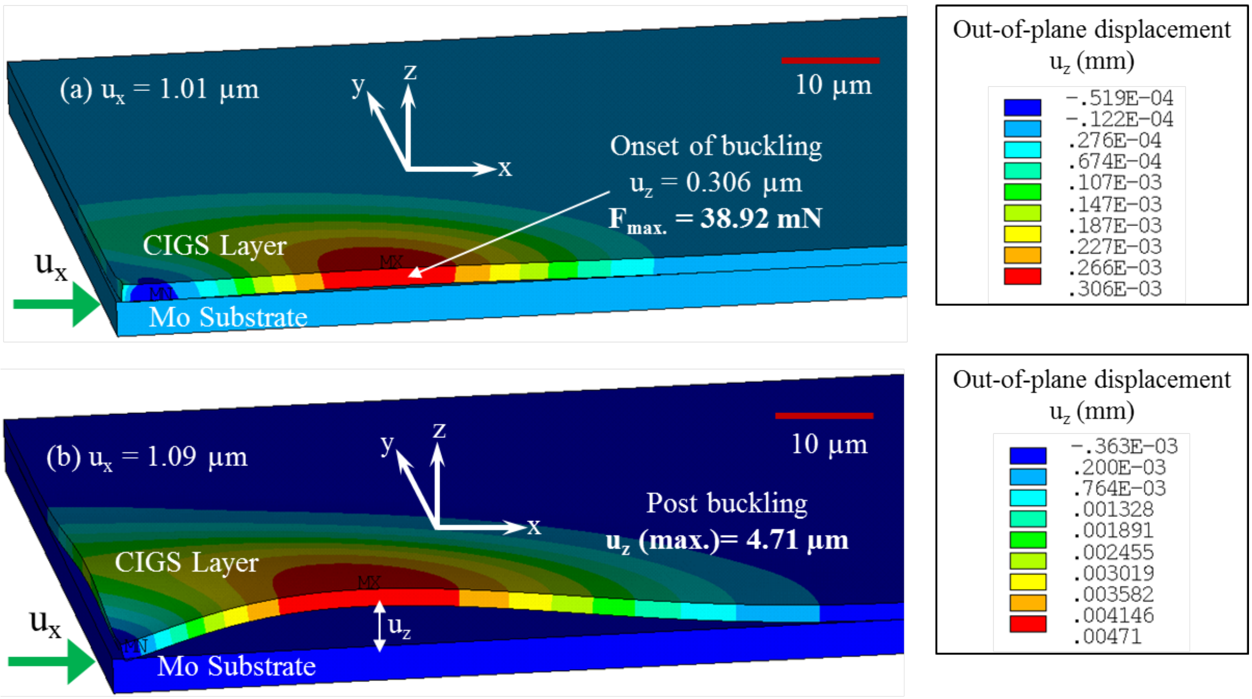

Figure 4.35: *Contour plot for nodal out-of-plane displacement (u_z) of CIGS thin-film (isometric view) showing the (a) onset of buckling and (b) post buckling at u_x = 1.09 μm; adhesion (shear) strength of CIGS/Mo interface is zero; green arrow represents the direction of needle displacement, u_x.*

Figure 4.35 shows the isometric view for the contour plot of nodal out-of-plane displacement of the CIGS thin-film. The onset of buckling of the CIGS layer takes place at the needle displacement of 1.01 μm as depicted in Figure 4.35 (a). The scribing force reaches its maximum value of 38.92 mN which represents the critical buckling load for the thin-film. Figure 4.35 (b) depicts the post buckling of CIGS thin-film at the needle displacement of 1.09 μm. As can be seen in the figure, the CIGS layer has buckled up from the molybdenum substrate with out-of-plane displacement reaching the maximum value of 4.71 μm.

Figure 4.36 shows the force-displacement curve obtained as a result of the simulation. It can be seen that the scribing force continues to increase till the needle displacement of 1.01 μm and then starts falling down. The maximum value of scribing force (F_{max}) is determined to be 38.92 mN as indicated in the figure. The maximum value of scribing force represents the onset of buckling of the CIGS thin-film.

The scribing force (F_s) is plotted against the nodal out-of-plane displacement of the CIGS thin-film after the specimen being loaded as depicted in Figure 4.37. As indicated in the plot, the delamination at the CIGS/Mo interface initiates at the scribing force of 24.31 mN (F_{DI}) and u_z equal to 0.0245 μm. Thereafter, the force continues to increase very fast with the slight increase in u_z and finally reaches the maximum value of 38.92 mN being described as the critical buckling load. This represents the onset of buckling. The behavior of CIGS thin-film after this point, represents the post buckling behavior. As can be seen from the figure, the scribing force falls down very fast with the significant increase in u_z. Finally, the out-of-plane displacement reaches its maximum value of 4.71 μm.

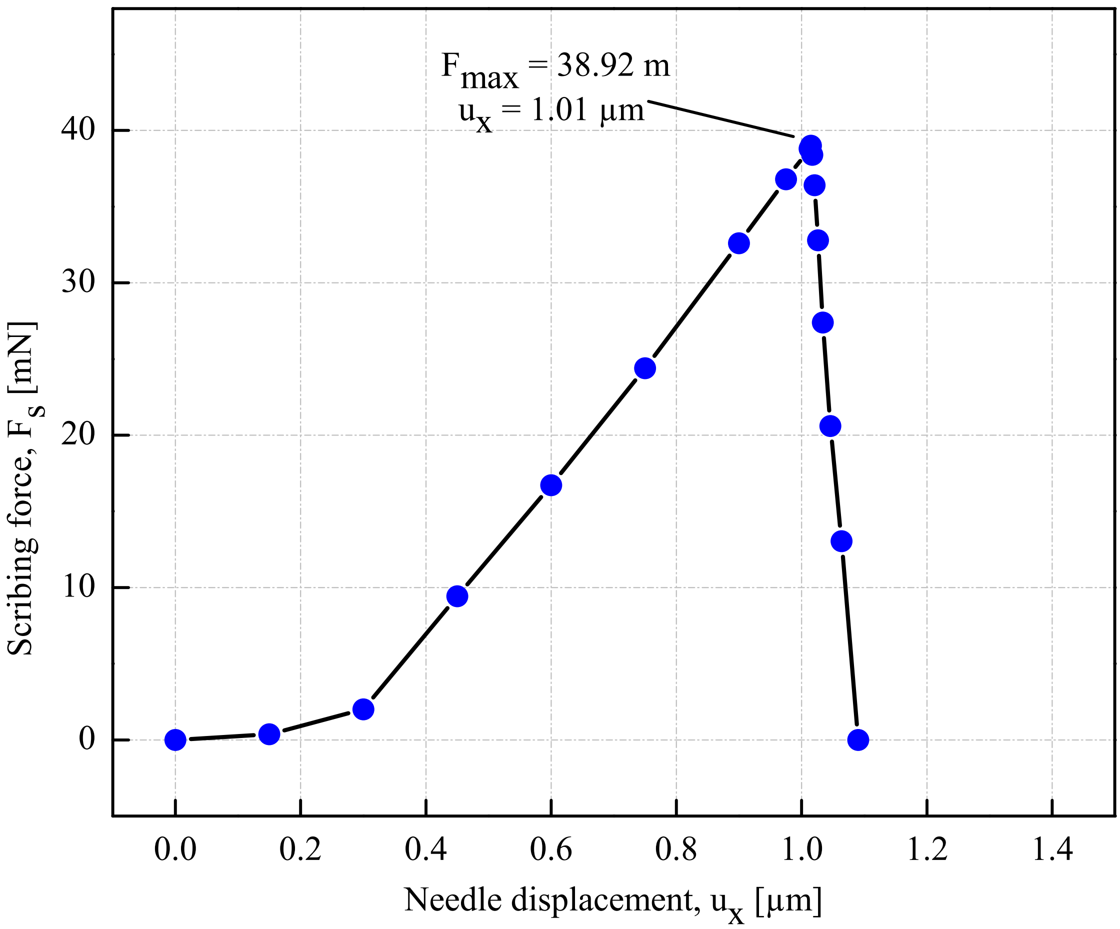

Figure 4.36: *Scribing force (F_s) plotted against the needle displacement (u_z) for 3D finite element model of buckling and delamination; adhesion (shear) strength of CIGS/Mo interface is zero.*

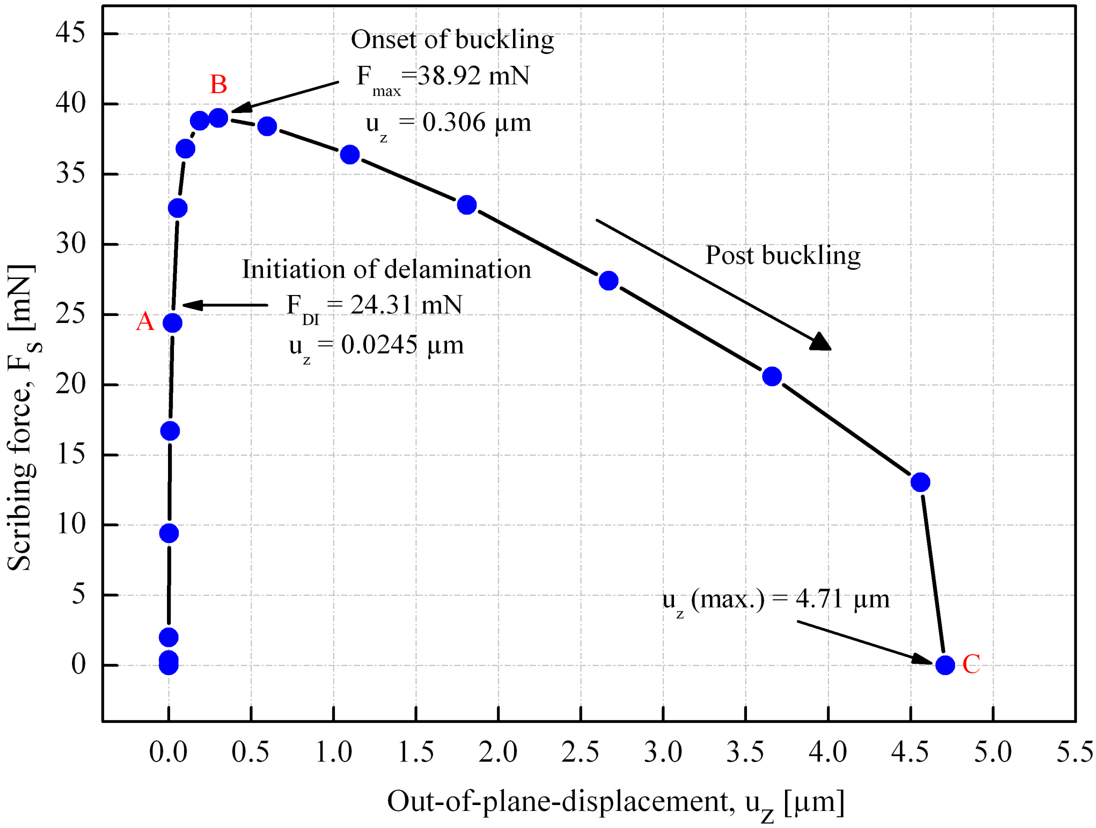

Figure 4.37: *Scribing force (F_s) plotted against the out-of-plane displacement (u_z) of the CIGS thin-film after the specimen being loaded; adhesion (shear) strength of CIGS/Mo interface is zero.*

Figure 4.38 shows the variation of out-of-plane displacement (u_z) of the CIGS thin-film after the specimen being loaded with the needle displacement (u_x). It can be seen that there is almost no increase in u_z till the needle displacement reaches the value of 0.6 μm. After that, there is slight increase in u_z and it reaches a value of 0.0245 μm at point *A* where the needle displacement is 0.75 μm. This predicts the delamination initiation at the CIGS/Mo interface. After this point, the u_z continues to increase, however rather slightly, with the increase in needle displacement till the point *B* where u_z reaches a value of 0.301 μm at the needle displacement of 1.01 μm. This point *B*, represents the onset of buckling of CIGS layer. After this, the behavior of CIGS film with the further increase in needle displacement is represents the post buckling behavior. During this post buckling stage, u_z increases very fast with the slight increase in needle displacement till the point *C* and reaches its maximum value of 4.71 μm at the needle displacement of 1.09 μm.

4.5.3 Numerical results for the crack path

Figure 4.39 presents the distribution and direction of first principal stresses in the contact surface of the CIGS thin-film after being loaded at the needle displacement of 1.09 μm. It can be seen that the first principal stresses are tensile in nature near the region, where the needle is in contact with the CIGS layer. The maximum tensile stresses of the magnitude of 2354.68 MPa occur in the contact surface represented by red color. The direction of white arrows which can be seen in

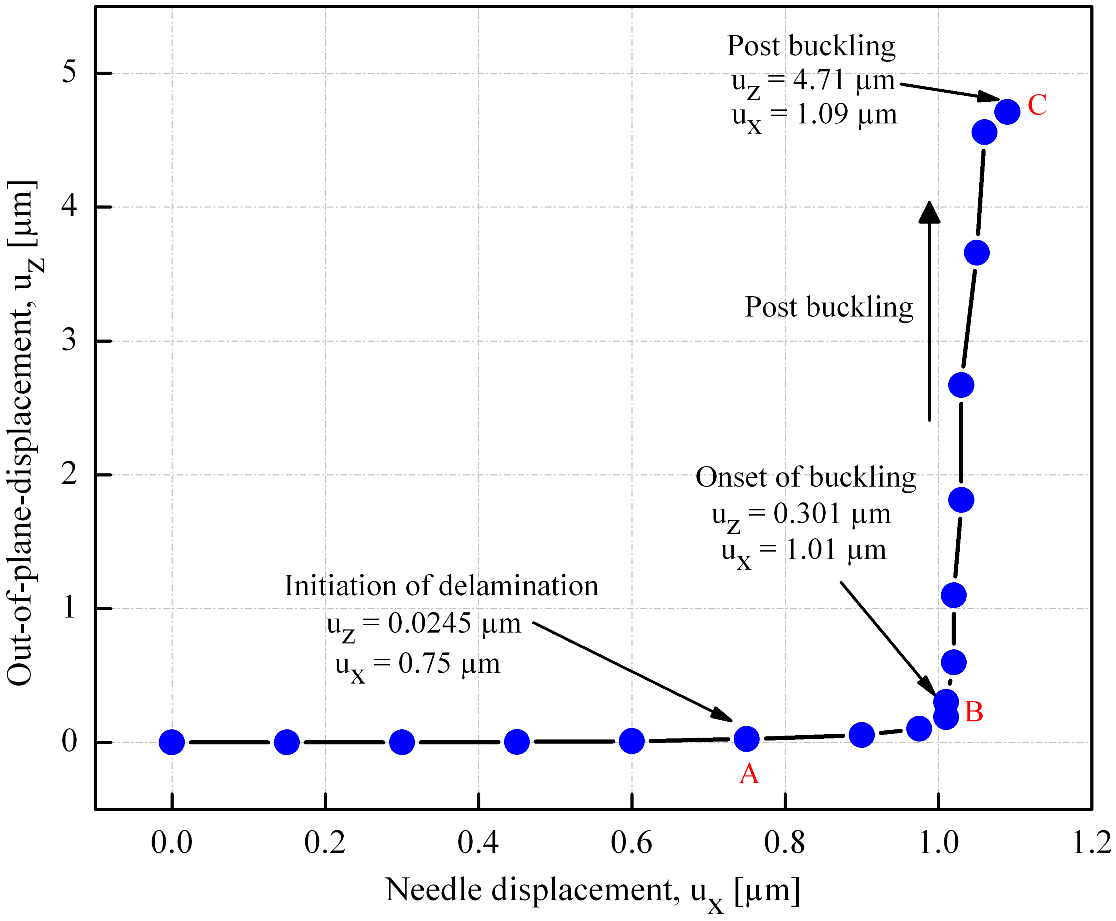

Figure 4.38: *Variation of out-of plane displacement (u_z) of CIGS thin-film with the needle displacement (u_x) for the 3D finite element model of buckling driven delamination; adhesion (shear) strength of CIGS/Mo interface is zero.*

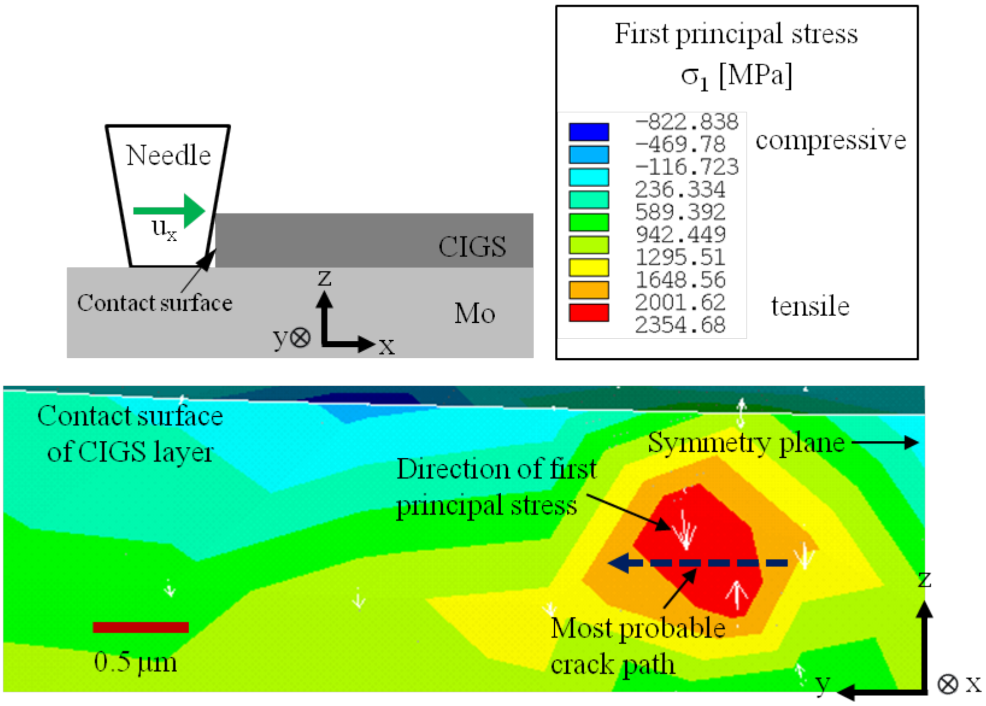

__Figure 4.39:__ Distribution and direction of first principal stresses in the contact surface of CIGS layer at the needle displacement of 1.09 μm showing the most probable direction of crack propagation represented by the dotted dark blue color arrow; the region in red color shows the maximum tensile stresses; adhesion (shear) strength of CIGS/Mo interface is zero.

the figure represents the direction of first principal stresses in the contact surface. Under mode-I (opening mode) failure of the material, the crack propagates perpendicular to the direction of the first principal stresses. According to this, the crack must propagate along the contact surface in the positive y-direction parallel to the CIGS layer as indicated by the dotted dark blue color arrow. It appears that this crack may split the CIGS layer along the thickness, however, since the layer is very thin with 2 μm thickness, it is very unlikely that this crack may result in the splitting of thin film along its thickness. Anyhow, this is not the crack which may propagate through the CIGS layer and finally taking up the nearly circular shape in front of the scribing needle. So, in the next step, the tensile stresses generated in the top surface of CIGS thin-film are analyzed.

The distribution and direction of first principal stresses in the top surface of the CIGS thin-film after being loaded at the needle displacement of 1.09 μm are presented in the Figure 4.40. The gray color in the figure represents the compressive stresses present in the top surface of the layer. It can be seen in the figure that the first principal stresses are tensile in nature in front of the needle near the region where the needle is in contact with the CIGS layer. The maximum tensile stresses of the magnitude of 1116.35 MPa occur in the top surface represented by the red color. The direction of white arrows which can be seen in the figure represent the direction of first principal stresses in the top surface. Under the mode-I failure of the material, the crack must propagate in the direction perpendicular to the direction of first principal stresses. Therefore, the crack will most likely propagate along the path as indicated by the dotted dark blue color lines starting most

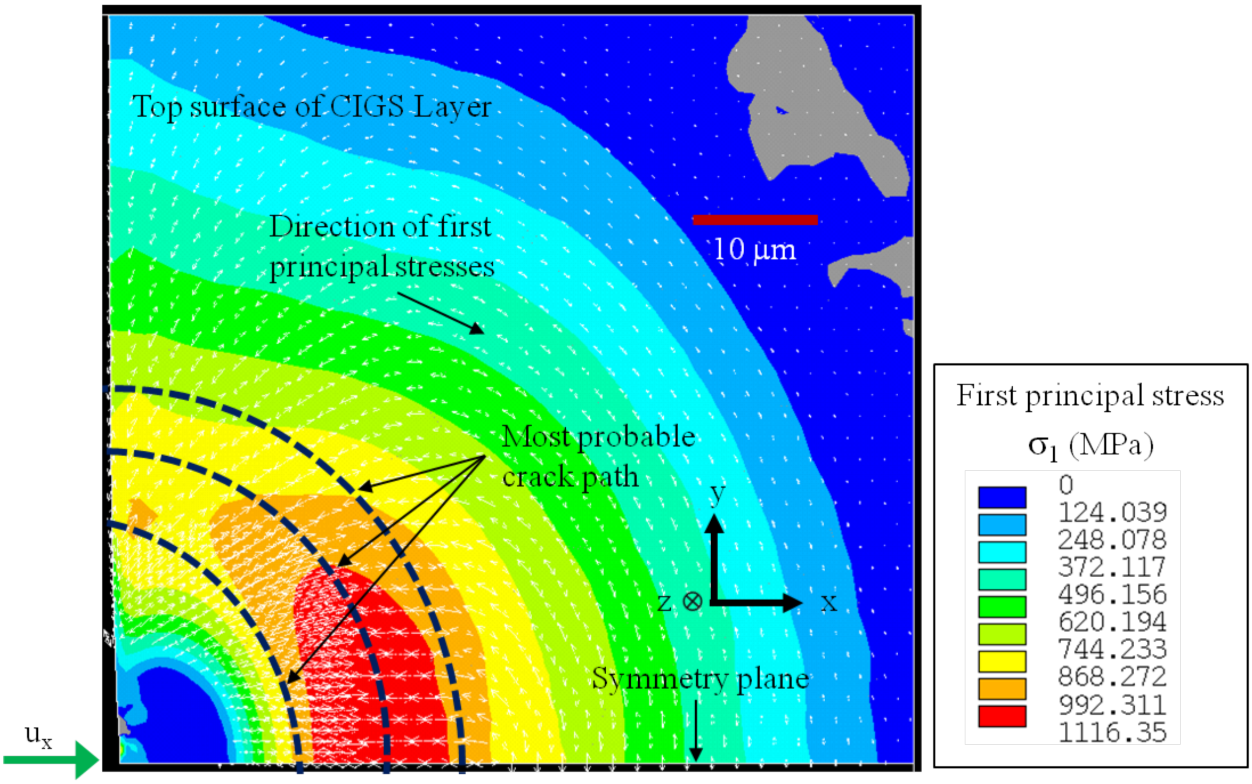

Figure 4.40: *Distribution and direction of first principal stresses in the top surface of CIGS thin-film at the needle displacement of 1.09* μ*m showing the most probable direction of crack propagation; the region in red color shows the maximum tensile stresses; adhesion (shear) strength of CIGS/Mo interface is zero; green arrow shows the direction of needle displacement,* u_x*.*

probably from very near to the red colour region as shown in the figure. In the next step, the tensile stresses generated in the bottom surface of CIGS thin-film are analyzed.

Figure 4.41 shows the distribution and direction of first principal stresses in the bottom surface of the CIGS thin-film after being loaded at the needle displacement of 1.09 μm. The gray color in the figure represents the compressive stresses present in the bottom surface of the layer. It can be seen in the figure that the first principal stresses are tensile in nature near the region where the needle is in contact with the CIGS layer. The maximum tensile stresses of the magnitude of 1919.44 MPa occur in the bottom surface represented by the red color. The direction of white arrows which can be seen in the figure represent the direction of first principal stresses in the bottom surface. Under mode-I (opening mode) failure of the material, the crack propagates perpendicular to the direction of the first principal stresses. Therefore, the crack will most likely propagate along the path as indicated by the dotted dark blue color arrows as shown in the figure. It can be seen that the crack first propagates forward along the positive x-direction and parallel to the layer and then most probably deviates towards the positive y-direction.

4.5.4 Influence of adhesion (shear) strength of CIGS/Mo interface

In order to study the influence of adhesion (shear) strength of CIGS/Mo interface on delamination and buckling of the CIGS thin-film, a relatively smaller sized 3D finite element model is simulated

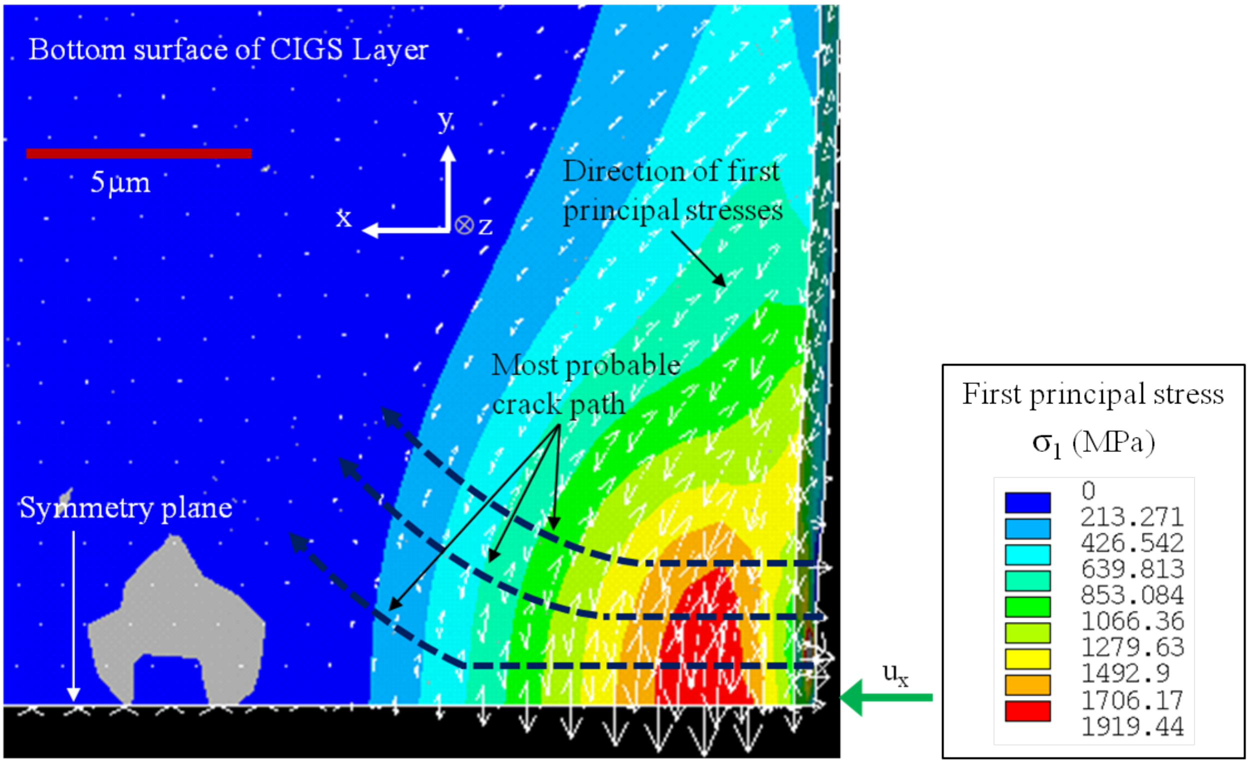

Figure 4.41: *Distribution and direction of first principal stresses in the bottom surface of CIGS thin-film at the needle displacement of 1.09 μm showing the most probable direction of crack propagation; the region in red color shows the maximum tensile stresses; adhesion (shear) strength of CIGS/Mo interface is zero; green arrow shows the direction of needle displacement, u_x.*

with the needle displacement of 2 μm. All the cohesive zone parameters of the CIGS/Mo interface are described in Table 3.2. Four sets of cohesive zone parameters are considered for the finite element simulations, where, model-1 has the minimum value of the interface adhesion (shear) shear strength, T_t = 0.936 MPa and model-4 represents the maximum value of the interface adhesion (shear) strength, T_t = 23.4 MPa. Experimental investigations revealed the shear strength values of CIGS/Mo interface for the low and high adhesion strength specimens to be 4.68 MP and 10.7 MPa respectively. So, taking in to consideration these experimental values for the interface adhesion (shear) shear strength, model-2 and model-3 are constructed to represent the shear strength of interface to be 4.68 MPa and 10.7 MPa respectively. The influence of variation in interface adhesion (shear) shear strength on the scribing force at which delamination initiates at the interface, maximum scribing force and the buckle length is presented in the following sections.

Effect on delamination initiation at the interface

The force at which the delamination initiates at the CIGS/Mo interface, F_{DI}, is plotted against the adhesion (shear) strength in Figure 4.42. For the model-1 which represents the minimum value of adhesion (shear) strength, the delamination starts at the lowest force value of 27.6 mN. However, the model representing the maximum value of adhesion (shear) strength yields the delamination initiation at the highest force value of 60.6 mN. For model-2 and model-3 with intermediate adhesion (shear) strength values of 4.68 MPa and 10.7 MPa respectively, the delamination initiates at

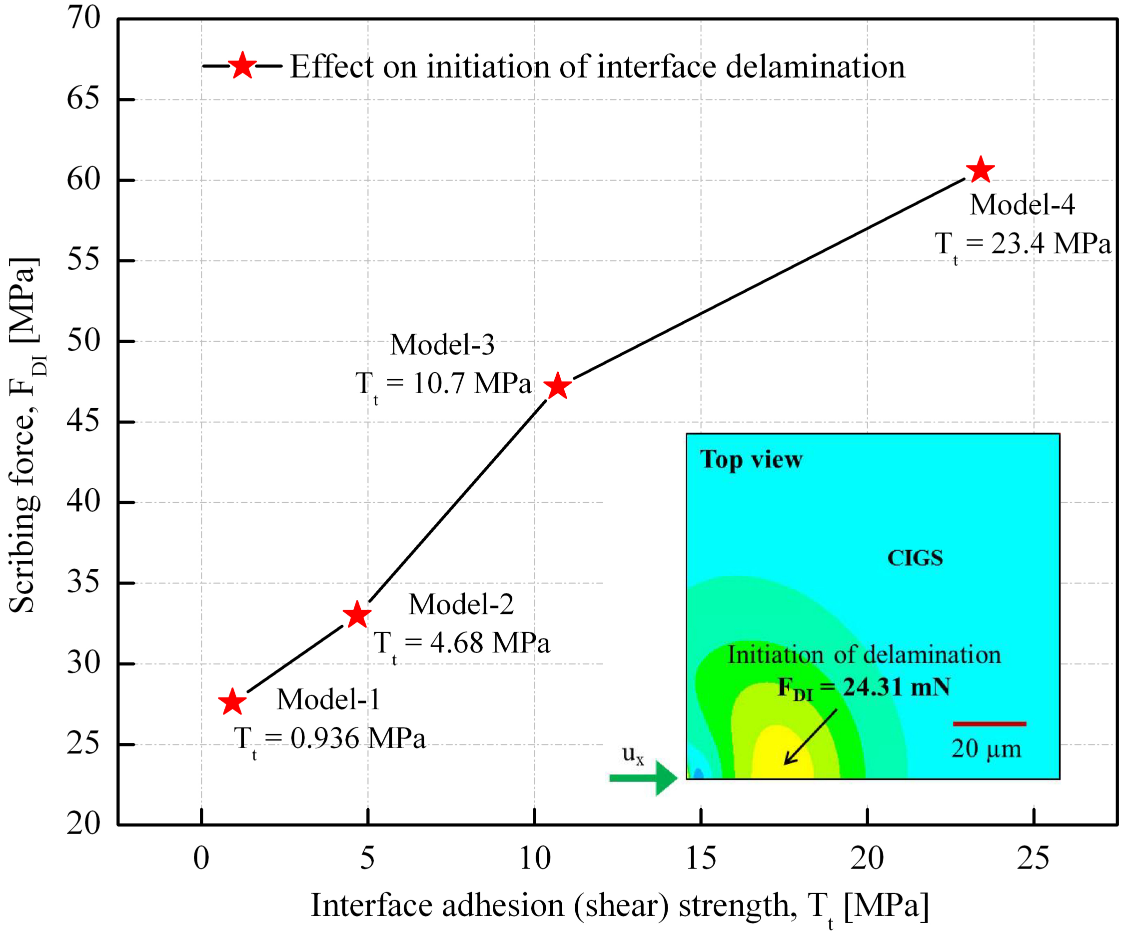

Figure 4.42: *Dependence of scribing force at which interface delamination initiates (F_{DI}) on the adhesion (shear) strength of the CIGS/Mo interface (T_t) for 3D FE model of buckling and delamination model with cohesive zone interface; description about the four sets of cohesive zone parameters for CIGS/Mo interface is given in Table 3.2.*

33 MPa and 47.2 MPa respectively. So, it is observed that the force value at which the delamination initiates at the interface increases with increase in adhesion (shear) strength of the CIGS/Mo interface.

Similarly, the value of needle displacement at which the delamination initiates at the CIGS/Mo interface, u_{DI}, is plotted against the adhesion (shear) strength in Figure 4.43. For the model-1 which represents the minimum value of adhesion (shear) strength, the delamination starts at the lowest value of needle displacement of 0.75 μm. However, the model-4 representing the maximum value of adhesion (shear) strength yields the delamination initiation at the highest value of needle displacement of 1.15 μm. For model-2 and model-3 with intermediate adhesion (shear) strength values of 4.68 MPa and 10.7 MPa respectively, the delamination initiates at 0.85 μm and 1.05 μm respectively. So, it is observed that the value of needle displacement at which the delamination initiates at the interface increases with increase in interface adhesion (shear) strength

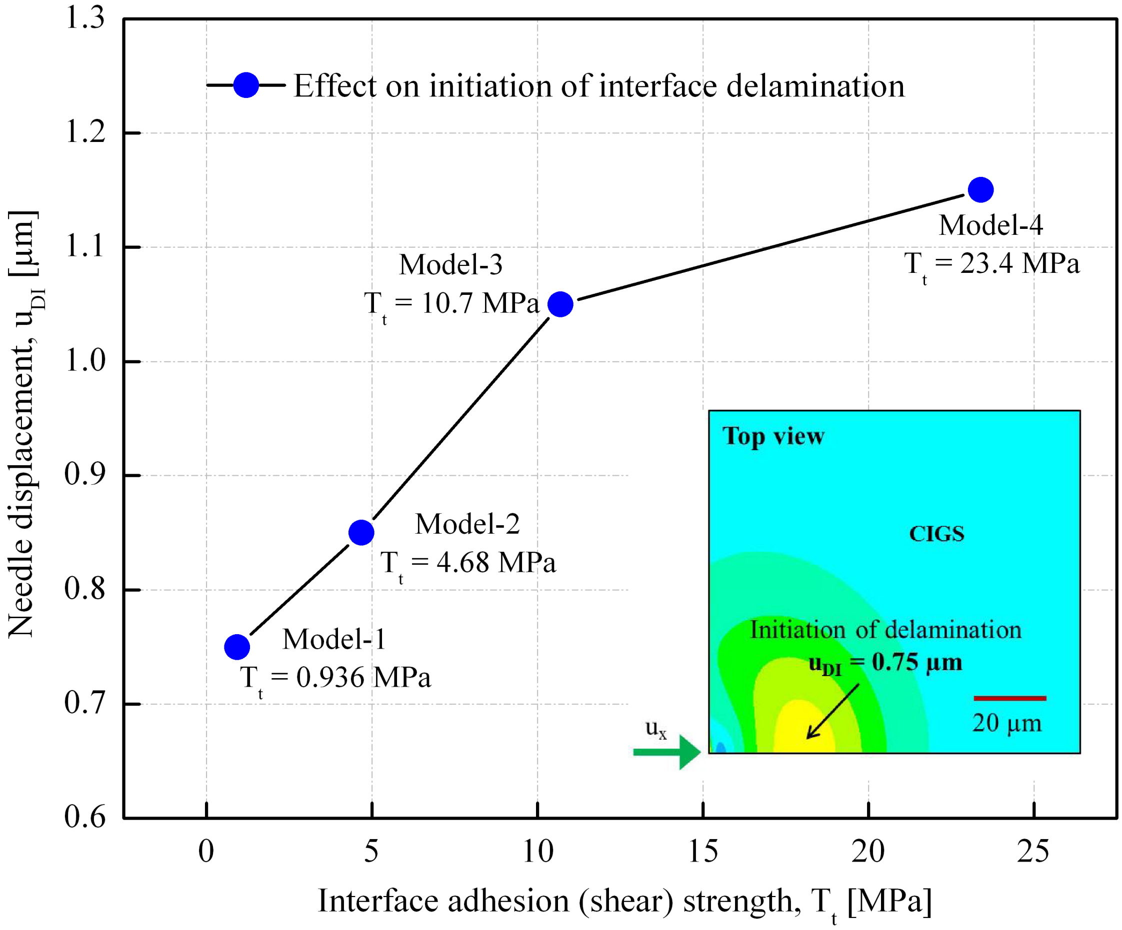

Figure 4.43: *Dependence of needle displacement at which interface delamination initiates (u_{DI}) on the adhesion (shear) strength of the CIGS/Mo interface (T_t) for 3D FE model of buckling and delamination model; description about the four sets of cohesive zone parameters for CIGS/Mo interface is given in Table 3.2.*

Effect on the maximum scribing force

Maximum scribing force, F_{max}, represents the scribing force value at which the onset of buckling takes place and therafter, the force starts falling down with the further increase in needle displacement. Figure 4.44 presents the variation of maximum scribing force with the interface adhesion (shear) strength. Model-1 with the minimum value of interface adhesion (shear) strength of 0.936 MPa gives the lowest value of maximum scribing force as 39 mN and the model-4 with the maximum value of interface adhesion (shear) strength of 23.4 MPa gives the highest value of maximum scribing force as 63.2 mN. Similarly, the other two models that is model-2 and model-3 with interface adhesion (shear) strengths of 4.68 MPa and 10.7 MPa respectively yielded the maximum scribing force values of 52.6 mN and 54.2 mN respectively. So, it was revealed that the maximum scribing force at which the buckling starts increases with the increase in adhesion (shear) strength of CIGS/Mo interface. The maximum scribing force at which the buckling starts for the CIGS specimen with lower interface adhesion (shear) strength of 4.68 MPa is determined to be 52.6 mN from the FE simulations which fits well with the experimental mean value of 45.46 ± 10.07 mN. Likewise, for the CIGS specimen with relatively higher interface adhesion (shear) strength of 10.7 MPa, the FE simulations revealed the maximum scribing force value to be 54.2 mN which also fits well with the experimental mean value of 53.54 ± 5.85 mN. So, the simulation results are in agreement with the experimental findings regarding the maximum scribing force values.

Effect on buckle length

Figure 4.45 presents the simulation results for the out-of-plane displacement of the CIGS thin-film illustrating the buckle length, L_b, for all the four FE models with different values of the adhesion (shear) strength of CIGS/Mo interface as described in Table 3.2. It can be seen in the figure that for model-1 with lowest adhesion (shear) strength 0f 0.936 MPa, the buckle produced at the needle displacement of 1.06 μm has the highest buckle length value of 101.7 μm, however, for the model-2 which has relatively higher adhesion (shear) strength 0f 4.68 MPa, the buckling has not been even initiated at the needle displacement of 1.06 μm. However, the buckling initiates relatively later at the needle displacement of 1.16 μm and the buckle length decreases to 88.6 μm at the displacement of 1.16 μm. For model-3 with adhesion (shear) strength of 10.7 MPa, the buckle produced at the needle displacement of 1.17 μm has the buckle length of 80 μm. Finally, for model-4 with highest adhesion (shear) strength of 23.4 MPa, the buckle produced even at the realtively higher needle displacement of 1.2 μm has the minimum buckle length of 58.6 μm.

So, it was found that the buckle length decreases with the increase in adhesion (shear) strength of the CIGS/Mo interface as can be seen in Figure 4.46. Model-1 with the minimum value of adhesion (shear) strength of the CIGS/Mo interface gives the highest value of buckle length and the model-4 with the highest value of adhesion (shear) strength gives the minimum buckle length of buckle produced as a result of buckling of the CIGS thin-film.

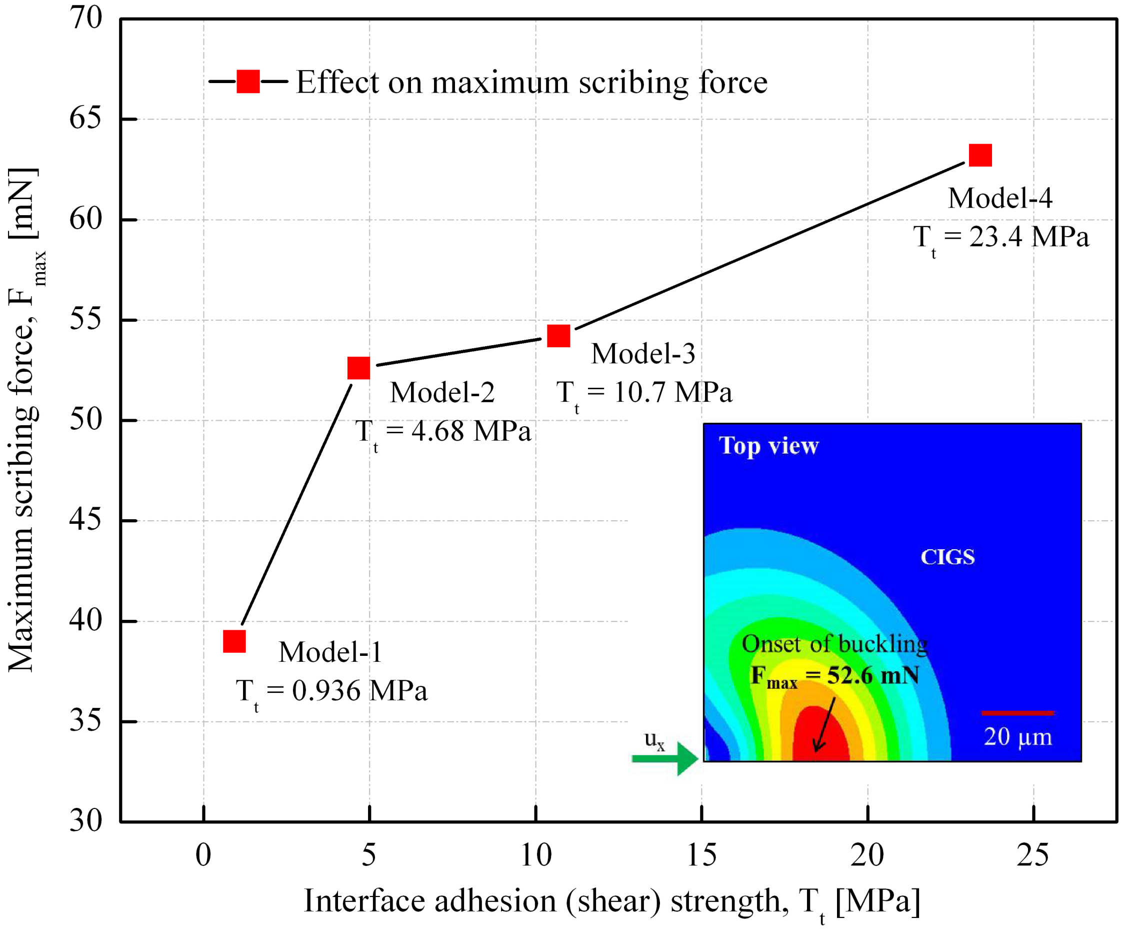

Figure 4.44: *Maximum scribing force (F_{max}) versus adhesion (shear) strength of the CIGS/Mo interface (T_t) for 3D FE model of buckling and delamination model with cohesive zone interface; description about the four sets of cohesive zone parameters for CIGS/Mo interface is given in Table 3.2.*

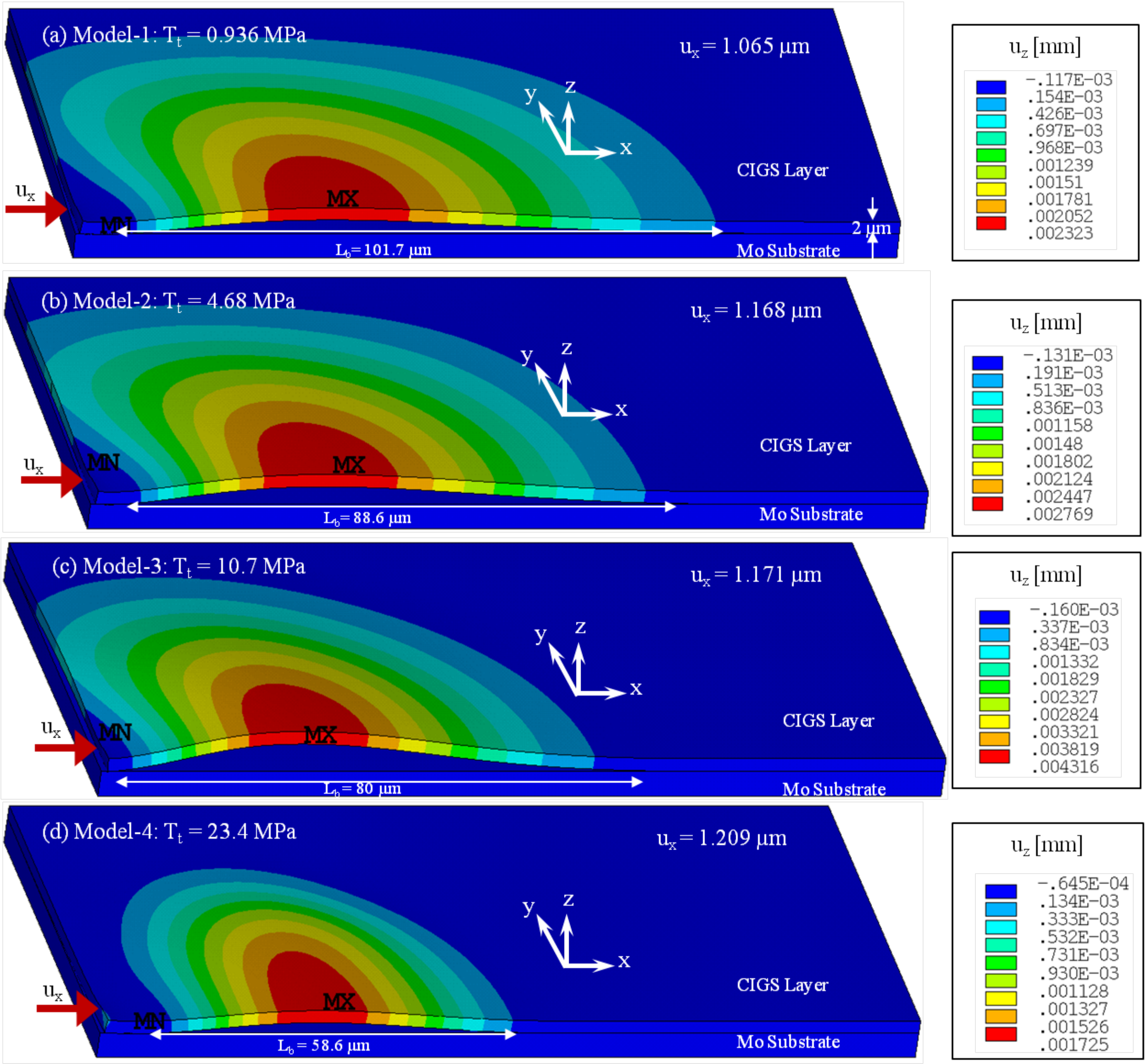

Figure 4.45: *Influence of adhesion (shear) strength of CIGS/Mo interface on the buckle length; buckle length decreases with the increase in adhesion (shear) strength; T_t, L_b and u_z represent the adhesion (shear) strength of CIGS/Mo interface, buckle length and out-of-plane displacement respectively; description about the four sets of cohesive zone parameters for CIGS/Mo interface is given in Table 3.2.*

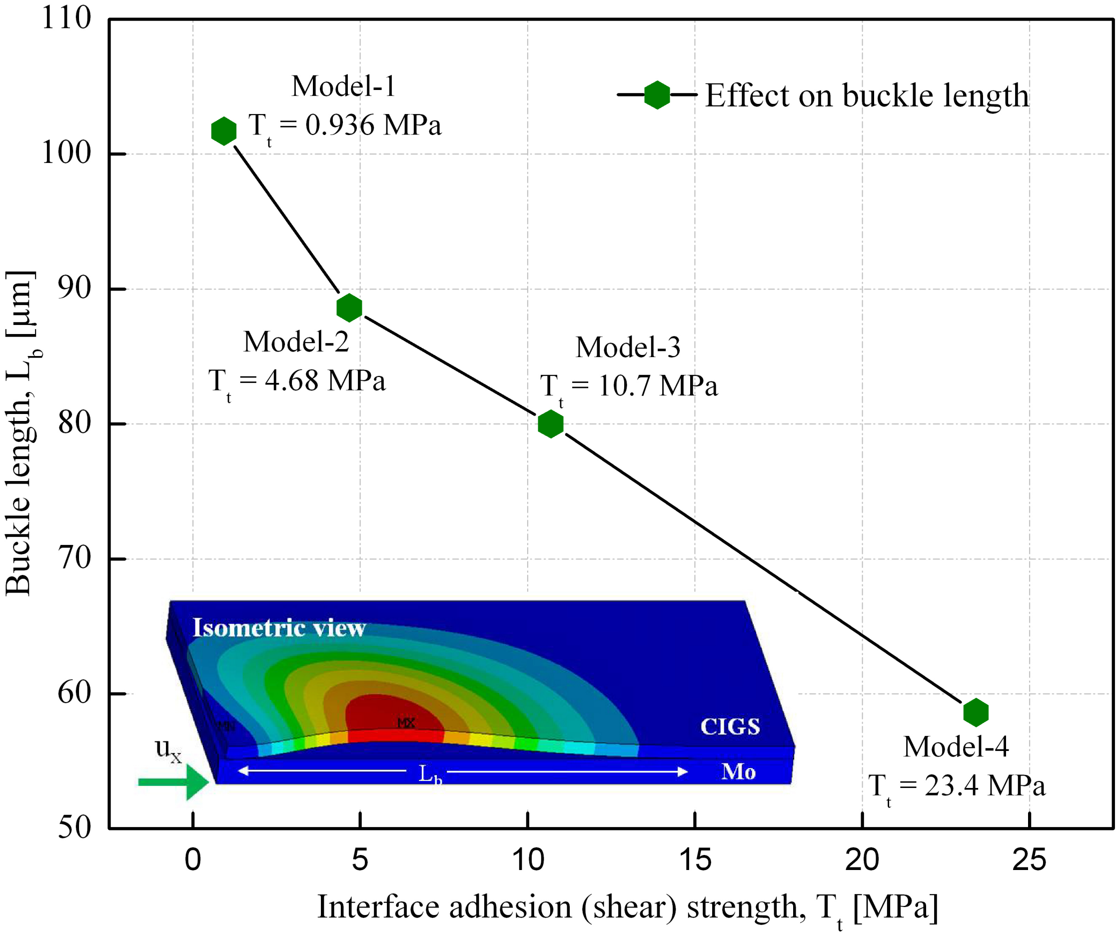

Figure 4.46: *Buckle length (L_b) versus adhesion (shear) strength of the CIGS/Mo interface (T_t) for 3D FE model of buckling and delamination model with cohesive zone interface; description about the four sets of cohesive zone parameters for CIGS/Mo interface is given in Table 3.2.*

5 Proposed mechanism for the mechanical scribing process

This chapter presents the scheme of mechanism for the mechanical scribing process which is being proposed after analyzing the experimental and simulation results described in the previous chapter. Thereafter, the experimental observation of the nearly circular shaped crack at the end of P3 mechanical scribe is explained and discussed schematically at the end of the chapter. In the previous chapter, the results of mechanical scribing experiments performed to produce P2 and P3 structures on the CIGS solar cell specimens were presented. Thereafter, the numerical results of simulation obtained with the half symmetric 2D FE model (top view) and the 3D FE model for buckling and delmaination were described. After the detailed analysis of experimental and simulation results for the mechanical scribing of CIGS thin-film solar cell specimens, a scheme of mechanism for the mechanical scribing process is proposed in this chapter. The scheme of proposed mechanism comprises of three stages. Figure 5.1 shows the scribing force versus time curve for the single chip of the mechanical scribe describing the various stages of the proposed mechanism. This force-time curve represents the typical curve for the single chip in the chipping mode of mechanical scribing process and is taken from the complete force-time plot for the P2 mechanical scribe produced on the CIGS specimen with relatively lower interface shear strength of 4.68 MPa as shown in Figure 4.13. The complete force-time curve for the single chip comprises of the three different stages of the scribing process as illustrated in the figure. The microscopic image of the corresponding chip is also shown in the figure wherein the approximate position of the scribing needle is also marked along the scribe length. Figure 5.2 describes the behavior of CIGS thin-film during the different stages of the proposed mechanism for the mechanical scribing process. The detailed description of these three stages of the scheme of proposed mechanism for the mechanical scribing process is as follows:

Stage 1: Linear increase of scribing force (crack initiation takes place but interface stays intact): The scribing needle presses against the CIGS thin-film in order to perform the mechanical scribe. The pressing of needle generates the high tensile stresses in the thin-film near the contact region between the scribing needle and the thin-film. The presence of these high tensile stresses suggests that the crack most probably starts propagating from very near to the contact region. As soon as the scribing force exceeds the frictional force between the scribing needle and the molybdenum layer, the needle starts moving forward into the thin-film. The scribing force increases continuously and almost linearly till the point **A** is reached which indicates that CIGS/Mo interface stays intact during this stage.

Stage 2: Initiation and subsequent growth of delamination at CIGS/Mo interface: Since molybdenum is relatively stiff as compared to CIGS thin-film, the pre-existed defects at the CIGS/Mo interface will result in initiation of delamination of the film from the substrate. Point **A** represents the most probable initiation of delamination at the interface. With the further increase in scribing force, the out-of-plane displacement of the CIGS film from the molybdenum substrate starts increasing further indicating that the delamination at interface grows and grows further till the onset of buckling at the point **B** as indicated in the figure. So, this stage represents the initiation and the subsequent growth of delamination at the interface.

Stage 3: Buckling driven delamination of CIGS thin-film with the simultaneous crack propagation leading to the flipping away of the chipping: Point **B** represents the onset of buckling of CIGS thin-film. At this point, the out-of-plane displacement of the CIGS film becomes quite significant. The scribing force reaches the maximum value at this point, F_{max}. At the same time, high tensile stresses are generated in the CIGS film due to buckling resulting in the crack propagation through the CIGS film. The buckling driven delamination at the CIGS/Mo interface takes place with the simultaneous crack propagation through the film. The crack continues to propagate through the film thickness, which then finally takes up nearly the circular shape. The chipping is then removed completely and hence flipped away finally. In this way, the subsequent removal of nearly circular shaped chips results in performing the mechanical scribes on the CIGS thin-film solar cell specimens.

The P3 mechanical scribes were investigated at the point where the scribing needle finally stopped after completely the full scribe. A nearly circular shaped crack was observed at the end of P3 mechanical scribe as shown in Figure 4.6. This experimental observation regarding the circular crack is explained schematically in Figure 5.3 (b) on the basis of scheme of the proposed mechanism for the mechanical scribing process. As can be seen in Figure 5.3 (b), when the scribing needle is initially at position **L**, it presses against the CIGS thin-film thereby generating the high tensile stresses near the contact region between the scribing needle and the CIGS layer. The presence of these high tensile stresses indicates that the crack most probably starts propagating from very near of the contact region. Position **M** of the needle in Figure 5.3 (b) is the approximate position of scribing needle as being observed in Figure 5.3 (a). Position **M** of the needle indicates that the stage 3 of the proposed mechanism has been reached. Stage 3 of the proposed mechanism comprises of the buckling driven delamination of the CIGS thin-film from the molybdenum layer with the simultaneous crack propagation through the thin-film resulting in the flipping away of the chipping. So, as the scribing needle travels in forward direction from position **L** to position **M**, buckling driven delamination of CIGS thin-film takes place with the simultaneous crack propagation which most probably starts from very near of the contact region as shown in Figure 5.3 (b). The nearly circular shaped crack is being formed which is then responsible for the CIGS material being removed in the form of nearly circular shaped chips. It has also been already observed that

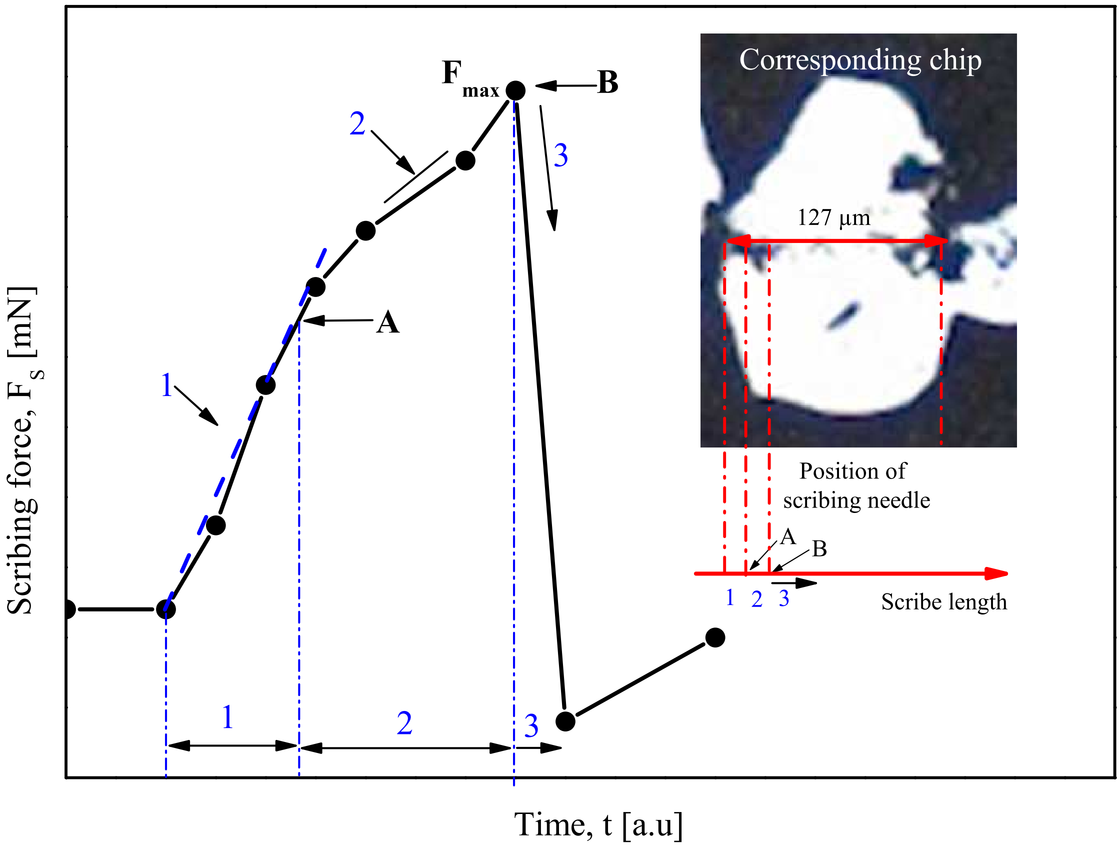

Figure 5.1: *Scribing force versus time curve for the single chip of mechanical scribe describing various stages of the scheme of proposed mechanism for the mechanical scribing process, corresponding chip is also shown where the approximate position of needle is marked along the scribe length; 1 - Linear increase of scribing force(crack initiation takes place but interface stays intact), 2 - Initiation and subsequent growth of delamination at CIGS/Mo interface (Point A represents the initiation of delamination), 3 - Buckling driven delamination with the simultaneous crack propagation leading to the chip being flipped away: (Point B represents the onset of buckling which is characterized by maximum scribing force,* F_{max}*).*

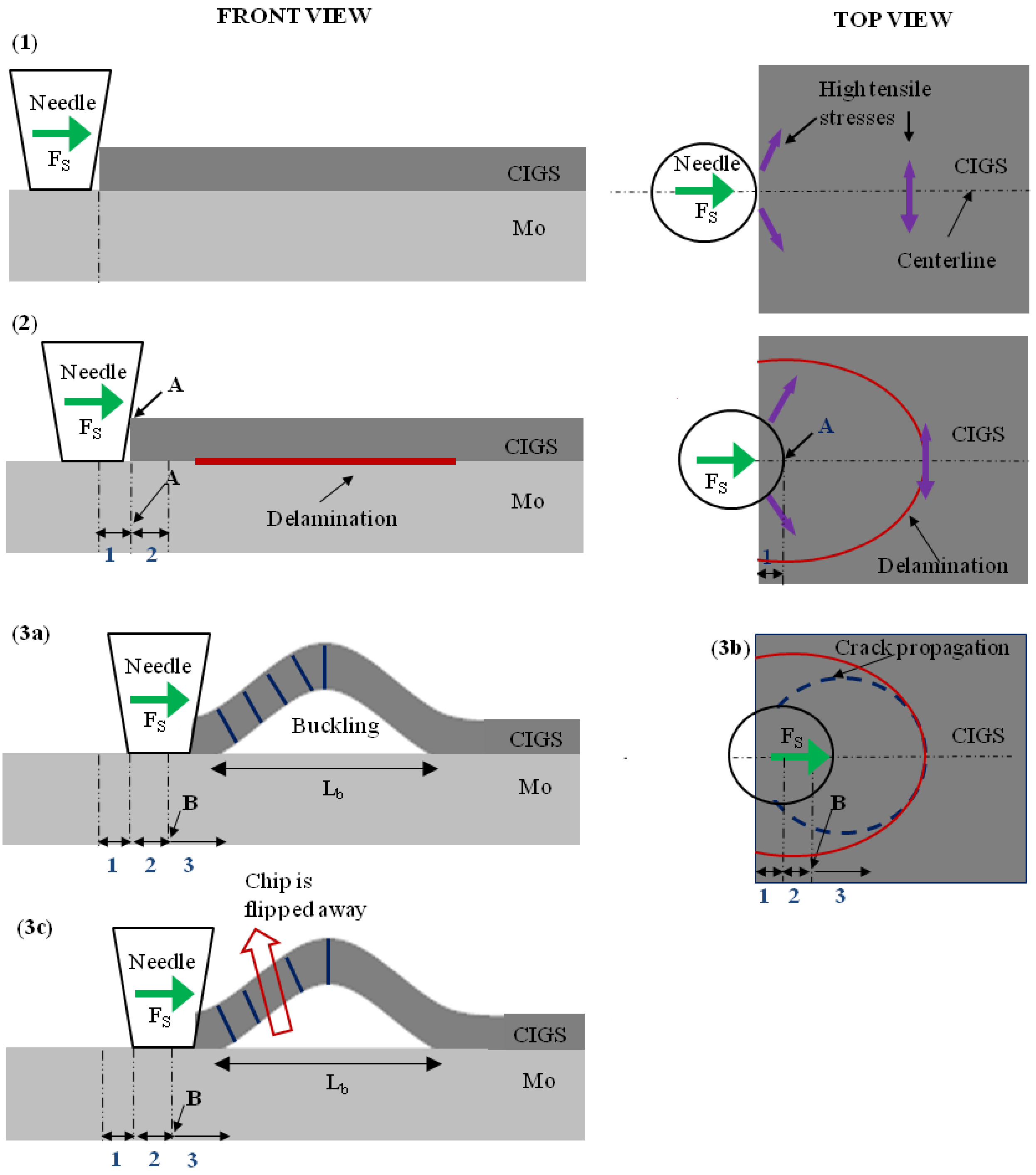

Figure 5.2: Behavior of CIGS thin-film during different stages of the scheme of proposed mechanism for the mechanical scribing process, namely: 1 - Linear increase of scribing force (crack initiation takes place but interface stays intact), 2 - Initiation and subsequent growth of delamination at CIGS/Mo interface (Point A represents the initiation of delamination), 3 - Buckling driven delamination with the simultaneous crack propagation leading to the chip being flipped away: (Point B represents the onset of buckling which is characterized by maximum scribing force, F_{max}), L_b stands for the buckle length.

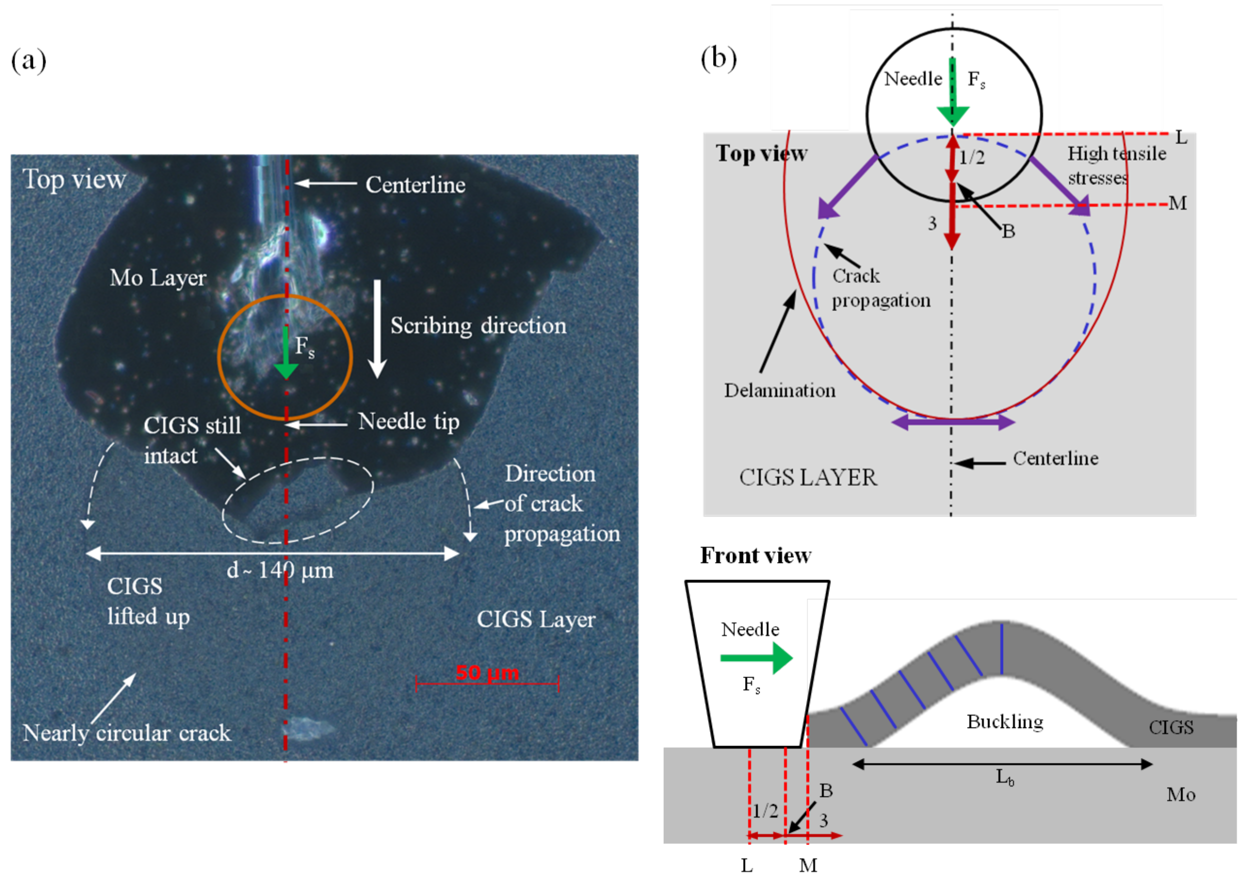

Figure 5.3: *(a) Optical microscope image (top view) of the P3 mechanical scribe revealing the nearly circular shaped crack at the end of scribe, and (b) Schematic explanation of the circular crack on the basis of proposed mechanism for the mechanical scribing process; d,* F_s *and* L_b *stand for diameter of crack, scribing force and buckle length respectively; L represents the initial position of scribing needle; M: approximate position of scribing needle as observed in experiments; 1, 2 and 3 refer to the different stages of proposed mechanism.*

the mechanical scribe normally comprises of the number of the nearly circular shaped chippings as can be seen in Figure 4.5 for P3 structure and Figure 4.17 (a) for P2 structure, where the chipping takes place in a stepwise manner.

6 Discussion

In this chapter, the results obtained from the mechanical scribing experiments and numerical simulations are discussed in detailed. Section 6.1 presents the discussion regarding the difference in the experimentally determined values of frictional force beetween the scribing needle and the Mo layer for the two different types of CIGS specimens with low (4.68 MPa) and relaively higher (10.7 MPa) interface shear strength. Both the P3 and P2 mechanical scribing experiments revealed almost the same piece of information regarding the key features of delamination/chipping of CIGS material and the shape of the chippings. So, for the sake of simplicity and to save the simulation time, the two layer system (CIGS/Mo) as in P2 experiments was considered for the 3D FE simulation and the simulation results were correlated with the findings of P2 mechanical scribing experiments where the CIGS layer was being scribed off from the top of Mo layer with the help of scribing needle. Section 6.2 presents the correlation between the simulation results obtained from the 3D FE model and the experimental findings from P2 mechanical scribing experiments regarding the influence of interface shear strength and needle tip geometry on the scribe form, most probable shape of crack path and the diameter of the crack.

6.1 Frictional force between the scribing needle and Mo layer

For the CIGS specimen with low interface adhesion (shear) strength of 4.68 MPa, the frictional force between scribing needle and the Mo layer was determined to be 18 mN and accordingly the coefficient of friction was calculated to be 0.12. However, for the CIGS specimen with relatively higher interface adhesion (shear) strength of 10.7 MPa, the frictional force was determined to be 10.67 mN and the coefficient of friction was calculated to be 0.07. So, it was revealed that the frictional force varied with the adhesion (shear) strength of the CIGS/Mo interface. Higher value of frictional force was obtained for the specimen with relatively lower interface adhesion (shear) strength. This variation in frictional force is most probably due to the different crystal orientation of the grains in $MoSe_2$ layer and the variation in thickness of $MoSe_2$ layer which is formed at the CIGS and Mo interface. It has been reported in the past that a $MoSe_2$ layer is formed at the CIGS and Mo interface since the BCC structured Mo converts into hexagonal $MoSe_2$ layer while selenization [154–156]. The $MoSe_2$ compound forms due to the diffusion of Se into the CIGS film and the reaction with Mo above 440°C [157]. The *c*-axis of $MoSe_2$ layer is perpendicular to the Mo layer for the selenization temperature of 550 °C and is parallel to the Mo layer for the higher selenization temperature of 580 °C. The orientation of *c*-axis affects the mechanical and electrical properties of the $MoSe_2$. Van-der-Waals bonding is found between the Se-Mo-Se sheaths along the c-axis, whereas perpendicular to the c-axis, parallel to the basal planes of the hexagonal $MoSe_2$ structure, the bonding is of covalent type. Therefore, the adhesion is deteriorated when $MoSe_2$ forms with a c-axis in average perpendicular to the Mo surface. This may lead to delamination between Mo/$MoSe_2$ and CIGS, as it often occurs when mechanical stress is applied on a SLG/Mo/$MoSe_2$/CIGS stack. Also, the increase in substrate temperature increases the diffusion of Se through $MoSe_2$ which in turn results in the increased thickness of $MoSe_2$ layer formed between CIGS and Mo [158]. Thus, the difference in crystal orientation of the $MoSe_2$ grains and the thickness of $MoSe_2$ layer might be responsible for the difference in frictional forces for the two different CIGS specimens.

6.2 Correlation between experimental and simulation results

Experiments were performed to produce the P3 and P2 scribes on the CIGS specimens. P3 scribing experiments involve the removal of two layers namely the CIGS material and the zinc oxide front contact from the top of molybdenum back contact, whereas P2 scribe is relatively simple which involves the removal of only CIGS material from the top of Mo layer. Both the P3 and P2 mechanical scribing experiments revealed almost the same piece of information regarding the key features of delamination/chipping of CIGS material and the shape of the chippings. So, for the sake of simplicity and to save the simulation time, the two layer system (CIGS/Mo) as in P2 scribing experiments (CIGS/Mo/Glass) was considered to construct the 3D FE model of buckling and delamination. Therefore, in this section, the results of P2 mechanical scribing experiments are correlated with the simulation results obtained from the 3D FE model of buckling and delamination. The simulation and experimental results are correlated regarding the influence of interface shear strength and needle tip geometry on the scribe form, most probable shape of crack path and the diamter of the crack. Subsection 6.2.1 presents the comparison between experimental and simulation findings regarding the influence of interface shear strength on the scribe form. The correlation regarding the influence of needle tip geometry on the scribe form is presented in subsection 6.2.2. Finally, the discussion on the most probable shape of the crack path and the dimeter of the crack is done in subsection 6.2.3 and subsection 6.2.4 respectively.

6.2.1 Influence of interface shear strength on the scribe form

The values of adhesion (shear) strength (T_t) of CIGS/Mo interface for two different types of CIGS specimens used for P2 mechanical scribing experiments were determined to be 4.68 MPa and 10.7 MPa approximately. Experimental investigations revealed that the CIGS specimen with relatively higher interface adhesion (shear) strength of 10.7 MPa produces scribes with relatively lower scribe widths (W_s) as compared to that of the specimen with relatively lower adhesion (shear) strength of 4.68 MPa (see Figure 4.18). Likewise, the simulation results obtained from the 3D FE model of buckling and delamination showed that the buckle width (W_b) decreases with the increase in interface adhesion (shear) strength. Figure 6.1 presents the comparison of experimental and simulation results regarding the influence of interface adhesion (shear) strength on the scribe width. It can be seen in Figure 6.1(a) that the P2 mechanical scribe produced on the specimen with relatively lower adhesion (shear) strength of 4.68 MPa revealed the higher value of scribe width of 182 μm and the FE simulations carried out for the CIGS specimen with the same adhesion (shear) strength produced the buckle with the buckle width of 106 μm as a result of buckling of CIGS thin-film. Similarly, Figure 6.1(b) shows that the P2 mechanical scribe produced on the CIGS specimen with relatively higher interface adhesion (shear) strength of 10.7 MPa exhibits relatively lower value of scribe width of 125 μm and correspondingly the FEA results revealed the lower value of buckle width of 92 μm. This can be explained as, that, if the interface adhesion (shear) strength is less, the buckling of thin-film initiates at the lower value of scribing force (see Figure 4.44) and as a result, a buckle with relatively higher buckle width is generated at the same value of scribing force as seen in FE simulation which in turn is responsible for the bigger sized crack and thereby the higher value of scribe width as observed in experiments. Similarly, if the interface adhesion (shear) strength is more, the buckling of thin-film initiates at the relatively higher value of the scribing force (see Figure 4.44) and as a result, a buckle with relatively lower buckle width is produced at the same value of scribing force which in turn is responsible for the relatively smaller sized crack and hence the lower value of scribe width as observed in experiments. Hence, the simulation results regarding the buckle width fit well quantitatively with the experimental findings regarding the scribe width. However, the difference in experimental and simulation values is most probabaly due to the fact that in the present 3D FE model, the initial crack is not assumed to be present and therefore the crack propagation is not considered. Also, the real values of cohesive zone parameters for the interface other than the shear strength are not used and are rather suitably assumed. Considering the crack propagation and the complete knowledge about all the cohesive zone parameters of CIGS/Mo interface may result in even better correlation between the experimenatal and simulation values.

6.2.2 Influence of needle tip geometry on the scribe form

The experimental investigations revealed that the P2 mechanical scribes obtained with flat tip needle comprises of near to circular shaped chips of considerable size (see Figure 4.18). Chipping seems to happen in a stepwise manner, one after the other. So, the dominant scribing mode is chipping while scribing with a flat tip needle. However, scribing with the slightly rounded tip needle reduced the chipping significantly for both the CIGS specimens with low and relatively higher adhesion (shear) strength of CIGS/Mo interface. So, the dominant scribing mode is grinding while scribing with the slightly rounded tip needle (see Figure 4.19). Likewise, the simulation results from the 3D FE model of buckling and delamination indicated that the tensile stresses are generated in the bottom surface of CIGS layer while scribing with flat tip needle. These tensile stresses are most probably responsible for the chipping mode of scribing. Figure 6.2 presents the comparison of experimental and simulation results regarding the influence of needle tip geometry

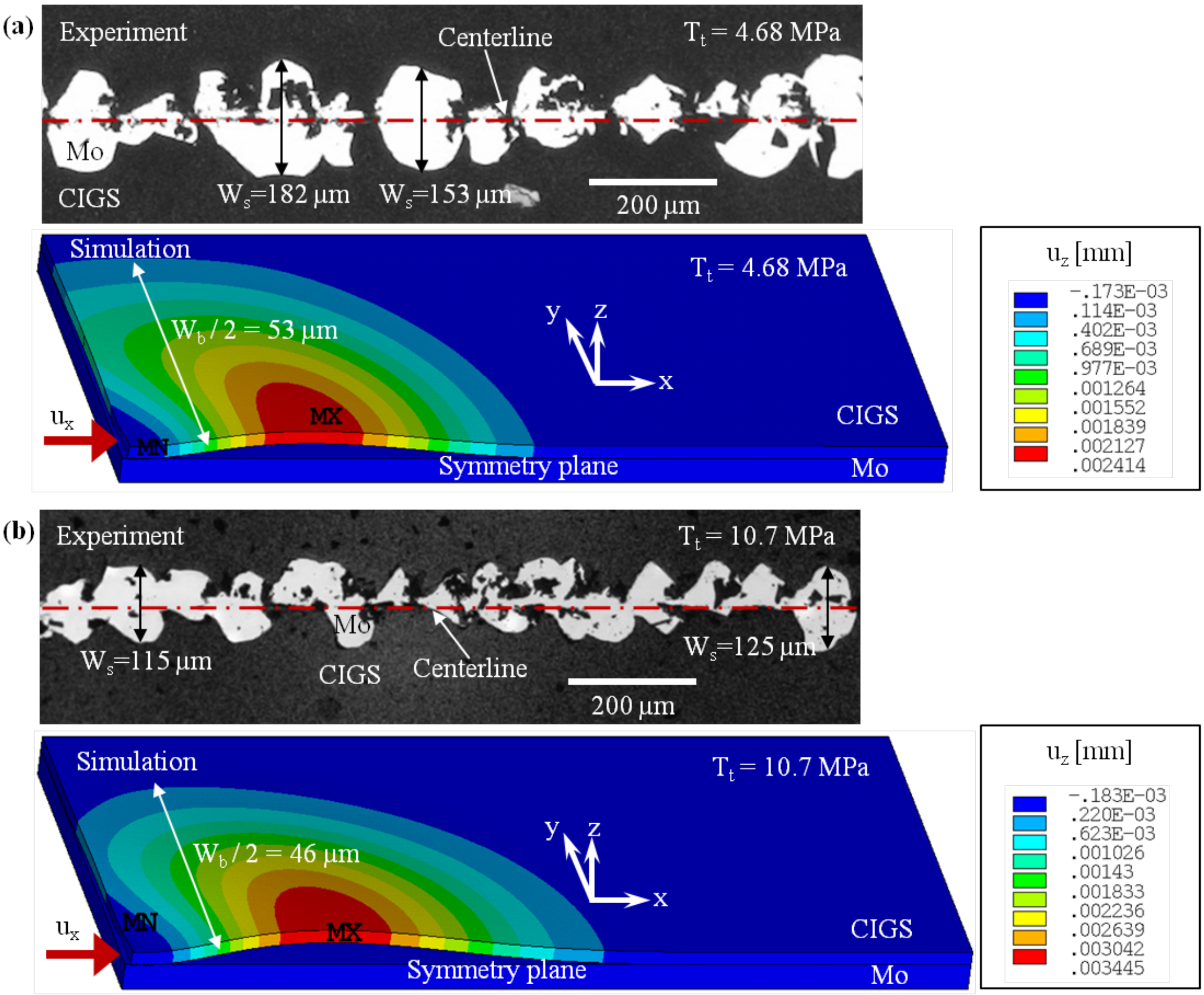

Figure 6.1: *Comparison of experimental and simulation results regarding the influence of interface shear strength on the scribe form (a) P2 mechanical scribe produced on specimen with interface shear strength of 4.68 MPa and comparison with the simulation results in terms of buckle width, and (b) P2 mechanical scribe produced on specimen with interface shear strength of 10.7 MPa and comparison with simulation results in terms of buckle width; T_t, W_s, W_b and u_z stand for interface adhesion (shear) strength, scribe width, buckle width and out-of-plane displacement respectively.*

on the scribe form. In the case of flat tip scribing needle, the included angle between needle and the top surface of CIGS layer is relatively higher than in the case of slightly rounded tip needle and is measured to be $\alpha = 72^0$. So, the resultant force (F_{res}) is acting less into the CIGS film but rather more in the forward direction as shown in the figure. This resulted in tensile stresses in the bottom surface of CIGS layer obtained as result of numerical simulation of the 3D FE model for buckling and delamination (see Figure 4.32). The presence of tensile stresses in the bottom surface of layer help the crack (if, present already) to propagate. Additionally, the buckling driven delamination at the CIGS/Mo interface in front of the scribing needle help the crack to propagate further and most probably the crack finally takes up nearly the circular shape. So, the CIGS material is removed in the form of subsequent chips leading to the chipping mode of scribing. However, in the case of slightly rounded tip needle, the diameter of curved part of the needle which comes in to contact with the CIGS film was measured to be 32 μm. Then, keeping in to mind that the thickness of CIGS film is 2 μm, the included angle between needle and film is determined to be $\alpha = 29^0$ which is less as compared to that in the case of flat tip needle. Due to relatively lower value of the included angle, the resultant force is acting more into the thin-film rather than in the forward direction as can be seen in the Figure 6.2. As a result, compressive stresses are most probably generated in the bottom surface of CIGS layer. The presence of compressive stresses in the bottom surface of layer does not allow the crack (if, present already) to propagate further. It results in crushing of the CIGS film and produces the very small pieces of the film material. This leads to grinding mode of scribing and hence near to ideal scribes are performed. Hence, the simualtion results fit well with the experimental findings regarding the influence of needle tip geometry on the scribe form.

6.2.3 Shape of crack path

Figure 6.3 (a) presents the optical microscope image of the P2 mechanical scribe performed by the flat tip scribing needle showing that the scribe comprises of the nearly circular shaped chippings. This experimental observation regarding the shape of crack path is validated by the finite element simulation using the 3D FE model of buckling and delamination. Figure 6.3 (b) describes the schematic explanation for the most likely path of crack propagation in the CIGS thin-film after the specimen is being loaded on the basis of distribution and direction of first principal stresses (σ_1) in the CIGS film revealed by the finite element simulations. The distribution and direction of first principal stresses in the contact, bottom and top surface of CIGS thin-film was obtained as a result of finite element simulation of the 3D FE model for buckling and delamination. The most probable crack path obtained on the basis of the distribution and direction of first principal stresses in the contact surface of CIGS thin-film indicates that the crack will most likely propagate in the positive y-direction parallel to the surface as can be seen in Figure 4.39. However, this is not the crack which may be responsible for the generation of nearly circular shaped chippings of the CIGS material. The solid dark blue color curve in Figure 6.3 (b) represents the most probable path of crack propagation on the basis of distribution and direction of first principal stresses in the bottom surface of CIGS layer as shown in Figure 4.41. Similarly, the solid red color curve

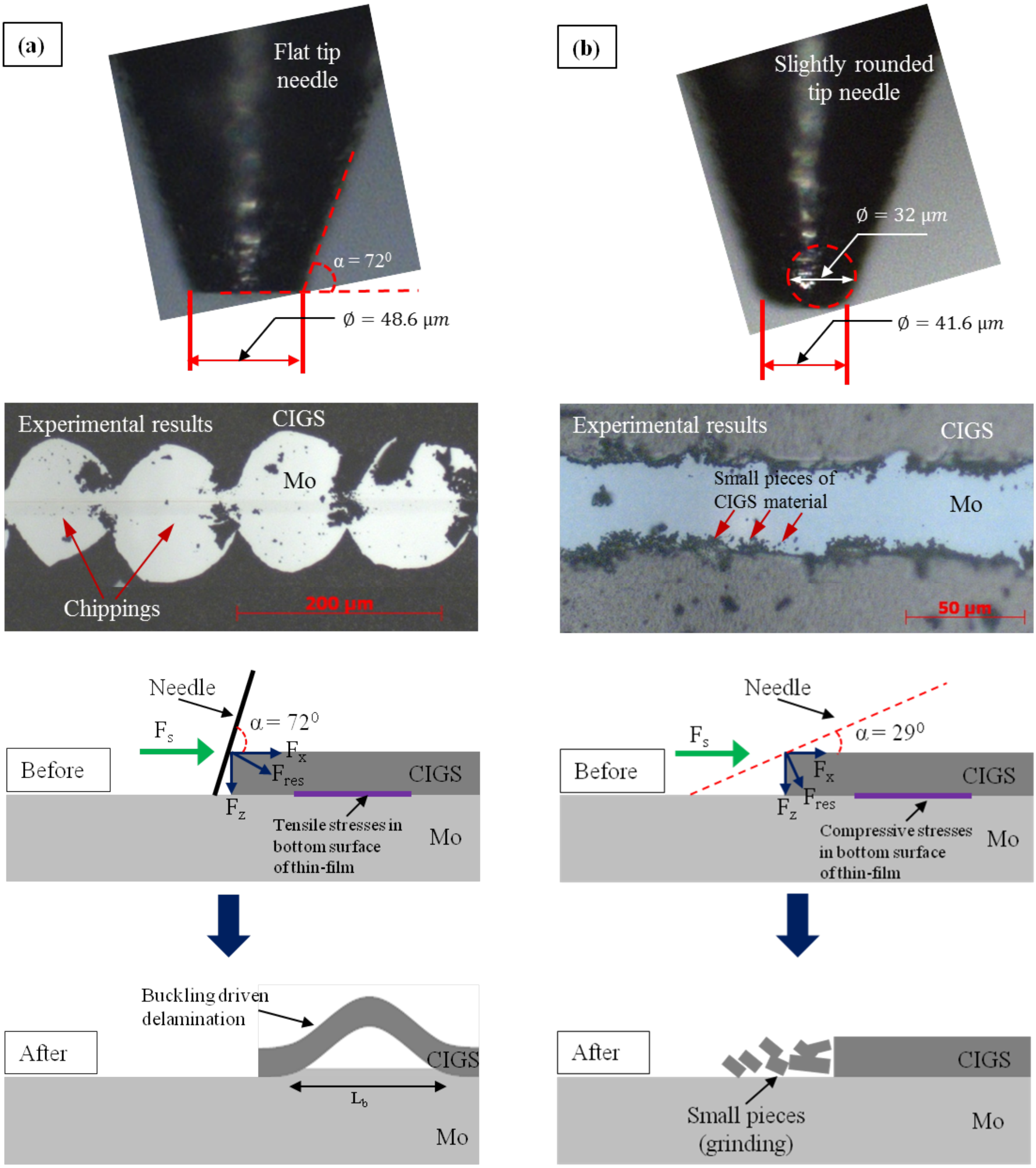

Figure 6.2: *Comparison of experimental and simulation results regarding the influence of needle tip geometry on the scribe form (a) flat tip scribing needle: chipping mode of scribing, and (b) slightly rounded tip scribing needle: grinding mode of scribing; schematic explanation is given on the basis of simulation results obtained with the flat tip needle;* F_s, F_{res}, α, ϕ *and* L_b *stand for the scribing force, resultant scribing force, included angle between needle and CIGS thin-film, diameter of needle tip and buckle length respectively; green arrow gives the direction of scribing force.*

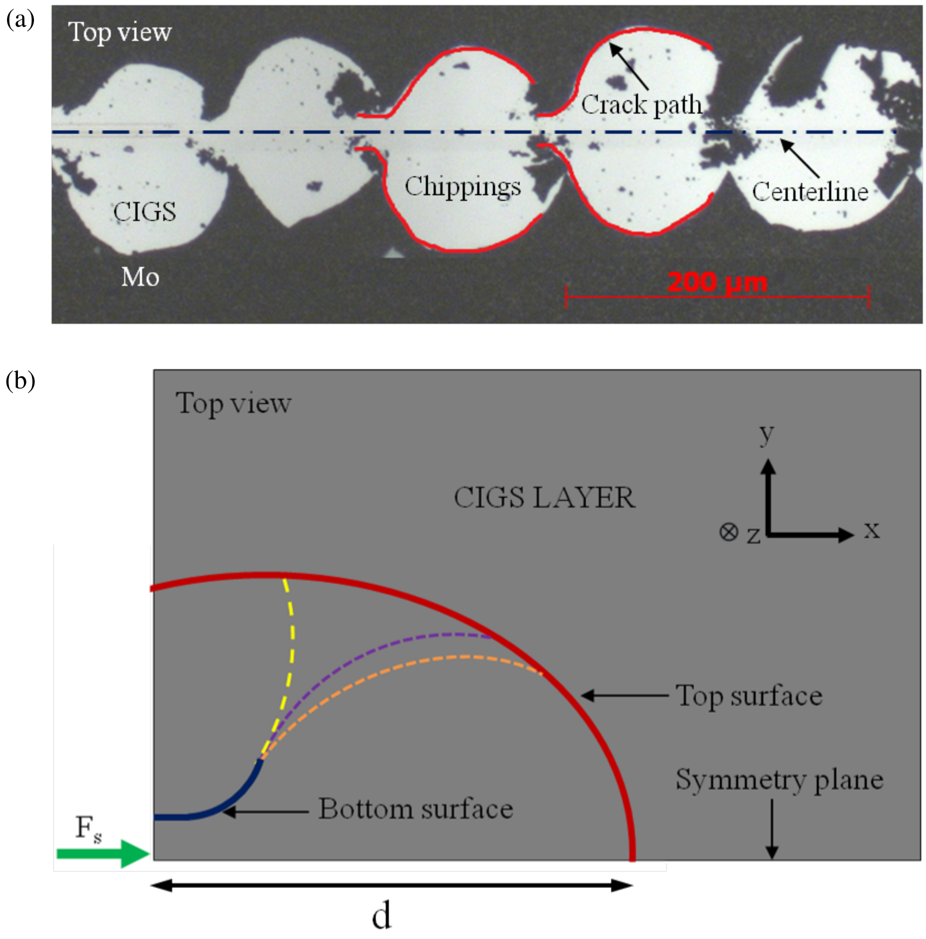

Figure 6.3: *Comparison of experimental and simulation results regarding the shape of crack path (a) P2 structure performed by mechanical scribing showing the nearly circular shaped crack path, (b) Schematic explanation for the most likely path of crack propagation on the basis of distribution and direction of first principal stress in top and bottom surfaces of CIGS thin-film; d: diameter of nearly circular shaped crack; green arrow shows the direction of scribing force,* F_s.

represents the most probable path of crack propagation on the basis of distribution and direction of first principal stresses in the top surface of CIGS layer as shown in Figure 4.40. However, finite element simulations do not provide the information about the crack path for some region. For this region, the three different most likely crack paths are sketched by the thin dotted lines of yellow, purple and orange color as can be seen in the Figure 6.3 (b). As per the experimental observations, it can be concluded that the crack will most likely propagate along the path sketched in purple color in this region so that the final crack looks like having the nearly circular shape as depicted in the Figure 6.3 (a). Therefore, the crack originating from very near of the contact region between the scribing needle and the CIGS layer (solid dark blue color curve) may propagate further along the thin dotted purple curve and finally join the crack path indicated by the solid red color curve. Thereby, the crack path most likely takes up nearly the circular shape finally. This outcome from the finite element simulations fits well with the experimental observation of the nearly circular circular shaped crack as seen in Figure 6.3 (a). Hence, the mechanical scribing takes place with the CIGS thin-film material being chipped away in the form of nearly circular shaped chips.

6.2.4 Diameter of the crack

Figure 6.4 (a) presents the optical microscope image of the P2 mechanical scribe performed by the flat tip scribing needle revealing the crack diameter of 115 μm. Figure 6.4 (b) presents the position of maximum tensile stresses in the top surface of CIGS thin-film for the different values of needle displacement regarding the 3D FE model for buckling and delamination (see Figure 3.9). Here the adhesion (shear) strength of CIGS/Mo interface is 0 MPa. The farthest position of maximum tensile stress is obtained to be 33.83 μm along the positive x-direction for the needle displacement of 1.09 μm. This position of maximum tensile stress represents the diameter of the nearly circular shaped crack as indicated in the Figure 6.3. So, the finite element simulations revealed the diameter of the nearly circular shaped crack to be 33.83 μm which is less than that obtained in the experimental investigations which was nearly 115 μm in one of the mechanical scribes (see Figure 6.4 (a)). This difference in experimental and simulation value is most probabaly due to the fact that in the present FE model, the initial crack is not assumed to be present and therefore the crack propagation is not considered. Also, the real values of cohesive zone parameters for the interface are not used and are rather suitably assumed. However, assuming the initial crack for the numerical simulation may result in the reduced stiffness of the CIGS thin-film because of which the position of maximum tensile stress may move further from 33.83 μm. Also, the complete information about all the cohesive zone parameters of CIGS/Mo interface may result in different results regarding the farthest position of maximum tensile stress. Nevertheless, the simulation results are able to explain the experimental investigations for the mechanical scribing process regarding the diameter of the nearly circular shaped crack.

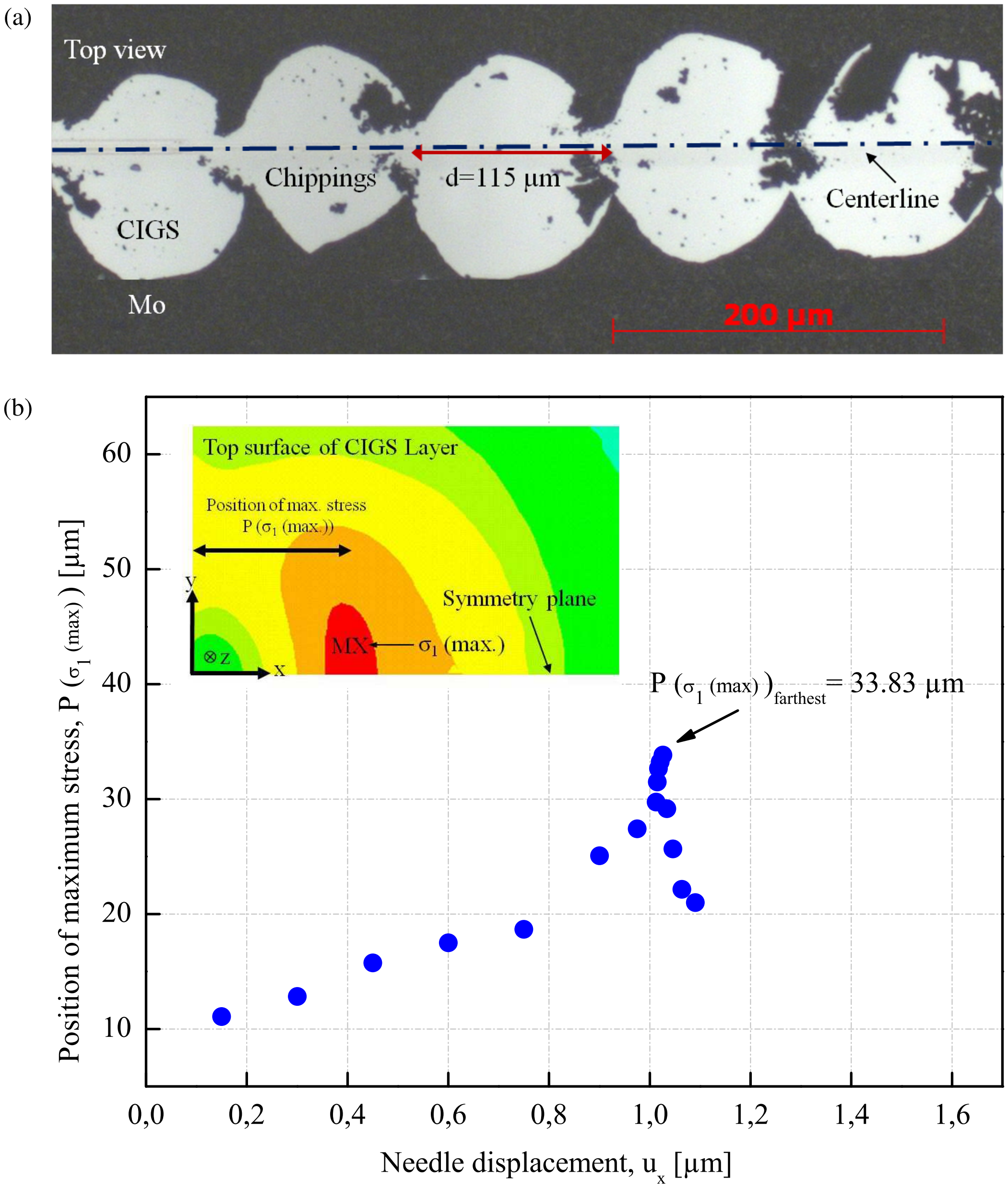

Figure 6.4: *Comparison of experimental and simulation results regarding the diameter of crack (a) P2 structure performed by mechanical scribing showing the revealing the crack diameter of 115 µm, and (b) Position of maximum tensile stresses in the top surface of CIGS thin-film along the positive x-direction obtained from the 3D model of buckling and delamination plotted against the needle displacement; the farthest position of maximum tensile stress represents the diameter of nearly circular shaped crack; adhesion (shear) strength of CIGS/Mo interface is zero.*

7 Summary and outlook

For photovoltaic modules based on CIGS, a mechanical tip is most commonly used in order to scribe back-to-front contact interconnecting pattern (P2) and front contact isolation pattern (P3). However, the non-deterministic nature of the material removal mechanism in mechanical scribing yields wide, irregular scribe lines resulting in chipping and random lift-offs that necessitate large spacing between adjacent scribes. The increased non-productive area called as dead area thereby results in the loss of active solar cell area. As a result, the CIGS modules suffer decreased efficiency. The narrower the scribes and the closer they are spaced together, more efficient is the solar module, as the solar module efficiency is based on the active solar cell area available for power generation. Therefore, the mechanism of material removal during the mechanical scribing process needs to be analyzed and understood.

In this work, nanoindentation experiments were carried out to determine the Young's modulus of CIGS thin-film. The mechanical scribing of CIGS thin-film solar cells is investigated by experiments and numerical models. Mechanical scribing experiments for P3 structure were performed with the help of flat tip tungsten needle with tip diameter of 48.6 μm. However, P2 mechanical scribing experiments were carried out with the help of flat tip and slightly rounded tip tungsten needles with tip diameters of 48.6 μm and 41.6 μm respectively on the CIGS thin-film solar cell specimens with low and relatively higher adhesion strength of CIGS/Mo interface. Numerical Simulations were performed with the use of ANSYS simulation software to simulate the mechanical scribing process. Half-symmetric 2D finite element model (top view) was constructed to analyze the most possible crack initiation during the mechanical scribing, however, 3D FE model was used to investigate the buckling and delamination of CIGS thin-film during the scribing pricess. In order to study the influence of interface shear strength on the scribe form, the interface was modeled using the cohesive zone layer concept, where, a damage criterion based on mixed mode failure was defined for the interface. The experimentally determined values for the interface shear strength of the two types of CIGS specimens were used to define the shear strength of the CIGS/Mo interface in the 3D FE model. Other interface parameters were suitably assumed in order to completely define the cohesive interface. Both the P3 and P2 mechanical scribing experiments revealed almost the same piece of information regarding the key features of delamination/chipping of CIGS material and the shape of the chippings. So, for the sake of simplicity and to save the simulation time, the two layer system (CIGS/Mo) as in P2 experiments was considered for the 3D FE simulation and the simulation results were correlated with the findings of P2 mechanical scribing experiments where the CIGS layer was being scribed off from the top of Mo layer with the help of scribing needle.

The mean value of Young's modulus of the CIGS thin-film was determined to be 78.22 GPa with the help of nanoindentation experiments in the present work. This value of Young's modulus is in close agreement with the previous reported results. From the experimental investigations and the numerical simulations for mechanical scribing, it could be concluded that both the P2 and P3 mechanical scribes were broadened because of chipping. The scribing parameters such as force normal to the specimen and scribing speed do not influence the scribe characteristics such as scribe width and line width for both P2 and P3 structures performed by the mechanical scribing, however the higher value of the scribing speed caused the chips of CIGS material to move out of the scribe area. Due to the limitation of the present experimental setup, it was only possible to perform the scribes with the speed not more than 200 mm/s. However, in the industrial mechanical scribing process, the speed is kept at around 1.5 m/s. So, it is quite possible that performing the scribes with speeds higher than 200 mm/s may reveal some influence of scribing speed on the scribe form. It was concluded from the experiments that there is no correlation between the maximum scribing force and the chip area of the different chippings produced in the mechanical scribe. Some of the scribes were non-homogeneous at the upper side and were quite homogeneous at the lower side of the scribe. The probable reason being the geometry of the scribing needle and the tip surface of the needle may not be completely parallel to the specimen surface.

While observing the end of mechanical scribes performed in the experiments, it was seen that the crack was more prominent near the contact region between the scribing needle and the CIGS layer and then faded away as it moved away from the contact region which indicated that the crack most probably starts propagating from very near of the contact region. The simulation results agree well with this experimental observation. The simulation results of half-symmetric 2D FE model (top view) without assuming the initial crack showed the high tensile stresses near the contact region between scribing needle and the CIGS layer. Numerical simulations performed for the half-symmetric 2D FE model (top view) with vertical initial crack revealed the continuous increase in the value of mode-I stress intensity factor while moving towards the contact region between the scribing needle and the CIGS layer. Finally, 3D FE model for buckling and delamination predicted the high tensile stresses in the bottom surface of CIGS thin-film. The presence of high tensile stresses near the contact region and the continuous increase in the value of K_I while moving towards the contact region indicated that the crack most probably starts propagating from very near of the contact region between the scribing needle and the CIGS layer. So, the FE simulations produce the results regarding the most possible crack initiation which fit quite well with the experimental observation.

Experimental scribing force versus time curves were obtained for the P2 mechanical scribes produced on both the CIGS specimens with low and relatively higher adhesion strength of CIGS/Mo interface. Similarly, scribing force versus needle displacement curve was obtained from the numerical simulations using the 3D FE model for buckling and delamination. Experiments revealed the interface shear strength values of 4.68 MPa and 10.7 MPa for the two types of CIGS specimens. The maximum scribing force at which the buckling starts for the CIGS specimen with lower interface shear strength of 4.68 MPa is determined to be 52.6 mN from the FE simulations which fits well with the experimental value of 45.46 ± 10.07 mN. Likewise, for the CIGS specimen with relatively higher interface shear strength of 10.7 MPa, the FE simulations revealed the maximum scrbing force value to be 54.2 mN which also fits well the experimental value of 53.54 ± 5.85 mN. Both the experimental and simulation investigations show that the maximum scribing force increases with the increase in adhesion (shear) strength of the CIGS/Mo interface. However, more sophisticated implementation of interface behavior is required concerning the cohesive zone parameters which describe the interface in FE simulation in order to have even better correlation between the simulation and experimental results. Nevertheless, the simulation results fit quite well with the experimental findings and these results can be used for the optimization of the mechanical scribing process and the design of scribing setups.

For the CIGS specimen with low interface shear strength of 4.68 MPa, the frictional force between scribing needle and the Mo layer was determined to be 18 mN and accordingly the coefficient of friction was calculated to be 0.12. However, for the CIGS specimen with relatively higher interface shear strength of 10.7 MPa, the frictional force was determined to be 10.67 mN and the coefficient of friction was calculated to be 0.07. So, it was revealed that the frictional force varied with the adhesion (shear) strength of the CIGS/Mo interface. Higher value of frictional force was obtained for the specimen with relatively lower interface shear strength. This variation in frictional force is most probably due to the different crystal orientation of the grains in $MoSe_2$ layer and the variation in thickness of $MoSe_2$ layer which is formed at the CIGS and Mo interface.

The simulation results regarding the shape of crack path fit well with the experimental findinds. Experiments revealed the the crack takes up almost the circular shape and the mechanical scribing is a result of subsequent circular cracks seen as a wavy scribe topology. The distribution and direction of first principal stresses in the top and bottom surface of CIGS thin-film indicated that the crack most probably follows nearly the circular path which may be responsible for the generation of nearly circular shaped chippings. The maximum diameter of nearly circular path traced by the propagating crack was determined to be 33.83 μm from the simulation of 3D FE model on the basis of farthest position of the occurrence of maximum tensile stresses in the top surface of CIGS layer, whereas, the experiments revealed the diameter of crack to be equal to 115 μm nearly. However, with the inclusion of propagating crack and with the better knowledge of all the cohesive zone parameters required to describe the cohesive zone interface behavior in FE simulations, there is a strong possibility for this value of diameter to increase further most probably due to the reduced stiffness of the CIGS layer and therfore getting more and more closer to the experimental value. So, the simulation results are able to explain the experimental findings regarding the diameter of nearly circular shaped crack.

The specimen with relatively higher interface shear strength of 10.7 MPa produced chippings with relatively lower scribe width values as compared to the specimen with lower interface shear strength. This experimental observation fits well with the FEA results on the basis of buckle width of the buckle produced as a result of buckling of CIGS thin-film. Lower the adhesion (shear) strength of CIGS/Mo interface, higher is the buckle width in the FE simulations which correlates to the higher scribe width of the chippings produced in the experiments. Similarly, higher adhesion (shear) strength results in relatively smaller buckle width which correlates to the lower scribe width of the chippings.

The simualtion results agree well with the experimental findings regarding the influence of needle tip geometry on the scribe form. Simulations performed with the flat tip needle predicted the presence of high tensile stresses in the bottom and top surface of CIGS layer. Additionally, the buckling driven delamination at the CIGS/Mo interface in front of the scribing needle help the crack to propagate further and the crack finally takes up the nearly circular shape which most probably leads to the chipping mode of scribing as observed in the scribing experiments. Performing simulation with slightly rounded tip needle will most probably result in compressive stresses in the bottom surface of CIGS layer due to the resultant scribing force acting more into the layer rather than in the forward direction leading to crushing of the thin-film and hence resulting in the grinding mode of scribing as observed in the scribing experiments. Scribing the specimen having relatively higher interface shear strength of 10.7 MPa with the slightly rounded tip needle produced the near to ideal scribes with the line width of as low as 51 μm in the present work. So, it was revelaed that in order to produce the near to ideal scribes, the mechanical scribing should be performed with the slightly rounded tip needle on the spicimen with the higher adhesion (shear) strength of th CIGS/Mo interface.

In the present work, it was revealed that the scribing speed has no influence on the scribe form, however, scribing at the higher speeds caused the chips to move out the scribe area. Due to the limitation of the present experimental setup used for the mechanical scribing experiments, it was not possible to perform the scribes with a speed of more than 200 mm/s. However, industrial mechanical scribing is generally performed at the speed of nearly 1.5 m/s. So, it is quite possible that performing the scribes with speeds higher than 200 mm/s and nearly equal to 1.5 m/s may reveal some influence of scribing speed on the scribe form. Therefore in the future work, the experimental setup may be modified in such a way that the scribing experiments may be performed at the speeds of around 1.5 m/s as in industrial applications, in order to produce the scribes more similar to as in commercial production processes. In this way, the influence of scribing speed on the scribe form can also be studied. In the present work, the shear strength of the CIGS/Mo interface was determined and the was used as a cohesive zone parameter to model the interface behavior in the 3D FE model of buckling and delamination. However, the buckling of CIGS thin-film is a mixed-mode failure process, therefore, both the normal and shear strength values of the CIGS/Mo interface are required to model completely and accurately, the cohesive zone interface behavior in the FE model. So, the experiments such as peel test and pull test may be performed in the future work to determine the normal strength of the CIGS/Mo interface. The interface normal strength value thus obtained may be then used to model the cohesive zone interface behavior. There is a strong possibility of better correlation between the simulation and experimental results, if we can obtain the more and better information regarding the cohesive zone interface parameters with the help of experiments. In the present work, the static simulations were performed with the help of scribing needle and the real time crack propagation was not considered. So, in the future work, the dynamic simulations may be performed with the moving scribing needle and also, the real time crack propagation through the CIGS thin-film may also be incorporated in the present 3D FE model. In this way, the modified finite element model may yield the better simulation results which may correlate better to the expermental findings. Furthermore, the finite element simulations may also be performed with the help of slightly rounded tip scribing needle which may yield the interesting results, since the mechanical scribing experiments performed with the slightly rounded tip needle produced almost the near to ideal scribes in the present work.

Bibliography

[1] D. Chapin, C. Fuller, and G. Pearson, "Solar energy converting apparatus," 1957. US Patent 2,780,765.

[2] P. Jackson, D. Hariskos, R. Wuerz, O. Kiowski, A. Bauer, T. M. Friedlmeier, and M. Powalla, "Properties of $\mathrm{Cu(In,Ga)Se_2}$ solar cells with new record efficiencies up to 21.7%," *Physica Status Solidi (RRL)-Rapid Research Letters*, vol. 9, no. 1, pp. 28–31, 2015.

[3] M. A. Green, *Solar cells: operating principles, technology, and system applications*. Prentice-Hall Inc., Englewood Cliffs, NJ, Jan. 1982.

[4] T. Tinoco, A. Polian, D. Gomez, and J. Itie, "Structural studies of $\mathrm{CuInS_2}$ and $\mathrm{CuInSe_2}$ under high pressure," *Physica Status Solidi (b)*, vol. 198, no. 1, pp. 433–438, 1996.

[5] A. D. Compaan, I. Matulionis and S. Nakade, "Laser scribing of polycrystalline thin films," *Optics and Lasers in Engineering*, vol. 34, no. 1, pp. 15–45, 2000.

[6] L. Eldada, B. Sang, M. Taylor, P. Hersh, and B. J. Stanbery, "Rapid reactive transfer printing of CIGS photovoltaics," in *SPIE Solar Energy + Technology*, pp. 74090N–74090N, International Society for Optics and Photonics, 2009.

[7] A. D. Compaan, I. Matulionis, M. J. Miller and U. N. Jayamaha, "Optimization of laser scribing for thin-film photovoltaics," in *Photovoltaic Specialists Conference, Conference Record of the Twenty Fifth IEEE*, pp. 769–772, May 1996.

[8] I. Matulionis, S. Nakade, and A. D. Compaan, "Wavelength and pulse duration effects in laser scribing of thin films," in *Photovoltaic Specialists Conference, Conference Record of the Twenty-Sixth IEEE*, pp. 491–494, Sep. 1997.

[9] A. R. Jha, *Solar cell technology and applications*. CRC press, 2009.

[10] P.-O. Westin, U. Zimmermann, and M. Edoff, "Laser patterning of P2 interconnect via in thin-film CIGS PV modules," *Solar Energy Materials and Solar Cells*, vol. 92, no. 10, pp. 1230–1235, 2008.

[11] P.-O. Westin, U. Zimmermann, M. Ruth, and M. Edoff, "Next generation interconnective laser patterning of CIGS thin film modules," *Solar Energy Materials and Solar Cells*, vol. 95, no. 4, pp. 1062 – 1068, 2011.

[12] G. Eberhardt, H. Banse, U. Wagner, and T. Peschel, "Structuring of thin film solar cells," 2010.

[13] B. Burger, K. Kiefer, C. Kost, S. Nold, S. Philipps, R. Preu, R. Schindler, T. Schlegl, G. Stryl-Hipp, G. Willeke, *et al.*, "Photovoltaics report," pp. 1–42, 2014.

[14] F. Andorka, *CIGS Solar Cells, Simplified.* 2014.

[15] T. Tinoco, C. Rincón, M. Quintero, and G. Pérez, "Phase Diagram and Optical Energy Gaps for $\mathrm{CuIn_yGa_{1-y}Se_2}$ Alloys," *Physica Status Solidi Applied Research*, vol. 124, pp. 427–434, 1991.

[16] B. J. Stanbery, "Copper Indium Selenides and Related Materials for Photovoltaic Devices," *Critical Reviews in Solid State & Materials Sciences*, vol. 27, pp. 73–117, Apr. 2002.

[17] J. Hedstrom, H. Ohlsen, M. Bodegard, A. Kylner, L. Stolt, D. Hariskos, M. Ruckh, and H. Schock, "$\mathrm{ZnO/CdS/Cu(In,Ga)Se_2}$ thin-film solar cells with improved performance," in *Photovoltaic Specialists Conference, Conference Record of the Twenty Third IEEE*, pp. 364–371, May 1993.

[18] L. Kronik, D. Cahen, and H. W. Schock, "Effects of sodium on polycrystalline $\mathrm{Cu(In,Ga)Se_2}$ and its solar cell performance," *Advanced Materials*, vol. 10, no. 1, pp. 31–36, 1998.

[19] J. H. Scofield, A. Duda, D. Albin, B. Ballard, and P. Predecki, "Sputtered molybdenum bilayer back contact for copper indium diselenide-based polycrystalline thin-film solar cells," *Thin Solid Films*, vol. 260, no. 1, pp. 26 – 31, 1995.

[20] T. Wada, N. Kohara, S. Nishiwaki, and T. Negami, "Characterization of the $\mathrm{Cu(In,Ga)Se_2/Mo}$ interface in CIGS solar cells," *Thin Solid Films*, vol. 387, no. 1, pp. 118–122, 2001.

[21] V. K. Kapur, A. Bansal, P. Le, and O. I. Asensio, "Non-vacuum processing of $\mathrm{CuIn_{1-x}Ga_xSe_2}$ solar cells on rigid and flexible substrates using nanoparticle precursor inks," *Thin solid films*, vol. 431, pp. 53–57, 2003.

[22] J. R. Tuttle, T. Berens, J. Keane, K. Ramanathan, J. Granata, R. Bhattacharya, H. Wiesner, M. Contreras, and R. Noufi, "Investigations into alternative substrate, absorber and buffer layer processing for $\mathrm{Cu(In,Ga)Se_2}$ based solar cells," in *Photovoltaic Specialists Conference, Conference Record of the Twenty Fifth IEEE*, pp. 797–800, 1996.

[23] J. J. M. Binsma and H. A. van der Linden, "Preparation of thin $\mathrm{CuInS_2}$ films via a two-stage process," *Thin Solid Films*, vol. 97, no. 3, pp. 237–243, 1982.

[24] M. Powalla and B. Dimmler, "Scaling up issues of CIGS solar cells," *Thin Solid Films*, vol. 361 - 362, pp. 540–546, 2000.

[25] C. P. Bjorkman, T. Torndahl, D. Abou-Ras, J. Malmstrom, J. Kessler and L. Stolt, "Zn(O,S) buffer layers by atomic layer deposition in $\mathrm{Cu(In,Ga)Se_2}$ based thin-film solar cells: band alignment and sulfur gradient," *Journal of Applied Physics*, vol. 100, no. 4, p. 4506, 2006.

[26] T. Toerndahl, C. Platzer-Bjoerkman, J. Kessler, and M. Edoff, "Atomic layer deposition of $\mathrm{Zn_{1-x}Mg_xO}$ buffer layers for $\mathrm{Cu(In,Ga)Se_2}$ solar cells," *Progress in Photovoltaics: Research and Applications*, vol. 15, no. 3, pp. 225–235, 2007.

[27] N. F. Cooray, K. Kushiya, A. Fujimaki, I. Sugiyama, T. Miura, D. Okumura, M. Sato, M. Ooshita, and O. Yamase, "Large area ZnO films optimized for graded band-gap $\mathrm{Cu(InGa)Se_2}$-based thin-film mini-modules," *Solar energy materials and solar cells*, vol. 49, no. 1, pp. 291–297, 1997.

[28] U. Rau and H. W. Schock, “$\mathrm{Cu(In,Ga)Se_2}$ solar cells,” *Clean Electricity from Photovoltaics*, pp. 277–292, 2001.

[29] B. Dimmler and H. Schock, “Scaling-up of CIS technology for thin-film solar modules,” *Progress in Photovoltaics: Research and Applications*, vol. 4, no. 6, pp. 425–433, 1996.

[30] V. Probst, F. Karg, J. Rimmasch, W. Riedl, W. Stetter, H. Harms, and O. Eibl, “Advanced stacked elemental layer process for $\mathrm{Cu(InGa)Se_2}$ thin film photovoltaic devices,” in *MRS Proceedings*, vol. 426, p. 165, Cambridge Univ Press, 1996.

[31] C. Molpeceres, S. Lauzurica, J. Ocana, J. Gandia, L. Urbina, and J. Carabe, “Microprocessing of ITO and a-Si thin films using ns laser sources,” *Journal of Micromechanics and Microengineering*, vol. 15, no. 6, p. 1271, 2005.

[32] R. Murison, C. Dunsky, M. Rekow, C. Dinkel, J. Pern, L. Mansfield, T. Panarello, and S. Nikumb, “CIGS P1, P2, P3 laser scribing with an innovative fiber laser,” in *Photovoltaic Specialists Conference (PVSC), 2010 35th IEEE*, pp. 179–184, 2010.

[33] F. Pern, L. Mansfield, S. Glynn, B. To, C. DeHart, S. Nikumb, C. Dinkel, M. Rekow, R. Murison, T. Panarello, *et al.*, “All-laser scribing for thin-film $\mathrm{CuInGaSe_2}$ solar cells,” in *Photovoltaic Specialists Conference (PVSC), 2010 35th IEEE*, pp. 003479–003484, IEEE, 2010.

[34] U. Rau and H. Schock, “Chapter IC-3–$\mathrm{Cu(In,Ga)Se_2}$ thin-film solar cells,” *Solar Cells*, pp. 261–304, 2013.

[35] P. Gecys, G. Raciukaitis, M. Ehrhardt, K. Zimmer, and M. Gedvilas, “ps-laser scribing of CIGS films at different wavelengths,” *Applied Physics A*, vol. 101, no. 2, pp. 373–378, 2010.

[36] G. Heise, A. Heiss, H. Vogt, and H. P. Huber, “Ultrafast lasers improve the efficiency of CIS thin film solar cells,” *Physics Procedia*, vol. 39, pp. 702–708, 2012.

[37] B. Audoly, “Stability of straight delamination blisters,” *Physical Review Letters*, vol. 83, no. 20, p. 4124, 1999.

[38] J. W. Hutchinson and Z. Suo, “Mixed mode cracking in layered materials,” *Advances in applied mechanics*, vol. 29, no. 63, p. 191, 1992.

[39] H. Yin, R. Huang, K. Hobart, J. Liang, Z. Suo, S. Shieh, T. Duffy, F. Kub, and J. Sturm, “Buckling suppression of SiGe islands on compliant substrates,” *Journal of Applied Physics*, vol. 94, no. 10, pp. 6875–6882, 2003.

[40] H. Chai, C. D. Babcock, and W. G. Knauss, “One dimensional modelling of failure in laminated plates by delamination buckling,” *International Journal of Solids and Structures*, vol. 17, no. 11, pp. 1069–1083, 1981.

[41] D. Nir, “Stress relief forms of diamond-like carbon thin films under internal compressive stress,” *Thin solid films*, vol. 112, no. 1, pp. 41–50, 1984.

[42] G. Gille, “Strength of thin films and coatings,” *Current topics in materials science*, vol. 12, pp. 420–471, 1985.

[43] A. G. Evans and J. W. Hutchinson, "On the mechanics of delamination and spalling in compressed films," *International Journal of Solids and Structures*, vol. 20, no. 5, pp. 455–466, 1984.

[44] A. S. Argon, V. Gupta, H. S. Landis and J. A. Cornie, "Intrinsic toughness of interfaces between SiC coatings and substrates of Si or C fibre," *Journal of materials science*, vol. 24, no. 4, pp. 1207–1218, 1989.

[45] G. A. J. Amaratunga and M. E. Welland, "Electron beam defined delamination and ablation of carbon-diamond thin films on silicon," *Journal of Applied Physics*, vol. 68, no. 10, pp. 5140–5145, 1990.

[46] A. Föppl, "Vorlesungen uber technische Mechanik, Die wichtigsten Lehren der hoheren Elastizitatstheorie. B. G. Teubner, Leipzig," vol. 5, 1907.

[47] T. V. Karman, "Encyklopadie der Mathematischen Wissenschaften," 1910.

[48] S. Timoshenko, "Theory of Plates and Shells," *Mc Graw-Hill*, 1940.

[49] H. L. Langhaar, *Energy methods in applied mechanics*. John Wiley & Sons Inc, 1962.

[50] G. Gioia and M. Ortiz, "Delamination of compressed thin films," *Adv. Appl. Mech*, vol. 33, pp. 119–192, 1997.

[51] B. Audoly, B. Roman, and A. Pocheau, "Secondary buckling patterns of a thin plate under in-plane compression," *The European Physical Journal B-Condensed Matter and Complex Systems*, vol. 27, no. 1, pp. 7–10, 2002.

[52] F. Paumier, R. Gaboriaud, and C. Coupeau, "Buckling phenomena in Y_2O_3 thin films on GaAs substrates," *Applied physics letters*, vol. 82, p. 2056, 2003.

[53] K. M. Crosby and R. M. Bradley, "Pattern formation during delamination and buckling of thin films," *Physical Review E*, vol. 59, no. 3, p. R2542, 1999.

[54] T. Murotani, H. Hirose, T. Sasaki, and K. Okazaki, "Study on stress measurement of PVD-coating layer," *Thin Solid Films*, vol. 377, pp. 617–620, 2000.

[55] J. S. Wang and A. G. Evans, "Measurement and analysis of buckling and buckle propagation in compressed oxide layers on superalloy substrates," *Acta Materialia*, vol. 46, no. 14, pp. 4993–5005, 1998.

[56] X. C. Zhang, F. Z. Xuan, Y. K. Zhang and S. T. Tu, "Multiple film cracking in film/substrate systems with mismatch strain and applied strain," *Journal of Applied Physics*, vol. 104, no. 6, p. 063520, 2008.

[57] M. D. Thouless, J. W. Hutchinson and E. G. Liniger, "Plane-strain, buckling-driven delamination of thin films: model experiments and mode-II fracture," *Acta metallurgica et materialia*, vol. 40, no. 10, pp. 2639–2649, 1992.

[58] G. Parry, C. Coupeau, J. Colin, A. Cimetière, and J. Grilhé, "Buckling and post-buckling of stressed straight-sided wrinkles: experimental AFM observations of bubbles formation and finite element simulations," *Acta materialia*, vol. 52, no. 13, pp. 3959–3966, 2004.

[59] G. Parry, A. Cimetière, C. Coupeau, J. Colin, and J. Grilhé, "Stability diagram of unilateral buckling patterns of strip-delaminated films," *Physical Review E*, vol. 74, no. 6, p. 066601, 2006.

[60] G. Parry, J. Colin, C. Coupeau, F. Foucher, A. Cimetière, and J. Grilhé, "Effect of substrate compliance on the global unilateral post-buckling of coatings: AFM observations and finite element calculations," *Acta materialia*, vol. 53, no. 2, pp. 441–447, 2005.

[61] F. Foucher, C. Coupeau, J. Colin, A. Cimetière, and J. Grilhé, "How does crystalline substrate plasticity modify thin film buckling?," *Physical review letters*, vol. 97, no. 9, p. 096101, 2006.

[62] J. Dundurs, "Dependence of stress on Poisson's ratio in plane elasticity," *International Journal of Solids and Structures*, vol. 3, no. 6, pp. 1013–1021, 1967.

[63] C. Harrison, C. M. Stafford, W. Zhang, and A. Karim, "Sinusoidal phase grating created by a tunably buckled surface," *Applied Physics Letters*, vol. 85, no. 18, pp. 4016–4018, 2004.

[64] M. Watanabe, H. Shirai, and T. Hirai, "Wrinkled polypyrrole electrode for electroactive polymer actuators," *Journal of Applied Physics*, vol. 92, no. 8, pp. 4631–4637, 2002.

[65] S. P. Lacour, S. Wagner, Z. Huang, and Z. Suo, "Stretchable gold conductors on elastomeric substrates," *Applied Physics Letters*, vol. 82, no. 15, pp. 2404–2406, 2003.

[66] C. M. Stafford, C. Harrison, K. L. Beers, A. Karim, E. J. Amis, M. R. VanLandingham, H.-C. Kim, W. Volksen, R. D. Miller, and E. E. Simonyi, "A buckling-based metrology for measuring the elastic moduli of polymeric thin films," *Nature materials*, vol. 3, no. 8, pp. 545–550, 2004.

[67] E. A. Wilder, S. Guo, S. Lin-Gibson, M. J. Fasolka, and C. M. Stafford, "Measuring the modulus of soft polymer networks via a buckling-based metrology," *Macromolecules*, vol. 39, no. 12, pp. 4138–4143, 2006.

[68] C. M. Stafford, B. D. Vogt, C. Harrison, D. Julthongpiput, and R. Huang, "Elastic moduli of ultrathin amorphous polymer films," *Macromolecules*, vol. 39, no. 15, pp. 5095–5099, 2006.

[69] T. W. Shield, K. S. Kim and R. T. Shield, "The buckling of an elastic layer bonded to an elastic substrate in plane strain," *Journal of Applied Mechanics*, vol. 61, no. 2, pp. 231–235, 1994.

[70] J. Groenewold, "Wrinkling of plates coupled with soft elastic media," *Physica A: Statistical Mechanics and its Applications*, vol. 298, no. 1, pp. 32–45, 2001.

[71] Z. Y. Huang, W. Hong and Z. Suo, "Nonlinear analyses of wrinkles in a film bonded to a compliant substrate," *Journal of the Mechanics and Physics of Solids*, vol. 53, no. 9, pp. 2101–2118, 2005.

[72] H. Mei, R. Huang, J. Y. Chung, C. M. Stafford, and H.-H. Yu, "Buckling modes of elastic thin films on elastic substrates," *Applied Physics Letters*, vol. 90, no. 15, p. 151902, 2007.

[73] R. Huang, C. M. Stafford, and B. D. Vogt, "Effect of surface properties on wrinkling of ultrathin films," *Journal of Aerospace Engineering*, vol. 20, no. 1, pp. 38–44, 2007.

[74] C. Coupeau, “Atomic force microscopy study of the morphological shape of thin film buckling,” *Thin Solid Films*, vol. 406, no. 1, pp. 190–194, 2002.

[75] M. Moon, H. M. Jensen, J. W. Hutchinson, K. Oh, and A. Evans, “The characterization of telephone cord buckling of compressed thin films on substrates,” *Journal of the Mechanics and Physics of Solids*, vol. 50, no. 11, pp. 2355–2377, 2002.

[76] B. Cotterell, “The past, present, and future of fracture mechanics,” *Engineering fracture mechanics*, vol. 69, no. 5, pp. 533–553, 2002.

[77] H.-H. Yu and J. W. Hutchinson, “Influence of substrate compliance on buckling delamination of thin films,” *International Journal of Fracture*, vol. 113, no. 1, pp. 39–55, 2002.

[78] L. Freund and S. Suresh, “Thin films materials,” 2003.

[79] J. W. Hutchinson and Z. Suo, “Mixed mode cracking in layered materials,” *Advances in applied mechanics*, vol. 29, no. 63, p. 191, 1992.

[80] J. B. Pethica, R. Hutchings, and W. C. Oliver, “Hardness measurement at penetration depths as small as 20 nm,” *Philosophical Magazine A*, vol. 48, no. 4, pp. 593–606, 1983.

[81] M. F. Doerner and W. D. Nix, *A method for interpreting the data from depth-sensing indentation instruments.* PhD thesis, 1986.

[82] W. Oliver and G. Pharr, *An improved technique for determining hardness and elastic modulus using load and displacement sensing indentation experiments.* PhD thesis, 1992.

[83] P. Bertrand-Lambotte, J. Loubet, C. Verpy, and S. Pavan, “Nano-indentation, scratching and atomic force microscopy for evaluating the mar resistance of automotive clearcoats: study of the ductile scratches,” *Thin Solid Films*, vol. 398, pp. 306–312, 2001.

[84] M. Bamber, K. Cooke, A. Mann, and B. Derby, “Accurate determination of Young’s modulus and Poisson’s ratio of thin films by a combination of acoustic microscopy and nanoindentation,” *Thin Solid Films*, vol. 398, pp. 299–305, 2001.

[85] W. J. Chou, G. P. Yu and J. H. Huang, “Mechanical properties of TiN thin film coatings on 304 stainless steel substrates,” *Surface and Coatings Technology*, vol. 149, no. 1, pp. 7–13, 2002.

[86] H. C. Barshilia and K. S. Rajam, “Characterization of Cu/Ni multilayer coatings by nanoindentation and atomic force microscopy,” *Surface and Coatings Technology*, vol. 155, no. 2-3, pp. 195–202, 2002.

[87] A. Bolshakov and G. M. Pharr, “Influences of pileup on the measurement of mechanical properties by load and depth sensing indentation techniques,” *Journal of Materials Research*, vol. 13, pp. 1049–1058, 1998.

[88] J. C. Hay, A. Bolshakov, and G. M. Pharr, “A critical examination of the fundamental relations used in the analysis of nanoindentation data,” *Journal of Materials Research*, vol. 14, pp. 2296–2305, 1999.

[89] G. M. Pharr and A. Bolshakov, “Understanding nanoindentation unloading curves,” *Journal of Materials Research*, vol. 17, pp. 2660–2671, 2002.

[90] N. Chollacoop, M. Dao, and S. Suresh, "Depth-sensing instrumented indentation with dual sharp indenters," *Acta Materialia*, vol. 51, no. 13, pp. 3713–3729, 2003.

[91] Z. Shan and S. K. Sitaraman, "Elastic-plastic characterization of thin films using nanoindentation technique," *Thin Solid Films*, vol. 437, no. 1-2, pp. 176– 81, 2003.

[92] J. D. Bressan, A. Tramontin and C. Rosa, "Modeling of nanoindentation of bulk and thin film by finite element method," *Wear*, vol. 258, no. 1-4, pp. 115–122, 2005. Second International Conference on Erosive and Abrasive Wear.

[93] G. M. Pharr and W. C. Oliver, *Measurement of Thin Film Mechanical Properties Using Nanoindentation*. PhD thesis, 7 1992.

[94] F. Frolich, P. Grau, and W. Grellmann, "Performance and analysis of recording microhardness tests," *Physica Status Solidi (a)*, vol. 42, no. 1, pp. 79–89, 1977.

[95] D. Newey, M. A. Wilkins and H. M. Pollock, "An ultra-low-load penetration hardness tester," *Journal of Physics E: Scientific Instruments*, vol. 15, no. 1, pp. 119–122, 1982.

[96] W. C. Oliver and G. M. Pharr, "Measurement of hardness and elastic modulus by instrumented indentation: Advances in understanding and refinements to methodology," *Journal of Materials Research*, vol. 19, pp. 3–20, 2004.

[97] B. N. Lucas, W. C. Oliver and J. E. Swindeman, "The dynamics of frequency-specific, depth-sensing indentation testing," in *MRS Proceedings*, vol. 522, p. 3, Cambridge Univ Press, 1998.

[98] S. I. Bulychev and V. P. Alekhin *Industrial laboratory*, pp. 1091–1096, 1988.

[99] I. N. Sneddon, "The relation between load and penetration in the axisymmetric boussinesq problem for a punch of arbitrary profile," *International Journal of Engineering Science*, vol. 3, no. 1, pp. 47–57, 1965.

[100] A. Love, "Boussinesq's problem for a rigid cone," *The Quarterly Journal of Mathematics*, no. 1, pp. 161–175, 1939.

[101] A. E. H. Love, "The stress produced in a semi-infinite solid by pressure on part of the boundary," *Philosophical Transactions of the Royal Society of London. Series A, Containing Papers of a Mathematical or Physical Character*, pp. 377–420, 1929.

[102] J. W. Harding and I. N. Sneddon, "The elastic stresses produced by the indentation of the plane surface of a semi-infinite elastic solid by a rigid punch," *Mathematical Proceedings of the Cambridge Philosophical Society*, vol. 41, pp. 16–26, 6 1945.

[103] I. N. Sneddon and F. Transforms, "McGraw Hill Book Co," *Inc., New York*, 1951.

[104] C.-M. Cheng (Zheng Zhemin) and Y.-T. Cheng, "On the initial unloading slope in indentation of elastic-plastic solids by an indenter with an axisymmetric smooth profile," *Applied Physics Letters*, vol. 71, no. 18, pp. 2623–2625, 1997.

[105] M. Troyon and S. Lafaye, "About the importance of introducing a correction factor in the sneddon relationship for nanoindentation measurements," *Philosophical Magazine*, vol. 86, no. 33-35, pp. 5299–5307, 2006.

[106] J. B. Pethica and W. C. Oliver, "Tip Surface Interactions in STM and AFM," *Physica Scripta*, vol. 1987, no. T19A, p. 61, 1987.

[107] J. B. Pethica and W. C. Oliver, "Mechanical properties of nanometre volumes of material: use of the elastic response of small area indentations," in *MRS Proceedings*, vol. 130, p. 13, Cambridge Univ Press, 1988.

[108] J. E. Jakes, C. R. Frihart, J. F. Beecher, R. J. Moon, and D. Stone, "Experimental method to account for structural compliance in nanoindentation measurements," *Journal of materials research*, vol. 23, no. 04, pp. 1113–1127, 2008.

[109] A. A. Griffith, "The phenomena of rupture and flow in solids," *Philosophical transactions of the royal society of london. Series A, containing papers of a mathematical or physical character*, pp. 163–198, 1921.

[110] P. Schreurs, "Lecture notes-course 4A780 Concept version," *Materials Technology*, 2012.

[111] G. R. Irwin, "Analysis of stresses and strains near the end of a crack traversing a plate," *SPIE MILESTONE SERIES MS*, vol. 137, pp. 167–170, 1997.

[112] D. Dugdale, "Yielding of steel sheets containing slits," *Journal of the Mechanics and Physics of Solids*, vol. 8, no. 2, pp. 100–104, 1960.

[113] G. I. Barenblatt, "The mathematical theory of equilibrium cracks in brittle fracture," *Advances in applied mechanics*, vol. 7, no. 1, pp. 55–129, 1962.

[114] C. E. Inglis, "Trans. Inst. Naval Arch," *Engineering*, vol. 95, 1913.

[115] A. C. Fischer-Cripps and I. Mustafaev, *Introduction to contact mechanics*. Springer, 2000.

[116] A. Griffith, "The phenomena of flow and rupture in solids: Phil," *Trans. Roy. Soc. Lond. Ser. A*, vol. 221, pp. 163–98, 1920.

[117] H. Westergaard, "Bearing Pressures and Cracks," *Journal of applied mechanics*, 1939.

[118] I. N. Sneddon, "The distribution of stress in the neighbourhood of a crack in an elastic solid," in *Proceedings of the Royal Society of London A: Mathematical, Physical and Engineering Sciences*, vol. 187, pp. 229–260, The Royal Society, 1946.

[119] M. Williams, "On the stress distribution at the base of a stationary crack," 1997.

[120] T. L. Anderson and T. Anderson, *Fracture mechanics: fundamentals and applications*. CRC press, 2005.

[121] G. R. Irwin, "Fracture dynamics," *Fracturing of metals*, vol. 152, 1948.

[122] B. R. Lawn, *Fracture of brittle solids*. Cambridge university press, 1993.

[123] D. M. Marsh, "Plastic flow and fracture of glass," *Proceedings of the Royal Society of London. Series A, Mathematical and Physical Sciences*, pp. 33–43, 1964.

[124] K. L. Johnson and K. L. Johnson, *Contact mechanics*. Cambridge university press, 1987.

[125] B. N. Norden, "On the compression of a cylinder in contact with a plane surface," *Interagency Report*, pp. 73–243, 1973.

[126] O. Allix and P. Ladevèze, “Interlaminar interface modelling for the prediction of delamination,” *Composite Structures*, vol. 22, no. 4, pp. 235–242, 1992.

[127] O. Allix and A. Corigliano, “Modeling and simulation of crack propagation in mixed-modes interlaminar fracture specimens,” *International Journal of Fracture*, vol. 77, no. 2, pp. 111–140, 1996.

[128] G. T. Camacho and M. Ortiz, “Computational modelling of impact damage in brittle materials,” *International Journal of Solids and Structures*, vol. 33, no. 20-22, pp. 2899–2938, 1996.

[129] J. L. Chaboche, R. Girard and A. Schaff, “Numerical analysis of composite systems by using interphase/interface models,” *Computational Mechanics*, vol. 20, no. 1-2, pp. 3–11, 1997.

[130] A. Corigliano, “Formulation, identification and use of interface models in the numerical analysis of composite delamination,” *International Journal of Solids and Structures*, vol. 30, no. 20, pp. 2779–2811, 1993.

[131] A. Corigliano and M. Ricci, “Rate-dependent interface models: formulation and numerical applications,” *International Journal of Solids and Structures*, vol. 38, no. 4, pp. 547–576, 2001.

[132] L. Daudeville and P. Ladevèze, “A damage mechanics tool for laminate delamination,” *Composite Structures*, vol. 25, no. 1-4, pp. 547–555, 1993.

[133] Y. Mi, M. A. Crisfield, G. A. O. Davies and H. B. Hellweg, “Progressive delamination using interface elements,” *Journal of composite materials*, vol. 32, no. 14, pp. 1246–1272, 1998.

[134] A. Needleman, “An analysis of tensile decohesion along an interface,” *Journal of the Mechanics and Physics of Solids*, vol. 38, no. 3, pp. 289–324, 1990.

[135] V. Tvergaard and J. W. Hutchinson, “The relation between crack growth resistance and fracture process parameters in elastic-plastic solids,” *Journal of the Mechanics and Physics of Solids*, vol. 40, no. 6, pp. 1377–1397, 1992.

[136] V. Tvergaard and J. W. Hutchinson, “The influence of plasticity on mixed mode interface toughness,” *Journal of the Mechanics and Physics of Solids*, vol. 41, no. 6, pp. 1119 – 1135, 1993.

[137] X. P. Xu and A. Needleman, “Numerical simulations of fast crack growth in brittle solids,” *Journal of the Mechanics and Physics of Solids*, vol. 42, no. 9, pp. 1397–1434, 1994.

[138] G. I. Barenblatt and G. P. Cherepanov, “On brittle cracks under longitudinal shear,” *Journal of Applied Mathematics and Mechanics*, vol. 25, no. 6, pp. 1654–1666, 1961.

[139] E. T. Christensen, J. H. Sjolund and J. A. Glud, “Formulation of Cohesive Finite Element for Analysing Strength of Wrinkles in Glass-Epoxy Laminates,” Master’s thesis, Design of Mechanical Systems, Aalborg University, 2013.

[140] G. Alfano and M. A. Crisfield, “Finite element interface models for the delamination analysis of laminated composites: mechanical and computational issues,” *International journal for numerical methods in engineering*, vol. 50, no. 7, pp. 1701–1736, 2001.

[141] B. Canava, J. F. Guillemoles, J. Vigneron, D. Lincot and A. Etcheberry, "Chemical elaboration of well defined $\mathrm{Cu(In,Ga)Se_2}$ surfaces after aqueous oxidation etching," *Journal of Physics and Chemistry of Solids*, vol. 64, no. 9-10, pp. 1791–1796, 2003. 13th International Conference on Ternary and Multinary Compounds.

[142] Agilent Technologies, *Data sheet on Agilent Nano Indenter G200*, July 2009.

[143] R. Henning, *Data sheet on mechanical needle unit.* JENOPTIK Automatisierungstechnik GmbH, July 2011.

[144] Pizosystem Jena, *Data sheet on PZ 200 OEM / PZ, compact 1-axis translation stage*, March 2012.

[145] ME-Meßsysteme GmbH, *Data sheet on Multi-axis force sensor K3D60*, Nov. 2014.

[146] A. M. James and M. P. Lord, *VNR index of chemical and physical data.* Van Nostrand Reinhold, 1992.

[147] H. Mei, S. Gowrishankar, K. M. Liechti, and R. Huang, "Initiation and propagation of interfacial delamination in integrated thin-film structures," in *12th IEEE Intersociety Conference onThermal and Thermomechanical Phenomena in Electronic Systems (ITherm)*, pp. 1–8, 2010.

[148] Y.-C. Lin, X.-Y. Peng, L.-C. Wang, Y.-L. Lin, C.-H. Wu, and S.-C. Liang, "Residual stress in CIGS thin film solar cells on polyimide: simulation and experiments," *Journal of Materials Science: Materials in Electronics*, vol. 25, no. 1, pp. 461–465, 2014.

[149] S. Luo, J.-H. Lee, C.-W. Liu, J.-M. Shieh, C.-H. Shen, T.-T. Wu, D. Jang, and J. R. Greer, "Strength, stiffness, and microstructure of $\mathrm{Cu(In,Ga)Se_2}$thin films deposited via sputtering and co-evaporation," *Applied Physics Letters*, vol. 105, no. 1, 2014.

[150] A. Buzás and Z. Geretovszky, "Nanosecond laser-induced selective removal of the active layer of $\mathrm{cuingase_2}$ solar cells by stress-assisted ablation," *Phys. Rev. B*, vol. 85, p. 245304, Jun 2012.

[151] M. A. Hopcroft, W. D. Nix, and T. W. Kenny, "What is the Young's Modulus of Silicon?," *Journal of Microelectromechanical Systems*, vol. 19, no. 2, pp. 229–238, 2010.

[152] C. A. Schneider, W. S. Rasband, and K. W. Eliceiri, "NIH Image to ImageJ: 25 years of image analysis," *Nature methods*, vol. 9, no. 7, pp. 671–675, 2012.

[153] T. J. Collins *et al.*, "Imagej for microscopy," *Biotechniques*, vol. 43, no. 1 Suppl, pp. 25–30, 2007.

[154] J. Koo, S. C. Kim, H. Park, and W. K. Kim, "$\mathrm{Cu(InGa)Se_2}$ thin film photovoltaic absorber formation by rapid thermal annealing of binary stacked precursors," *Thin Solid Films*, vol. 520, no. 5, pp. 1484–1488, 2011.

[155] H. Park, S. C. Kim, S.-H. Lee, J. Koo, S. H. Lee, C.-W. Jeon, S. Yoon, and W. K. Kim, "Effect of precursor structure on $\mathrm{Cu(InGa)Se_2}$ formation by reactive annealing," *Thin Solid Films*, vol. 519, no. 21, pp. 7245–7249, 2011.

[156] J. Koo, S. Jeon, M. Oh, H.-i. Cho, C. Son, and W. K. Kim, “Optimization of Se layer thickness in Mo/CuGa/In/Se precursor for the formation of $\mathrm{Cu(InGa)Se_2}$ by rapid thermal annealing,” *Thin Solid Films*, vol. 535, pp. 148–153, 2013.

[157] W. K. Kim, E. A. Payzant, S. Yoon, and T. J. Anderson, “In situ investigation on selenization kinetics of Cu–In precursor using time-resolved, high temperature X-ray diffraction,” *Journal of crystal growth*, vol. 294, no. 2, pp. 231–235, 2006.

[158] S. Nishiwaki, N. Kohara, T. Negami, and T. Wada, “$\mathrm{MoSe_2}$ layer formation at $\mathrm{Cu(In,Ga)Se_2/Mo}$ Interfaces in High Efficiency $\mathrm{Cu(In_{1-x}Ga_x)Se_2}$ Solar Cells,” *Japanese Journal of Applied Physics*, vol. 37, no. 1A, p. L71, 1998.

Erklärung

Hiermit versichere ich, dass ich die vorliegende Arbeit selbstständig durchgeführt und verfasst habe. Außer den in der Arbeit genannten, standen mir keinerlei Hilfsmittel oder Hilfen zuteil. Die benutzten fremden Quellen habe ich vollständig aufgelistet und inhaltliche oder wörtliche Zitate als solche gekennzeichnet.

Die Dissertation wurde an keiner anderen Hochschule oder Universität eingereicht.

Shashi Bahl
Halle (Saale), March 2016

Acknowledgements

First of all, I would like to thank my supervisors Prof. Dr. Jörg Bagdahn and Prof. Dr. Roland Scheer for the guidance, discussions, comments, and support extended to me during this whole research period. Their encouragement and the critical reviews helped me immensely in shaping this thesis to meet their expectations.

I would like to thank warmly to Prof. Dr.-Ing. Stephan Schönfelder for his help, guidance, patience and advice. His enthusiastic and unremitting support during this course of time, and his teaching will benefit me in future, to which I show my greatest respect and most sincere gratitude from the core of my heart.

I extend my special thanks to Prof. Dr. Nobert Bernhard who supported me at all times in every administrative aspect, organizing all formal matters and clarifying questions.

I am thankful to Kai Kaufmann and Georg Lorenz for their kind support and guidance during the nanoindentation and mechanical scribing experiments of my doctoral research. I am highly grateful for their constant encouragement with wide range of ideas, support and discussions.

I deeply acknowledge the company of my colleagues during my doctoral research. They were great and I never felt lonely because of them only. Here I must specially mention the name of Felix Kaule and Marcus Oswald. They always put forward useful ideas and views regarding my work and helped me whenever the need prevailed.

My special thanks goes to my family. Words cannot express how grateful I am to all my family members. The loving support of my parents has been beyond words. My brother has always been a good source of creative inspiration for me. My wife has been a source of inspiration, guidance and support for me during the time of my doctoral research. Of course it is not out of place to mention the force of motivation which I received from my son and daughter to perform better for their future.

Publications

1. S. Bahl, K. Kufmann, S. Schönfelder and J. Bagdahn, Investigations and Modeling for Mechanical Scribing of CIGS Thin-Film Solar Cells, in Proceedings 28th European Photovoltaic Solar Energy Conference and Exhibition (EU-PVSEC), Paris (France), 2430-2434 (2009).
2. S. Bahl, K. Kufmann, S. Schönfelder and J. Bagdahn, Investigations and Modeling for Mechanical Scribing of CIGS Thin-Film Solar Cells, in 4th PV Symposium on Photovoltaic and Energy Transition, Bitterfeld-Wolfen (Germany) (2013).
3. S. Bahl, K. Kufmann, S. Schönfelder and J. Bagdahn, Simulation and Experimental Investigations for Mechanical Structuring of CIGS Thin-Film Solar Cells, in Proceedings 15th Young Scientists Conference (NWK 15), Magdeburg-Stendel (Germany), 159-165 (2014).

Curriculum vitae

First Name	Shashi
Family Name	Bahl
Date of Birth	October 20, 1977
Place of Birth	Gurdaspur, India
Nationality	India

EDUCATION

1996-2000	Bachelor of Technology, Mechanical Engineering Dr. B.R. Ambedkar National Institute of Technology Jalandhar, India
2007-2009	Master of Technology, Mechanical Engineering Indian Institute of Technology Roorkee Roorkee, India
2012-2016	Doctor of Philosophy at Institute of Physics Martin-Luther-University Halle-Wittenberg, Germany

---

PROFESSIONAL EXPERIENCE

2001-2007	Maharishi Markandeshwar Engineering College Mullana, India
2010-2012	Inder Kumar Gujral Punjab Technical University Kapurthala, India
2012-2015	Anhalt University of Applied Sciences, Köthen, Germany & Fraunhofer Center for Silicon Photovoltaics, Halle, Germany

---

Shashi Bahl

Halle (Saale), March 2016